

W.H. MASON

AFFDL-TR-77-122  
VOLUME I

**AN AUTOMATED PROCEDURE FOR COMPUTING THE  
THREE DIMENSIONAL TRANSONIC FLOW OVER  
WING-BODY COMBINATIONS, INCLUDING  
VISCIOUS EFFECTS**

**VOLUME I  
DESCRIPTION OF ANALYSIS METHODS AND APPLICATIONS**

*GRUMMAN AEROSPACE CORPORATION  
BETHPAGE, NEW YORK 11714*

FEBRUARY 1977

TECHNICAL REPORT AFFDL-TR-77-122, VOLUME I  
FINAL REPORT FOR PERIOD 1 MAY 1975 - 1 OCTOBER 1977

Approved for public release; distribution unlimited

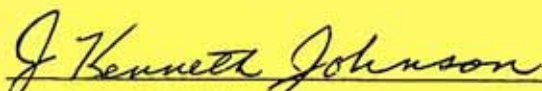
AIR FORCE FLIGHT DYNAMICS LABORATORY  
AIR FORCE WRIGHT AERONAUTICAL LABORATORIES  
AIR FORCE SYSTEMS COMMAND  
WRIGHT-PATTERSON AIR FORCE BASE, OHIO 45433

NOTICE

When Government drawings, specifications, or other data are used for any purpose other than in connection with a definitely related Government procurement operation, the United States Government thereby incurs no responsibility nor any obligation whatsoever; and the fact that the government may have formulated, furnished, or in any way supplied the said drawings, specifications, or other data, is not to be regarded by implication or otherwise as in any manner licensing the holder or any other person or corporation, or conveying any rights or permission to manufacture, use, or sell any patented invention that may in any way be related thereto.

Approved for public release; distribution unlimited.

This technical report has been reviewed and is approved for publication.



J. Kenneth Johnson  
Project Engineer



Dr. Thomas M. Weeks  
Supervisor

FOR THE COMMANDER



Alfred C. Draper  
Assistant for Research and Technology  
Aeromechanics Division

Copies of this report should not be returned unless return is required by security considerations, contractual obligations, or notice on a specific document.

REPORT DOCUMENTATION PAGE		READ INSTRUCTIONS BEFORE COMPLETING FORM
1. REPORT NUMBER AFFDL-TR-77-122, Volume I	2. GOVT ACCESSION NO.	3. RECIPIENT'S CATALOG NUMBER
4. TITLE (and Subtitle) AN AUTOMATED PROCEDURE FOR COMPUTING THE THREE-DIMENSIONAL TRANSONIC FLOW OVER WING-BODY COMBINATIONS, INCLUDING VISCOUS EFFECTS; VOLUME I DESCRIPTION OF ANALYSIS METHODS AND APPLICATIONS		5. TYPE OF REPORT & PERIOD COVERED FINAL REPORT MAY 1975 - OCTOBER 1977
		6. PERFORMING ORG. REPORT NUMBER
7. AUTHOR(s) WILLIAM H. MASON                      WILLIAM F. BALLHAUS* DONALD MACKENZIE                      JUANITA FRICK** MARK STERN		8. CONTRACT OR GRANT NUMBER(s)  F33615-75-C-3073
9. PERFORMING ORGANIZATION NAME AND ADDRESS GRUMMAN AEROSPACE CORPORATION BETHPAGE, NEW YORK 11714		10. PROGRAM ELEMENT, PROJECT, TASK AREA & WORK UNIT NUMBERS PROGRAM ELEMENT      62201F PROJECT 1476, TASK 147601 WORK UNIT 14760127
11. CONTROLLING OFFICE NAME AND ADDRESS AIR FORCE FLIGHT DYNAMICS LABORATORY WRIGHT-PATTERSON AIR FORCE BASE, OHIO 45433		12. REPORT DATE FEBRUARY 1978
		13. NUMBER OF PAGES 218
14. MONITORING AGENCY NAME & ADDRESS (if different from Controlling Office)		15. SECURITY CLASS. (of this report)  UNCLASSIFIED
		15a. DECLASSIFICATION/DOWNGRADING SCHEDULE
16. DISTRIBUTION STATEMENT (of this Report) Approved for public release; distribution unlimited.		
17. DISTRIBUTION STATEMENT (of the abstract entered in Block 20, if different from Report)		
18. SUPPLEMENTARY NOTES  *AMES RESEARCH CENTER, NASA and                      ** INFORMATICS-PMI, INC. AEROMECHANICS LAB, U.S. ARMY AVIATION R&D COMMAND      PALO ALTO, CALIFORNIA MOFFETT FIELD, CALIFORNIA		
19. KEY WORDS (Continue on reverse side if necessary and identify by block number)  AIRCRAFT AERODYNAMICS JETS, WAKES AND VISCID-INVISCID FLOW INTERACTIONS SUBSONIC AND TRANSONIC FLOW		
20. ABSTRACT (Continue on reverse side if necessary and identify by block number) This report describes a numerical method to predict the detailed pressure distribution and force and moment results for wing-body combinations at transonic Mach numbers less than one. The resulting computer code has been developed with the intent of providing the user with an easy to use and reliable tool that produces the most accurate possible engineering predictions. The basic inviscid prediction method is the modified transonic small disturbance theory program developed by Ballhaus, Bailey and Frick. In order to provide		

20. ABSTRACT (Continued)

accurate surface pressure predictions on the wing, several additional features of the typical transonic flow field have been incorporated. These consist of the viscous displacement effect, local strong viscous interaction at the shock wave foot and at the trailing edge (including an approximate treatment of local shallow separations), and finally, the interaction effect of the fuselage.

## FOREWORD

This final report was prepared by the Aerodynamics Section of the Grumman Aerospace Corporation, Bethpage, New York for the Flight Mechanics Division, Air Force Flight Dynamics Laboratory, Wright-Patterson Air Force Base, Ohio. The work was performed under Contract No. F33615-75-C-3073, which was initiated under Project No. 1476, "Advanced Wing-Body Aerodynamic Analysis and Design." Mr. J. Kenneth Johnson (FXM) was the Project Monitor of this contract.

The report consists of three volumes. Volume I, entitled "Description of Analysis Methods and Applications," describes the methods used to predict surface pressure distributions and aerodynamic forces on three-dimensional wing-body combinations at transonic speeds, including viscous effects. Volume I also contains an extensive set of comparisons between numerical predictions and experimental results. Detailed instructions required to use the program are provided in Volume II, "User's Manual and Code Description." Volume III was written at Sybucon, Inc., Atlanta, Georgia and contains a complete description of the theory and program that computes the full three-dimensional boundary layer over the wing. This work was performed by Sybucon under subcontract to Grumman Aerospace. Although this program operates independently of the program described in Volume II, the input data set required for the full three-dimensional boundary layer computation is generated by the code documented in Volume II.

Mr. F. Berger was the Program Manager; Dr. W. Mason and Mr. D. MacKenzie served as Project Engineers. The work was performed in close cooperation with the co-authors from the NASA Ames Research Center, Dr. W. F. Ballhaus and Ms. J. Frick. Additional contributors to the project included G. Simpers, A. Vachris, D. Raila, P. Aidala, M. Sturm and A. Bunnell of Grumman, and Drs. F. R. Bailey and T. Holst of NASA Ames. Moreover, contributions have been made by A. Chen of Boeing, Drs. R. Melnik, B. Grossman and G. Volpe of the Grumman Research Department and Grumman Consultants Prof. A. Jameson, Prof. J. Werner and Dr. E. Murman. As noted above, the three-dimensional boundary layer program was written by Dr. J. Nash and Dr. R. Scruggs of Sybucon, Inc.

TABLE OF CONTENTS

SECTION	PAGE
I. ANALYSIS METHODS . . . . .	1
1. Introduction . . . . .	1
2. Inviscid Calculation Method . . . . .	5
3. Viscous Calculation Method . . . . .	14
4. Coupling of Inviscid and Viscous Programs . . . . .	38
a) General . . . . .	38
b) Shock Boundary-Layer Interaction Effects. . . . .	47
c) Separation Treatment . . . . .	62
5. Body Model . . . . .	64
6. Transonic Wave Drag on Swept Wings . . . . .	72
a) General . . . . .	72
b) Exact Expression for Lift and Drag . . . . .	73
c) First and Higher Order Expansions . . . . .	75
d) The Drag Integral . . . . .	79
e) Wave Drag . . . . .	81
7. Fully Three-Dimensional Boundary Layer Calculation . . . . .	87
II. APPLICATIONS . . . . .	89
1. Introduction . . . . .	89
2. Experiences and Limitations of the Code - How To Successfully Run the Code . . . . .	90
3. Examples of Configurations Computed and Typical Agreement With Experiment . . . . .	95
a) ONERA M6 . . . . .	97
b) RAE "A" . . . . .	98
c) L54H18 . . . . .	99
d) TN D712 . . . . .	100
e) L51F07 . . . . .	100
f) A55B21 . . . . .	101
g) Forward Swept Wing . . . . .	102
h) Low Aspect Ratio, Highly Tapered . . . . .	102
i) Transonic Transport . . . . .	103
j) Advanced Fighter . . . . .	104
k) Summary . . . . .	104

4.	Detailed Data Comparisons - TACT and F-8 . . . . .	138
	a) TACT . . . . .	138
	b) F-8 . . . . .	154
5.	Common Input/Output . . . . .	168
	a) Introduction . . . . .	168
	b) Common I/O - - A Systems Viewpoint . . . . .	168
	c) Common I/O - - The Aerodynamicist . . . . .	169
	d) Common I/O - - NASF . . . . .	170
	e) QUICK - - A Baseline Code for Generating Body Definition . . . . .	170
	f) Wing Definition . . . . .	172
	g) Feasibility of Including Graphical Results . . . . .	172
	h) Common Output . . . . .	172
	i) Recommendations For Common I/O . . . . .	173
6.	Design Feasibility . . . . .	177
	a) Introduction . . . . .	177
	b) Review of Design Process . . . . .	178
	c) Review of 2-D Transonic Design Methods . . . . .	180
	d) Review of 3-D Transonic Design Methods . . . . .	183
	e) Application of the 3-D Transonic Program to Wing Design Problems. . . . .	185
	f) A Practical Approach to an Intermediate Design Code. . . . .	188
	g) Conclusions on Design Feasibility . . . . .	190
III.	CONCLUSIONS . . . . .	197
IV.	RECOMMENDATIONS FOR FUTURE WORK . . . . .	199
	REFERENCES . . . . .	201

LIST OF ILLUSTRATIONS

FIGURE	PAGE
1. Semispan Wing . . . . .	13
2. Wing Planform Transformation . . . . .	13
3. Infinite Yawed Wing Notation . . . . .	25
4. Effect of Wing Sweep on Boundary Layer Development . . . . .	26
5. Comparison with the Nash Test Case $C_L = .15$ . . . . .	27
6. Comparison with the Nash Test Case $C_L = .50$ . . . . .	28
7. Comparison with Adams 3-D Test Case Zero Lift . . . . .	29
8. Comparison with Adams 3-D Test Case $C_L = 0.74$ Case . . . . .	30
9. Comparison with the Compressible Adams Test Case $\delta^*/c, \theta/c$ . . . . .	31
10. Comparison with the Compressible Adams Test Case $C_{fx}$ . . . . .	32
11. Comparison of Bradshaw 3-D Program and Modified Chordwise Methods . . . . .	33
12. Comparison of Modified Chordwise and 3-D Calculation Methods . . . . .	34
13. Flat Plate Results - $0^\circ$ and $45^\circ$ Sweep . . . . .	35
14. Spanwise Component of Shear Stress at Wall . . . . .	36
15. Spanwise Component of Wall Shear Stress . . . . .	37
16. Some Viscous-Inviscid Interactions in Transonic Flow . . . . .	44
17. Examples of Viscous Flow Solutions . . . . .	45
18. Types of Shock - Turbulent Boundary Layer Interactions . . . . .	53
19. Pressure Rise Across Shocks . . . . .	54
20. Yoshihara's Viscous Wedge Model . . . . .	55
21. Shock Polar . . . . .	56
22. Rubber Wall Model . . . . .	57
23. Comparison of Empirical & Theoretical Models . . . . .	58
24. Implementation . . . . .	59
25. Example of Viscous Wedge Effect . . . . .	60
26. Shock Boundary Layer Interaction Effects . . . . .	61
27. Schematic of Boundary Conditions Support Surface . . . . .	67
28. Simple Body Input for Infinite Body Boundary Condition Surface . . . . .	68
29. Equivalent Body Source Model . . . . .	69
30. Wing-Body Interaction Effects - Geometry & Wing Pressures . . . . .	70



LIST OF ILLUSTRATIONS (Contd)

31. Wing-Body Interaction Effects - Comparison of Pressures at the Wing-Body Junction . . . . .	71
32. ONERA M6 . . . . .	105
33. RAE "A" With Body . . . . .	109
34. L54H18A . . . . .	113
35. TN D-712 . . . . .	117
36. L51F07 . . . . .	121
37. A55B21 . . . . .	125
38. Forward Swept Wing . . . . .	127
39. Low Aspect Ratio . . . . .	129
40. Transonic Transport . . . . .	131
41. Advanced Fighter . . . . .	134
42. Three-View Drawing of TACT Supercritical Wing Airplane . . . . .	141
43. TACT Wing Section Streamwise Profile Near Midspan . . . . .	141
44. TACT Wing Twist . . . . .	142
45. TACT Wing Aeroelastic Twist Increments . . . . .	142
46. TACT Wing Pressure Orifice Locations . . . . .	143
47. TACT Wing Aeroelastic Effects . . . . .	144
48. TACT Comparison Case $M=0.9, \alpha=5.2^\circ$ . . . . .	148
49. TACT Comparison Case $M=0.85, \alpha=8^\circ$ . . . . .	151
50. Local Trailing Edge and Cove Separation . . . . .	153
51. Three-View Drawing of F-8 Supercritical Wing Airplane . . . . .	157
52. F-8 Wing Section Streamwise Profile Near Midsemispan . . . . .	157
53. F-8 Wing Twist . . . . .	158
54. Location of Wing Pressure Orifices on F-8 . . . . .	159
55. Tunnel and Flight Test Spanload for NASA F-8 . . . . .	160
56. F-8 Comparison Case $M=0.9, \alpha=4^\circ$ . . . . .	162
57. F-8 Comparison Case $M=0.99, \alpha=3^\circ$ . . . . .	165
58. Typical Point Design Data Flow . . . . .	174
59. Typical Design Data Flow Requirements . . . . .	175
60. QUICK Geometry . . . . .	176
61. Advanced Airfoil Synthesis . . . . .	191
62. Low $C_{m_0}$ Tailored Airfoil . . . . .	192
63. Inviscid Drag Minimization . . . . .	193
64. Wing Drag Minimization . . . . .	194
65. Wing Design Example . . . . .	196

LIST OF TABLES

TABLE		PAGE
I	EXAMPLE CONFIGURATIONS	96

LIST OF SYMBOLS

A	Influence coefficient matrix
AR	Aspect ratio
a	Speed of sound
$C_D$	Coefficient of drag
$C_f$	Coefficient of skin friction
$C_L$	Coefficient of lift
$C_p$	Coefficient of pressure
$C^*$	Leading edge transition parameter
c	Local chord
$\bar{c}$	Mean aerodynamic chord
D	Total drag
F(x)	Body shape in Murman Bump
$\hat{i}$	Unit vector in x direction
K	Transonic similarity parameter
L	Total lift
M	Mach number
$M_\infty$	Freestream Mach number
n	Exponent in Mach number relation in governing equation
P	Pressure
q	Velocity in expansion
Re	Reynolds Number
$\bar{S}$	Area of boundary condition support surface
S(x)	Local cross-section area of body
$S_L, S_c,$ $S_{wake}$	Regions for integration
s	Arc length
$U_e$	Edge velocity

LIST OF SYMBOLS (Continued)

$u_{1,2,etc.}$	Shock velocities
$V_{c_{j,k}}$	Finite difference expression in transonic equation
$W_e$	Spanwise edge velocity in yawed wing coordinate system
$w_{1,2,etc.}$	Shock velocities
$\bar{w}_{s1_{max}}$	Crossflow profile in boundary layer
$x,y,z$	Aircraft coordinate system
$\tilde{x},\tilde{y},\tilde{z}$	Yawed wing coordinate system

Subscripts

exp	Experiment
LE	Leading edge
max	Maximum
n	Streamwise coordinate
pre	Prediction
s	Perpendicular to streamwise coordinate
sonic	Sonic condition
TE	Trailing edge
w	Wall

Greek

$\alpha$	Angle-of-attack
$\alpha_{eff}$	Effective angle-of-attack
$\alpha_{geo}$	Geometric angle-of-attack
$\gamma$	Ratio of specific heats
$\delta$	Boundary layer thickness
$\delta^*$	Displacement thickness
$\delta^2 \epsilon^2$	Expansion parameters
$\bar{\delta}_x$	Ballhaus finite difference notation
$\epsilon$	Convergence criterion
$\phi$	Potential
$\eta$	$y/\text{span}$

LIST OF SYMBOLS (Continued)

$\Lambda$	Sweep angle
$\lambda$	Cosine between yawed wing direction and streamline direction
$\tau$	Shear stress
$\omega$	Relaxation factor
$\rho$	Density
$\theta$	Momentum thickness
$\theta_z$	Momentum thickness in yawed spanwise direction
$\xi$	Planform grid
$\chi$	Cross flow transition parameter
$\nu$	Viscosity

## SECTION I

### ANALYSIS METHODS

#### 1. INTRODUCTION

This report describes a numerical method of predicting the detailed pressure distribution and integrated forces and moments for wing-body combinations at transonic Mach numbers less than one. The resulting computer code has been developed with the intent of providing the user with a convenient, accurate and reliable engineering tool. The basic inviscid prediction method is the modified transonic small disturbance theory program developed by Ballhaus, Bailey and Frick (Reference 1). To provide accurate surface pressure predictions on the wing, several additional features of the typical transonic flow-field have been incorporated. These consist of the viscous displacement effect, local strong viscous interaction at the shock wave foot and at the trailing edge (including an approximate treatment of local shallow separations), and the interaction effect of the fuselage.

The resulting code is a synthesis of the best methods available at the initiation of the study, and represents contributions of a number of different individuals throughout the U. S. and British Aerospace community. The program has been applied to a large number of cases for which experimental data is available, and to several examples of extreme geometric configurations for which the method will operate successfully, although no data is available. The experience gained during the effort has been used to reduce the complexity of the program input to a simple practical form, allowing the user to concentrate on the aerodynamic aspects of the analysis. The program should not be expected to produce results if there are significant regions of separated flow, and this fact can be used to determine the limits of the program applicability for any particular case. Body effects are incorporated into the program by providing an infinite rectangular cross-section upon which the fuselage slopes are applied. Suitable modification of these slopes is made via slender body theory to take into account the transfer of the boundary condition from the fuselage surface to the rectangular cross-section boundary condition support surface. In addition, the program is assembled in a modular form that allows for an easy upgrading as various improved analysis methods become available.

Practical numerical methods for transonic flows became available in the early seventies, as a result of the pioneering work by Murman and Cole (Reference 2),

who introduced the concept of the "mixed differencing" relaxation method for the solution of the transonic small disturbance equation. The standard two-dimensional analysis program quickly became the Jameson (Reference 3) circle plane program, which provides a numerical solution of the full potential equation over arbitrary airfoil sections. It was soon determined that for airfoils with a significant degree of aft loading, the effects of the boundary layer had to be included in order to obtain good agreement with data. Bavitz (Reference 4) produced one of the first programs that iteratively computed the inviscid and boundary layer flows until a converged viscous solution was obtained. These methods all contain some empiricism at the trailing edge to account for the local strong interaction and wake effects, neither of which were included in the calculations. Recently, Melnik, Chow and Mead (Reference 5) developed a theory that explicitly includes these effects. However, the present three-dimensional method employs an empirical model consistent with the earlier two-dimensional methods. This situation exists, in general, with three-dimensional methods which, as might be expected, are not developed to the same level of sophistication as the two-dimensional methods at any particular time.

Three-dimensional transonic flow calculation methods were initially developed by F. R. Bailey and W. F. Ballhaus at the NASA Ames Research Center, using the classical transonic small disturbance equations. A three-dimensional method that solved the full potential equation was later developed by Jameson (Reference 6) for three-dimensional wings. Other programs to predict three-dimensional transonic flows have been developed by Hall (Reference 7) and co-workers at the RAE, and Schmidt (Reference 8) and co-workers at Dornier in Germany. Experience with the classical transonic small disturbance theory for wings with moderate to large sweep indicated that some refinement had to be incorporated into the small disturbance theory in order to properly simulate swept shock waves. The first modifications were proposed by Lomax (Reference 9), et al., and it is this particular equation which has been implemented in the baseline inviscid code employed in the present method. This inviscid code is also the only available method which can, at present, simulate relatively general fuselage configurations routinely. The code makes use of the embedded grid scheme developed by Boppe (Reference 10) in order to reduce the execution time and storage requirements, while retaining maximum accuracy on the surface.

Viscous effects are investigated and accounted for in the present method through two different approaches. The full viscous-inviscid iteration is carried out assuming a boundary layer of the infinite swept wing type at each span station, augmented by local treatments of the strong interaction regions at the shock foot and trailing edge, and regions with shallow separations. In addition to this calculation, an entirely new program has been written by Nash and Scruggs (Reference 11) to compute the fully three-dimensional laminar and/or turbulent boundary layer on finite wings. The Nash-Scruggs program is not fully coupled with the inviscid calculation, however, the inviscid/strip viscous program will automatically produce the input data set for the 3-D BL program. The resulting 3-D boundary layer prediction is then tabulated in a form that allows for the generation of a data deck that could be used to make a fully 3-D correction to the actual airfoil ordinates. The only other reported effort to automatically combine viscous and inviscid flow calculation at transonic speeds is the work by Schmidt and Hedman (Reference 12), which presents calculations for conventional airfoils only. Kordulla (Reference 13) has also investigated the coupling of a 3-D boundary layer method with the Bailey-Ballhaus Program.

The present method is described in a three volume report. Volume I describes the theoretical foundation of the various elements of the method and how they are combined into a single computer program. No attempt is made to repeat the excellent and detailed theoretical descriptions contained in the references. Instead, the volume concentrates on providing the user with a practical overview of the methods and a working knowledge of those aspects of the methods which the user can control. Such aspects are seldom detailed in the theoretical papers. This volume also contains a large number of examples of the application of the program to a complete range of aircraft configurations. These include correlations on the F-8 and TACT aircraft. The volume concludes with some observations on the general integration of computational aerodynamic tools into a uniform system with common input and output sets, and an examination of the potential applications to the design problem using the present analysis program as a baseline method. Volume II contains the detailed instructions required for program operation, including a review of the output results and the associated notation/definition. The first part also contains a sample case which should provide a complete illustration of the use of the program. The second part of this volume contains a description of the actual computer

program in sufficient detail so that a user can learn the code well enough to make modifications. The three-dimensional boundary layer method is treated as an independent program and is entirely described in Volume III. That volume contains both the theoretical description and the user's manual and code description.



## 2. INVISCID CALCULATION METHOD

The inviscid transonic flowfield prediction is obtained using the current version of the small disturbance theory program developed at NASA Ames. This program has been under constant development for a number of years, as reported in a series of publications. The work has now reached a relatively mature stage of development and forms the basis for the present method, which is intended to be used as a reliable engineering tool. The program was developed on the CDC 7600 computer and the structure of the code reflects the requirements of that particular machine. It can, however, be readily converted to operate on IBM machines that have an operating system with the VS feature. The program is big and long running by present engineering standards (although these are changing rapidly), so that users will require access to moderately advanced computers. Although the detailed machine requirements are discussed in Volume II, the user should study the method with these considerations in mind.

The present section is intended to provide the salient features of the method, along with a candid description of the assumptions and approximations that have been adopted. Recall that transonic small disturbance theory is valid in a double limit as  $M_\infty \rightarrow 1$ ,  $\delta \rightarrow 0$ , where  $M_\infty$  is a freestream Mach number and  $\delta$  is a measure of the disturbance size such as the thickness to chord ratio of the basic airfoil. Ballhaus (Reference 14) has recently reviewed the 3-D small disturbance theory in the general context of contemporary transonic aerodynamics and the review is recommended as an excellent introduction to the intricacies of the 3-D small disturbance methods.

A modified form of the small disturbance equation (MSD) is included as the basic option in the code. Its use is recommended for the treatment of flows about configurations with swept wings (References 9 and 1). The MSD equation, written in conservation form, is

$$\left[ (1-M_\infty^2)\phi_x - \left(\frac{\gamma+1}{2}\right) M_\infty^n \phi_x^2 + \frac{1}{2} (\gamma-3) M_\infty^2 \phi_y^2 \right]_x + \left[ \phi_y - (\gamma-1) M_\infty^2 \phi_x \phi_y \right]_y + \left[ \phi_z \right]_z = 0 \quad (1)$$

where  $\phi$  is the disturbance potential,  $\gamma$  is the ratio of specific heats, and  $M_\infty$  is the freestream Mach number.

Figure 1 indicates the orientation of the vehicle with respect to the coordinate system. Note that the program computes the flowfield in the wind axis system. The parameter "n" that appears as an exponent of the Mach number in the coefficient of the traditional non-linear transonic term can be used to improve the small disturbance approximation to the correct shock jump conditions. The value of  $n = 1.75$  has been found very satisfactory for the calculations performed thus far ( $n = 2$  being the classical value).

The solution of equation (1) subject to the boundary conditions specified below is obtained by approximating the terms by finite differences and solving the resulting set of algebraic equations by successive line overrelaxation (SLOR) in a computational mesh space.

The wing boundary conditions are applied at the wing reference plane, which forms a slit between mesh lines in the computational space. The linearized boundary condition is modified in order to include a Krupp-type scaling (Reference 15), which has been found necessary to provide good results:

$$\phi_z(x,y,\pm 0) = \frac{1}{M_\infty} \frac{1}{4} \left\{ \frac{dz}{dx}(x,y,\pm 0) - \alpha \right\} \quad (2)$$

The computational mesh is truncated at a distance several wing spans from the wing, and the potential is specified by the asymptotic farfield formula given by Klunker (Reference 16). Only that part of the potential due to the aircraft lift is specified, the rest of the contributions being of higher order. Recall that in three-dimensions, the potential decays as  $(1/r)$ , while in 2-D, the potential varies as  $\log(r)$ , where  $r$  is the origin of the wing/airfoil system. This indicates that the asymptotic matching between the numerical and analytical value of the potential is not as critical in 3-D flows as for 2-D transonic flows. The trailing vortex sheet extends downstream in the plane of the wing. Although initially the Trefftz plane problem was solved explicitly at the downstream boundary, it was found numerically simpler to require  $\phi_x = 0$  at the downstream boundary. This procedure is automatically equivalent to the traditional Trefftz plane boundary condition.

Once the computation is completed, the value of the pressure coefficient is determined from the standard linearized relationship.

$$C_p = -2 \phi_x \quad (3)$$

The numerical solution scheme devised by Murman and Cole (Reference 2) is an elegantly simple method that manages to capture the physical characteristics of a flowfield which contains regions of both supersonic and subsonic flow. When the local flow is subsonic and hence, governed by an elliptic partial differential equation locally, central difference finite difference approximations are employed. When the flow is locally supersonic, the locally hyperbolic nature of the governing equation is enforced by the use of an upwind finite difference approximation for the  $\phi_{xx}$  term in the classical transonic small disturbance theory. Equation (1) differs from the classical small disturbance equation (CSD) by the addition of the two underlined terms, which come from the full-potential equation.

These two terms introduce some additional complexity into the finite-difference algorithm for supersonic regions. For the CSD equation, the x-coordinate is the axis of the characteristic cone. Thus, upwind differencing the x derivatives and central differencing the y and z derivatives leads to a numerical domain of dependence that always includes the mathematical domain of dependence; consequently, a necessary condition for stability is maintained. However, for the MSD equation, the characteristic cone axis lies in a direction that corresponds to the local flow direction. To maintain stability, domains of dependence requirements are satisfied by proper combinations of central and upwind differences.

The proper combination of central and upwind differences can be determined by expressing the principal part of the governing equation in an intrinsic coordinate system (Reference 6).

$$(a^2 - q^2) \phi_{ss} + a^2 \phi_{nn} + a^2 \phi_{zz} = 0 \quad (4)$$

where q and a are particle and sound speeds, and s and n are the local stream and stream-normal directions in the x-y plane. The  $\phi_{xx}$ ,  $\phi_{xy}$  and  $\phi_{yy}$  contributions to  $\phi_{ss}$  are upwind differenced and the remaining terms are central differenced. The terms in equation (4) can be written, approximately, in the form

$$(a^2 - q^2)/a_\infty^2 = 1 - M_\infty^2 - (\delta + 1) M_\infty^n \phi_x$$

$$\phi_{ss} = \phi_{xx} + 2 \phi_y \phi_{xy}$$

$$a^2/a_\infty^2 = 1 - (\delta - 1) M_\infty^2 \phi_x$$

$$\phi_{nn} = -2 \phi_y \phi_{xy} + \phi_{yy} \quad (5)$$

The mixed central-upwind difference procedure is implemented in the following way. To begin with, all terms in the equation are centrally differenced. Then a test is performed to determine if the flow is supersonic. The supersonic condition is (approximately) from equation (5),  $(a^2 - q^2)/a_\infty^2 < 0$ . If the flow is supersonic, the following terms are added to the previously computed central difference approximation to equation (1).

$$\left\{ \Delta x \bar{\delta}_x (V_{c_{j,k}} \delta_{xx}) + 2 \phi_y V_{c_{j,k}} \left[ \bar{\delta}_x (v \bar{\delta}_y + (1-v) \bar{\delta}_y) - \delta_{xy} \right] \right\} \phi_{j,k} \quad (6)$$

where  $\delta_{xx}$  and  $\delta_{xy}$  are central difference operators that operate on  $\phi_{j,k}$  to give  $\phi_{xx}$  and  $\phi_{xy}$ ;  $\delta_x$  is an operator such that  $\delta_x A_{i,j} = \Delta x^{-1} (A_{i,j} - A_{i-1,j})$ ;  $\bar{\delta}_y$  and  $\bar{\delta}_y$  are similar forward and backward difference operators in the y direction;  $V_{c_{j,k}}$  is a finite-difference approximation to  $1 - M_\infty^2 - (\gamma + 1) M_\infty^n \phi_x$ ; and  $v = \begin{pmatrix} 0 \\ 1 \end{pmatrix}$  for  $\phi_y (\leq)$  zero. Note that the first term in equation (6) is treated conservatively; the other term, the one involving  $\phi_{xy}$ , is not. The differencing in equation (6) is complicated by the use of the wing planform transformation but can be implemented in a direct manner.

The resulting equations are solved by a line overrelaxation scheme that marches through the flowfield along vertical lines, starting at the upstream boundary and proceeding to each downstream mesh plane by working outward from the center line to the outboard limit of the mesh. The general mathematical theory of relaxation applied to the solution of partial differential equations of mixed type in transonic flows has been discussed in some detail by Jameson in References 17 and 18.

Although the mathematical problem has been fully described above, several additional refinements are introduced in order to obtain a rapid, practical and reliable numerical solution scheme. These include the choice of meshes,

a numerical transformation to a coordinate system more closely aligned with the planform, a proper choice of the overrelaxation factor  $\omega$ , and a leading edge boundary condition modification via Riegels' Rule\* in order to improve the accuracy of the solution in regions where the local coordinate system is not aligned with the leading edge. The next several paragraphs describe the purpose, implementation and use of these refinements in sufficient detail for the user to gain enough insight and understanding to work with the program.

The choice of computational mesh can have an important effect on the accuracy and cost of the inviscid solution. The program internally generates a mesh system which has been found to provide a good solution at reasonable computing time. However, the user can override the internal mesh with an input mesh of his own choice. The program requires two basic mesh systems in order to obtain the solution using the Boppe (Reference 10) embedded mesh scheme. An exterior coarse Cartesian mesh is used over most of the computational domain and an embedded fine mesh is employed in a region very near the wing surface, where the flow gradients are large and the solution is of the most interest. The embedded mesh is placed in a coordinate system locally aligned with the planform.

In general, the exterior mesh should extend about 10 root chords above, below, fore and aft of the wing. The present program allows for a maximum of 20 vertical, 20 spanwise and 30 streamwise stations. At each span station, at least four streamwise mesh stations should occur on the wing in the crude grid. This requirement usually leads to the use of the maximum 30 streamwise mesh stations. The typical span mesh contains about two-thirds of the mesh within the wing tip, with the tip centered between mesh lines and the mesh widening rapidly as the distance outboard of the wing tip increases. The vertical mesh is normally placed symmetrically about the wing plane with the first mesh points about 10% of the reference chord above and below the wing. All meshes should vary smoothly. Specifically, the second difference of the mesh spacings should vary smoothly.

---

\* Although the relationship of Riegels' Rule to subsonic small disturbance theory is well understood (see Reference 19), its use in transonic small disturbance theory is purely ad hoc at present. Nevertheless, it has been found to aid in obtaining the solution for some cases. Numerical studies have shown that Riegels' Rule virtually eliminates any mesh dependence on the solution.

The fine mesh is much denser and is confined to a region close to the wing. Typically, the mesh extends  $1/3 \sim 1/2$  chord length upstream and downstream of the wing, about 10% of the semispan past the tip and about two chords above and below the wing. The vertical mesh is symmetrically placed about the wing with the first mesh points about  $1 \sim 2\%$  above and below the surface. The typical values for the inner mesh are 20 vertical, 30 spanwise and 60 streamwise stations. The smooth variation of the fine mesh is especially crucial to the efficient operation of the program. Uneven meshes not only degrade the accuracy, but also have been found to cause numerical iteration convergence problems. These problems can cause the solution to become much more expensive due to a reduced convergence rate, and in some cases, even cause the solution to diverge. It is well known that solutions to the small disturbance equations are dependent on the mesh distribution near the leading edge. In addition, the exact solution of the equation contains a singularity at the leading edge and it has been shown that the exact solution of the small disturbance theory is not a good approximation to the full potential equation for a distance of several nose radii downstream of the leading edge (Reference 20). Hence, the mesh is usually distributed about the leading edge in a manner that leads to an incorrect solution of the small disturbance equation, but a better approximation to the full potential equation. This is typical of small disturbance solution methods.

The proper choice of coordinate system is important in obtaining accurate numerical solutions. In three-dimensional flows about wing-body combinations, the choice of a single coordinate system that is appropriate everywhere on the vehicle is extremely difficult. In fact, the study of coordinate systems and the resulting numerical meshes is presently the pacing item in the development of more advanced inviscid transonic programs. In fact, the latest Jameson/Caughey (Reference 21) program is significant in that the numerical procedure is independent of the specified coordinate system. The success of small disturbance theory in large part is due to the geometric simplification which arises from the transfer of the boundary condition to a planar coordinate surface. The Boppe embedded mesh scheme is also important to the success of the numerical method by allowing a dense mesh to be placed in the regions where it is actually required. Moreover, a "planform" coordinate system has been employed in the small disturbance theory by introducing a change of variables, which allows

for the spanwise variation of the planform shape. The appropriate mapping is,

$$\xi (x,y) = \frac{x - x_{\xi=0} (y)}{x_{\xi=1} (y) - x_{\xi=0} (y)} \quad (7)$$

$$\eta (y) = y$$

where  $x_{\xi=0} (y) = x_{LE} (y)$  and  $x_{\xi=1} (y) = x_{TE} (y)$  over the main part of the planform, allowing for the same number of mesh points to cover the airfoil at each span station, yielding a very efficient mesh distribution. A uniform spanwise distribution of the streamwise mesh about the leading edge is particularly important to eliminate wiggles. There are, however, some regions on the wing where the  $\xi = 0$  and  $\xi = 1$  lines do not correspond to the leading and trailing edges. Figure 2 shows the mapping in general, along with the special areas where the  $\xi = \text{constant}$  lines deviate from lines of constant percent chord. The main deviation occurs due to the requirement that the mapping intersect the fuselage side perpendicularly. This requirement leads to a departure of the  $\xi = 0$  line from the leading edge at the wing root juncture. For gloved configurations, this bending usually results in a loss of resolution of the solution in the vicinity of the body. Although the mapping and meshes are generated internally, the user can input his own mapping. This would allow for a special concentration of the mesh near the body and glove in cases where the user wishes to concentrate on the glove results. Leading edge sweep angles of up to  $70^\circ$  have been treated without difficulty during the present study.

Another feature of the present method is the use of an artificial time step in order to ensure a stable numerical scheme. This approach was first adopted by Jameson (Reference 6) for transonic flow solutions. The program assigns a numerical value for the degree of artificial time damping to be used. The automatically specified value can be overridden by the user if desired. In general, the larger the value of the damping factor, the more stable the iteration procedure, at the expense of a reduced convergence rate. Thus, the smallest value of damping which allows for stable convergence is the proper choice. Normally, the automatically specified value is a good compromise and it will not have to be adjusted except in highly unusual cases.

The same advice holds for the value of the overrelaxation factor  $\omega$  (always  $< 2$ .) which can be tuned for particular cases, but in general, will not require adjustment. We note that independent values of  $\omega$  and artificial time damping ( $\phi_{x_t}$  damping) can be specified for each mesh.



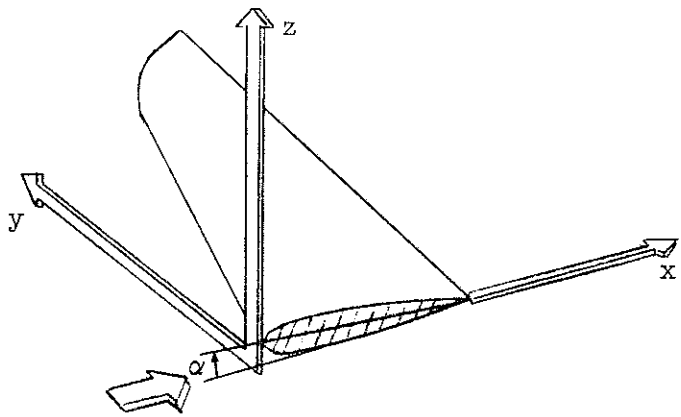


Figure 1 Semispan Wing

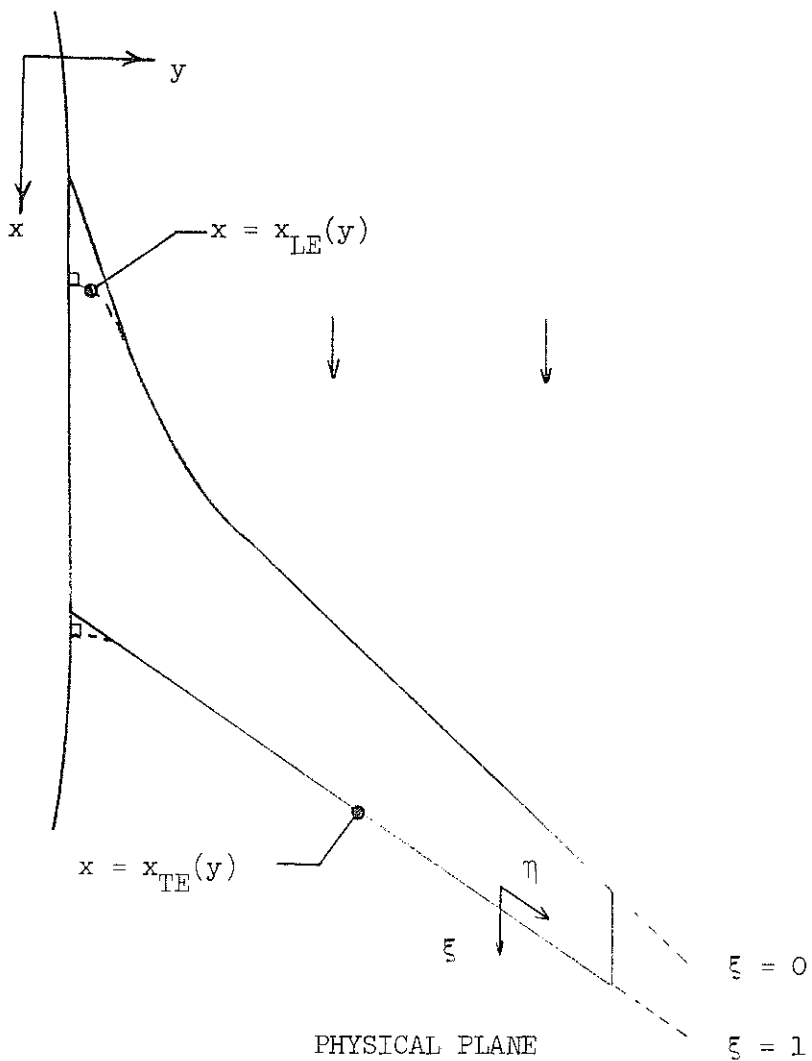


Figure 2 Wing Planform Transformation

### 3. VISCOUS CALCULATION METHOD

Viscous-inviscid interaction effects are predicted in the present method by iterating between the inviscid flow solution obtained in the manner described in the previous section and a boundary layer prediction obtained by assuming at each spanwise station that the boundary layer is of the infinite swept wing type. The resulting displacement thickness is then added to the airfoil ordinates in order to incorporate the weak interaction effects. The strong interaction effects, which require special treatment, at shock waves, the trailing edge and for locally shallow flow separations are described in the next section. In this section, we describe the approach used to obtain the infinite swept wing boundary layer prediction. A great deal of three-dimensional boundary layer methodology development work occurred concurrently with the development of the present program (including the contribution of Volume III of this report). The method adopted for the simulation of the three-dimensional viscous effects consisted of a simple extension to the method used successfully at Grumman in two-dimensions. Its availability allowed for immediate coupling with the inviscid program. Consideration of the replacement of this method with other emerging codes, such as the program contained in Volume III or the latest program by Professor Bradshaw (Reference 22), awaits an extensive assessment of all the new codes as well as a specific need for such a revision. This need was not demonstrated during the extensive code operation that was conducted during this effort.

The infinite yawed wing coordinate system is shown in Figure 3. This coordinate system is rotated by the sweep angle  $\Lambda$  from the coordinate system of the inviscid program. These rotated coordinates are denoted by  $\tilde{x}$ ,  $\tilde{y}$ ,  $\tilde{z}$ . Figure 4 shows results computed in the infinite yawed wing coordinated system and presented in the streamwise direction. The need for an infinite yawed wing type boundary layer calculation as opposed to a 2-D streamwise strip is brought out clearly. The computation of the boundary layer in the  $\tilde{x}$ ,  $\tilde{z}$  coordinate system can be computed as 2-D only if the flow is laminar and incompressible. This property is called the independence principle and it does not hold for turbulent boundary layers or compressible laminar boundary layers. However, it has been found (Reference 23) that for typical transonic boundary layers, the laminar boundary layer can be computed assuming the independence principle holds without making appreciable errors. This approach has been

used by Nash and Scruggs (Reference 24) for the computation of the transonic boundary layer development on the F-8 supercritical wing. It is also justified in view of the point transition model, the insensitivity of the turbulent boundary layer development to the details of the laminar-transition point calculation, and the small region of laminar flow on swept wings. Thus, the laminar boundary layer is computed in the present program by the method of Thwaites generalized for compressible flow using the inviscid flow normal to the leading edge. The turbulent boundary layer calculation does require modification in order to simulate the three-dimensional effects. We will use the modifications suggested by Nash and Tseng (Reference 25) for incompressible flow over an infinite yawed wing. Their analysis method is similar to the Bradshaw (Reference 26) analysis in use at Grumman in that an equation for the shear stress is solved along with the usual momentum and continuity equations. The extra equation in the Bradshaw method, as compared with algebraic eddy viscosity methods, provides the flexibility that allows the 2-D program to simulate the 3-D effects.

The modified chordwise method was devised based on the following features that Nash observed as a result of some numerical experiments for flow over an infinite yawed wing:

- o A 2-D calculation performed in the chordwise ( $\tilde{x}$ ) direction takes the effect of pressure gradients on the boundary layer development into account properly.
- o A 2-D calculation performed in the streamline direction would account for the shear stress direction and magnitude "properly."

By assuming that the shear acts in the local inviscid surface streamline direction throughout the shear layer, Nash has shown that the equation governing the chordwise component of shear stress is nearly identical to the usual two-dimensional shear stress equation. If we write the chordwise component of the shear stress as

$$\tau_{\tilde{x}} = \cos \left[ \tan^{-1} \frac{W_e}{U_e} \right] \cdot \tau = \lambda \tau \quad (8)$$

and assume that  $\lambda$  varies slowly in the  $\tilde{x}$ -direction compared to the shear stress change, then the equation for the shear stress is identical to the 2-D form,

with slightly modified forms of the Bradshaw empirical functions. These approximations are the basis of the modified chordwise method. The incorporation of this scheme into the 2-D Bradshaw program is straightforward. Equation (8) leads to the requirement that, at each point on the surface, the shear stress vector acts in the same direction all the way through the boundary layer. This approximation is acceptable for most cases except in the neighborhood of separation lines.

The possible compressibility effects were not considered by Nash. In the general 3-D scheme used for compressible flow over finite wings, Nash and Scruggs assume that the shear stress equation is unaltered by compressibility effects. This assumption is used in the equations solved by Nash and Scruggs in the full 3-D program described in Volume III. In the Bradshaw analysis employed in the 2-D calculation, an additional term arises in the turbulent kinetic energy equation due to compressible effects. This term introduces yet another empirical constant into the scheme. A numerical experiment was made in which this constant was set to zero (so that the extra compressibility term was omitted from the calculation). For transonic flow speeds, it was found that this term did not affect the results. Thus, although the term is retained in the present calculation method without alteration, the basic difference in the compressible turbulent shear stress equations used by Bradshaw and Nash does not appear in the predicted results at transonic flow conditions. The only modification to the method to take into account 3-D compressible effects arises in the use of the Crocco Integral in order to obtain the density variation. The density appears explicitly in the equations only through the combination  $(\partial\rho/\partial x_i)/\rho$ . Employing the Crocco Integral, this combination can be written as,

$$\frac{1}{\rho} \frac{\partial\rho}{\partial\tilde{y}} = r \left\{ \underbrace{1 + \frac{W}{U} \frac{\partial W/\partial\tilde{y}}{\partial U/\partial\tilde{y}}}_{\text{Additional factor due to 3-D flow effects.}} \right\} (\gamma-1) \frac{M_{\tilde{x}}^2(\tilde{x},\tilde{y})}{U} \frac{\partial U}{\partial\tilde{y}} \quad (9)$$

Additional factor due to 3-D flow effects.

For infinite yawed wings, we find no change in the  $\tilde{x}$ -direction expression due to 3-D effects. The additional factor in equation (9) requires a knowledge of the spanwise flowfield, which the modified chordwise method does not provide. Physically, the effect of neglecting the extra piece in the Crocco Integral is to keep the wall from reaching the full adiabatic wall temperature.

Comparison with a compressible solution shows that the modified chordwise technique predicts separation ( $\tau_{\tilde{x}} = 0$ ) before the 3-D solution. Recall that as the wall becomes warmer, the separation point moves forward. Hence, it appears that if the 3-D contribution shown in equation (9) were included in the modified chordwise solution agreement with the 3-D solution would not be improved. Thus, it appears that neglecting the 3-D contribution to the Crocco Integral is consistent with the other approximations in the method.

The remaining modification of the 2-D program to simulate 3-D effects requires the introduction of an effective Reynolds number which is found by requiring the component of the shear in the  $\tilde{x}$ -direction to bear the same relationship to an effective Reynolds number that the actual shear stress has to the specified Reynolds number. To find this effective Reynolds number, the Karman-Schoenherr formula was used so that the Reynolds number based on momentum thickness (which is specified at transition) was used. Compressibility effects were incorporated although Mach number effects on the value of the effective Reynolds number were found to be small. Typically, for a  $40^\circ$  sweep angle, the effective Reynolds number is about 40% of the actual Reynolds number.

Finally, as previously noted, it is important to realize that the solution in the spanwise direction cannot be computed using the modified chordwise technique, and some other method must be used to compute this information. An approximation for the spanwise component of shear stress can be obtained by making use of the observed features of the viscous flow over an infinite yawed wing and the chordwise solution. The first important observation is that the spanwise flow is basically "flat plate like" in nature since there is no spanwise pressure gradient (Reference 27). The second observation is that the spanwise and chordwise momentum thicknesses are roughly equal for the flow conditions at which the modified chordwise method is useful (Reference 28). Hence, we can assume that  $\tau_z$  can be related to  $\theta_z$  by a typical flat plate skin-friction formula. Here we pick the Squire-Young formula:

$$\frac{\tau_{wz}}{\rho_\infty W_\infty^2} = \frac{1}{[5.89 \log_{10} \{4.075 \bar{R}_e \left(\frac{\theta_z}{c}\right)\}]^2} \quad (10)$$

where  $\overline{Re}$  is the Reynolds number based on  $W_\infty$  and an effective viscosity found using the same method that Nash proposed for the effective "chordwise viscosity." The resulting values of  $\tau_{wz}$  are in rough agreement with other more exact prediction methods.

a. Boundary Layer Transition on Swept Wings

When the wing sweep angle is greater than about  $15^\circ$ , transition occurs due to three-dimensional instabilities basically different than those which cause transition in two-dimensional flow. Because the 3-D instabilities cause transition before the 2-D type instabilities are fully developed, transition criterion based on 2-D flows are of little value in 3-D flows. Adams (Reference 29) has reviewed the 3-D transition criterion. It appears that there are basically two parameters of engineering interest. The first parameter is used to determine if the boundary layer will be initially turbulent at the stagnation line and can be written as,

$$C^* = \tan \Lambda \sin \Lambda \frac{Re_{\bar{c}}}{d(U_e/U_\infty)/d(\bar{x}/c) \Big|_{\frac{\tilde{x}}{s} = 0}} \quad (11)$$

where  $\bar{x}$  is measured in the  $\tilde{x}$ -direction along the airfoil and  $s$  is the total arc length. If  $C^* > 4 \times 10^5$ , the boundary layer may be turbulent initially. If  $C^* > 1.4 \times 10^5$ , the boundary layer will remain turbulent if tripped.

The second parameter can be used to predict 3-D transition if the flow is laminar at the stagnation line. It is given as,

$$\chi = \left[ \frac{\bar{W}_{sl, \max}}{V_e} \right] Re_{e\delta} \quad (12)$$

where

$$Re_{e\delta} = \frac{\tilde{V}_e \delta}{\nu_e} \quad (13)$$

and  $\tilde{V}_e = \sqrt{U_e^2 + V_e^2}$ .  $\delta$  is the local boundary layer thickness.  $\bar{W}_{sl, \max}$  is the maximum crossflow when the boundary layer profile is calculated in the

streamline coordinate system. Transition is assumed to occur when  $X > X_{crit} \approx 175$ . In many cases,  $X_{crit}$  is found to occur very near the leading edge.

Attempts to estimate  $X$  assuming a Pohlhausen profile for the chordwise and spanwise velocity distributions led to poor correlation with the sample case presented by Adams (Reference 29). Because an accurate value of  $X$  can be found only if the crossflow profile is actually computed, transition based on  $X$  has not been included as an option in the basic modified chordwise boundary layer program. It can be computed using the more detailed program described in Volume III.

b. Comparisons with Nash and Tseng Results (Reference 25)

Figures 5 and 6 show the comparison between the modified chordwise method results and the fully three-dimensional (incompressible) predictions of Nash and Tseng (Reference 24) for a  $35^\circ$  untapered swept wing with an NACA 65<sub>1</sub>A012 airfoil. This is the case for which the modified chordwise method was originally developed, and as might be expected, we find excellent agreement. In Figure 5, the displacement thickness agrees closely with the full 3-D calculation and the difference in the initial shear stress development may be due to the difference in the transition calculation. Also shown on the figure is a calculation made assuming a two-dimensional boundary layer with the same pressure distribution. The 2-D calculations underpredict both displacement thickness and shear stress by approximately 6-10%. Figure 6 is for the same wing at an increased lift coefficient. The same conclusions and trends can be seen for this case. As would be expected, the good agreement with shear stress becomes poor near the trailing edge. The  $\delta^*$  prediction remains excellent, however. When the flow approaches separation, the simulation of 3-D effects by the 2-D program becomes poor. This is due to the fundamental difference between 2-D and 3-D flowfields near separation lines. However, these results indicate that the growth of the error is confined to regions within 2 or 3% of separation.

c. Comparison with Experiment and Other Prediction Methods

Figures 7 and 8 provide comparisons with one of the few cases for which experimental results are available; incompressible flow over a  $45^\circ$  swept wing with an NACA 63<sub>1</sub>-012 airfoil. The data is reproduced from NACA TN 2500 (Reference 28). Also included is the prediction of Adams (Reference 29) three-

dimensional eddy-viscosity method. Figure 7 presents the zero lift case. The agreement between both prediction methods and the experimental results are good, with the modified chord method actually better for the deltastar results. Since no comparisons for skin friction are available, these predictions of the modified chordwise method have not been included. Figure 8 presents the results for the lifting airfoil case. Also included on this figure is the prediction of the Bradshaw (Reference 30) incompressible 3-D program. Under these more severe conditions, all the prediction methods underpredict the displacement and momentum thickness. The 3-D Bradshaw and Adams methods are very nearly identical, while the modified chordwise method lies slightly below the predictions of the other methods. Agreement with experiment is better for the momentum thickness than the displacement thickness. The underprediction of the displacement thickness by the modified chordwise method compared to the 3-D Bradshaw method is a trend found in all comparisons to date.

#### d. Comparisons for a Compressible Flow Case

It appears that no experimental results are available for compressible flow over an infinite swept wing. Thus, Figures 9 and 10 present a comparison between a  $30^\circ$  swept wing compressible case given by Adams (Reference 29) and the results of the modified chordwise method. No transition location was specified and some numerical experimentation indicated that a transition point located at  $.022c$  produced the initial conditions indicated in the results presented by Adams. The displacement thickness predictions are in good agreement and the momentum thickness predictions are in excellent agreement. Figure 10 shows the comparisons for the chordwise component of shear stress. Again we see that the skin friction prediction deteriorates as separation is approached. Since separation actually occurs, the shear stress results are in worse agreement than in the previous cases. Nevertheless, the separation prediction is within 3% of the Adams prediction. Again, note that even near separation the deltastar prediction is in reasonably close agreement with Adams. Although the  $30^\circ$  sweep angle may seem moderate, it is typical of the midchord sweep angles encountered in practice.



e. Parametric Study of the Effect of Sweep, Including Comparison With The Bradshaw 3-D Program (Incompressible)

Figures 11 and 12 show the results of a parametric study in which the zero sweep pressure distribution of the Nash-Tseng airfoil and Reynolds number were held constant, while the sweep angle  $\Lambda$  was varied from  $0^\circ \rightarrow 60^\circ$ , and simple sweep theory was used to predict the actual chordwise pressure distribution. Cases were run for both the modified chordwise and 3-D Bradshaw programs. Figure 11a shows the comparison between 3-D and modified chordwise programs for a case at zero sweep. At this sweep angle, the modified chord procedure is reduced to the standard 2-D compressible Bradshaw program. This shows that the two different programs produce slightly different results, independent of the modified chordwise procedure. This small difference shows the typical differences between different numerical implementations of the same basic theory. Figure 11b shows the displacement thickness distribution for  $\Lambda = 50^\circ$ . An increase in the difference between the two methods occurs with the modified chord method underpredicting the growth boundary layer. Because of the good agreement with the Nash 3-D method, these calculations represent a comparison between the Bradshaw and Nash 3-D methods. The disagreement could be attributed to the difference in the basic assumption in the methods. Bradshaw allows the shear stress vector to act in a different direction than the velocity vector's normal gradient. Nash assumes that both act in the same direction. Thus, we have obtained a quantitative measure of the difference in the results produced by the two different methods.

Figure 12 shows the difference between the modified chord method and the incompressible Bradshaw 3-D method as a function of the sweep angle for the infinite yawed wing case of Nash and Tseng (Reference 25). The trends are the same in both cases, while the quantitative difference grows with  $\Lambda$  as would be expected. The displacement and momentum thicknesses are consistently underpredicted by the modified chord methods, as are the shear stresses. Also, the agreement is worse at the trailing edge and improves forward of this station. For this case, it appears that the two methods start diverging at about  $50^\circ$  sweep angle.

#### f. Flat Plate Study, Including Compressibility

Figure 13 shows the infinite flat plate results for sweep angles of  $1^\circ$  and  $45^\circ$ . For the  $1^\circ$  sweep case, we see very good agreement between the 2-D and 3-D programs. We can see a large effect on the displacement thickness due to compressibility effects. At  $45^\circ$  sweep, there is a larger difference (5% at the trailing edge) between the two methods. Although the compressibility effects are still quite large, they are not quite as large as the 2-D case. The flat plate comparison shows that the shear stress effects on the boundary layer are only approximately determined in the modified chordwise method. Boundary layers which develop mainly due to pressure gradient effects are computed more accurately than those which are dominated by shear stress effects when the modified chordwise method is used. Fortunately, the boundary layer development over wings is dominated by the pressure gradient.

#### g. Comparison of Spanwise Shear Stress Predictions

The modified chord method was developed to predict the chordwise properties of the boundary layer. However, an estimate of the shear stress in the spanwise direction can be made using equation (10), where  $\theta_z$  is assumed to equal to  $\theta_x$ , as discussed previously. Figure 14 shows a comparison of this estimate with the predictions of the detailed computations carried out by Nash and Tseng (Reference 25). The good agreement is surprising and perhaps fortuitous. Figure 15 shows the comparison with the results presented by Adams (Reference 29). The 30% difference seems to be a more reasonable result in view of the approximations used in obtaining equation (10). The filled circles show the results of a more refined equation derived using the same approximations made in obtaining equation (10). There is little benefit from the more refined equation. Finally, note that the spanwise shear stress will be sensitive to departures from infinite yawed wing conditions.

#### h. Comments on the Performance of the Method

We have demonstrated that the modified chordwise method produces good agreement with data and other prediction methods for a large range of conditions. The correct qualitative results were obtained for all conditions tested. When assessing the applicability of the method, it appears that four basic criteria must be examined.

- o Sweep Angle - Results obtained here indicate that the method provides accurate predictions for sweep angles of 40-45°. Beyond this sweep angle, the predictions diverge from (but maintain the same trend as) the predictions of the 3-D Bradshaw program (incompressible).
- o Separation - In the present scheme, the boundary layer calculation terminates when  $\tau_x \rightarrow 0$ . The position at which this occurs is called the chordwise flow separation line. Since the flowfield in this region is fully three-dimensional, the modified chordwise method must fail at this point. This breakdown is reflected in the slightly premature separation prediction (as much as 3% in the cases studied).
- o Compressibility - It appears that for typical transonic Mach numbers compressibility effects do not affect the performance of the method. A lack of experimental data in this area makes a thorough evaluation impossible.
- o Spanwise Inviscid Flow Gradients - The difference between any method based on the infinite yawed wing approximation and the actual boundary layer on a finite wing has not been evaluated. The basic parameters are the taper ratio and aspect ratio with tip and root non-uniformities of interest also. For wings operating near a design point, where the constant isobar sweep is maintained, the spanwise gradients are low and the prediction of the present method can be used with confidence. It appears that an experimental program that investigates the effects of taper, root and tip non-uniformities, and off-design pressure fields is required in order to assess the impact that neglecting these effects has on the accuracy of the prediction methods.

### i. Method of Computation

The results presented in this section were computed using pressure distributions tabulated in Abbott and von Doenhoff or taken from Adams' paper (Reference 29) in the compressible case. The difference between the arc length and the distance along the chord line  $\tilde{x}$  was neglected. The good results obtained in the present section serve to validate this approximation which is consistent with the method developed by Bavitz (Reference 4). For the Nash and Tseng (Reference 24) comparisons, the pressure at the trailing edge was adjusted to avoid flow separation, in the manner indicated in their paper (Reference 25).

The modified chord turbulent b.l. program starts with a given  $\theta/C$  and  $H$ . The fully 3-D program starts with  $\theta/C$  and  $C_f$  specified. The results indicate that these different starting conditions do not affect the boundary layer development after a few boundary layer thicknesses downstream of the transition point. In the application of the code to tapered wings, the characteristic sweep is taken to be the sweep of the midchord line. Again, a lack of experimental data makes the choice of this angle difficult to verify. This value could be easily changed by the user to the sweep of any percent chord line.

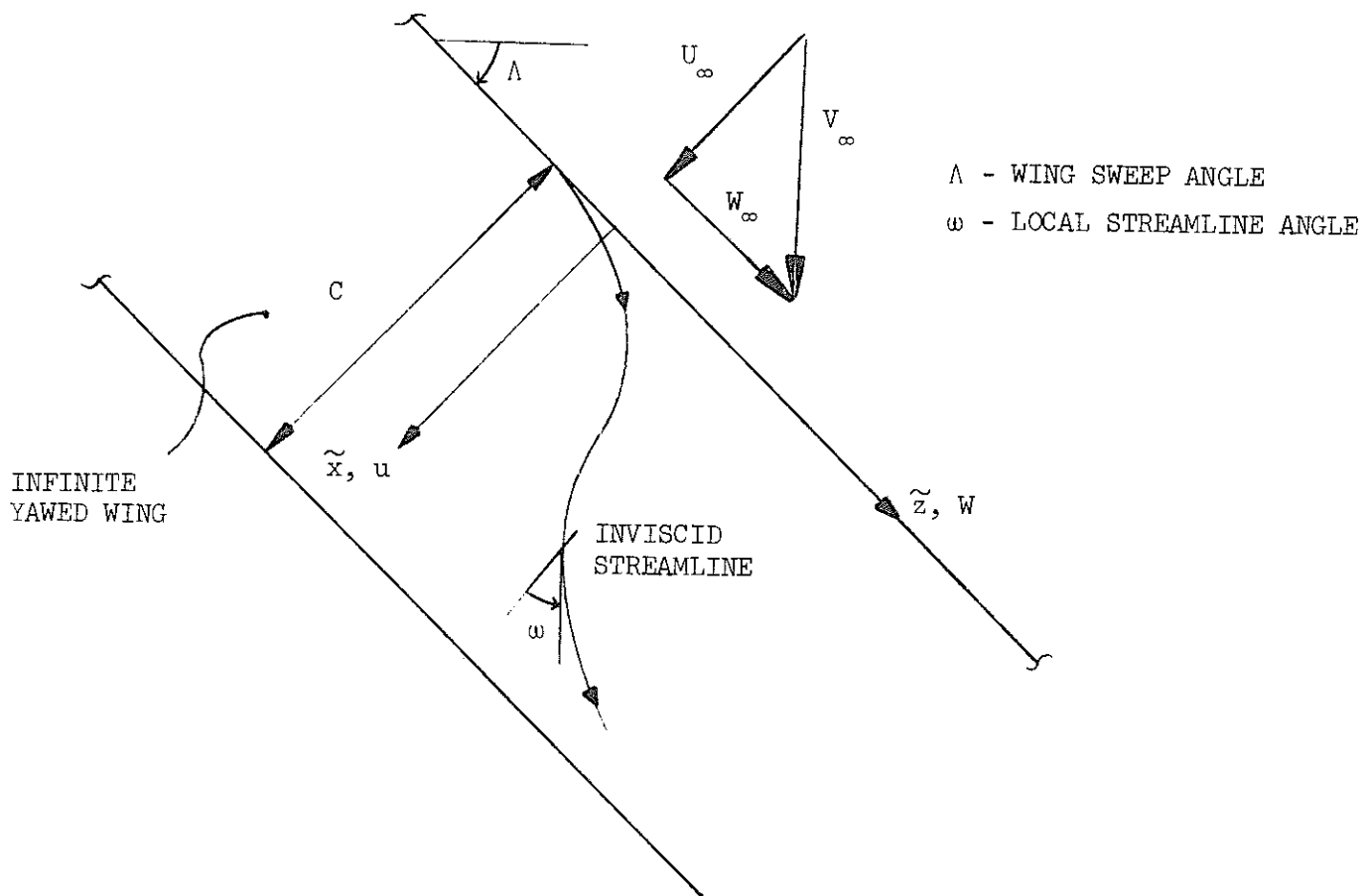


Figure 3. Infinite Yawed Wing Notation

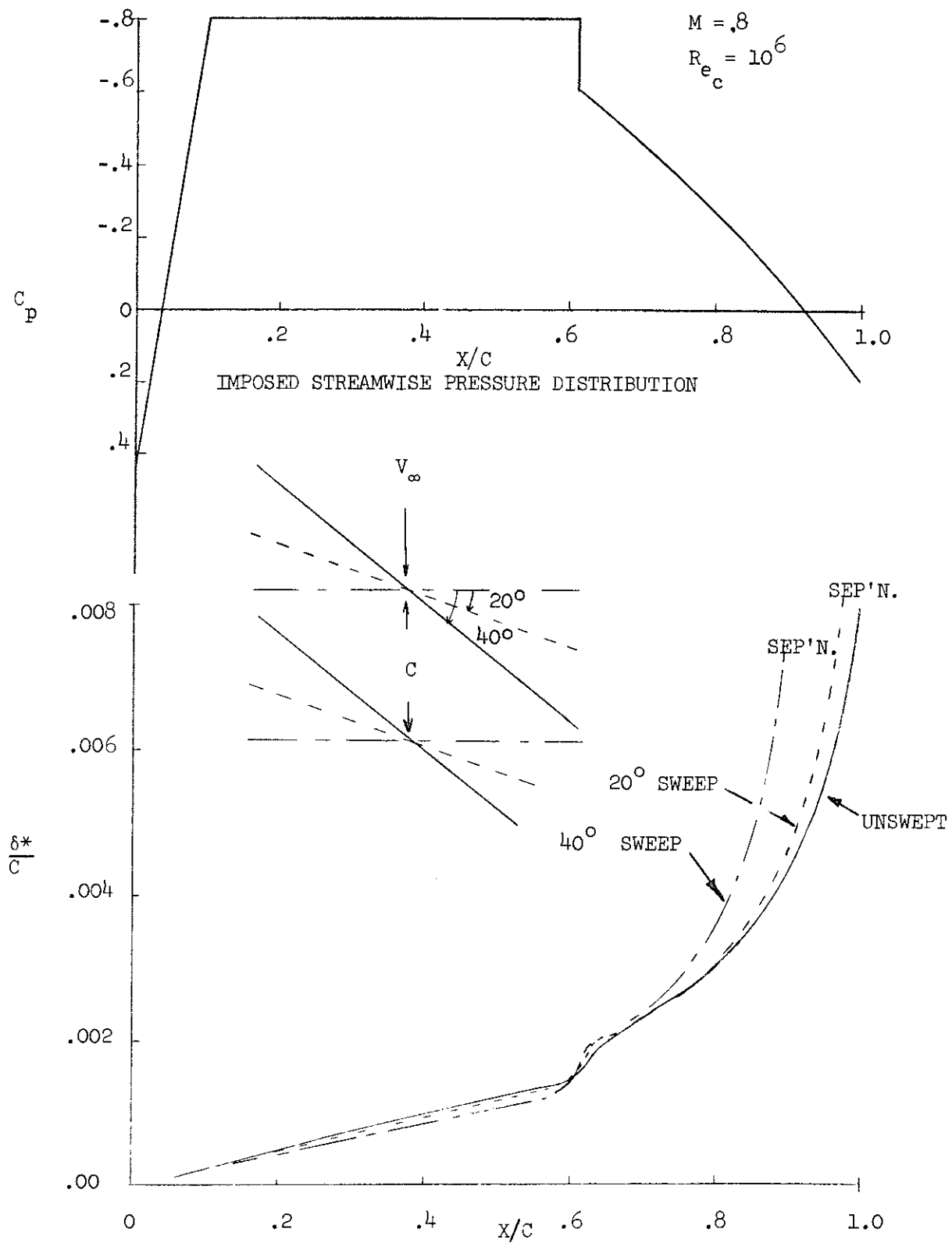


Figure 4 Effect of Wing Sweep on Boundary Layer Development

NACA 65, A012

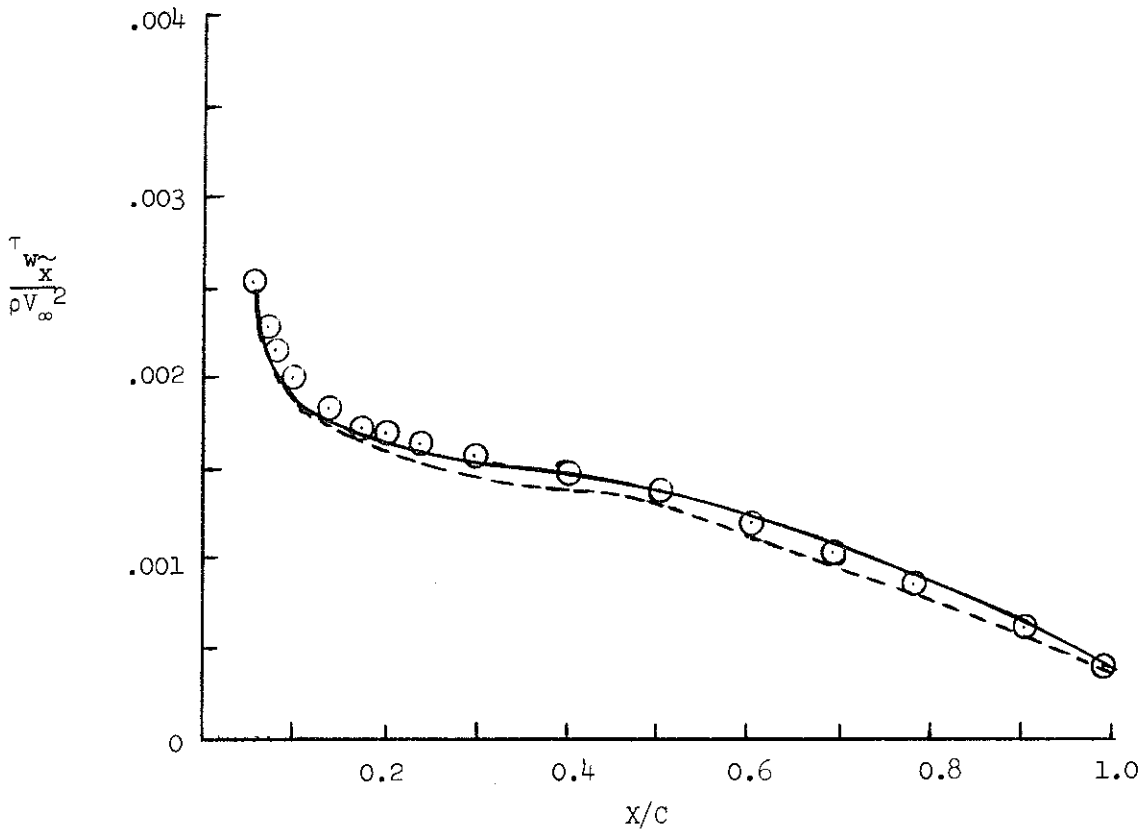
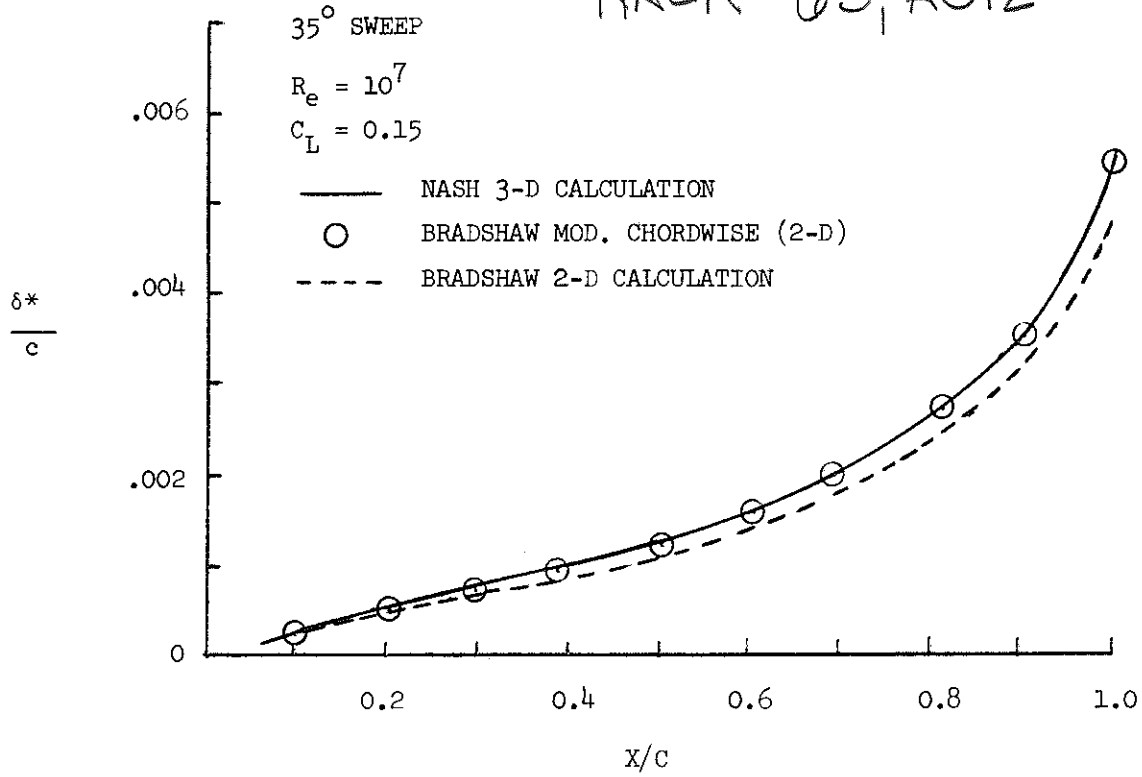


Figure 5 Comparison with the Nash Test Case

$C_L = .15$

# NACA 65A012

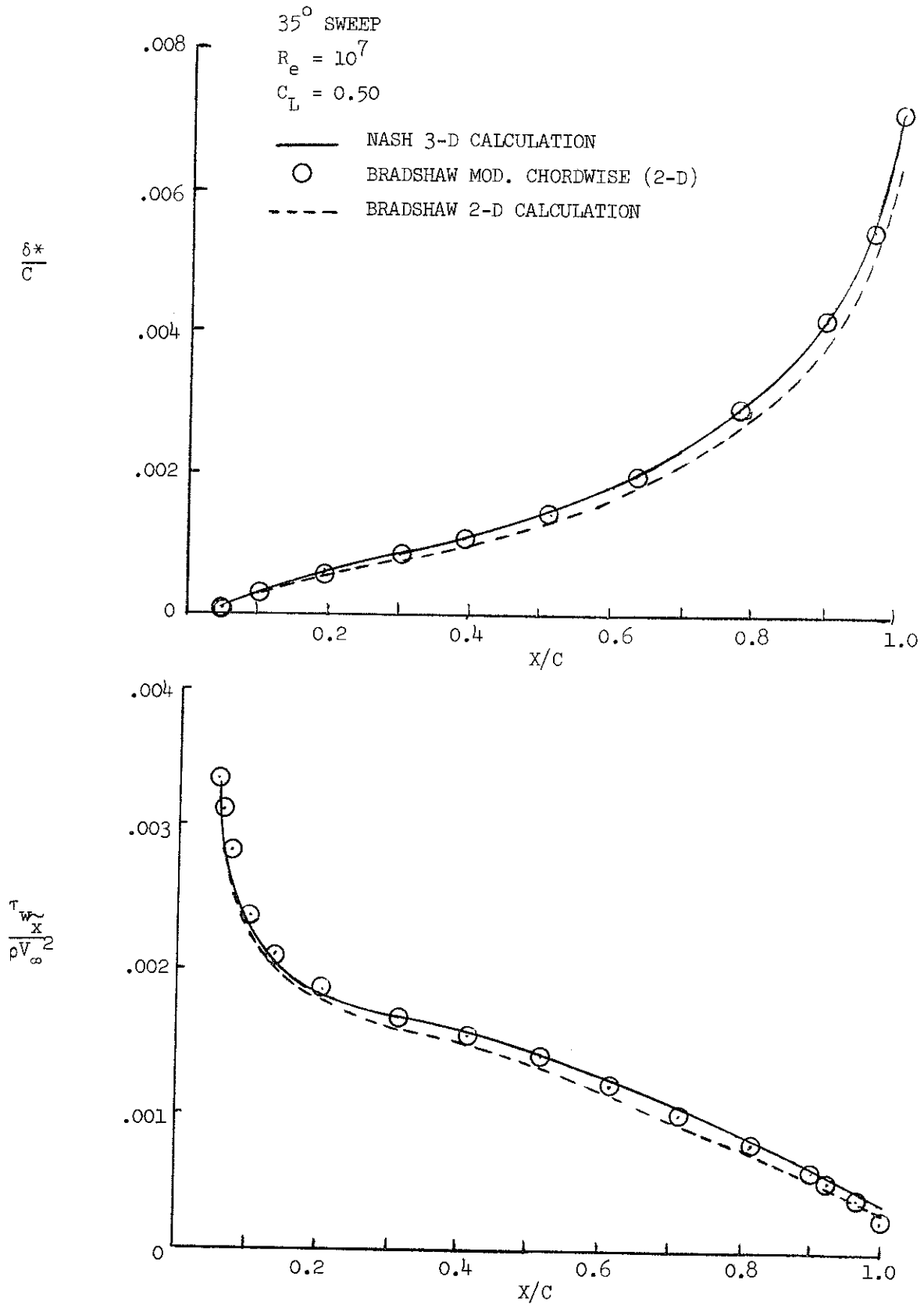


Figure 6 Comparison with the Nash Test Case

$C_L = .50$



# NACA 63,-012 Foil

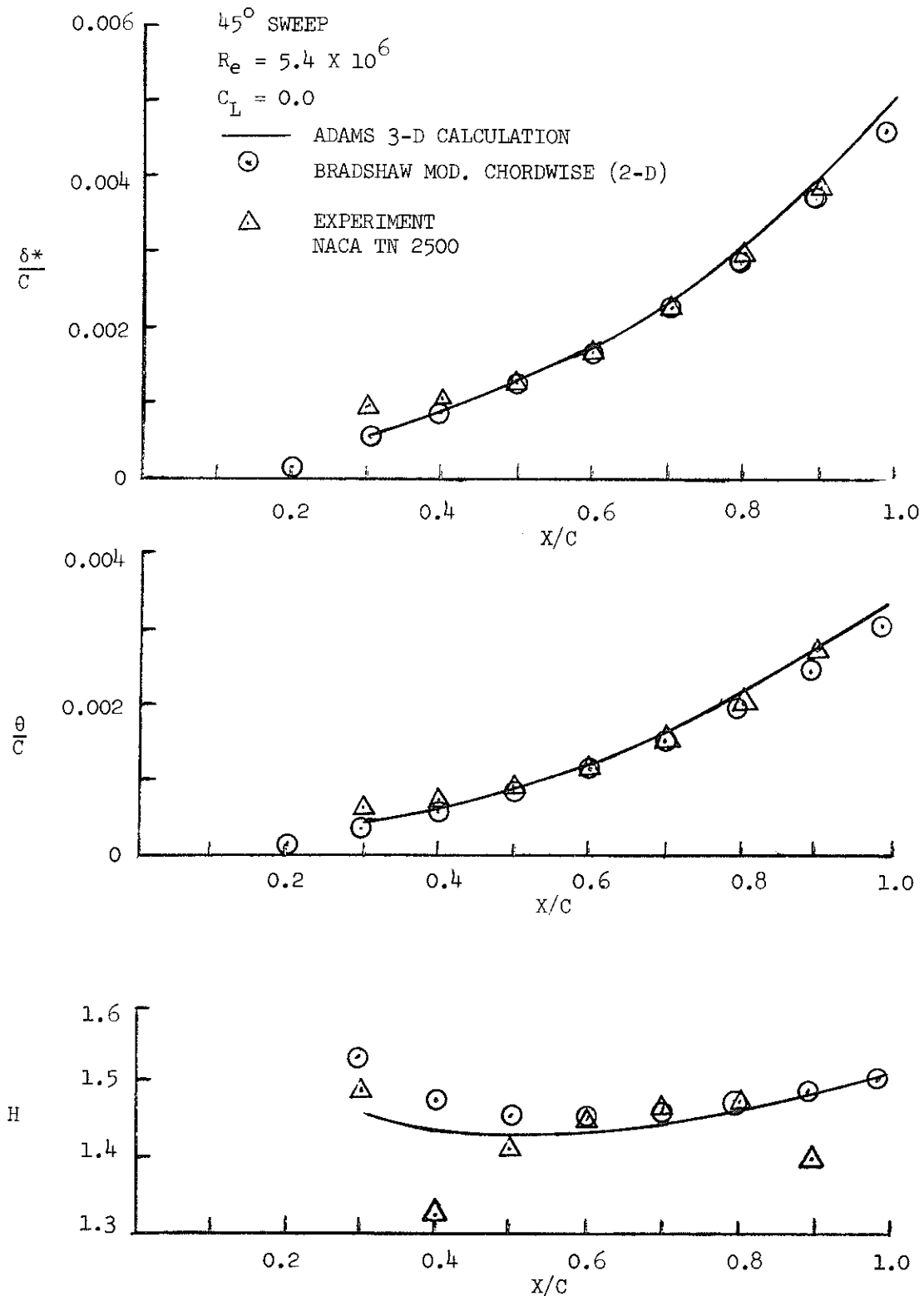


Figure 7 Comparison with Adams 3-D Test Case Zero Lift

# NACA 03, -012

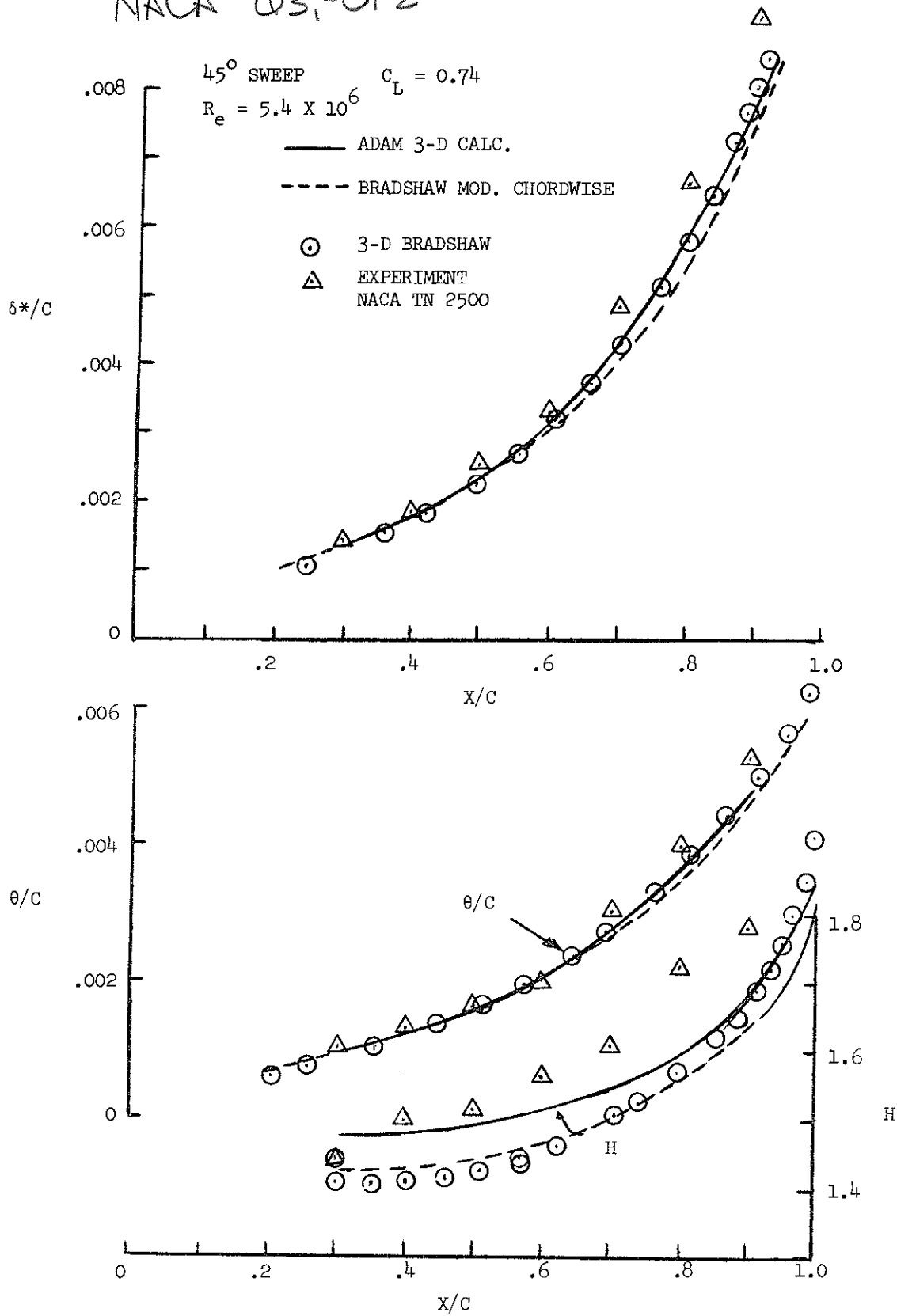


Figure 8 Comparison with Adam 3-D Test Case

$C_L = 0.74$  Case

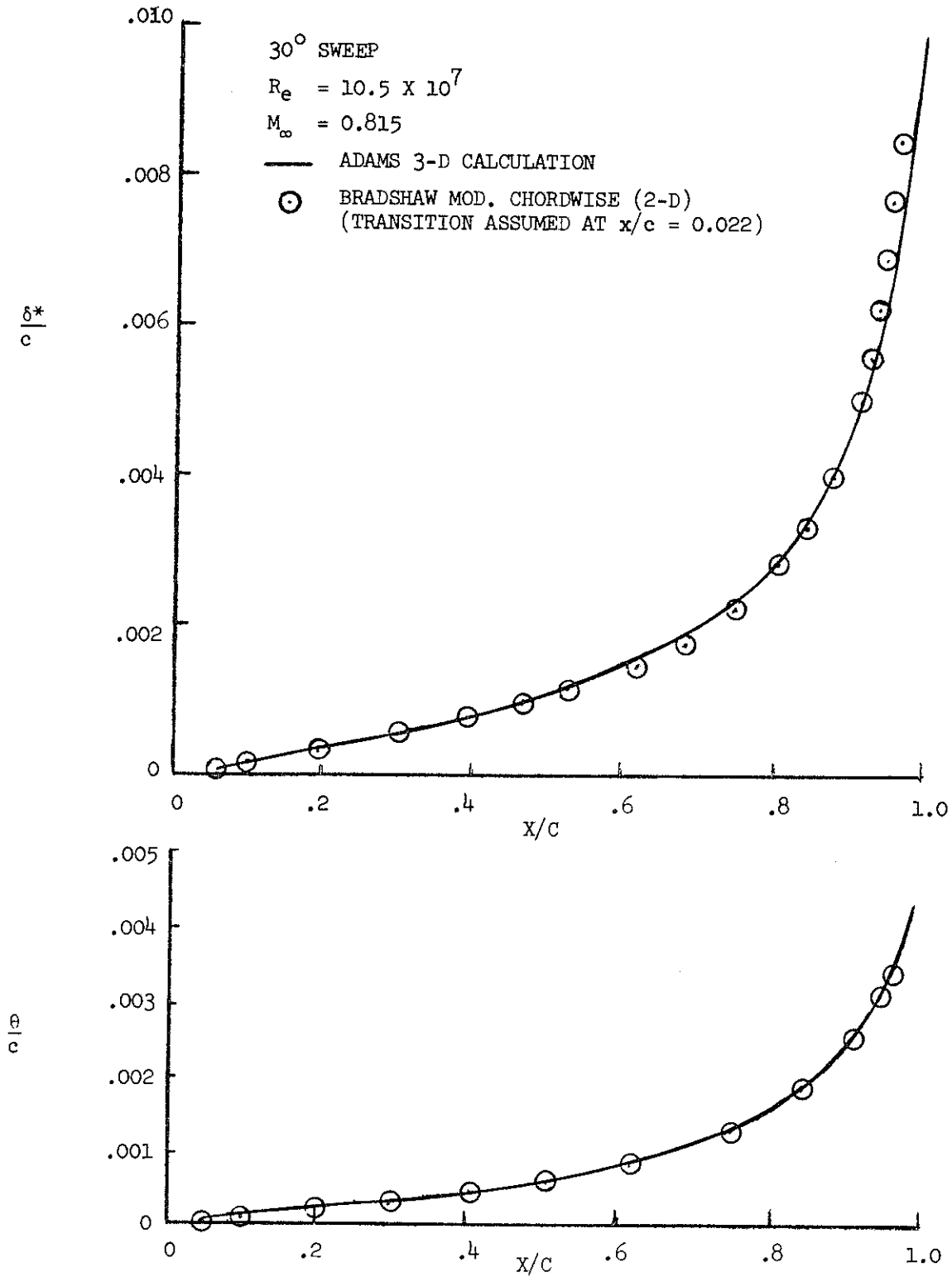


Figure 9 Comparison with the Compressible Adams Test Case

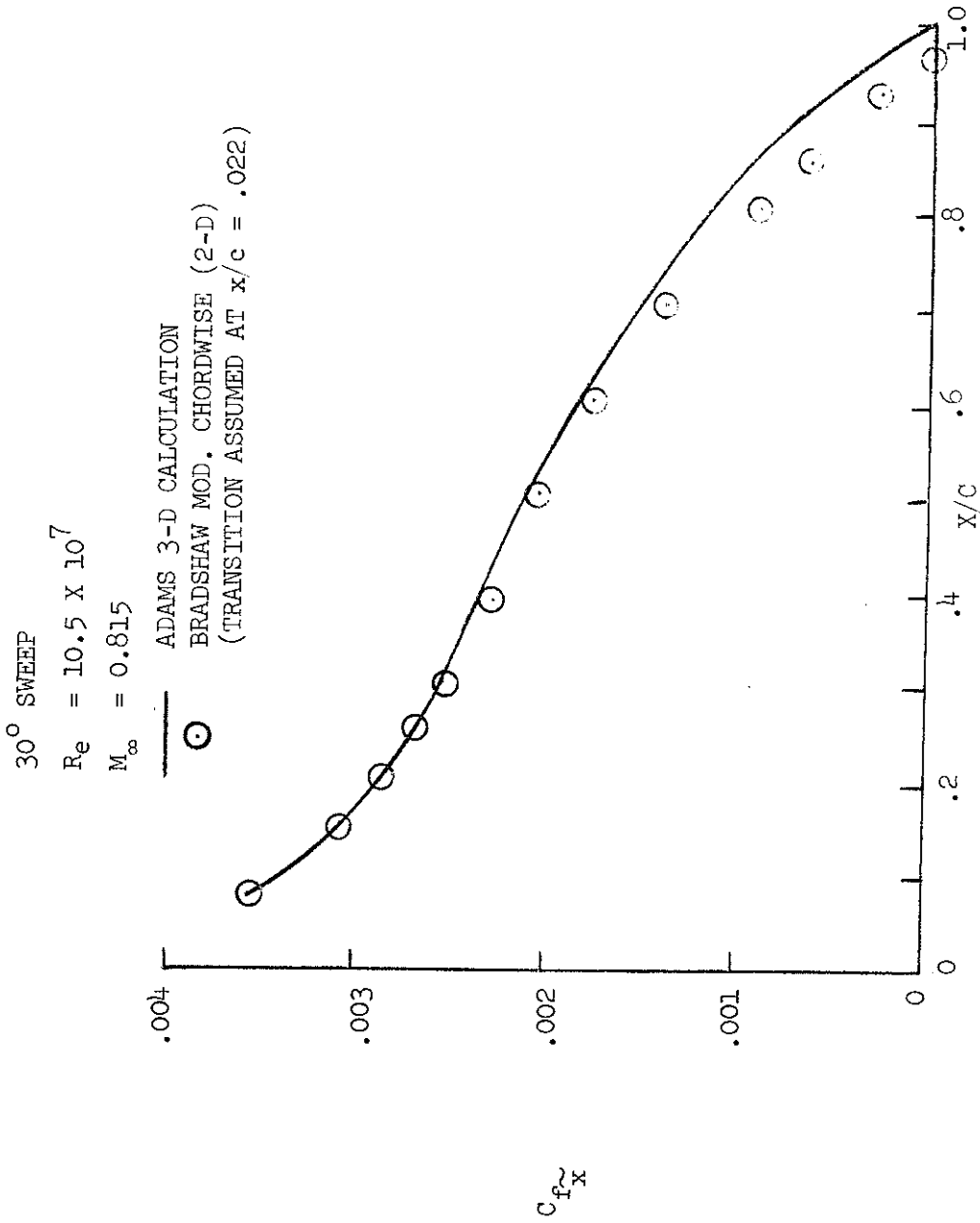


Figure 10 Comparison with the Compressible Adams Test Case

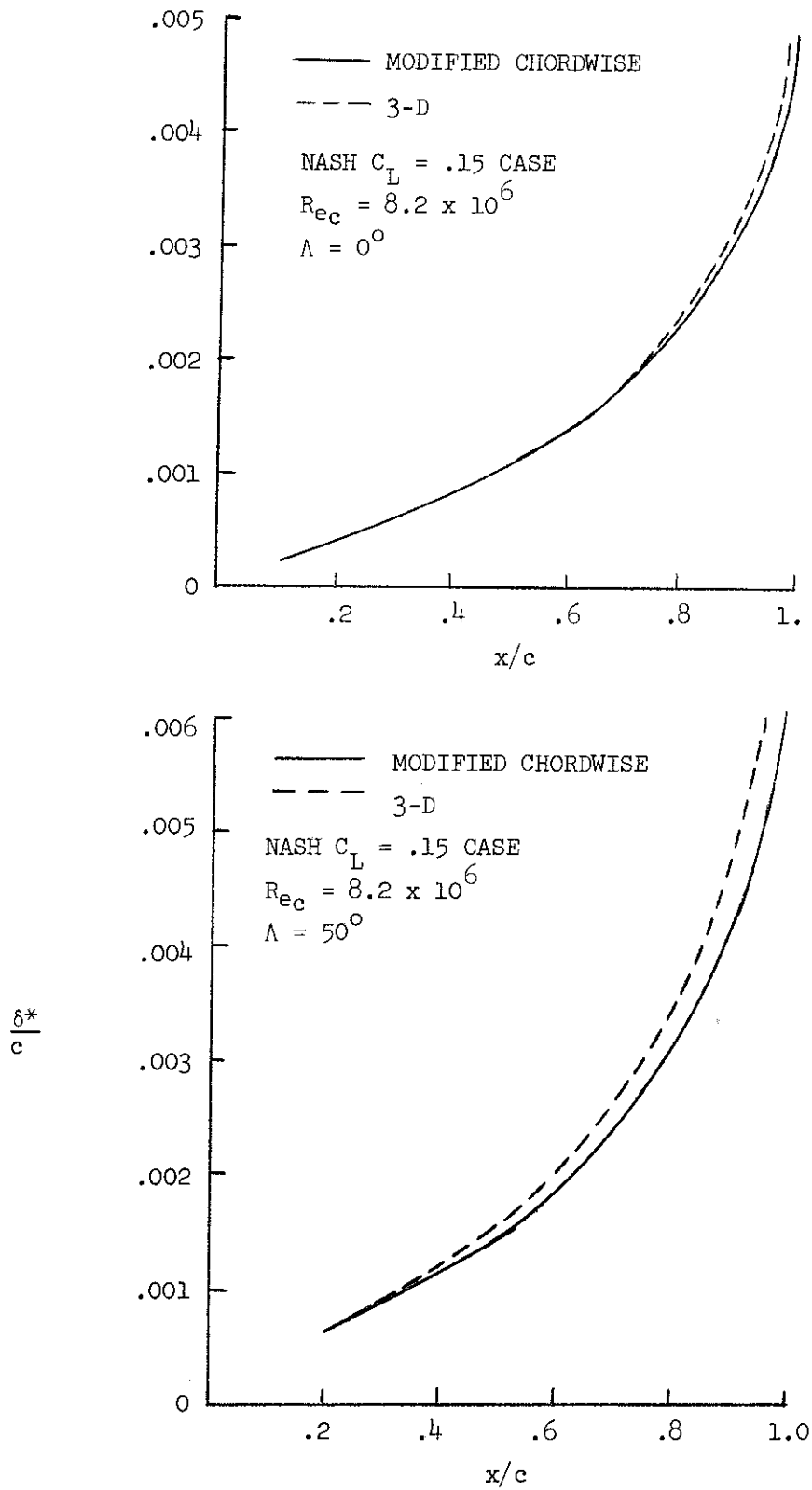


Figure 11. Comparison of Bradshaw 3-D Program and Modified Chordwise Method

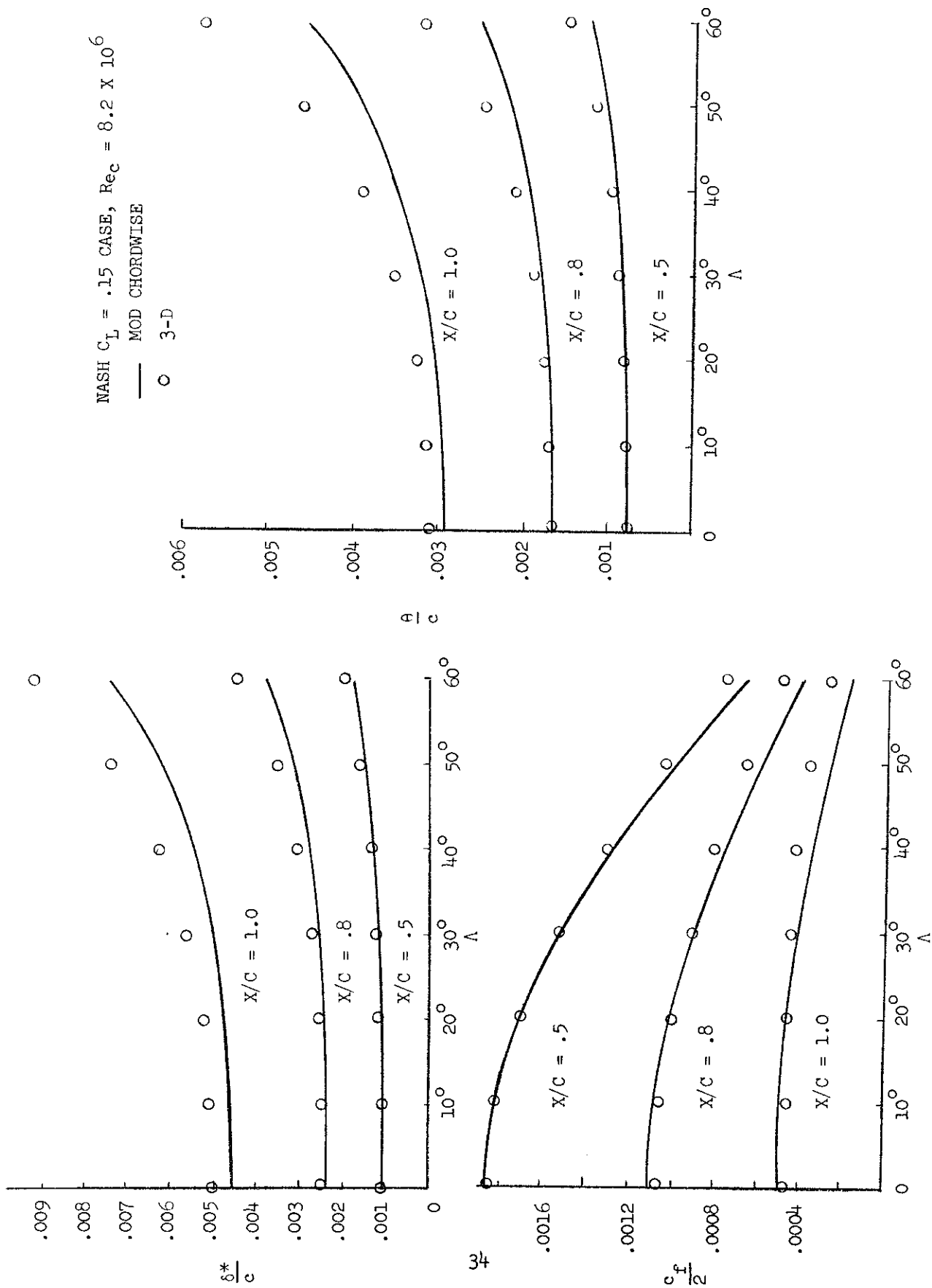


Figure 12 Comparison of Modified Chordwise and 3-D Calculation Methods

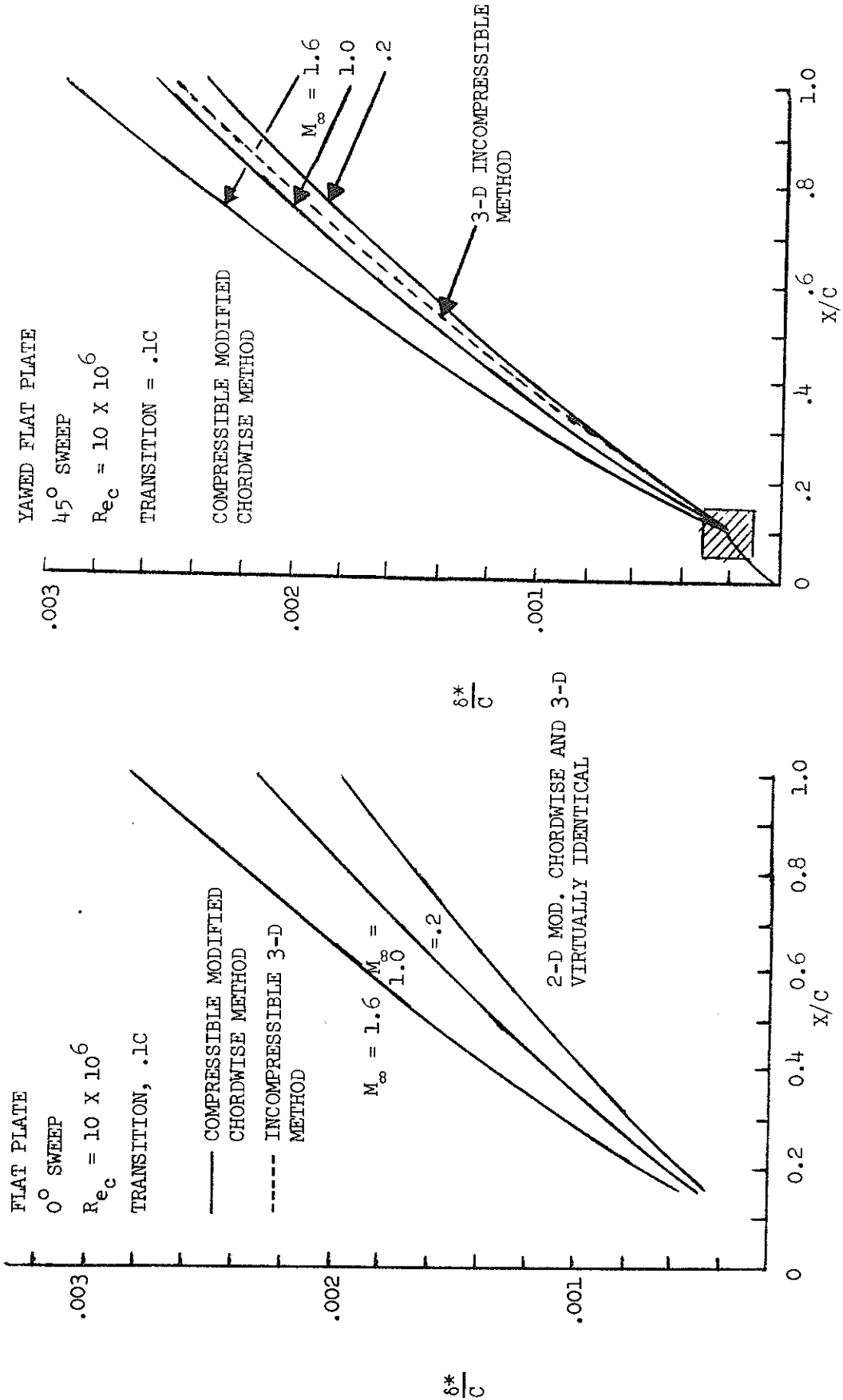


Figure 13 Flat Plate Results - 0° and 45° Sweep

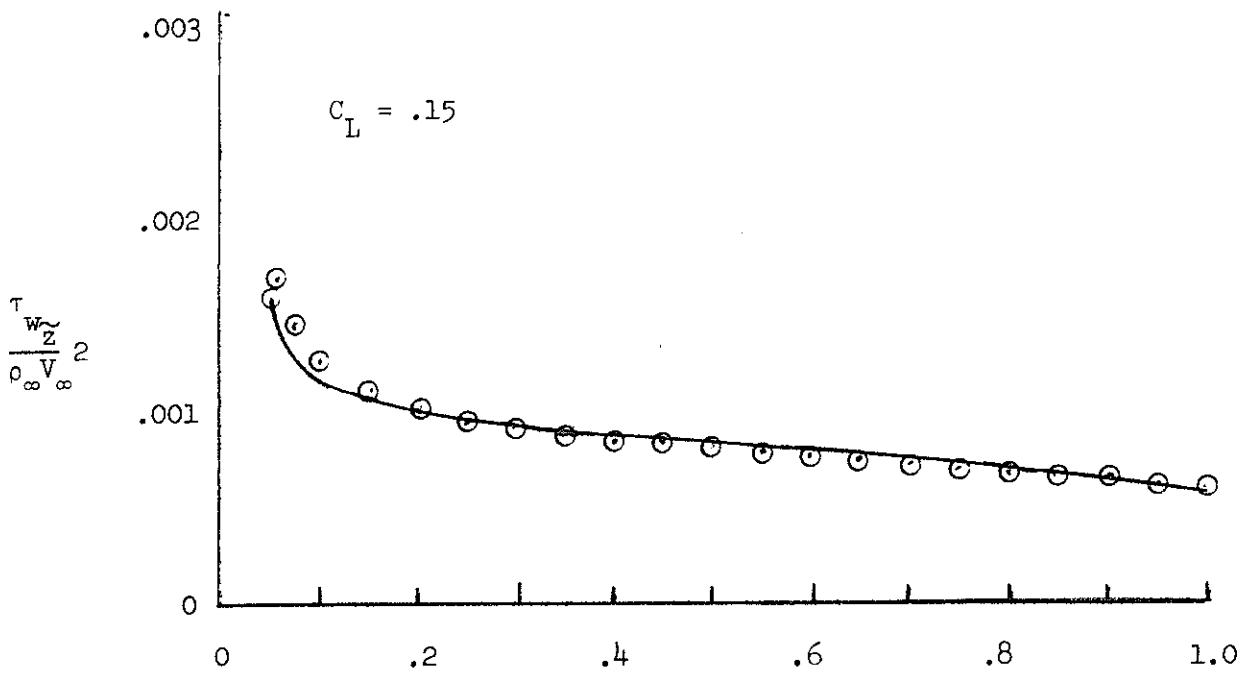
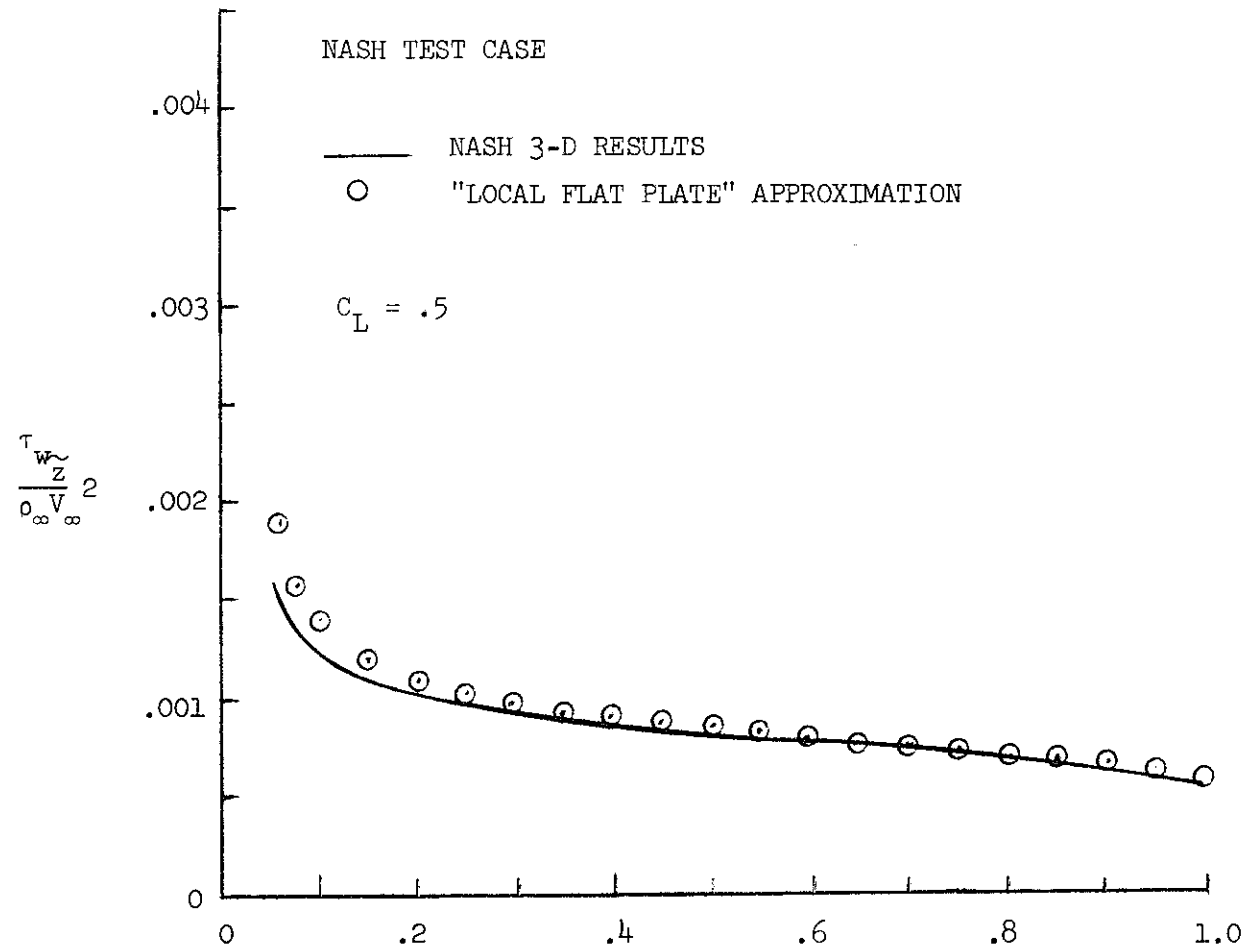


Figure 14 Spanwise Component of Shear Stress at Wall



ADAMS TEST CASE -  $M_\infty = .815$

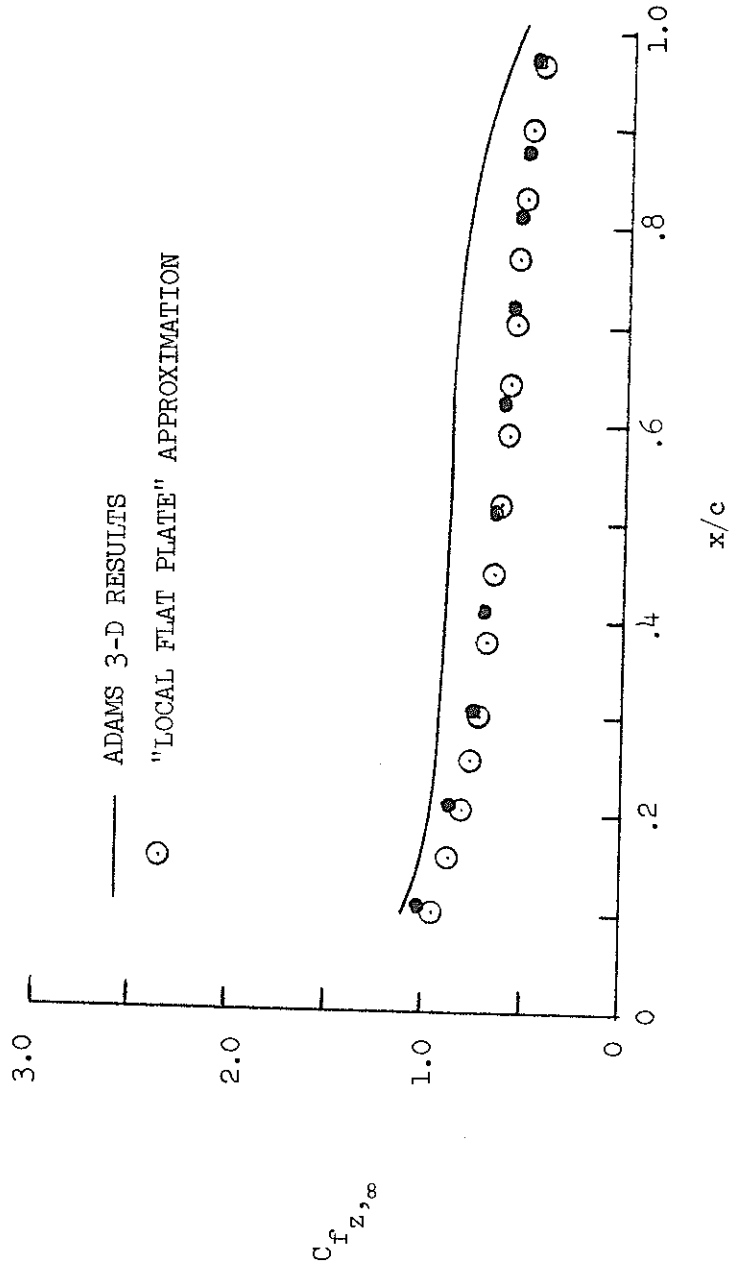


Figure 15. Spanwise Component of Wall Shear Stress

#### 4. COUPLING OF THE INVISCID AND VISCOUS CALCULATION METHODS

##### a. General

The interaction solution that combines both the outer inviscid flow-field and the thin viscous shear layer immediately adjacent to the body has been the subject of numerous investigations, virtually all of which have considered two-dimensional flow. The idea of iteratively computing the potential flow about a body with an additional displacement surface due to viscous effects was apparently originated by Prandtl (Reference 31). Although viscous airfoil methods were continually under study, the development of the aft-loaded airfoil designs for efficient transonic flight were found to demand viscous methods in order to predict theoretically, the experimental pressure distributions accurately. The potential for increased airfoil performance employing advanced aerodynamic concepts brought about a renewed and intense interest in the theoretical prediction of transonic flows. The development of accurate 2-D boundary layer programs, followed by the breakthrough of Murman and Cole (Reference 2) in inviscid transonic flow predictions, together with the ever increasing capabilities of computers led to the successful development of the first 2-D transonic viscous computer programs (References 4 and 32, for example).

Aft-loaded airfoils produce a rapidly thickening boundary layer on the upper surface and a thinning boundary layer on the lower surface. The resulting highly asymmetrical viscous flowfield acts to reduce the effective aft-camber associated with the rear-loaded or so-called "supercritical" airfoils. It is this feature of the flowfield which causes viscous effects to become so much more important for aft-loaded airfoils than for conventional sections. Viscous effects arise in several ways. Figure 16 shows the various regions where the effects differ in character. Over most of the airfoil, the viscous effects can be handled by adding the displacement surface to the airfoil and recomputing the potential flow. When the inviscid flow is being computed by a small disturbance theory, the displacement effect is treated by adding the slope of the displacement thickness to the slope of the airfoil, with the resulting boundary condition being applied at the axis. For inviscid solutions that treat the geometry more exactly, either the flow over an equivalent body must be computed or the flow over the correct geometrical body with a normal velocity specified at the surface is computed in order to simulate the source flow effect that the boundary layer has on the outer inviscid flow. The latter

method is generally preferred because only a single geometric shape must be considered. The detailed analysis of displacement effect treatment has been given by Preston (Reference 33) and Lighthill (Reference 34). The displacement surface effect is a weak interaction, wherein the comparatively small local displacement effect of the boundary layer and wake, when integrated over the whole surface, leads to a reduction in lift and an increase in the pressure drag on the wing.

There are several regions on the airfoil where locally strong interactions occur. The interaction at the trailing edge is the most important. This is due to the control that the local solution at the trailing edge has on the global circulation and therefore lift. Naturally, the detailed solution at the trailing edge depends both on the boundary layer development near the trailing edge and the viscous wake just aft of the trailing edge. The explicit computation of the wake and its effect on the trailing edge interaction has been included in the 2-D viscous predictions by Hall and Firmin (Reference 7) and more recently, by Melnik, Chow and Mead (Reference 5). Melnik's results show explicitly the large variations in pressure across the interaction region near the trailing edge. This type of inviscid pressure distribution was first obtained by Pinkerton (Reference 35), who reduced the circulation to the measured value and disregarded the Kutta condition, thereby, obtaining improving agreement with experimental results. The wake effects can be split into thickness and curvature components. In the present method, the modification of the surface slope boundary conditions leads to the implicit modeling of the wake as a constant thickness layer with no curvature and hence, constant pressure on the two sides. The wake curvature appears to be the dominate effect of the wake contribution to the trailing edge interaction. In the present method, the wake is taken into account by the empirical treatment of the trailing edge problem where the displacement model at the trailing edge has been developed by correlation with experimental data.

The viscous region at the foot of the shock-wave is another area of strong local interaction. As long as the shock-wave is not strong enough to cause a massive separation of the boundary layer, this region does not dominate the overall solution. Often the inviscid solution "smears" out the shock jump due to the lack of resolution which arises due to a coarse mesh (it takes about 3 mesh points in order to define a shock and a typical mesh point is

spaced every 2% chord in the three-dimensional methods). For strong shocks, a "viscous wedge" can be placed at the foot of the shock in order to model the strong interaction that occurs due to the thickening of the boundary layer. We note that in transonic flows, the direct drag due to the presence of the shock (wave drag) is usually small compared to the effect of the thickened boundary layer on the pressure drag.

An additional complication of the 3-D transonic flowfield simulation, in contrast to the 2-D case, is the typical existence of complex 3-D shock structure (Rogers and Hall, Reference 36).

Another important aspect of the interaction solution is the occurrence of separation on the airfoil. Local separation under shock waves appears to be adequately treated by either the viscous ramp or the simple thickening of the boundary layer at the foot of the shock. Small regions of upper surface separation can be treated by a simple empirical extrapolation of the displacement surface slope. A similar treatment is employed on the lower surface when separation occurs in the cove region. Cove separation can be termed a "shallow" separation, where the region of separation is confined to a very thin layer such that it can continue to sustain a pressure gradient (and in fact, this was why it was not noticed on the early supercritical airfoils). These shallow separations usually do not noticeably degrade the performance of the airfoil. Although a rational engineering theory is needed for these types of shallow separations, the empirical treatment employed in the present program has proven reliable. The apparent success of the present method rests on an interesting property of boundary layers on the verge of separation. It can be readily determined that when a boundary layer is about to separate, very small changes in the imposed pressure distribution lead to large changes in the displacement thickness. From the other viewpoint, this fact means that large changes in  $\Delta C_p$  result in only minor changes in the pressure distribution. This property is largely responsible for the success of the transonic viscous flow codes, and should be exploited whenever possible. Although a rational engineering theory is needed for these types of shallow separations, the empirical treatment has proven acceptable in the present program. There is a regime between the shallow separations that can be treated in the present method and massive "constant pressure" separation calculation methods reported recently by Maskew and Dvorak (Reference 37) and Milgram (Reference 38)

for incompressible flows, where a more realistic flowfield model for separated flows will have to be incorporated in order to make reliable predictions.

For more extensive discussion of the physics of transonic viscous-inviscid interactions, the reader is directed to the excellent reviews by Green (Reference 39) and Pearcy (Reference 40), et al.

There have been very few investigations of transonic viscous-inviscid interactions on finite wings. One of the reasons for this is that fully three-dimensional boundary layer calculation methods have only recently become available (Reference 11, 41). An interesting initial examination has been reported by Piers, Schipholt and van den Berg (Reference 42) for subsonic flow. Hedman (Reference 12) has reported an interaction method which treats the weak displacement effects, while Kordulla (Reference 13) has also used the Bailey-Ballhaus inviscid program to investigate the effects of viscous-inviscid interactions in transonic flow. The present work describes the first unified approach to an easy to use and reliable engineering tool.

The detailed implementation of the present viscous interaction scheme can be described as follows. First, the character of the inviscid solution must be established. This can be done by either starting from a previously saved solution, or by running a number of inviscid cycles less than the number required for a converged solution. It has been found to be more economical to recompute the boundary layer effect every forty or fifty inviscid cycles rather than to reconverge the solution completely before each boundary layer addition. In this manner, the number of inviscid cycles required for a viscous solution can be held to less than twice the number of cycles for an inviscid solution, and more typically about 1-1/2 times the basic number of iterations required for an inviscid solution.

Starting from the inviscid solution, the boundary layer is computed at each spanwise station using the modified chord method described in Section III. The pressure distributions are modified slightly for the boundary layer calculation. Because the small disturbance theory has a singularity at the leading edge, the pressure at the leading edge was reset to the actual stagnation pressure. Any pressure computed behind the leading edge above a straight line between the stagnation value and the tangent to the pressure distribution with the maximum angle is reset to fall on this line. We note that although the two-dimensional small disturbance theory programs often produce only a single

pressure coefficient that has to be readjusted, the three-dimensional solution sometimes predicts pressure values above the stagnation value at several mesh points downstream of the leading edge. In addition, the cove pressure distribution is smoothed several times in order to reduce the artificially large compression of the flow and resulting extreme acceleration near the trailing edge.

The boundary layer is computed using the midchord sweep at each span station as the effective sweep angle. Once the boundary layer is computed, the displacement thickness distribution produced by the boundary layer is interpolated to the inviscid solution grid. At this point, the displacement thickness is linearly extrapolated aft of the separation point, and the separation point is saved for future use. Once the basic displacement surface is known on the inviscid grid, the trailing edge interaction effects are treated by linearly extrapolating the slope of the displacement thickness from a prescribed point slightly upstream of the trailing edge, to the trailing edge. It has been found that an extrapolation from about 96% or 97% of the chord is appropriate for many airfoils. This factor can vary slightly between airfoil sections and its location is available as an input for the user to adjust if he desires. No extrapolation is required on the lower surface of supercritical airfoils. The wing surface slope boundary conditions used in the inviscid solution are altered by use of the relaxation formula:

$$\frac{dz}{dx}_{input}^k = \frac{dz}{dx}_{geometric} + \left( \omega \frac{d\delta^*^k}{dx} + (1-\omega) \frac{d\delta^*^{k-1}}{dx} \right) \quad (14)$$

where k denotes the iteration number and  $\omega$  is the relaxation factor. Typically,  $\omega$  is specified as .5, although for a particular case its optimum value may be slightly higher or lower. This procedure forms the basis of the viscous interaction procedure. It has been found beneficial to introduce several spanwise smoothings at the trailing edge in order to avoid abrupt changes in the spanwise boundary condition. This is especially important if separation is present, as described below. Examples of the attached flow results are shown in Figure 17 for the 2-D case of a supercritical airfoil for which data is available and the ONERA M6 wing. Note that for attached flow, the viscous effects are small for conventional sections.

The basic parameters that the user can adjust for a particular case include the number of inviscid cycles between boundary layer corrections, the relaxation factor, and the extrapolation location for the deltastar slope. This permits freedom to tune the method for a particular case. Along these lines, it is interesting to quote the recent paper by Rose and Seginer (Reference 43), who discuss the computing time and manhours required to obtain transonic viscous solutions:

"Probably the hardest to estimate and least talked about machine times are those spent before the final, acceptable solutions are obtained. It has been our experience that from 4 to 10 times more machine time is used to obtain the final solution (than the actual computing time of a single case)."

Considerably less than 4 to 10 times the basic run time should be used in obtaining results with the present code. Nevertheless, some adjustments of the parameters may be required and the user should not be naive about the typical results published by the research community.

After the basic displacement surface modifications are made, the program determines the extent of separation present. If the separation occurs ahead of the position where the extrapolation is applied, then the separation region is treated as described in Section c., after which the inviscid solution iteration is reinitiated with the modified boundary conditions. A typical convergence history is shown below for the F-8 case, starting from a previously saved solution:

K	$C_L$	Inviscid Iterations	$\epsilon_{Upper}$	$\epsilon_{Lower}$
1	.412	45	1743	228
2	.371	45	56	45
3	.357	45	43	21
4	.357	45	32	17

$$\text{where } \epsilon = \sum \left| \begin{matrix} C_{p_{i,j}}^k \\ C_{p_{i,j}}^{k-1} \end{matrix} \right| .$$

After four iterations, this case was considered converged because the lift was effectively constant between iterations.

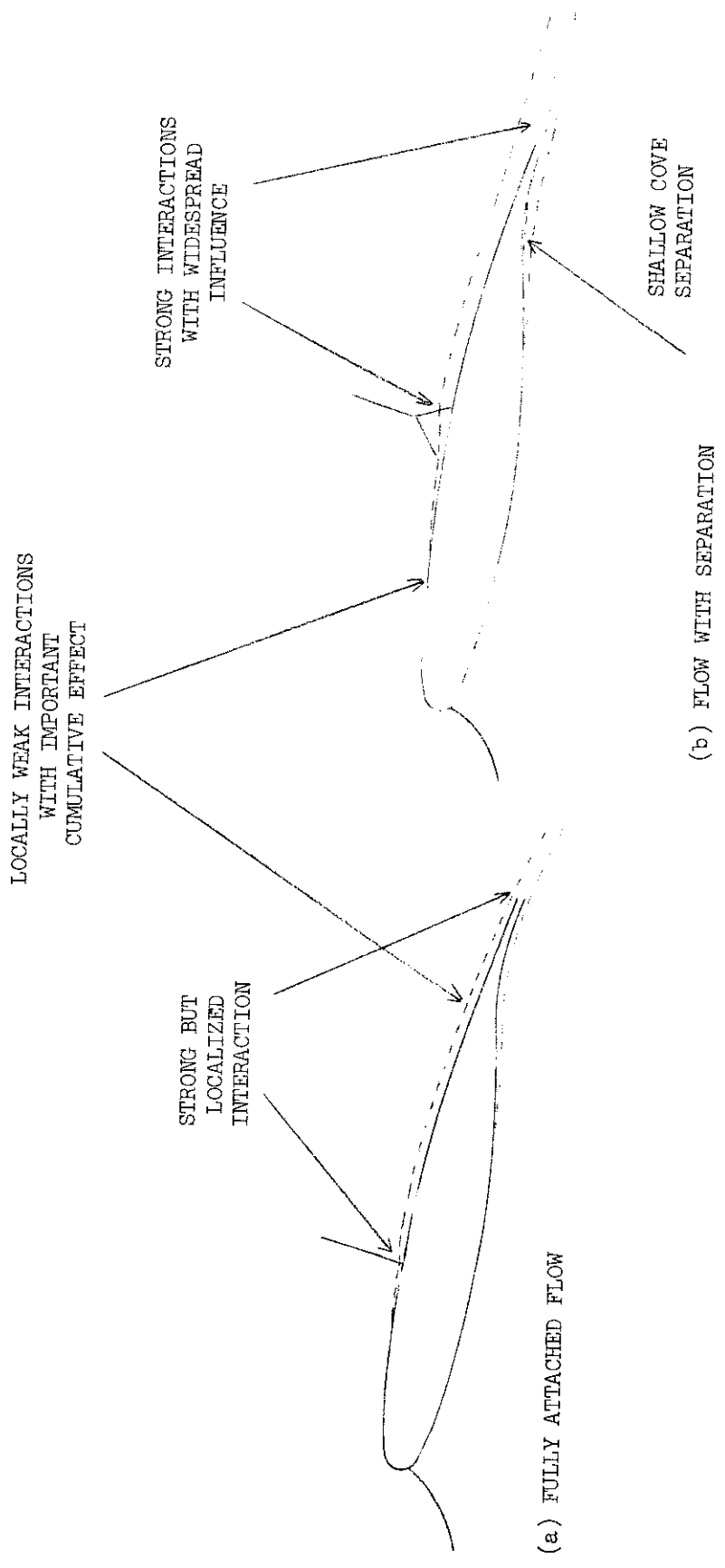
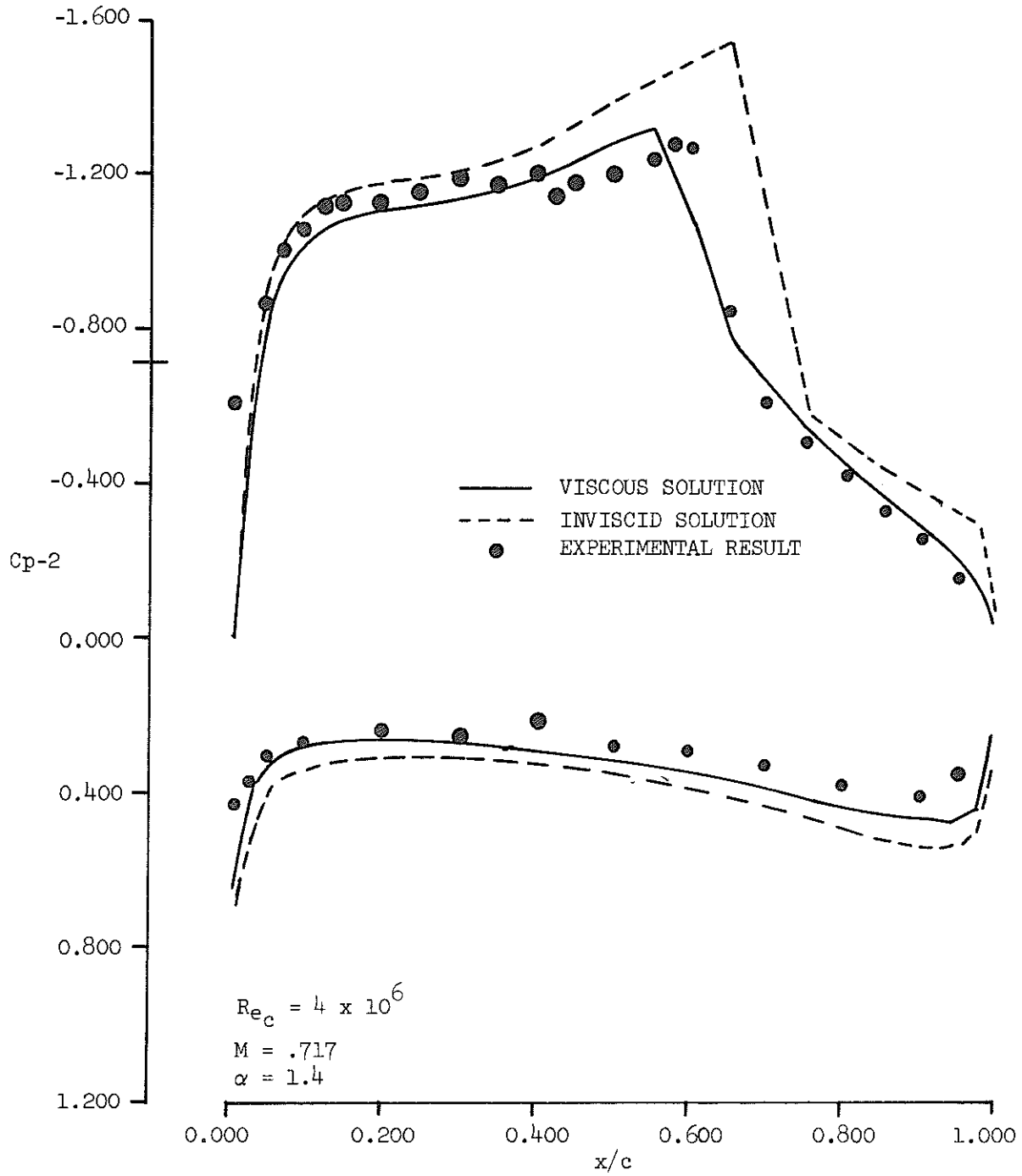


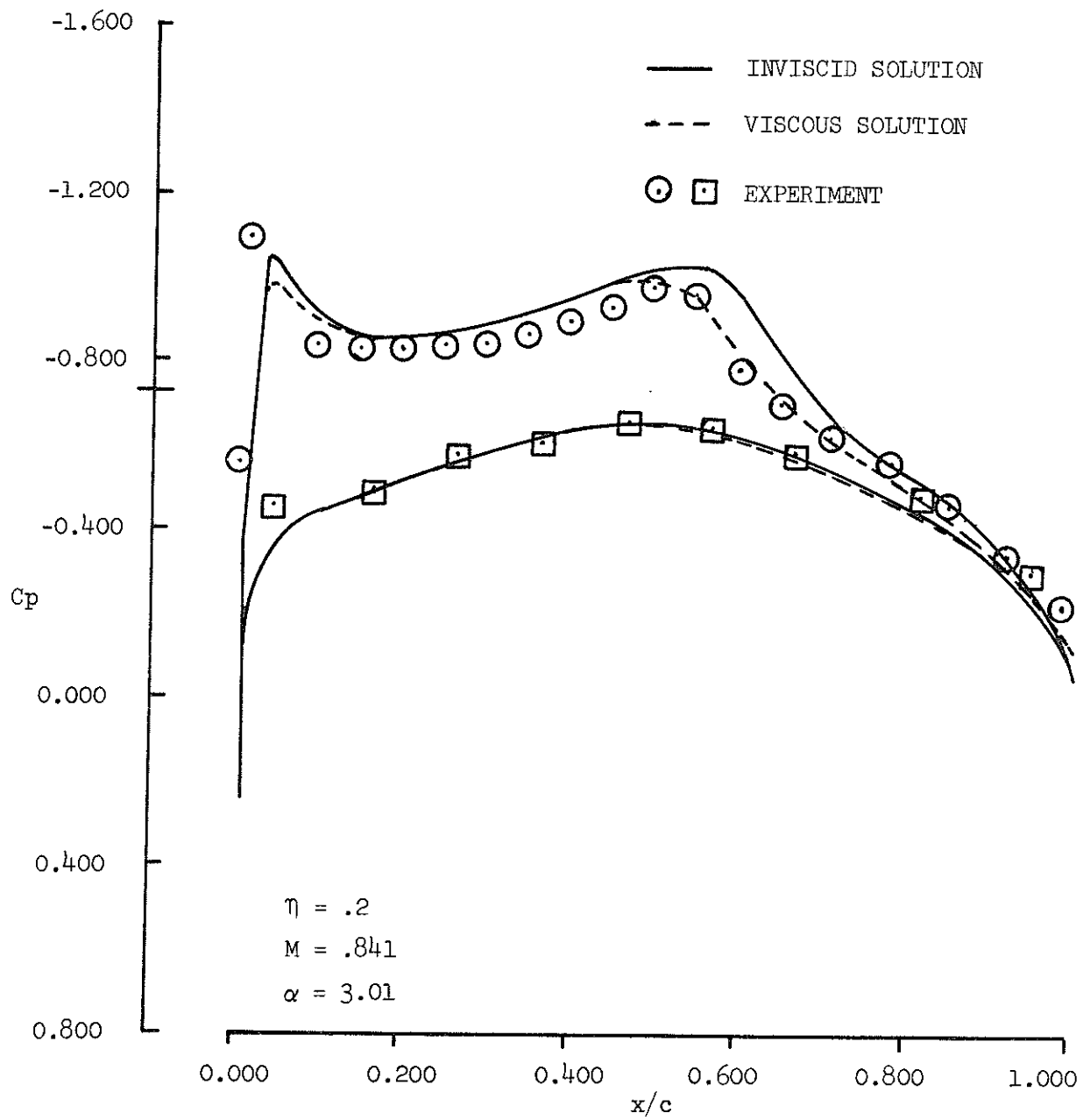
Figure 16 Some Viscous-Inviscid Interactions in Transonic Flow





a) Typical 2-D Supercritical Airfoil

Figure 17. Examples of Viscous Flow Solutions



b) Typical 3-D Conventional Wing

Figure 17. Examples of Viscous Flow Solutions

## b. Shock Boundary Layer Interaction Effects\*

It is well known that the transonic flow over airfoils and wings often contain embedded shock waves which have subsonic downstream states. These shocks are normal at the body surface and become oblique above the airfoil. For most aircraft design conditions, a turbulent boundary layer is present on the body surface and there is a resulting shock wave -- turbulent boundary layer interaction. Several types of interaction may occur (e.g., see References 36, 39 and 40). Reviewing the 2-D situation first, we divide the interaction into 3 categories (Figure 18).

o  $M \leq 1.05 - 1.10$ . There is a weak interaction which perturbs the flow field only locally near the foot of the shock.

o  $M \approx 1.10 - 1.30$ . A strong interaction occurs such that the shock location and overall strength are changed from the inviscid value. There may or may not be a localized separation bubble. It will be assumed that if a bubble is present, reattachment occurs and the closed bubble is small compared to the boundary layer thickness. In general, data shows that shocks of these strengths lie below incipient separation.

o  $M \geq 1.30$ . There is large-scale separation initiated at the shock wave and the resulting inviscid-viscous interaction is strong.

The purpose of this section is to provide a phenomenological method for modeling the effects of the strong interaction on the inviscid flow for case 2. As such, the method has been incorporated into inviscid transonic computational methods as a first step in a complete inviscid-viscous solution.

### (1) A 2-D Phenomenological Model

The measured pressure increase through a shock on an airfoil or a wing is typically less than the normal shock value for the corresponding upstream Mach number. Figure 19 (see Lomax, Bailey and Ballhaus, Reference 9) contains a plot of experimentally determined pressure increase through a shock wave as a function of the shock Mach number for a wide range of Reynolds numbers. The curve labeled Rankine-Hugoniot is the corresponding normal shock pressure rise.

---

\* This section is based on a consulting report by Earll M. Murman.

Yoshihara (Reference 44) has proposed that the boundary layer thickening at the foot of the shock may be viewed as a "viscous-wedge" as shown in Figure 20. The wedge formed by the displacement surface relieves the requirement of a normal shock and allows the shock to become locally an attached oblique shock. Although the viscous wedge model is not necessarily the true shape of the displacement surface, it is a convenient and consistent explanation for the effect of the boundary layer on the inviscid flow.

Figure 21 shows schematically a shock polar for the allowable downstream pressures  $P_2$  and viscous wedge angles  $\theta$ . To adopt Yoshihara's model, we must require that the oblique shock wave be attached, that is  $\theta \leq \theta_{\max}$ . In addition, we postulate that the flow downstream of the shock is to be subsonic so that  $\theta \geq \theta_{\text{sonic}}$ . The corresponding pressure jump for these two flow angles is shown in Figure 19. It can be seen that the measured data generally fall between these two limits for  $M \leq 1.3$ . For larger Mach numbers, it can be expected that the flow separates and consequently is not of interest here.

The above considerations lead to the following phenomenological procedure for modeling the influence of the boundary layer on altering the shock wave strength and location (Figure 22). The airfoil surface is allowed to have a "rubber wall" which deflects at the foot of any shock which impinges on the airfoil surface. The initial slope of the deflected displacement surface is chosen as  $\theta_{\max}$ . The surface is then bent back to a required slope by an "ad hoc" shape function. The deflecting surface continually moves with the shock to model the strong interaction feature. At this stage, there is no attempt to calculate the resulting boundary layer displacement surface. This would represent a next step in the solution.

The choice of  $\theta_{\max}$  as the unique angle for the viscous wedge is based on the following reasoning. The inviscid solution tries to place a normal shock at the airfoil surface. This shock wave is formed by compression and expansion waves emanating from the surface of the airfoil and sonic line upstream of the interaction. This wave structure is basically unaffected by the interaction at the foot of the shock wave. On the other hand, the boundary layer must weaken the shock to obtain a compatible flow. We postulate that the resulting shock wave is the strongest oblique and attached shock wave allowed; i.e.,  $\theta = \theta_{\max}$ . Since the surface downstream of the shock must bend back in a stream-wise direction, an expansion of the subsonic flow will result. It is not

inconsistent then that the measured pressures (Figure 19) will always be equal to or less than  $P_{2\theta_{\max}}$

The choice of the shape function needed to bend back the displacement surface remains arbitrary at this time. Several shapes have been tried with the most successful to date being a cubic curve. Figure 23 shows the comparison with an exponential shape motivated by the theoretical analysis in Reference 45. Let the airfoil shape be given by  $z = \delta F(x)$  where  $\delta$  is the thickness ratio. Then the modified shape is given by

$$z = \delta(F(x) + \Delta F(x))$$

where (see Figure 22),

$$\Delta F(x) = \begin{cases} 0 & x < x_s \\ \theta_{\max}(\eta - \eta^2 + \frac{1}{3}\eta^3)\xi & x_s \leq x \leq x_s + \xi \\ \frac{1}{3}\xi\theta_{\max} & x_s + \xi < x \end{cases} \quad (15)$$

$$\eta = \frac{x - x_s}{\xi}$$

where  $x_s$  is the location of the apex of the viscous wedge and  $\xi$  is a free parameter defining the length of the displacement surface. The above formula conforms to the conditions:

$$\Delta F = 0; \quad \Delta F' = \theta_{\max} \quad \text{at } x = x_s$$

$$\Delta F' = 0; \quad \Delta F'' = 0 \quad \text{at } x = x_s + \xi.$$

A final displacement thickness equal to  $\xi\theta_{\max}/3$  results. For simplicity, the above formulation is termed a "cubic-wedge" displacement function.

## (2) Implementation of Model into 2-D Inviscid Calculations

The above formulation has been incorporated into the inviscid small disturbance program. At the end of each relaxation sweep through the field, the airfoil surface slope is modified if a "shock point" has been detected to occur at the airfoil surface. Referring to Figure 24, the point  $x_s$  is taken as the x-location one mesh point ahead of the shock point. The formula for  $\theta_{\max}$  is given from the shock polar equation for the small disturbance equation (see Murman and Cole, Reference 46) as

$$\theta_{\max} = \pm \frac{4}{\gamma + 1} \left( \frac{(\gamma + 1)\phi_{x1} - K}{3} \right)^{3/2} \quad (16)$$

with the plus (minus) sign for the upper (lower) surface. The velocity  $\phi_{x1}$  is calculated from a centered difference formula for the location two mesh points upstream of  $x_s$ . If this value of  $\phi_{x1}$  leads to a negative argument in the above,  $\theta_{\max}$  is set to zero.

The above procedure has been tested on several airfoils, some representative 2-D results are shown in Figure 25. A value of  $\xi = .1$  was found to be adequate to move the shock upstream and not cause too severe a reexpansion downstream of the shock. A case was computed for a shock moving upstream and then downstream to check uniqueness of the final position. Also, the uniqueness with mesh refinement was checked. Some calculations have been done using  $\theta_{\text{sonic}}$  instead of  $\theta_{\max}$ . No major differences were detected.

The Murman Bump is a model which participates actively in each inviscid iteration. During the integration of the method into the code, it was found that the original idea for "hooking" the origin of the ramp to a mesh point inevitably led to instabilities in the numerical solution. The cause of the instability was the tendency of the origin to alternate between mesh points. By interpolating the solution locally to determine the actual position of the sonic point in the smeared shock, the origin of the bump could be attached to a point that did not change in discrete steps, but rather continuously. It was found that this modification uncoupled the physical model from the numerics and led to a reliable iteration procedure. In addition, it was found that the convergence was improved if the bump was only "turned on" after the basic solution had been allowed to converge to the point where the character of the inviscid solution has fully emerged. A modification of the scheme to use a

"refined" ramp equation which more closely duplicated the strong interaction in model problems led to results essentially the same as the original polynomial, while the more complex formula required a considerable increase in computational time due to the use of an exponential. Hence, the 'polynomial bump' has been retained in the code and the study with the better physical model can be viewed as verification that the results are insensitive to the fine scale details of the bump.

The results obtained from these runs suggested that the origin of the ramp should indeed be placed slightly upstream of the sonic location in the shock as the original method specified in order to better simulate the upstream influence of the interaction. Indeed, it appears that some improvement can be obtained by doing this. A nominal shift of  $1 \sim 2\%$  chord appears to improve correlation and has been left as a user option at this time.

The model can be extended to three-dimensions by considering the three-dimensional shock relations. The shock polar for a 3-D shock which is the weak solution of the equation

$$\left(Ku - \frac{\gamma + 1}{2} u^2\right)_x + \tilde{v}_y + \tilde{w}_z = 0 \quad (17)$$

is (see Murman and Cole, Reference 46)

$$\left(K - \frac{\gamma + 1}{2} (u_2 + u_1)\right) (u_2 - u_1)^2 + (v_2 - v_1)^2 + (w_2 - w_1)^2 = 0. \quad (18)$$

Taking  $\tilde{y}$  as the spanwise direction and  $\tilde{z}$  as the direction normal to the air-foil (mean) surface, we then want to find the maximum value of  $w_2$  for  $u_1$ ,  $v_2$ ,  $v_1$  and  $w_1 = 0$  given quantities. This result follows from setting  $\partial w_2 / \partial u_2 = 0$  to find the value of  $u_2$  giving maximum  $w_2$ . The result is

$$u_{2_{w_2 \max}} = \frac{1}{3} \left( \frac{4K}{\gamma + 1} - u_1 \right)$$

and

$$w_{2 \max} = \pm \sqrt{\frac{16}{27} \frac{1}{(\gamma + 1)^2} \left( (\gamma + 1)u_1 - K \right)^3 - (v_2 - v_1)^2} \quad (19)$$

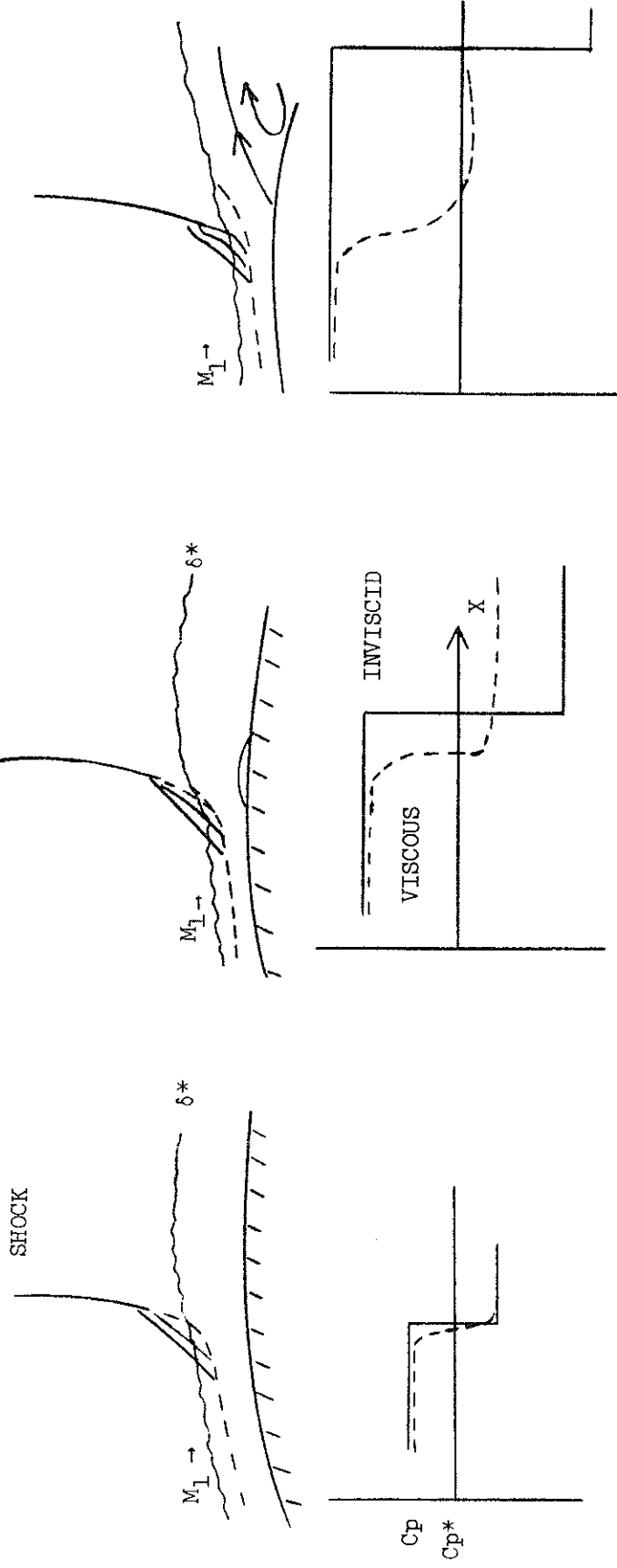
where the plus (minus) sign is for the upper (lower) surface. Thus, the maximum value of  $w_2$  occurs when  $v_2 = v_1$ ; i.e., the shock is normal to the free-stream. The minimum value of  $w_2 = 0$  occurs when the deflection in the spanwise direction is the maximum allowable turning angle to the given upstream Mach number.

The 3-D calculation is made by computing  $x_s$  and  $\phi_{x_1}$  as in the 2-D case, and then calculating  $v_1$  at the same point as  $\phi_{x_1}$  and  $v_2$  at the next point downstream of the shock point. This then gives the value of  $w_{2\max}$  for the calculated values of  $u_1$ ,  $v_1$  and  $v_2$ .

Figure 26 shows some results for the 3-D case. The general experience indicates that the majority of the work done with the present computer code will be carried out with wings at or near design conditions, so that the shock strengths will typically be minimal and the explicit use of the present model may or may not be called for, as shown in the figure, where the changes due to the ramp were small.

A calculation using both the strip boundary layer and the Murman Bump raises a question as to the proper use of both of these options simultaneously. At first it appears that this would produce a "double count" of the shock boundary layer interaction because the strip viscous correction also simulates the shock boundary layer interaction. However, because the Bump reduces the strength of the shock, the displacement surface rise at the shock foot is substantially reduced. In a similar fashion, the displacement surface reduces the strength of the shock so that the Murman Bump does not operate with the strength which it would have if the viscous displacement correction was not in effect. Thus, the two methods tend to compensate for each other, and the strong shock boundary layer interaction is not doubly accounted for in the present method when both options are in effect. The precise details of the complete interaction process do present an area for additional study.





(i)

$M_1 \approx 1.05 - 1.10$

Weak Interaction  
Not Separated

(ii)

$M_1 \approx 1.10 - 1.30$

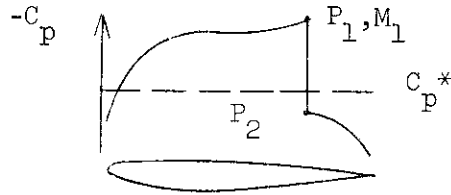
Strong Interaction  
Below Incipient  
Separation

(iii)

$M_1 \geq 1.30$

Strong Interaction  
Separated

Figure 18 Types of Shock - Turbulent Boundary Layer Interactions



EXPERIMENTS

- KACPRZYNSKI-OHMAN,  $Re_c = 21 \times 10^6$
- YOSHIHARA-ZONARS-CARTER,  $Re_c = 30 \times 10^6$
- ◇ PEARCEY,  $Re_c = 2 \times 10^6$
- † FLIGHT, XI,  $Re_c = 20 \times 10^6$
- △ SINNOTT-OSBORNE,  $Re_c \approx 2 \times 10^6$

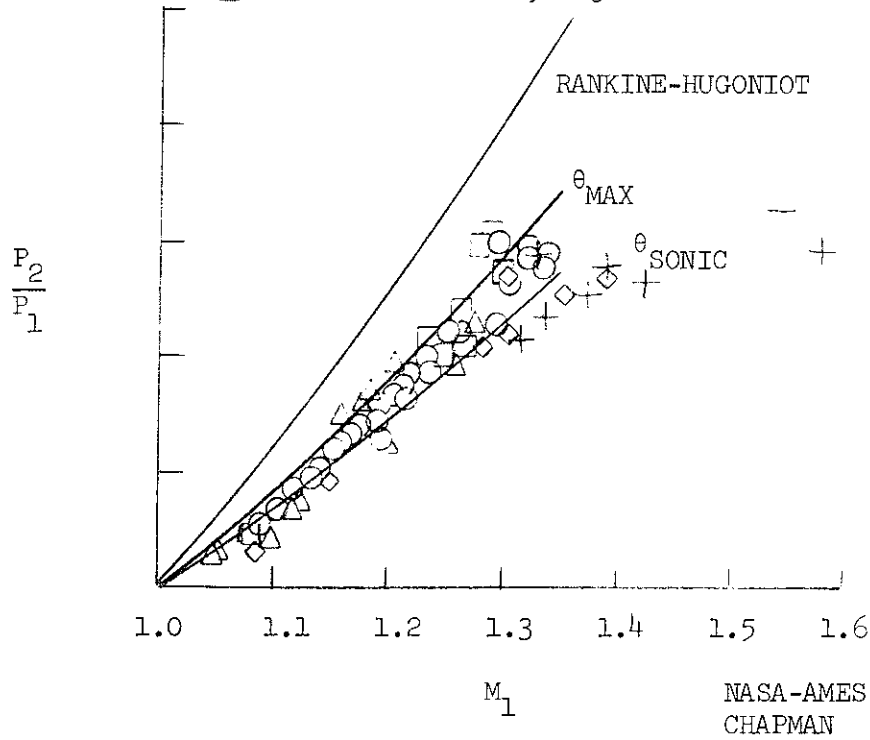
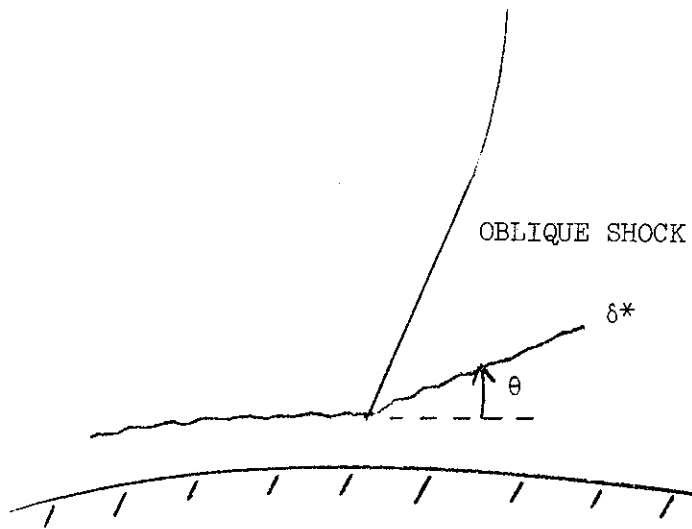


Figure 19 Pressure Rise Across Shocks



$\delta^*$  FORMS WEDGE LIKE SURFACE WHICH PUSHES SHOCK FORWARD AND WEAKENS SHOCK.

Figure 20 Yoshihara's Viscous Wedge Model

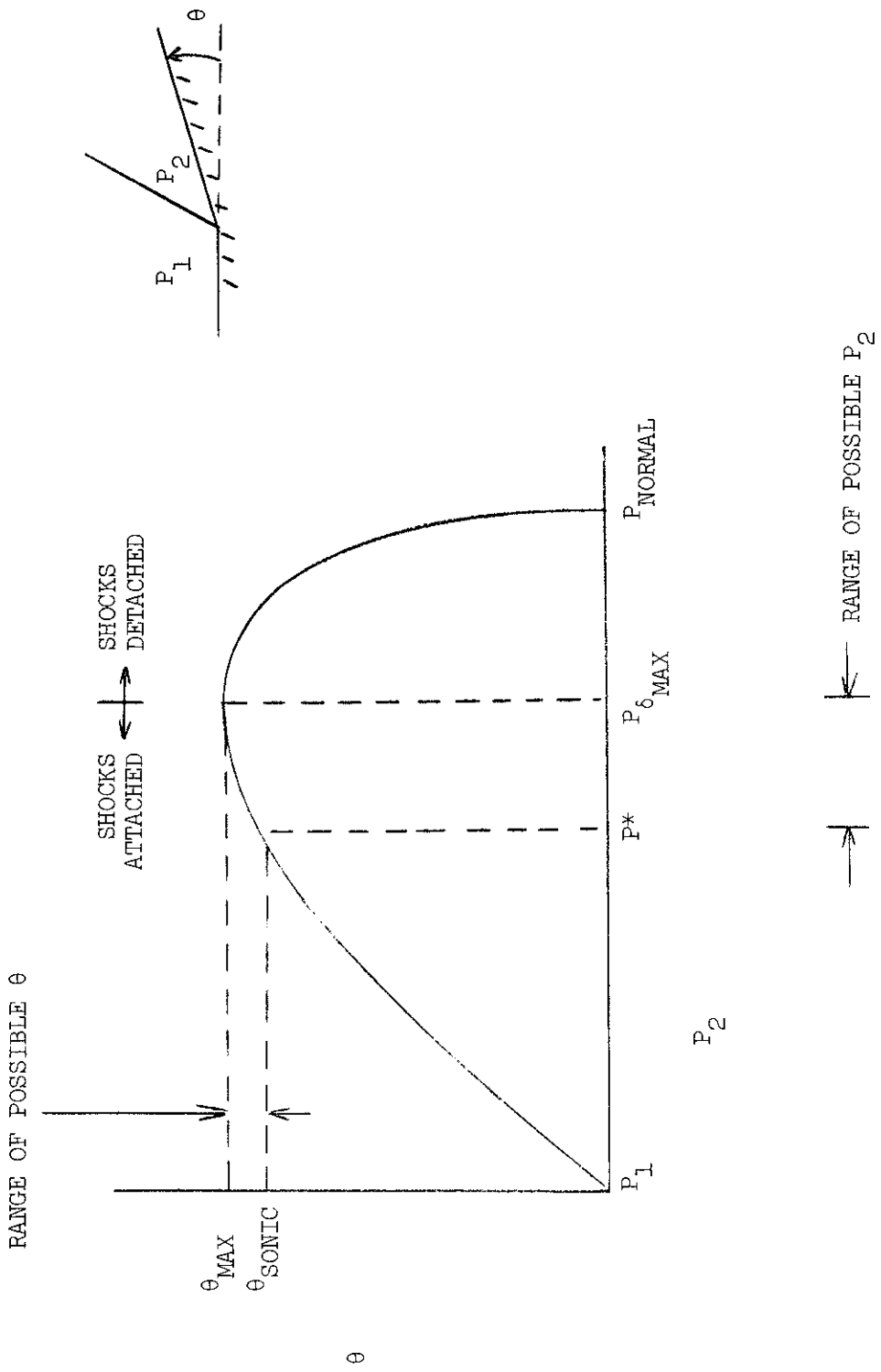
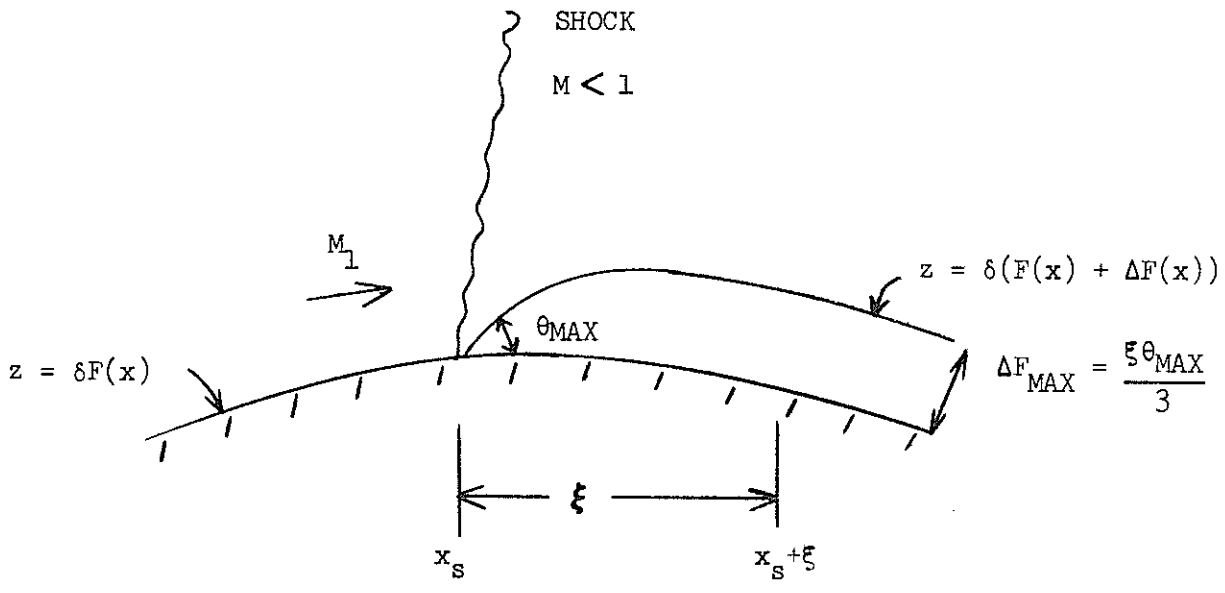


Figure 21 Shock Polar



CUBIC WEDGE DISPLACEMENT FUNCTION

$$\Delta F = \left\{ \begin{array}{ll} 0 & x < x_s \\ \theta_{MAX} \xi \left( \eta - \eta^2 + \frac{1}{3} \eta^3 \right) & x_s \leq x \leq x_s + \xi \\ \frac{1}{3} \xi \theta_{MAX} & x > x_s + \xi \end{array} \right.$$

$$\eta = \frac{x - x_s}{\xi}$$

Figure 22 Rubber Wall Model

<u>CUBIC</u>	$y = \delta (x - x^2 + \frac{x^3}{3})$	B.C.'s	$y(0) = 0, y'(0) = \delta$
<u>EXPONENTIAL</u>	$y = \frac{\delta}{3} (1 - e^{-3x})$		$y(1) = \frac{\delta}{3}, y'(1) = 0$
	$y(0) = 0, y'(0) = \delta$		
	$y(\infty) = \delta/3$		$y''(1) = 0$

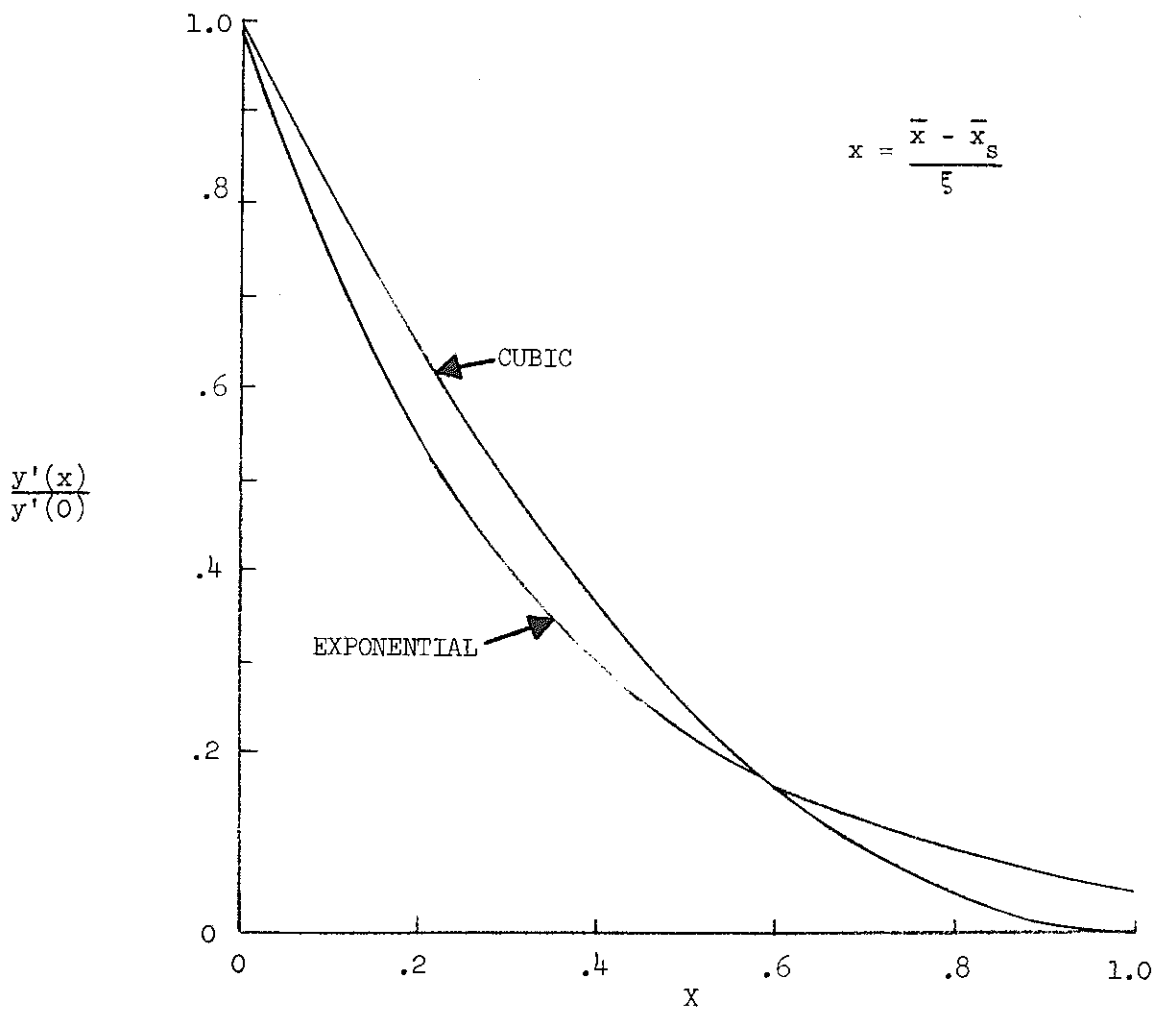
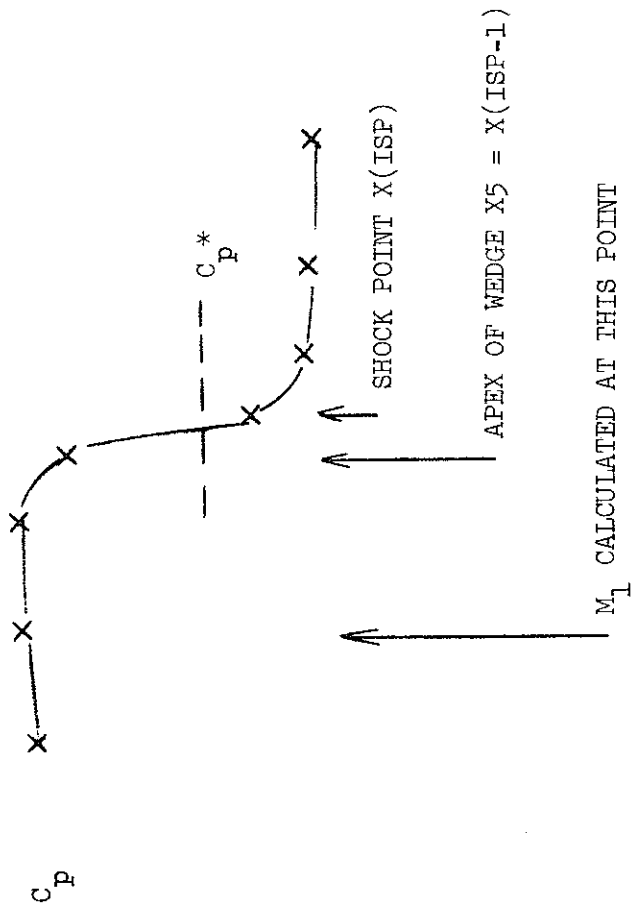


Figure 23 Comparison of Empirical & Theoretical Models



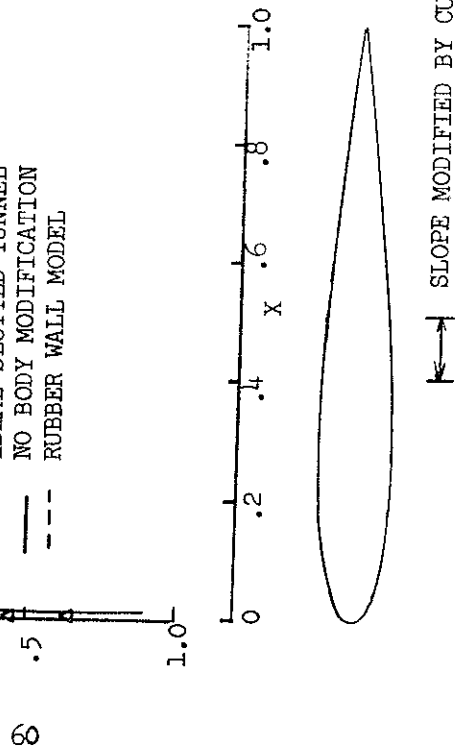
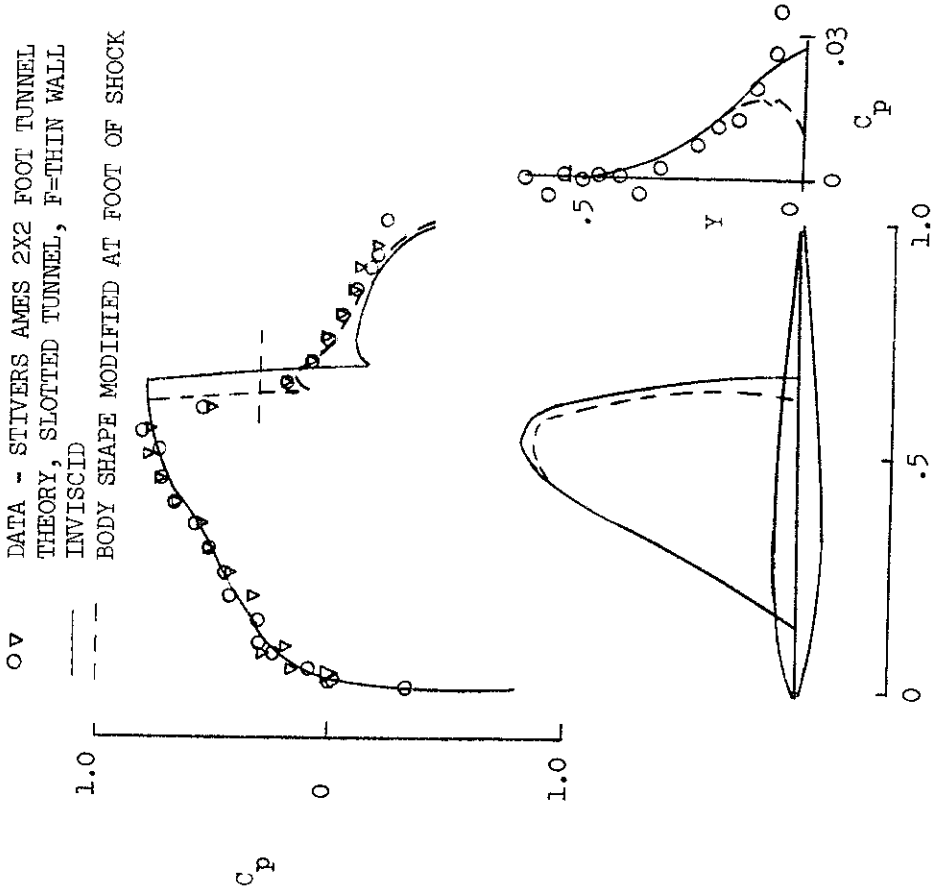
- o  $\xi \approx .10$
- o SLOPE MODIFIED AFTER EACH RELAXATION SWEEP IS FINISHED

Figure 24 Implementation

64A010 AIRFOIL

$M = .84 \quad \alpha = 0^\circ$

DATA - STIVERS AMES 2X2 FOOT TUNNEL  
 THEORY, SLOTTED TUNNEL, F-THIN WALL  
 INVISCID  
 BODY SHAPE MODIFIED AT FOOT OF SHOCK



←→ SLOPE MODIFIED BY CUBIC

Figure 25 Example of Viscous Wedge Effect



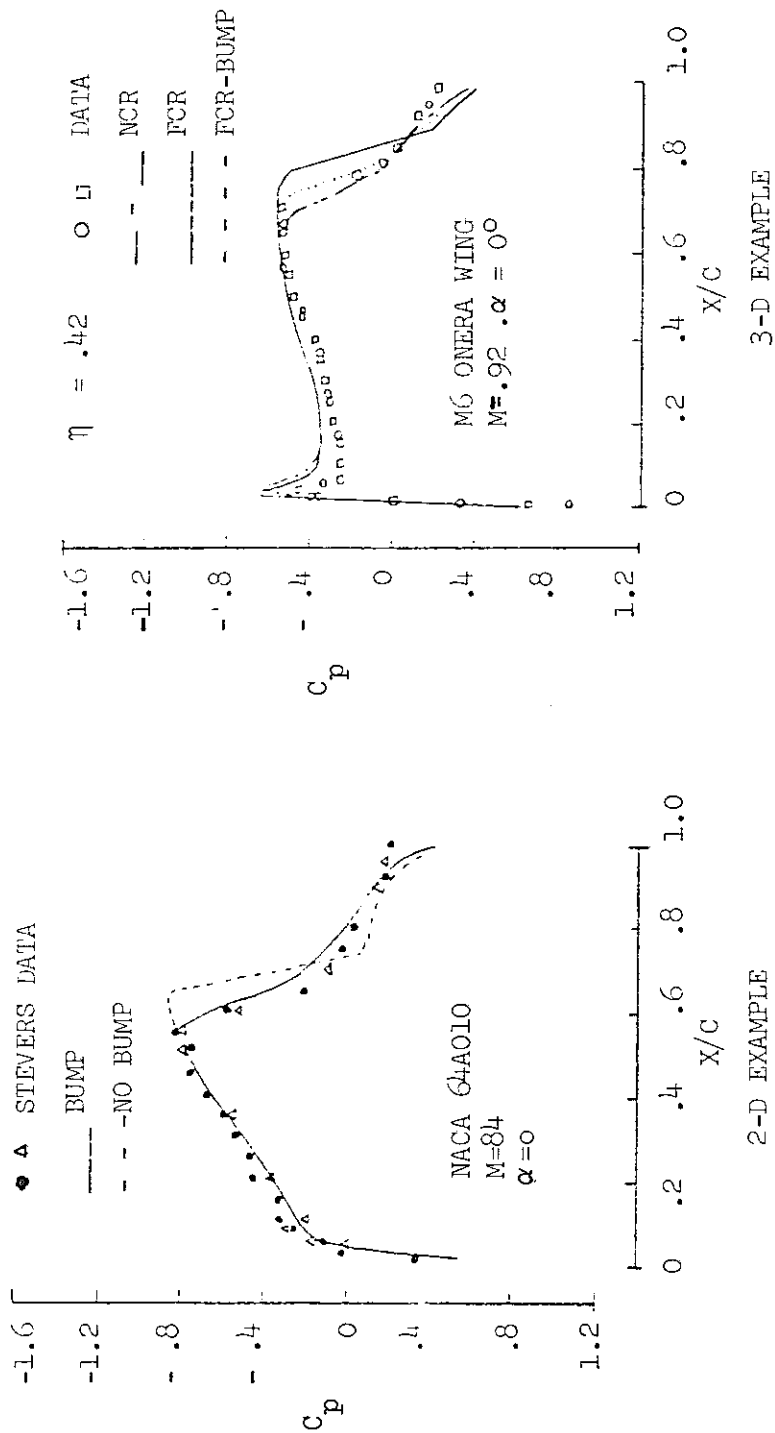


Figure 26 Shock Boundary Layer Interaction Effects

### c. Separation Treatment

In the analysis of transonic flow about finite wings and wing-body combinations, it is important to be able to treat regions of shallow separated flow. Most airfoils can be expected to operate with a region of separation occurring on the upper surface near the trailing edge, this is especially true of airfoils at transonic maneuver conditions. Current supercritical airfoils often experience an additional region of separation on the lower surface, in the cove. It is important to treat these separated flow regions in such a way as to prevent the computer code from failing when it detects such regions.

The procedures used for treating these shallow separation regions follow those of Bavitz (Reference 4). Because of the equivalence between the 2-D displacement thickness and the 3-D displacement surface for the special case of the infinite swept wing approximation employed in the present method, the extension of the methods employed in 2-D to 3-D is self-consistent. Care should be taken in using these ideas when a more elaborate 3-D boundary layer calculation is employed. On the upper surface, shallow separations are treated by holding the slope of the equivalent inviscid airfoil constant from the separation point to the trailing edge. On the lower surface, the treatment used in the presence of shallow cove separation is to select a representative displacement thickness shape so as to allow the iteration procedure to continue. In order to define  $\delta^*$  for the separated region, four points are chosen along the chord. The first point chosen is 10% chord ahead of the separation point. The second point is located 8% chord ahead of the separation point. The third point is located halfway between the separation point and the trailing edge and the last point is located at the trailing edge itself. The values of  $\delta^*$  at the first two of the above points are taken to be those previously calculated. The value of  $\delta^*$  at the third point is determined by incrementing the value at the first point according to an empirical equation based on the pressure coefficient difference between the two chordwise points. The relationship used in this treatment (which was developed as a result of an extensive correlation study with supercritical airfoils) is:

$$\frac{\delta^*_{L_3}}{c} = \frac{\delta^*_{L_1}}{c} + .033 \left( C_{P_{L_3}} - C_{P_{L_1}} \right) - .022 \left[ \left( \frac{x}{c} \right)_3 - \left( \frac{x}{c} \right)_1 \right]. \quad (20)$$

At the trailing edge,  $\delta^*$  is taken to be the average of the first and third  $\delta^*$  values. A third degree polynomial is fit to these four values of  $\delta^*$  to describe the variation of  $\delta^*$  from the separation point to the trailing edge. As Bavitz points out, the most arbitrary values in the model, those near the third chord-wise station above, are defining the equivalent inviscid shape in the cove region, where the slope is approximately zero. In this region, the effect of small geometric perturbations on the pressure distribution is negligible. Under these circumstances, it seems that qualitatively reproducing the shape is sufficient to allow reasonable calculations to proceed. It should be noted that the empirical relationship above, was determined from a detailed study of early Whitcomb airfoils.

The separation treatments described above are designed solely for engineering use. That is, it is understood that the pressure distributions determined aft of the separation point may be in error. However, these treatments do allow the code to function and yield accurate  $C_p$ 's ahead of the separated region and reasonable engineering approximations beyond the separation point. Thus, the code can continue to supply reasonable results under situations in which the lack of such treatment would have caused the code to halt without yielding any information at all. As the code was developed in modular form, replacement of these empirical treatments with more rigorous treatments as they become available is facilitated.

## 5. BODY MODEL\*

It is well known that fuselage effects will strongly influence the wing pressure distribution in transonic flows. In order to obtain a truly useful engineering tool for transonic flow analysis of actual aircraft configurations, some representation of the body must be included. In the present program, it has proven effective and simple to model the body by providing a constant rectangular cross-section boundary condition support surface upon which the streamwise flow inclination angle can be specified. Figure 27 shows the way in which this surface appears in the computational space. This approach provides the user with a great deal of flexibility in modeling any desired geometric effects. Because the detailed slope input is very laborious, the program has a simple body model input treatment which should be acceptable in most cases. The required input information is shown in Figure 28. The program then assumes an elliptic cross-section body defined by the input body lines. Body slopes are generated using the elliptic cross-section model, together with the input body lines.

In order to provide the most accurate possible body effects for transonic wing analysis and design, the slopes specified on the boundary condition support surface should not be the actual body slopes, but rather some suitably modified set of slopes that take into account the difference between the location of the actual body and the prismatic surface on which the slope boundary condition is applied. Slender body theory can be used to determine the appropriate modifications to the actual boundary conditions required when they are transferred to the computational surface. According to slender body theory, the body thickness effects should be represented by a source with strength proportional to rate of change of body area,  $S'(X)$ , where  $S(X)$  is the cross-sectional area. When considering the boundary condition to be specified over the computational surface at a particular streamwise plane, we require the source strength over this surface to be the same as the source strength for the actual body at this streamwise cross-section location. In this manner, we ensure the correct global effect of the body on the rest of the flow field. If we consider the

---

\* The authors would like to acknowledge the modifications to the inviscid program made by Allen Chen of Boeing and Jack Werner of the Polytechnic Institute of New York for providing the appropriate slender body corrections to the boundary conditions.

body cross-section to be specified by the curve  $C$ , and the prism to be specified by  $\bar{C}$ , then the requirement that the source strength of the two cross-sections be identical becomes

$$\int_c \frac{\partial \phi}{\partial n} dc = \int_{\bar{c}} \frac{\partial \phi}{\partial n} d\bar{c} \quad (21)$$

or

$$\sum_{j=0}^N \left. \frac{\partial \phi}{\partial n} \right|_j \Delta C_j = \sum_{j=0}^N \left. \frac{\partial \phi}{\partial n} \right|_j \Delta \bar{C}_j \quad (22)$$

so that the simple gradient specified on the prismatic surface is related to the actual boundary conditions by

$$\left. \frac{\partial \phi}{\partial n} \right|_{\text{prism}} = \frac{\Delta C}{\Delta \bar{C}} \left. \frac{\partial \phi}{\partial n} \right|_{\text{body}}. \quad (23)$$

This procedure is illustrated in Figure 29.

Angle of attack effects due to body incidence can be treated in a similar manner. In this case, we again follow slender body theory by considering equivalent doublet strengths required to produce the correct cross flow effect. Recall that the doublet strength is proportional to the cross-sectional area  $S(X)$ .

Since the body slopes have already been specified by considering the thickness distribution, the "correction" available for treating the body on the prism surface consists of modifying the actual geometric angle-of-attack to an appropriate "effective" angle-of-attack. The effective angle-of-attack can be selected by requiring

$$\alpha_{\text{EFF}} \bar{S} = \alpha_{\text{geo.}} S(X) \quad (24)$$

where  $\bar{S}$  is the prism cross-sectional area. This is the formal statement of doublet strength equality. The resulting boundary condition then becomes on

the top and bottom surface:

$$\begin{aligned}
 \phi_n \left| \begin{array}{l} \text{on BCSS} \\ \text{Top \& Bot.} \end{array} \right. &= \frac{\Delta C}{\Delta \bar{C}} \frac{\partial Z_B}{\partial X} - \alpha_{\text{EFF}} & (25) \\
 &= \frac{\Delta C}{\Delta \bar{C}} \frac{\partial Z_B}{\partial X} - \frac{S}{S} \alpha_{\text{geo.}}
 \end{aligned}$$

while the side slopes are not modified by the angle-of-attack so that they are given by

$$\phi_n \left| \begin{array}{l} \text{BCSS} \\ \text{SIDE} \end{array} \right. = \frac{\Delta C}{\Delta \bar{C}} \left( \frac{\partial Y_B}{\partial X} \right) . \quad (26)$$

Figures 30 and 31 show the agreement for a typical body case and also the capability to handle area rule effects. The results indicate the strong influence that the body has on the wing pressures.

- PLANE OF SYMMETRY ASSUMED ABOUT  $y = 0$  PLANE
- PRISM MODEL EXTENDS THROUGH UPSTREAM AND DOWNSTREAM COMPUTATION BOUNDARIES.

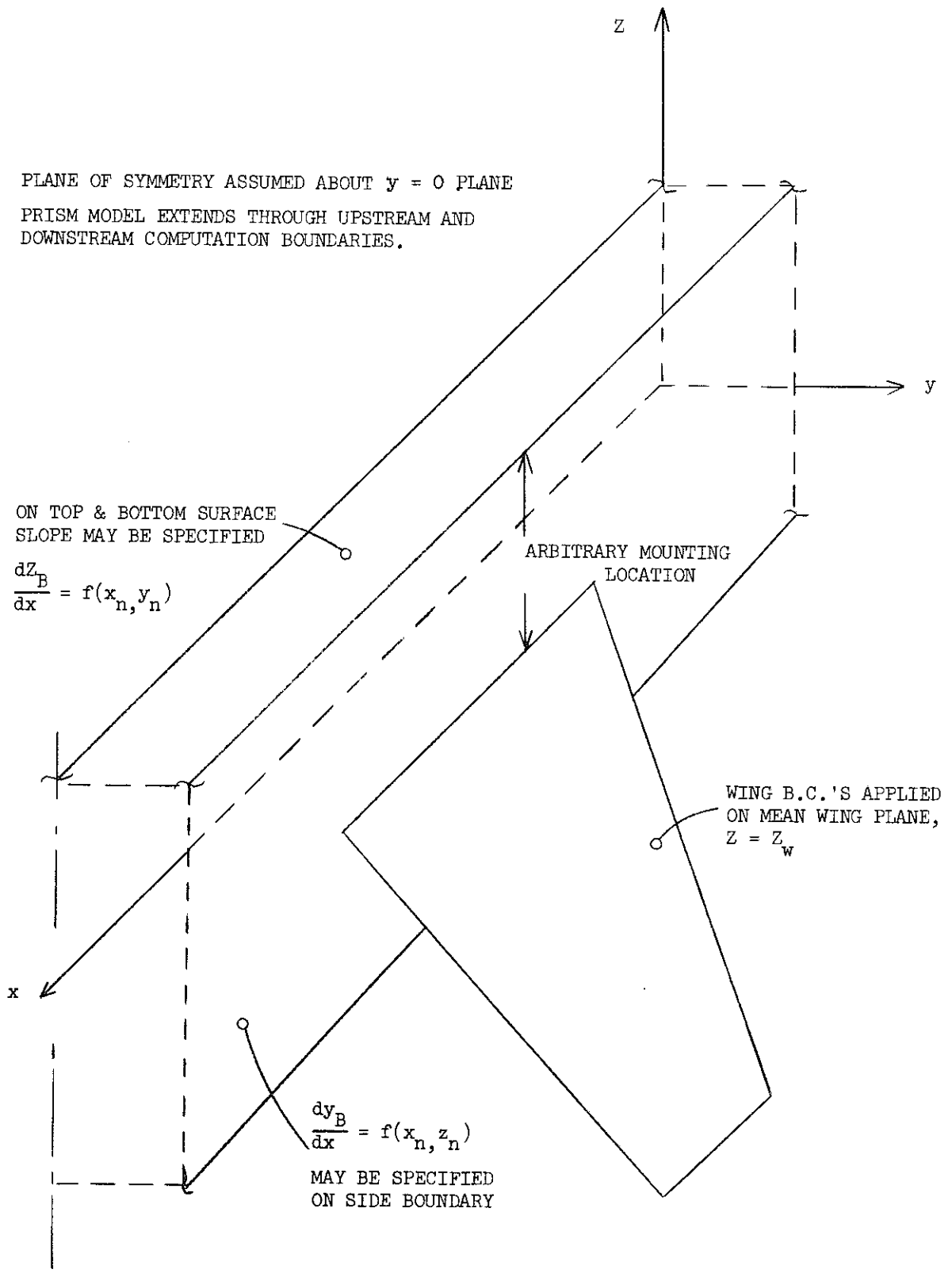
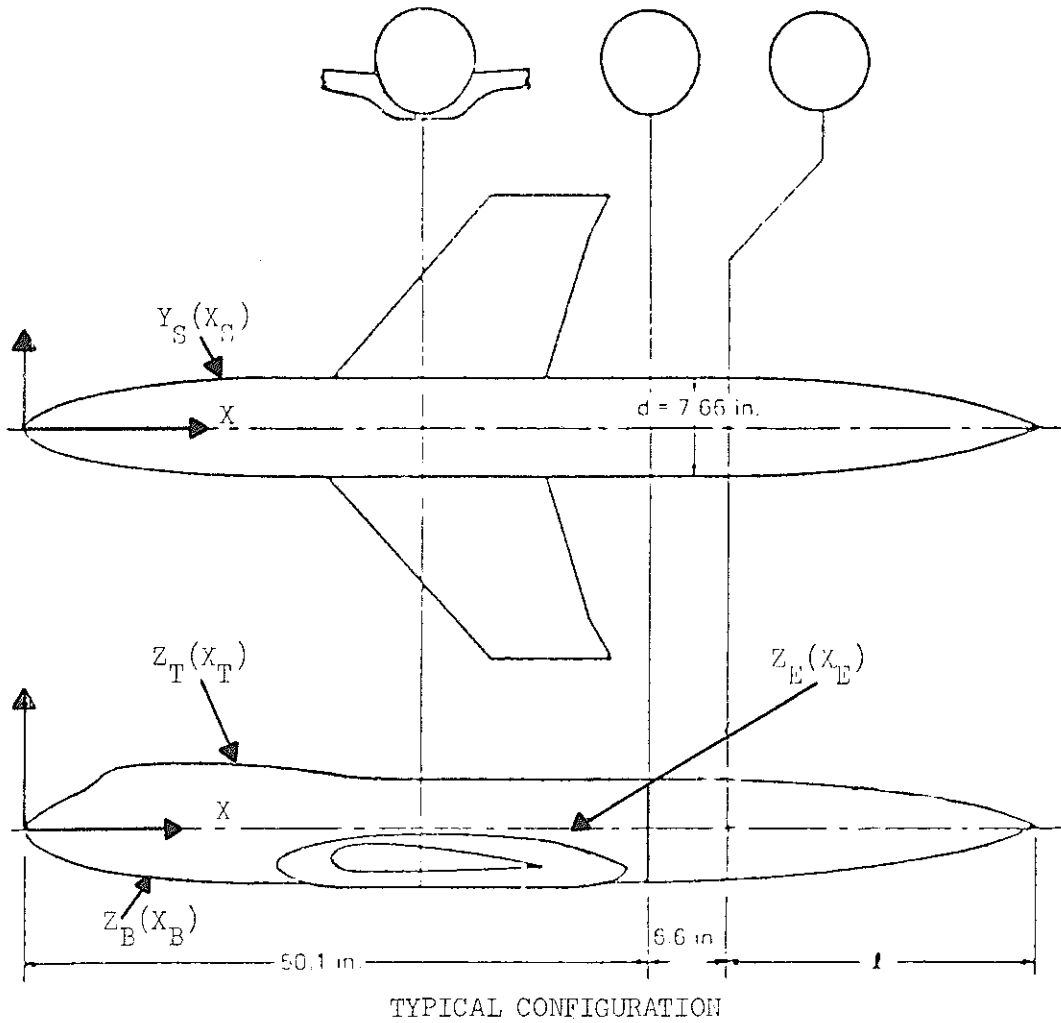


Figure 27 Schematic of Boundary Conditions Support Surface



Total Input for Body Simulation

1. Body Top Line,  $Z_T(X_T)$
2. Body Bottom Line,  $Z_B(X_B)$
3. Body Side Line,  $Y_S(X_S)$
4. Body Side Line Elevation,  $Z_E(X_E)$

Figure 28 Simple Body Input for Infinite Body Boundary Condition Surface



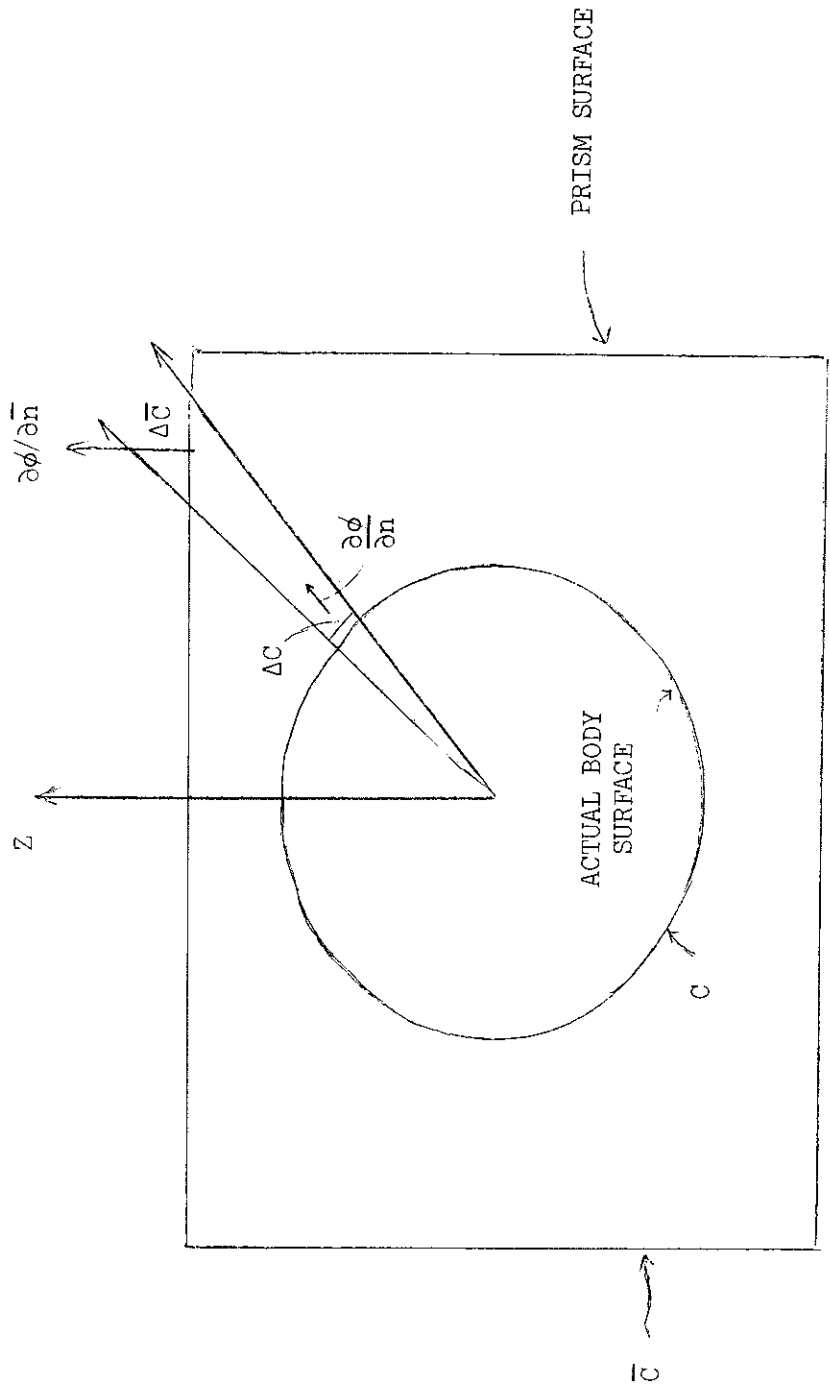


Figure 29 Equivalent Body Source Model

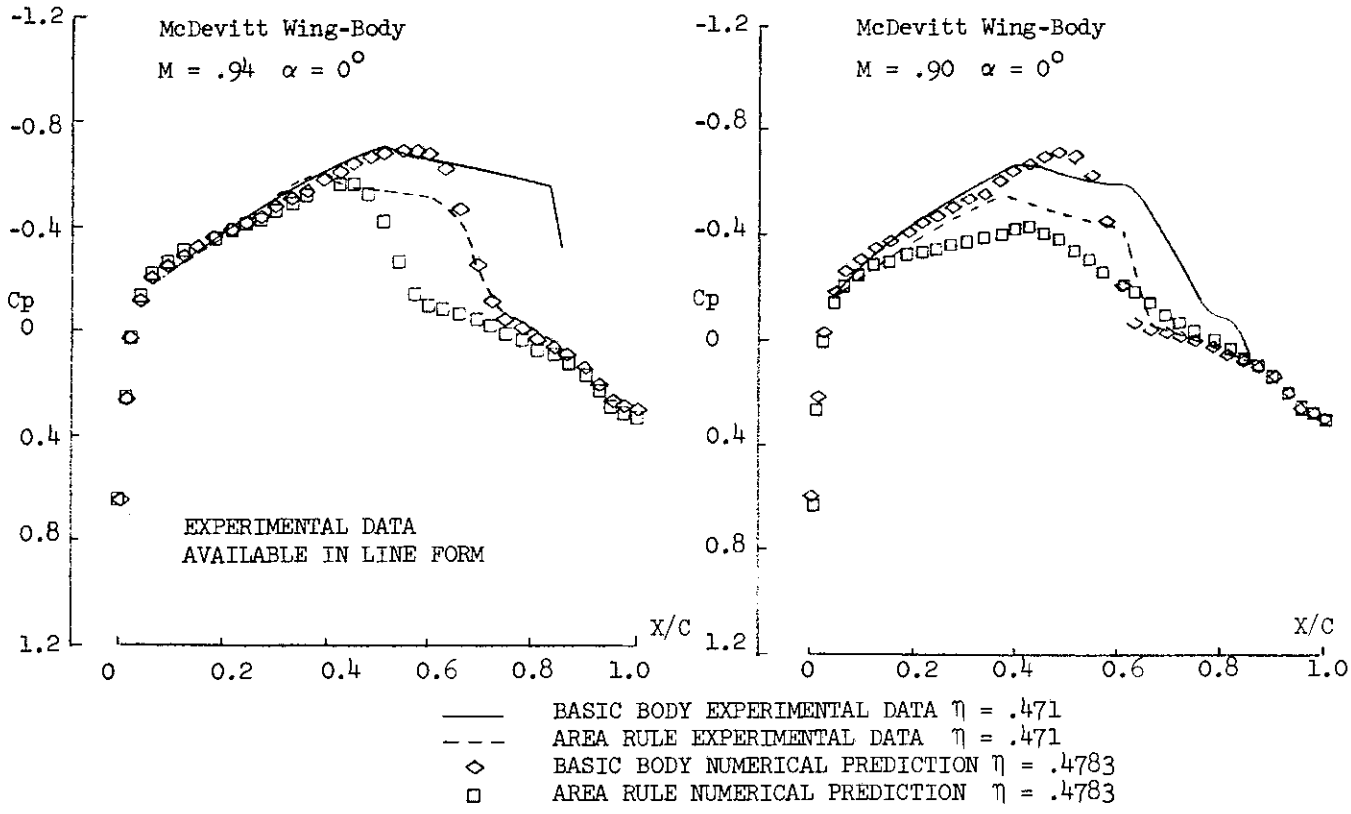
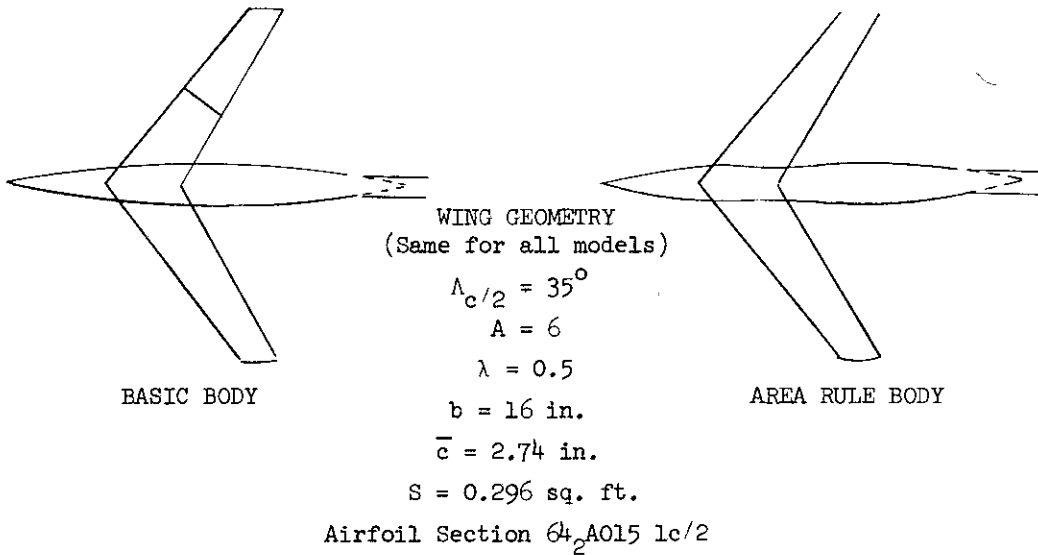
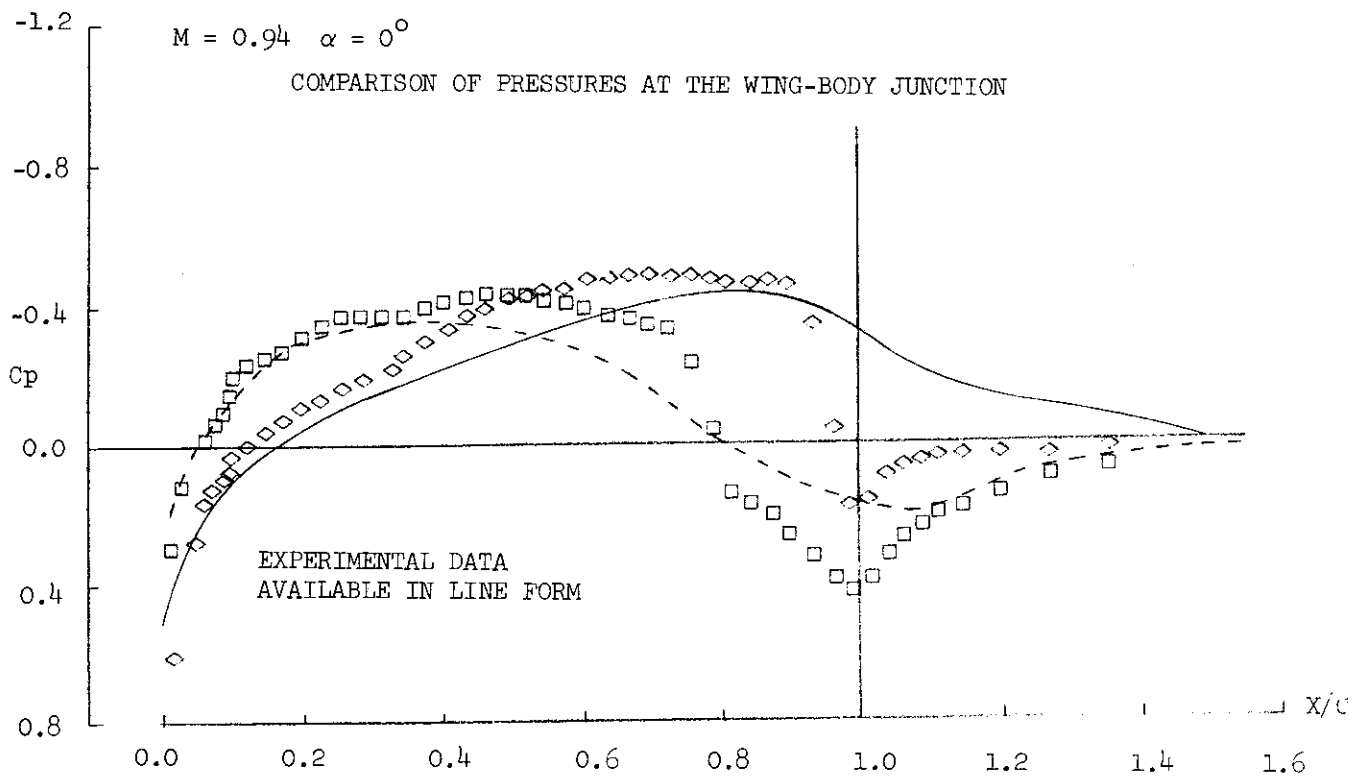
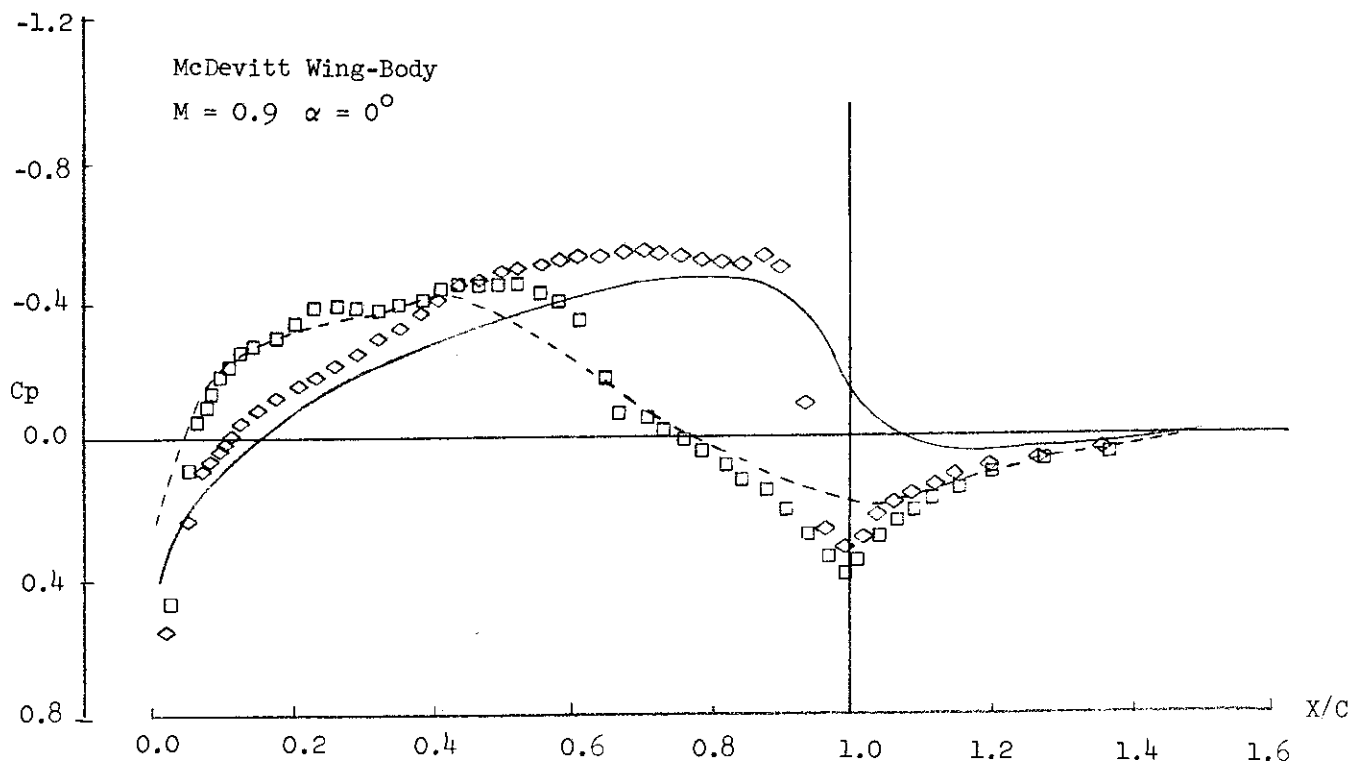


Figure 30 Wing-Body Interaction Effects - Geometry and Wing Station Results



- NUMERICAL PREDICTION AREA RULE BODY  $\eta = .12796$
- ◇ NUMERICAL PREDICTION BASIC BODY  $\eta = .12796$
- EXPERIMENTAL DATA BASIC BODY
- EXPERIMENTAL DATA AREA RULE BODY

Figure 31. Wing-Body Interaction Effects - Comparison of Pressures at the Wing-Body Juncture

## 6. TRANSONIC WAVE DRAG ON SWEEPED WINGS\*

### a. General

In this section we present an extension to the modified small disturbance theory for transonic flows by supplying the farfield drag formula equivalent to the farfield drag expression for the classical small disturbance theory.

An integral transonic drag relation valid for unswept wings has been derived by Murman & Cole, (Reference 46), proceeding directly from the classical small disturbance equation,

$$\left[ Ku - (\gamma + 1) \frac{u^2}{2} \right]_x + \nabla_T \cdot \vec{V}_T = 0.$$

This small disturbance equation was, in turn, derived from an asymptotic approach, (Reference 47), which made the implicit assumption that derivatives normal to the freestream were of a different order of magnitude from those in the streamwise direction. This assumption is implicit in the form adopted for the expansion of the velocity; i. e.,

$$\frac{\vec{q}}{U_\infty} = \hat{i}_x (1 + \epsilon u + \dots) + \hat{i}_y \delta v + \hat{i}_z \delta w$$

in which  $\epsilon$  and  $\delta$  are assumed of different order of magnitude. To be consistent with this assumption, any shock surfaces present must be almost normal to the freestream. This condition is generally violated over swept wings.

Bailey & Ballhaus (Reference 48) have modified the classical small disturbance equations by writing,

$$\left( Ku - (\gamma + 1) \frac{u^2}{2} + \epsilon (\gamma - 3) \frac{V_T^2}{2} \right)_x + \nabla_T \cdot (1 - \epsilon(\gamma - 1)u) \vec{V}_T = 0$$

adding terms which allow the resulting equation to reduce to the "correct small disturbance equation" for 2-D swept wings. The proposal of this equation for the calculation of 3-D swept wings implies that derivatives in the sweep direction are small compared to those normal to the sweep direction.

---

\* This section is based on a Grumman Aerospace Corporation, Aerodynamics Section Report (390-77-02, 12 May 1977) by Jack E. Werner, Consultant to Grumman.

For the swept case, an expansion analogous to that of References 45 and 46 would set:

$$\vec{U}_\infty = \hat{i}_n [\cos v + \epsilon u_n + \dots] + \hat{i}_t [\sin v + \delta V_T] + \hat{i}_z \delta w$$

where  $u_n$ ,  $v_t$  are speeds normal and tangential respectively to the sweep direction, and  $v$  is the sweep angle. This would lead to a small disturbance equation for the swept region which, unfortunately, would not hold where shocks are almost normal to the freestream (i.e., over the center section of a swept wing). Rather than pursue this approach, Bailey and Ballhaus have, in effect, proposed the first term of a "composite" expansion by including terms which are small in the unswept region but which become large enough to supply a correction in the swept region.

We now seek an integral relationship appropriate for the computation of drag from a solution of the Bailey-Ballhaus equation. If we proceed in a manner similar to Murman and Cole (Reference 46), we quickly encounter a serious difficulty in determining a divergence form associated with the drag and which would lead to a surface integral for the drag. To resolve this problem, we shall first explore the exact procedure of which Murman's and Cole's represents a first order approximation.

#### b. Exact Expression For Lift and Drag

An exact surface integral for the force on a wing surface may be obtained by considering the integral,

$$\int_V \vec{q} \cdot \nabla (\rho \vec{q}) dV$$

over a volume  $V$  over all space excluding the thin regions surrounding the wing, the wake and any shock surfaces present. Noting that the continuity equation renders the above integral identically zero, it may be transformed with the aid of Gauss' Theorem to obtain:

$$\int_V \vec{q} \cdot \nabla (\rho \vec{q}) dV \equiv 0 \equiv \int_A \rho \vec{q} (\vec{q} \cdot \vec{n}) dA - \int_V \rho (\vec{q} \cdot \nabla) \vec{q} dV \quad (27)$$

From the steady momentum equation,

$$-\rho (\vec{q} \cdot \nabla) \vec{q} = \nabla P \quad (28)$$

and a further application of Gauss' Theorem, we arrive at the equation,

$$\int_V \vec{q} \cdot \nabla \cdot (\rho \vec{q}) \, dV \equiv 0 \equiv \int_A \rho \vec{q} (\vec{q} \cdot \vec{n}) \, dA + \int_A \vec{p} n \, dA, \quad (29)$$

where the surface  $A = S_\infty + W + S_{\text{wake}} + S_c$  represents the closed surface formed by  $S_c$  surrounding shocks, the surface  $W$  about the wing,  $S_{\text{wake}}$  around the airfoil wake and  $S_\infty$  the remaining surface required for closure. Now,

$$\int_W \vec{p} n \, dA = \hat{i}_x D + \hat{i}_z L$$

is the net force on the wing. Also, we have the conditions  $\vec{q} \cdot \vec{n} = 0$  on the wing and over the wake surface, while  $p$  is continuous across the wake. These conditions allow us to write equation (29) in the form:

$$\int_V \vec{q} \cdot \nabla \cdot (\rho \vec{q}) \, dV \equiv 0 \equiv \int_{S_\infty} + \int_{S_c} (\vec{p} n + \rho \vec{q} (\vec{q} \cdot \vec{n})) \, dA + \hat{i}_x D + \hat{i}_z L. \quad (30)$$

The  $x$  component of the first surface integral on the right can be shown to yield the induced drag while the second surface integral is identified as the wave drag. If a solution of the classical small disturbance equation is substituted into the right hand side of equation (30) and only the first significant order of magnitude retained, the results yield the drag integral of Murman & Cole. The procedure, in effect, followed by Murman & Cole was to expand the left hand side of equation (30) directly, retain the first significant terms and apply Gauss' Theorem to the result. We shall proceed in a similar manner.

c. First and Higher Order Expansions

A combination of energy and continuity equations yields a convenient form of the continuity equation from which derivatives of the density  $\rho$  have been eliminated (Reference 49).

$$\nabla \cdot \left( \frac{\rho \vec{q}}{\rho_{\infty} U_{\infty}} \right) = \frac{\rho}{\rho_{\infty}} \left[ \nabla \cdot \frac{\vec{q}}{U_{\infty}} - \frac{\vec{q}}{U_{\infty}} \cdot \frac{\nabla (q^2 / 2U_{\infty}^2)}{(a/U_{\infty})^2} \right] \quad (31)$$

together with the energy equation,

$$\frac{a^2}{U_{\infty}^2} = \frac{1}{M_{\infty}^2} + \left( \frac{\gamma-1}{2} \right) \left( 1 - q^2 / U_{\infty}^2 \right) \quad (32)$$

Upon introducing the expansions:

$$\vec{q}/U_{\infty} = \vec{i}_x (1 + \epsilon u + \epsilon^2 u_2 + \dots) + \delta \vec{V}_T \quad (33)$$

$$\rho/\rho_{\infty} = 1 + \epsilon \sigma + \epsilon^2 \sigma_2 \quad (34)$$

$$1 - M_{\infty}^2 = \epsilon K \quad (35)$$

and the following relations obtained from the first order small disturbance theory:

$$\delta^2 = \epsilon^3 \quad (36)$$

$$\sigma = -u = \frac{p}{\gamma} \quad (37)$$

$$\nabla_{\mathbf{T}} u = \frac{\partial \vec{V}_{\mathbf{T}}}{\partial \mathbf{x}} \quad (38)$$

the continuity equation (31) in expanded form becomes,

$$\begin{aligned} \nabla \cdot \left( \frac{\rho \vec{q}}{\rho_{\infty} U_{\infty}} \right) = 0 = \epsilon^2 \left\{ \left( Ku - (\gamma+1) \frac{u^2}{2} \right)_{\mathbf{x}} + \nabla_{\mathbf{T}} \cdot \vec{V}_{\mathbf{T}} \right\} \\ + \epsilon^3 \left\{ -2 \left( \frac{V_{\mathbf{T}}^2}{2} \right)_{\mathbf{x}} - (\gamma-1) u \nabla_{\mathbf{T}} \cdot \vec{V}_{\mathbf{T}} + (\gamma-2) u \nabla_{\mathbf{T}} \cdot \vec{V}_{\mathbf{T}} \right. \\ + (\gamma-2) \left( K \frac{u^2}{2} - (\gamma+1) \frac{u^3}{3} \right)_{\mathbf{x}} + K (\gamma+1) \left( \frac{u^2}{2} \right)_{\mathbf{x}} \\ \left. + \left( Ku_2 - (\gamma+1) uu_2 \right)_{\mathbf{x}} + \left( \frac{\gamma+1}{2} \right) \left( \frac{u^3}{3} \right)_{\mathbf{x}} \right\} \\ + 0 (\epsilon^4) \end{aligned} \quad (39)$$



and proceeding from this to the expansion of  $\frac{\vec{q}}{U_\infty} \cdot \nabla \cdot \left( \frac{\rho \vec{q}}{\rho_\infty U_\infty} \right)$  :

$$\begin{aligned}
 \hat{i}_x \left( \hat{i}_x \cdot \frac{\vec{q}}{U_\infty} \cdot \nabla \cdot \left( \frac{\rho \vec{q}}{\rho_\infty U_\infty} \right) \right) &= \hat{i}_x \epsilon^3 \left( \left( \frac{K u^2}{2} - (\gamma+1) \frac{u^3}{3} - \frac{V_T^2}{2} \right)_x + \nabla_T \cdot (\vec{V}_T u) \right) \\
 + \hat{i}_x \epsilon^4 \left( -2u \vec{V}_T \cdot \nabla_T u - (\gamma-1) u^2 \nabla_T \cdot \vec{V}_T + (\gamma-2) u^2 \nabla_T \cdot \vec{V}_T \right. \\
 + \left( K \frac{(2\gamma-1)}{3} u^3 + \frac{(\gamma+1) - 2(\gamma+1)(\gamma-2)}{8} u^4 \right)_x \\
 + \left. \left( K u u_2 - (\gamma+1) u^2 u_2 \right)_x + u_2 \nabla_T \cdot \vec{V}_T \right) + \dots \quad (40)
 \end{aligned}$$

The term in  $\epsilon^3$  of this previous expansion was obtained by Murman & Cole directly from the classical small disturbance equation. Since the first two terms of the coefficient of  $\epsilon^4$  originate with the additional terms of Bailey and Ballhaus, the expansion of

$$\frac{\vec{q}}{U_\infty} \cdot \nabla \cdot \left( \frac{\rho \vec{q}}{\rho_\infty U_\infty} \right) \quad (?)$$

corresponding to the Bailey-Ballhaus equation would be:

$$\frac{\vec{q}}{U_\infty} \cdot \nabla \cdot \left( \frac{\rho \vec{q}}{\rho_\infty U_\infty} \right) \approx \hat{i}_x \epsilon^3 \left( \left( \frac{K u^2}{2} - (\gamma+1) \frac{u^3}{3} - \frac{V_T^2}{2} \right)_x + \nabla_T \cdot (\vec{V}_T u) - \epsilon \left( 2u \vec{V}_T \cdot \nabla_T u + (\gamma-1) u^2 \nabla_T \cdot \vec{V}_T \right) \right) \quad (41)$$

Unfortunately, the last term of equation (41) cannot be written in divergence form, and the volume integral of this last expansion of,

$$\frac{\vec{q}}{U_\infty} \cdot \nabla \cdot \left( \frac{\rho \vec{q}}{\rho_\infty U_\infty} \right)$$

cannot be converted completely into a surface integral. As a result, this particular expansion of the left hand side of equation (30) cannot match up with any corresponding expansion of the right side such as might be obtained by substituting a solution of the Bailey-Ballhaus equation into the right hand expression.

It would thus appear that the form represented by equation (41) cannot properly be associated with any surface integral expression for the drag. To obtain the proper expansion of,

$$\frac{\vec{q}}{U_\infty} \cdot \nabla \cdot \left( \frac{\rho \vec{q}}{\rho_\infty U_\infty} \right)$$

for swept wings, it is first observed that for unswept wings, the Bailey-Ballhaus terms are small and may be included in the expansion without affecting its magnitude to within  $O(\epsilon^3)$ . On the other hand, when swept shocks are present, these terms represented by the two leading terms in the coefficient of  $\epsilon^4$  in equation (40) become large and must be considered along with the  $\epsilon^3$

term. But, if these first two terms are now included, so should the third term be included since it is almost equal in absolute value to the second term. Inclusion of this third term now allows the resulting expansion to be written as a divergence; i. e.,

$$\begin{aligned}
 \frac{d}{dt} \nabla \cdot \left( \frac{\rho \vec{q}}{\rho_\infty U_\infty} \right) &\approx \hat{i}_x \epsilon^3 \nabla \cdot \vec{M} \\
 &\approx \hat{i}_x \epsilon^3 \left( \left( K \frac{u^2}{2} - (\gamma+1) \frac{u^3}{3} - \frac{V_T^2}{2} \right)_x + \nabla_T \cdot \left( \vec{V}_T u(1-\epsilon u) \right) \right) \\
 &= 0
 \end{aligned} \tag{42}$$

This establishes a vector  $\vec{M}$  analogous to that of Murman & Cole, but appropriate to the computation of drag for swept wings.

#### d. The Drag Integral

Integrating the pressure over the wing surface represented by  $z = \delta F(x,y)$ , an expression for the drag is obtained,

$$D = \delta^{4/3} P_\infty \iint_W \left[ p \frac{\partial F}{\partial x} \right]_w dx d\tilde{z} \tag{43}$$

where  $[ ]_w$  represent the jump across  $W$  and  $\tilde{z} = \delta^{1/3} z$ . Writing the boundary condition on the wing in the form

$$\frac{v}{1 + \epsilon u} = \frac{\partial F}{\partial x} \approx v(1 - \epsilon u) \tag{44}$$

The drag integral becomes with the substitution for p from equation (37)

$$\begin{aligned}
 D &= -\delta^{4/3} P_\infty \gamma \iint_W [uv (1-\epsilon u)] \, dx \, d\tilde{z} \\
 &= \delta^{4/3} P_\infty \gamma \iint_W \vec{M} \cdot \vec{n}_w \, dx \, d\tilde{z}
 \end{aligned} \tag{45}$$

Since,

$$\int \nabla \cdot \vec{M} \, dV = 0$$

from equation (42), an application of Gauss' Theorem to the volume bounded by  $S_c$ ,  $W$ ,  $S_{wake}$ ,  $S_\infty$  and substitution of the results into equation (45) yields:

$$\frac{D}{\delta^{4/3} P_\infty \gamma} = - \iint_{S_\infty} \vec{M} \cdot \vec{n} \, dA + \iint_{S_c} [\vec{M}] \cdot \vec{n}_c \, dS \tag{46}$$

where  $[\vec{M}]$  represents the jump in  $\vec{M}$  across the shock surface  $S_c$ , and from equation (42),

$$\vec{M} = \hat{i}_x \left( K \frac{u^2}{2} - (\gamma+1) \frac{u^3}{3} - \frac{V_T^2}{2} \right) + \vec{V}_T u (1-\epsilon u) \tag{47}$$

The integral over  $S_\infty$  may be interpreted to yield the induced drag and when integrated over the surface as  $x \rightarrow -\infty$  yields the same result as given by Murman & Cole, Reference (46).

e. Wave Drag

We now turn to the second integral in equation (46). But before dealing with it directly, an appropriate form of the kinematic shock jump condition;

$$[\vec{q}] \times \vec{n}_c = 0 \quad \text{on} \quad S(x,y,z) = 0 \quad (48)$$

must be developed. Letting  $\vec{n}$  represent the direction normal to the sweep direction and  $\vec{t}$  the direction tangent to it, equation (48) becomes,

$$\left( \hat{i}_n [u_n] + [\vec{V}_{T_1}] \right) \times \left( \hat{i}_n \frac{\partial S}{\partial n} + \nabla_{T_1} S \right) = 0 \quad (49)$$

or:

$$\hat{i}_n \times \left( [u_n] \nabla_{T_1} S - [\vec{V}_{T_1}] \frac{\partial S}{\partial n} \right) + [\vec{V}_{T_1}] \times \nabla_{T_1} S = 0$$

where  $T_1$  represents a direction in the plane transverse to  $\vec{n}$ .

Noting that the last term is of higher order than the preceding one, we may set the first term equal to zero resulting in:

$$\nabla_{T_1} S = \frac{\partial S}{\partial n} \frac{[\vec{V}_{T_1}]}{[u_n]} \quad (50)$$

A shock jump condition is derived by writing the small disturbance equation in the form:

$$\nabla \cdot \vec{q} = 0 \quad (51)$$

and applying Gauss' Theorem to the region surrounding the shock. This results in:

$$[\vec{q}] \cdot \vec{n}_c = 0 = \frac{[\vec{q}_n] \frac{\partial s}{\partial n} + [\vec{q}_T] \cdot \nabla_T s}{|\nabla s|} \quad (52)$$

Introducing the kinematic jump condition, equation (50), we have:

$$[q_n] [u_n] + [q_T] \cdot [\vec{V}_T] = 0 \quad (53)$$

or, since the scalar product is independent of axes rotation,

$$[q_x] [u] + [\vec{q}_T] \cdot [\vec{V}_T] = 0 \quad (54)$$

For the Bailey-Ballhaus equation, we have,

$$\begin{aligned} \vec{q} &= \hat{i}_x \left( Ku - (\gamma+1) \frac{u^2}{2} + \epsilon(\gamma-3) \frac{v_T^2}{2} \right) + \vec{V}_T (1 - \epsilon(\gamma-1)u) \\ &= \hat{i}_x q_x + \vec{q}_T \end{aligned} \quad (55)$$

Introducing this value of  $Q$  into the shock jump condition, equation (54), and employing results from the calculus of jumps (Reference 46) ; we obtain:

$$\left[ Ku - \frac{\gamma+1}{2} u^2 \right] [u] + [V_T]^2 - \epsilon [V_T]^2 [u] = \epsilon(\gamma-1) [V_T]^2 \langle u \rangle \quad (56)$$

It is of interest to note that setting  $\gamma = 2$  in the terms multiplied by  $\epsilon$  in equation (53), yields the NLR small disturbance equation (Reference 50). Alternatively, the NLR equation is obtained from equation (39) by applying the same considerations which led to equation (42) for  $\vec{M}$ ; i. e., retaining the first three terms in the coefficient of  $\epsilon^3$  instead of only the first two. In this respect, the NLR equation is seen to be wholly consistent with  $\vec{M}$  of equation (42) from the point of view of the expansion process.

We are now in a position to evaluate the wave drag integral:

$$\frac{D_{\text{WAVE}}}{\delta^{4/3} P_{\infty} \gamma} = \iint [\vec{M}] \cdot \vec{n}_c \, dA \equiv \iint J \, dA \quad (57)$$

Thus, with the aid of the kinematic condition, equation (50),

$$\begin{aligned} J &= [\vec{M}] \cdot \vec{n}_c = \frac{[M_n] \frac{\partial S}{\partial n} + \vec{M}_T \cdot \nabla_T S}{|\nabla S|} \quad (58) \\ &= \frac{[M_n] [u_n] + [\vec{M}_T] \cdot [\vec{V}_T]}{[u_n]} \frac{\partial S / \partial n}{|\nabla S|} \\ &= \frac{[M_x] [u] + [\vec{M}_T] \cdot [\vec{V}_T]}{[u_n]} \frac{\partial S / \partial n}{|\nabla S|} \end{aligned}$$

Substituting  $\vec{M}$  from equation (47) and again using the calculus of jumps:

$$J = \left( \left( \left[ Ku - (\gamma+1) \frac{u^2}{2} \right] [u] + [V_T]^2 - \epsilon \langle u \rangle [V_T]^2 - \epsilon [u] [V_T^2] \right) \frac{\langle u \rangle}{[u_n]} - \epsilon \frac{[V_T]^2}{[u_n]} \frac{[u]^2}{4} - \frac{(\gamma+1)}{12} [u]^3 \frac{[u]}{[u_n]} \right) \frac{\partial S / \partial n}{|\nabla S|} \quad (59)$$

This is considerably reduced by the introduction of the shock jump condition from equation (56),

$$J = - \frac{(\gamma+1)}{12} [u]^3 \frac{[u]}{[u_n]} + \epsilon (\gamma-2) \langle u \rangle^2 \frac{[V_T]^2}{[u_n]} - \epsilon \frac{[V_T]^2}{[u_n]} \frac{[u]^2}{4} \quad (60)$$

In keeping with previous comments, we shall assume that disturbance velocities in the sweep direction are small compared to disturbance velocities normal to the sweep. Thus, if  $\nu$  is the sweep angle, we have,

$$u_T = u \sin \nu + v \cos \nu \approx 0 \quad (61)$$

$$u_n = u \cos \nu - v \sin \nu \quad (62)$$



in consequence of which we obtain:

$$[u_n] = \frac{[u]}{\cos \nu} \quad (63)$$

Substituting equations (60) and (63) into equation (57) for the wave drag:

$$\begin{aligned} \frac{D_{\text{WAVE}}}{\delta^{4/3} P_{\infty}^{\gamma}} &= \frac{(\gamma+1)}{12} \iint_{S_c} [u]^3 \cos \nu \frac{\partial S / \partial n}{|\nabla S|} dA - \epsilon \iint_{S_c} \frac{[V_T]^2 [u]}{4} dx d\tilde{z} \\ &+ \epsilon (\gamma-2) \iint_{S_c} \frac{\langle u \rangle^2 [V_T]^2}{[u]} \cos \nu \frac{\partial S / \partial n}{|\nabla S|} dA \end{aligned} \quad (64)$$

Now  $\frac{\partial S / \partial n}{|\nabla S|} dA$  is the projection  $dS_v$  of the shock surface on  $x\tilde{z}$  or "sweep" plane while  $\cos \nu \cdot \frac{\partial S / \partial n}{|\nabla S|}$  is the further projection of  $S_v$  on the  $x\tilde{z}$  plane. If we reinterpret the sweep plane to be the local shock surface, the wave drag expression may be written in the final form:

$$\begin{aligned} \frac{D_{\text{WAVE}}}{\delta^{4/3} P_{\infty}^{\gamma}} &= \frac{(\gamma+1)}{12} \iint_{S_c} [u]^3 dx d\tilde{z} + \epsilon (\gamma-2) \iint_{S_c} \frac{\langle u \rangle^2 [V_T]^2}{[u]} dx d\tilde{z} \\ &- \epsilon \iint_{S_c} \frac{[V_T]^2 [u]}{4} dx d\tilde{z} \end{aligned} \quad (65)$$

In the neighborhood of normal shocks,  $[\vec{V}_T]$  is small compared to  $[u]$  and

the contribution from the last two integrals in equation (65) becomes negligible and the Murman and Cole result is recovered. It is also worth noting that if  $\vec{Q}$  is obtained from the NLR equation, the second term of equation (65) drops out. Near a swept shock  $[\vec{V}_T]$  may be large and the contribution from the last two terms is correspondingly significant.

Equation (65) is the farfield drag formula which must be used when the MSD equation is employed. The integration was not implemented in the present study. This equation would have to be implemented on the crude exterior grid, and the complexity of the final equation would probably lead to large numerical errors when implemented on such a coarse grid. Thus, the calculation of drag in the present program has been based completely on surface pressure integration.

## 7. FULLY THREE-DIMENSIONAL BOUNDARY LAYER CALCULATION

In order to increase the power of the present transonic viscous method, a new fully three-dimensional finite wing boundary layer program has been written by John Nash and Roy Scruggs of Sybucon, and is described in the self-contained document issued as Volume III of the present report. The data set required to execute the program is generated by the transonic analysis code, either from a direct inviscid calculation or after the interaction solution is obtained using the infinite swept wing strip viscous approach. The new program is a fully implicit numerical solution of the 3-D boundary layer equations. A compressible 3-D turbulent energy equation based on the incompressible equation derived by Nash (Reference 51) is used to obtain turbulent closure. As a result, we expect that this program could potentially be more accurate than the eddy-viscosity model programs that are now beginning to appear (Reference 41). In addition, input data requirements are greatly improved compared to the previous explicit program developed by Nash and Scruggs (Reference 24). In this section, we outline the features of the method so that the user of the programs can anticipate the complete capability provided by the set of programs described in the three volumes of the present report.

The 3-D BL program computes the laminar or turbulent boundary layer development over a finite swept wing of arbitrary planform and thickness in compressible steady flow. The program is structured in order to be amenable to interactive calculations, although the full coupling was not carried out in the present effort. The wing surface is segmented into quasi-quadrilateral panels and a locally orthogonal set of curvilinear coordinates is constructed following a conical development of the local region. Streamwise cuts are made over the planform at arbitrary spanwise locations and the number of surface points on each cut is the same. The calculation then proceeds from the planform leading edge as turbulent or laminar. The governing equations are finite-differenced with respect to the local surface normal coordinate  $y$ , and the locally transverse coordinate  $z$ , so that in the local  $y$ - $z$  plane, the difference equations are implicit. The solution is then obtained at each  $x$  (streamwise) station in succession. This chordwise forward-marching is applied with arbitrary step length proceeding from the leading edge to the trailing edge or until separation is encountered at some spanwise location. Provision is made to step past local separations by altering the local pressure distribution, if

desired. Transition location must be specified by the user.

Further flexibility in the new program has been achieved by adding the thermal energy equation to the set of governing equations. Although the program computes adiabatic boundary layers by specifying the adiabatic wall temperature, a simple modification would allow the program to compute boundary layers with arbitrary wall temperature. Another refinement is the solution of the finite difference equations all the way to the wall, removing the limitations associated with the matching to the law of the wall region as is usually done with turbulent kinetic equation methods. As a result of this refinement, the calculation of both laminar and turbulent flows can be carried out within the same basic framework.

Grumman has added a few additional calculations and revised the output slightly, in addition to verifying the program for a few simple cases for which comparisons can be made. Checks of the number of chordwise stations required to obtain a converged solution indicated essentially no difference between predictions using 26 and 41 chordwise points. The program is dimensioned for a maximum of 60 chordwise and 30 spanwise stations. It appears that 21 points across the boundary layer is sufficient. The computation of the standard integral thicknesses was added as well as the incorporation of a summary of the results, an option to punch some of the output for plotting and an option to provide several levels of output, depending on the type of information desired. With the exception of these minor additions, the program has been maintained in the form delivered to Grumman by Sybucon.

## SECTION II

### APPLICATIONS

#### 1. INTRODUCTION

In this part of the volume, we give a large number of examples of the application of the program to specific cases. The intent is to show typical accuracy that any user should expect to achieve. Although a knowledge of the underlying theory is desirable, it is not necessary. Experience at Grumman has indicated that good results can be obtained by users who do not know the details of the methodology as long as a few rules of thumb are followed. However, it is important to understand that the present programs are intended to provide an experienced aerodynamicist with information required for aerodynamic design studies. We expect that this program will be but one of a number of codes that form the aerodynamicist's bag of tools. As such, the user should constantly check the answers for consistency and overall "correctness." When the program does not produce answers that appear reasonable, an error in the input, or a simple misunderstanding in the operation of the program can usually be found to explain the anomalies in the results. We will warn the user repeatedly to study each run carefully, applying good aerodynamic judgement to the evaluation of the predictions. If this procedure is followed, the program will consistently provide predictions of at least the same quality as those presented in this part of the report.

The ten survey cases shown here have evolved over the course of the study. They constitute a wide range of configurations which would be very typical of the actual application of the code. Some of these cases have formed the basis for the original demonstration of various methods, while other cases have been used to demonstrate the use of the method to aircraft design projects.

The F-8 and TACT configurations are two of the most advanced aircraft designs for which flight test data is available. This section shows the typical correlation between flight, wind tunnel and theoretical predictions of the present method.

## 2. EXPERIENCES AND LIMITATIONS OF THE CODE -- HOW TO SUCCESSFULLY RUN THE CODE

Although extremely useful results can be obtained with the present set of computer programs, the code does have some geometric restrictions and aerodynamic limits. In this section, we review some of these limitations and discuss strategies that can be employed when the normal solution procedures fail to obtain a satisfactory result. The geometric limitations do not necessarily mean that the program cannot be used for these cases, but rather that the aerodynamicist will have to supply a more imaginative model to the program and judge the results with additional care, in order to extract the maximum possible value from the program.

Geometric features which the program does not explicitly handle are:

- o Multiple Lifting Surfaces (including canards and winglets)
- o Wings with Planform Discontinuities (such as snags)
- o Wing Dihedral
- o Inlets/Nozzles/Stores
- o Multi-Element Airfoil Sections
- o Fine Details of the Fuselage Geometry

Aerodynamic limitations include:

- o Mach numbers less than one
- o Attached flow over most of the surface
- o No suction/blowing effects on boundary layer
- o No heat transfer effects on boundary layer
- o Mid-chord wing sweeps less than about  $70^\circ$
- o Taper ratios greater than .05

In addition to these general limitations, a few specific configurations may require special treatment. When these cases occur, considerable additional flexibility is allowed so that it should prove possible to obtain a solution.

These alternate strategies can be grouped into several categories:

- o Families of Solutions
- o Geometry Simplification
- o Inviscid Iterative Procedures
- o Mesh/Mapping Alteration
- o Boundary Layer Relaxation

Before discussing the actual solution methods, we discuss some input problems. Extreme care must be exercised in setting up the data sets for

any computational aerodynamics type computer program. A large number of problems attributed to the earlier versions of the code by frustrated users have been traced to an input error. In the present program, the potential for user errors has been minimized by careful design of the input procedure, internal checks on the consistency of the data and a graphics package which provides graphical verification of all the input geometry as well as the computed results. The graphics package can be invaluable and we urge all users to make the effort required to adapt this part of the program to their own system. Although a number of internal checks have been included in order to keep the user from exceeding the limits of the various input values, undoubtedly it is still possible to make inputs that are not corrected or flagged by the program. Common errors have included specifying the mesh in some type of normalized units and the planform in physical dimensions or vice versa, and specifying the wrong index for grid locations such as the first mesh line past the tip. To repeat, experience has shown that a carefully set up data set will reduce problems to a minimum and reward the user with reliable results.

Families of solutions can sometimes be used to obtain results that are proving difficult to compute by the standard methods. In this scheme, a solution that can be readily computed is saved and the saved solution is used as the starting guess for another solution with a minor increase in difficulty. Typically, this approach can be used to obtain higher angles-of-attack, more extreme twist distributions, or extreme Mach numbers. Several increments can be used to obtain the final desired condition. Even when no difficulty is being experienced in obtaining a particular solution, this method can lead to reduced computing times and hence, more economical computing. This strategy can be particularly economical during design studies, where the effects of minor geometric changes are being studied.

Geometry simplification can correspond to both the planform and airfoil section treatment. Because the small disturbance theory has a singularity at the leading edge, the resulting large flow gradients near the leading edge can cause numerical solution problems for some cases. The program identifies the grid indices that locate the numerical difficulties in the grid, so that it is possible to determine if the problem occurs at mesh points about the leading edge. When this occurs, the mesh can be inspected to insure that the mesh distribution is smooth. The airfoil slopes should be inspected to verify

that the proper airfoil ordinates have been input and the (smooth) resulting slopes are reasonable (note that the input ordinates are spline fit in order to interpolate to the mesh locations and prescribe the slopes, requiring an accurate specification of the airfoil ordinates). If the ordinates are correct and the mesh is distributed smoothly, then the user has the option of reducing the leading edge slope in a systematic manner by employing Riegels' Rule. Riegels' Rule is a method that renders the first order thin airfoil solution valid near the leading edge in incompressible flow. Van Dyke (Reference 19) has investigated its application along with a number of other methods to improve thin airfoil theory. Unfortunately, Riegels' Rule has no theoretical foundation for transonic flows. It does, however, often allow the solution to proceed without numerical difficulty and has the interesting property of removing much of the mesh dependence of the solution around the leading edge. However, it should be used with caution because, for transonic solutions, it appears that the resulting solution may be inaccurate, particularly on the lower surface.

Another geometric difficulty can arise if the user is trying to prescribe non-streamwise wing tips. This can lead to an extreme bending of the computational mapping. In this case, the simplest improvement would be to model the tip as streamwise, with an equivalent planform area. If this is not acceptable, the user may have to specify the mapping himself. Attempts to include strakes as part of the planform will also lead to problems, because the strake constitutes a small fraction of the wing area, in a location where several extreme mesh bendings are required. The resulting loss of geometric resolution in the mesh bending process will produce a result that does not adequately model the strake and will introduce oscillation in the solution. Most gloves can be handled without difficulty. If difficulties are encountered while investigating planforms with severe geometry variations, some numerical experiments should be run in order to isolate the particular geometric feature that is causing the difficulty. Once the problem area is located, a review should be made of the modeling. It may be that a slight geometric simplification is perfectly acceptable. If not, then the span mesh may have to be concentrated about the region of interest and a combination of the methods discussed in this section employed in order to obtain the solution.



The inviscid iterative procedures can be changed to allow for a smaller value of  $w$  and a larger value of the damping coefficient for  $\phi_{xt}$ . Some trials at other Mach numbers and angles-of-attack may help clarify the source of the problem.

For example, if the inviscid iteration procedure is diverging, a lower angle-of-attack or Mach number may result in a converging result, or it may help to identify the location in the mesh at which the solution procedure is failing. Once this location is defined, inspection of the local mesh and geometry will probably identify an irregularity that can be corrected. In many cases, this is sufficient in order to obtain a solution. The print plot of the inviscid convergence history should be examined for each run. Both the exterior and interior mesh iteration histories are displayed and the particular mesh that the problem originates on can be determined. This can be used as a guide to determine which mesh should have the iteration parameters changed.

Mesh and mapping alterations have been mentioned previously. The program automatically generates a mesh that is a result of considerable experience with the code. The user, however, can input his own mesh and mapping. When this step must be used, it should be done with considerable care, following the instructions contained in the user's manual.

A rule of thumb that works well for troublesome cases in all instances investigated to date is that for regions where the mapping is bending, such as at glove-wing intersections, the spanwise mesh must be more closely spaced than elsewhere on the wing. For some extreme cases that are nearly pure delta wings, the mapping must be bent near or beyond the tip in order that the  $\xi = 0$  line remains in front of the  $\xi = 1$  line in the physical space. If this condition is violated, the program will give a warning and stop. To attempt to obtain a solution under these conditions will only result in a catastrophic failure of the iteration procedure.

The boundary layer iteration can be controlled by several methods. The degree of underrelaxation of the boundary layer can be controlled, the origin of the slope extrapolation can be varied independently on the upper and lower surface, and the number of inviscid iterations can be adjusted. In general, however, the viscous solution will break down when there is excessive flow separation present on the wing. The exact degree of separation that can exist and still obtain a convergent iteration will depend on the particular case. On supercritical wings, the iteration has converged for separation lines that

occur at 70% on the lower surface and 85-90% on the upper surface. Naturally, the larger the separated region becomes, the worse the approximation to the actual solution will become.

From the above discussion it should be clear that the more experience that is gained with the program, the more useful the code will become. While the program should operate satisfactorily with minimal experience, the code can be used to compute some exceptionally challenging cases in the hands of an experienced user.

### 3. EXAMPLES OF CONFIGURATIONS COMPUTED AND TYPICAL AGREEMENT WITH EXPERIMENT

This program has been tested on a number of configurations (see Table I) covering a wide range of flight conditions and geometries. These have included aspect ratios from 2 to over 6, wing leading edge sweeps from  $30^{\circ}$  to over  $60^{\circ}$ , glove sweeps in excess of  $74^{\circ}$  and taper ratios from under .025 to 0.6. In fact, even a forward swept wing has been successfully treated. The various flight conditions handled have included Mach numbers from 0.81 to 0.99 and angles-of-attack over a range from  $0^{\circ}$  to  $8.5^{\circ}$ . A representative sample of such cases has been included in this section. Many of these cases are classics, having been used as the original demonstration cases for some of the inviscid programs in use. Most of these cases consist of relatively simple "research" type geometric configurations for which transonic pressure data is generally available. Two of the cases, the low aspect ratio and forward swept wing, are included to show the capabilities of the program even though no experimental data is available for these cases. These cases have been quite useful even though some of the experimental data contains wind tunnel wall effects and many of the wings were not designed for transonic conditions. The present effort shows the need for establishing a new set of baseline experimental cases for use in aerodynamic tool development. Most of the good, modern, experimental pressure data is closely tied in with specific aircraft projects. As such, the configuration's geometric complexity is often of a nature to make it difficult to perform a basic code development comparison study. In addition, this type of data is often classified and can not be widely distributed. We have, however, included two such cases, the F-8 and TACT aircraft, which will be extensively discussed in the next section. These cases contain the most widely available supercritical wing data. The declassification of the F-8 program was particularly timely in this regard.

The results are presented in each case with some of the basic geometric data for the case. The detailed geometric data required to actually run these cases can be found in the references for each case. Comparisons of experimental pressure distributions with the program predictions are included. All of the presented results were computed with the final computer code, using the automatically generated meshes and mapping. The computations employed the FCR differencing of the MSD Equation, with inviscid solutions used for the cases with conventional sections and viscous flow solutions for cases with supercritical sections.

TABLE I  
EXAMPLE CONFIGURATIONS

No.	Configuration	Section	$\Lambda_{LE}$	$\Lambda_{TE}$	AR	$\lambda$	Mach	Alpha	Figure
1	ONERA M6	ONERA "D"	30.0°	15.8°	3.80	.562	.84	3°	32
2	RAE "A"	RAE 101	36.67°	22.34°	6	.333	.90	1°	33
3	L54HL8A	NACA 65A006	45.73°	38.15°	4	.60	.95	4°	34
4	TN D712	NACA 65A004	50.74°	18.44°	3	.20	.94	2.4°	35
5	L51F07	NACA 65A006	46.76°	39.11°	4	.60	.93	2°	36
6	A55B21 (Basic Body)	6 <sub>4,2</sub> A015	39.05°	30.54°	6.05	.50	.94	0°	37
7	A55B21 (Area Rule Body)	6 <sub>4,2</sub> A015	39.05°	30.54°	6.05	.50	.94	0°	37
8	Forward Swept	Best "K"	-31.12°	-43.0°	5.54	.374	.90	8.5°	38
9	Low AR	NACA 65A006	60.10	-5°	2.10	.023	.90	1.0°	39
10	Transonic Transport	Supercritical	31.88°	14.51°	6.18	.282	.81	2°	40
11.	Advanced Technology Fighter	Grumman "E"	42.5°	31.0°	5.472	.40	.90	7.05°	41

a. ONERA M6

The first case listed in Table I is the ONERA M6 (Reference 52). The ONERA M6 is an isolated wing case with a conventional type ONERA "D" airfoil section. This case was studied at a Mach number of 0.84 and an angle-of-attack of  $3^\circ$ . The wing has a leading edge sweep of  $30^\circ$  and a trailing edge sweep of  $15.8^\circ$ . The aspect ratio for this case was 3.8 and the taper ratio was 0.56. The basic configuration can be seen in Figure 32a. Figure 32b shows the three-dimensional pressure distribution over the wing. As can be expected, the shock location moves forward as one moves outboard on the wing. The first span station for which experimental data was available, was at  $\eta = 0.2$ . The closest span station at which the code gave predictions was at  $\eta = 0.182$ . Figure 32c shows the comparison of experimental data with the code's predictions. As can be expected, due to the fact that the program prediction is at  $\eta = 0.182$ , the shock location is predicted farther aft than the measurements indicate. The lower surface predictions agree quite well with the experimental data. In fact, at each span station of the ONERA solution, the lower surface agreement with data is excellent. The next span station (Figure 32d),  $\eta_{\text{exp}} = 0.44$  and  $\eta_{\text{pre}} = 0.436$ , shows excellent agreement with experiment over the leading edge. The upper surface leading edge pressure peak is predicted excellently with respect to both location and height. The shock location is predicted approximately 5% ahead of the location shown in the measurements. The upper surface leading edge pressure peak is again accurately predicted at the next span station,  $\eta_{\text{exp}} = 0.65$  and  $\eta_{\text{pre}} = 0.655$  (Figure 32e). The measurements show evidence of two shocks, at  $x/c = 0.15$  and  $x/c = 0.45$ . The second shock is predicted quite well, both in amplitude and location. The first shock, however, is not predicted as well. There is a relatively rapid drop in pressure from the leading edge peak, however, the shock does not appear explicitly. This could probably be corrected by increasing the number of points along the chord above the 44 used at this span station, and possibly increasing the angle-of-attack used in the program slightly. The next station,  $\eta_{\text{exp}} = \eta_{\text{pre}} = 0.8$  (Figure 32f) again predicts the leading edge peak and the second shock. However, the first shock is still missed and the same corrections could probably be made. At the two outboard span stations ( $\eta_{\text{exp}} = 0.90$ ,  $\eta_{\text{pre}} = 0.909$  and  $\eta_{\text{exp}} = 0.95$ ,  $\eta_{\text{pre}} = 0.945$ ) the leading edge peak is still well predicted but the shock is not as sharp as indicated by the data,

especially at  $\eta = 0.95$ . The pressure dip following the shock is well predicted as to height but the predicted location is approximately 10% ahead of that indicated by the measurements. Jameson and Caughey (Reference 21) have also performed inviscid calculations on the ONERA M6 with a numerical solution of the exact transonic potential flow equation. Their predicted shock location agrees with the data somewhat better than this code; however, their code was run at a slightly higher angle-of-attack and, as seen previously, a slight increase in angle-of-attack would seem to be indicated for this code also. Due to the concentration of points near the leading edge, the Jameson-Caughey code predicts the second pressure peak better than this code, however, an increase in the number of points along the chord would increase resolution and possibly show this better.

b. RAE "A"

The second case listed in Table I is the RAE "A" wing-body configuration. The experimental pressure data (Reference 53) was obtained at a Mach number of 0.90 and an angle-of-attack of  $1^\circ$ . Figure 33a shows the configuration used for this code. The airfoil section used in this case is the RAE 101 conventional type section. Figure 33b shows the 3-D pressure distribution over the wing. The predictions were obtained at an angle-of-attack of  $1^\circ$  and runs were made at Mach numbers of 0.90 and 0.91. The 3-D pressure distribution shown is for the Mach 0.91 case. Figure 33c gives the pressure distribution at  $\eta_{\text{exp}} = 0.1667$  and  $\eta_{\text{pre}} = 0.182$ . This span station for the predictions,  $\eta_{\text{pre}} = 0.182$ , is the first span station outside the body in the mesh generated by the code. As can be seen, the agreement between prediction and experiment is not very good at this span station. However, this is due in large part to the difference between the prediction and experimental span stations. In this region, the effect of the body is greatest, and the spanwise pressure gradients are the highest. Observing the predicted gradient between  $\eta_{\text{pre}} = 0.255$  and  $\eta_{\text{pre}} = 0.182$ , it is apparent that moving from  $\eta_{\text{pre}} = 0.182$  inboard to  $\eta = 0.1667$  would cause both the upper and lower predicted pressures to drop. Thus, if the program utilized  $\eta_{\text{pre}} = 0.1667$ , the predictions would more closely follow the experimental results. If the details of the pressure distribution near the body are desired, the user must input his own y-mesh, concentrating the mesh near the wing-body juncture. It is interesting,

however, to note that increasing the Mach number from 0.90 to 0.91 causes the shock location to shift aft about 10% and brings it to the correct location. Figure 33d shows the pressure distribution at  $\eta_{\text{exp}} = 0.25$  and  $\eta_{\text{pre}} = 0.255$ . Here, the agreement between experiment and prediction is much better. Note again that increasing the Mach number to 0.91 gives excellent agreement with data. The shock location again moves aft to the correct location seen in the data. Also, the lower surface pressures drop to the correct values. The next span station shown (Figure 33e) is at  $\eta_{\text{exp}} = \eta_{\text{pre}} = 0.4$ . Here again, the predictions show better agreement with data at Mach 0.91. At  $\eta_{\text{exp}} = 0.6$ ,  $\eta_{\text{pre}} = 0.618$ , (Figure 33f), the agreement is again better at Mach 0.91, although the upper surface pressure predictions are somewhat below the data. The lower surface shows excellent agreement with data. The final outboard span stations (Figures 33g and 33h) show similar characteristics with better agreement at Mach 0.91. These results clearly demonstrate the Mach number sensitivity to be expected in transonic flow calculations. Thus, in any comparison of predictions with experimental data, the Mach number used in the experimental work must be known accurately.

c. L54H18

The third case is the L54H18 (Reference 54). This case consists of a NACA 65A006 wing mid-mounted on a cylindrical body (Figure 34a). The wing is twisted from  $0.4^\circ$  at the wing-body juncture to  $-4.12^\circ$  at the wing tip. The flight conditions used for this case were a Mach number of 0.95 and an angle-of-attack of  $4^\circ$ . Figure 34b shows the 3-D pressure distribution for the L54H18 wing. The first span station ( $\eta_{\text{exp}} = 0.2$ ,  $\eta_{\text{pre}} = 0.218$ ) (Figure 34c) shows the same characteristics observed in the RAE "A" configuration. This, too, is a situation where, if the span station used for the predictions had been closer to that used for the experimental results, the results would have been closer. Again, when close to the body, where the spanwise pressure gradients are the largest, comparisons between prediction and experiment require the span stations used to be the same. Figure 34d shows better agreement with the data. In fact, except for the upper surface leading edge, the agreement is excellent. The leading edge peak does not reach the height of that observed experimentally. The shock location prediction agrees with the experimental location. In Figure 34e, we again see excellent agreement except for the height of the pressure peak at the leading edge. The next span

station ( $\eta_{\text{exp}} = \eta_{\text{pre}} = 0.80$ ) (Figure 34f) shows excellent agreement; however, the upper surface experimental results shows a second pressure peak and shock location at  $x/c = 0.35$ . This peak is not duplicated in the predictions. If the wing twist was increased slightly, the predictions could conceivably agree somewhat better. The final outboard section (Figure 34g) shows the same characteristics as the previous span station.

d. TN D712

The fourth case investigated was the TN D712 wing-body configuration (Reference 55). The flight conditions for this case was a Mach number of 0.94 and an angle-of-attack of  $2.4^\circ$ . The airfoil section used in this wing is a NACA 65A004. Figure 35a shows the basic geometry of this configuration. The 3-D pressure plot is seen in Figure 35b. The first span station shown ( $\eta_{\text{exp}} = 0.16$ ,  $\eta_{\text{pre}} = 0.182$ ) (Figure 35c), indicates excellent agreement between experiment and prediction. The only point at which agreement is not complete is at the trailing edge. The predictions are from an inviscid solution; a viscous solution would probably show better agreement at the trailing edge due to separation treatment. The code fails to predict the upper surface leading edge pressure peak at the next span station ( $\eta_{\text{exp}} = \eta_{\text{pre}} = 0.4$ ) (Figure 35d). However, the rest of the distribution at this station agrees quite well. In fact, over the rest of the span (Figures 35e, 35f and 35g), the code continues to fail to predict the leading edge pressure peak. However, except for the final span station, the shock location and magnitude is accurately predicted. The outboard span station ( $\eta_{\text{exp}} = 0.95$ ,  $\eta_{\text{pre}} = 0.945$ ) shows relatively poor agreement over the first 45% of the section. The lower surface shows a peak at  $x/c = 0.4$  which is not reproduced in the predictions. In addition, the upper surface distribution is not very well reproduced until beyond  $x/c = 0.45$ , at which point both upper and lower surface agreement is excellent.

e. L51FO7

The L51FO7 configuration is shown in Figure 36a. This consists of a wing-body combination with a NACA 65A006 airfoil section (Reference 56). The wing for this case is untwisted. The flight conditions for this case are a Mach number of 0.93 and an angle-of-attack of  $2^\circ$ . Figure 36b shows a plot of the upper surface isobars predicted by this program. The equivalent 3-D



upper surface pressure distribution is shown in Figure 36c. The first span station shown is for  $\eta_{\text{exp}} = 0.2$  and  $\eta_{\text{pre}} = 0.182$ . The predictions (Figure 36d) show excellent agreement except at the leading edge upper surface and the trailing edge. The leading edge can be accounted for by the fact that the span station used for the predictions is inboard of the span station used for the experimental work. The trailing edge discrepancy might be attributed to a viscous corner flow displacement effect not treated in the present program. On conventional airfoils, viscous effects are important primarily at the trailing edge and this is evidenced by the excellent agreement between the data and the inviscid solution over the rest of the section. The rest of the wing (Figures 36e, 36f, 36g and 36h) show similar characteristics with the exception that as one moves outboard, the agreement forward of  $x/c = .50$  tends to decrease. This could possibly be improved by increasing the computational angle-of-attack and/or Mach number slightly.

f. A55B21

The A55B21 case was run for two configurations (Reference 57). These configurations can be seen in Figures 37a and 37b. As can be seen, the wing planform and section ( $64_2A015_{\perp}c/2$ ) was the same for both configurations. However, the bodies used in the two configurations differed considerably. The airfoil sections originally used were determined by using the cosine of the mid-chord sweep angle since that was the specified reference sweep. A second set of airfoil ordinates with taper effects taken into account, were supplied by David Caughey. These ordinates, yielding slightly better results, are those for which the results are presented. The flight conditions used in the experimental wind tunnel work were for a Mach number of 0.94 and an angle-of-attack of  $0^\circ$ . The first configuration uses the basic body and the experimental results were obtained at  $\eta_{\text{exp}} = 0.471$ . The calculations were performed at  $\eta_{\text{pre}} = 0.473$ . As can be seen (Figure 37c), the agreement is, in general, good with the exception that the shock location is predicted about 5% forward of its actual location. The second configuration used an area rule body with the results determined at the same span locations (Figure 37d). Again, the rapid drop in pressure is predicted between 5 and 10% forward of the actual location. The effect of area rule body is to move the peak pressure from  $x/c_{\text{pre}} = .75$  forward to  $x/c_{\text{pre}} = 0.50$ . Thus, the program qualitatively

reproduces the experimental results.

#### g. Forward Swept Wing

The forward swept wing case was included to demonstrate the capabilities of the program. Although no experimental results exist for this case, the predictions are nevertheless interesting. Figure 38a shows the forward swept wing configuration (Reference 58). The leading edge sweep of this configuration is  $-31.1^\circ$  and the trailing edge sweep is  $-42.97^\circ$ . The wing has an aspect ratio of 5.22 and a taper ratio of 0.4. The airfoil section used was one of the Grumman "K" series supercritical airfoils. The flight conditions chosen for this case were of a Mach number of 0.9 and an angle-of-attack of  $8.5^\circ$ . Figure 38b shows the predicted 3-D pressure distribution on the upper surface of the forward swept wing. As can be seen, the chordwise pressure distribution is somewhat flatter than that predicted in most of the other cases. Figures 38c and 38d show the predicted pressure distributions at  $\eta = 0.4$  and  $\eta = 0.8$ . It is interesting that the lower surface pressure distributions are much flatter than those usually associated with supercritical airfoils. This provides an example of one of the non-standard configurations that this program can accept.

#### h. Low Aspect Ratio

The next case calculated consisted of a low aspect ratio wing-body case (Figure 39a). Again, no data exists for this configuration. The configuration consists of an F-102 body and planform (Reference 59). The airfoil section used in this case is a NACA 65A006 section. The wing planform has a leading edge sweep of  $60.1^\circ$  and a trailing edge sweep of  $-5^\circ$ . The aspect ratio of the configuration is 2.1 and the taper ratio is .023. The flight conditions used for this case are a Mach number of 0.90 and an angle-of-attack of  $4^\circ$ . Figure 39b shows the 3-D upper surface pressure distribution for this configuration. Figures 39c and 39d show the pressure distributions for span stations  $\eta = 0.4$  and  $\eta = 0.8$ . A case such as this is particularly taxing on the internal mesh generators. In this particular case, the interior mesh had to be adjusted beyond the tip to avoid having the  $XI = 0$  and  $XI = 1$  mesh lines cross beyond the tip. This leads to a large amount of mesh bending at the wing tip. It is apparent that some care must be exercised in setting up the geometry of such a configuration. However, this case demonstrates that the program can

handle such a case.

i. Transonic Transport

The configuration for the transonic transport is in Figure 40a (Reference 60) This was an isolated wing calculation; however, the experimental results are from wind tunnel tests of a wing-body configuration. As can be seen, this configuration is an example of a case with non-constant leading and trailing edge sweeps. The aspect ratio of the reference trapezoidal wing for this case was 8.55. The airfoil section used in this wing is a Grumman designed supercritical wing. The wing was designed for use in the presence of winglets at the tip and an engine nacelle over the trailing edge at the root. The effect of the nacelle is to virtually eliminate the shock inboard. The effect of the winglets is to straighten the isobars near the wing tip. Consequently, the results shown here do not truly represent the design conditions for the wing. The Mach number for this case is 0.81 and the angle-of-attack is  $2^\circ$ . The experimental results were obtained from wind tunnel tests at an angle-of-attack of  $3^\circ$ . There was some uncertainty as to the wing root incidence on the model. Since a computational angle-of-attack of  $2^\circ$  seemed to give better agreement with experimental data, this angle was used for all of the calculations. It should be noted that the airfoil ordinates used included a boundary layer. Consequently, only an inviscid calculation was performed. Figure 40b shows the upper surface pressure distribution for the isolated wing.

Figure 40c shows the pressure distribution at  $\eta_{\text{exp}} = 0.16$  and  $\eta_{\text{pre}} = .145$ . The agreement for this station is not very good. However, this is to be expected because the computations were carried out on an isolated wing, while the wind tunnel tests included the body. Figure 40d begins to show better agreement as the effects of the body begin to decay. At  $\eta_{\text{exp}} = 0.5$  ( $\eta_{\text{pre}} = 0.509$ ) (Figure 40e), the agreement gets better although the drop in the upper surface pressure at  $x/c = 0.45$  is not predicted. At  $\eta_{\text{exp}} = 0.70$  ( $\eta_{\text{pre}} = 0.727$ ) the agreement between prediction and experiment is quite good. The effect of the body is obviously felt quite far out on the span. This case shows that pressure distributions on wings in the presence of bodies cannot be accurately predicted from isolated wing cases except possibly over the outer quarter of the span. Consequently, it is important to include the body in the geometry model and the more accurate the body model the better

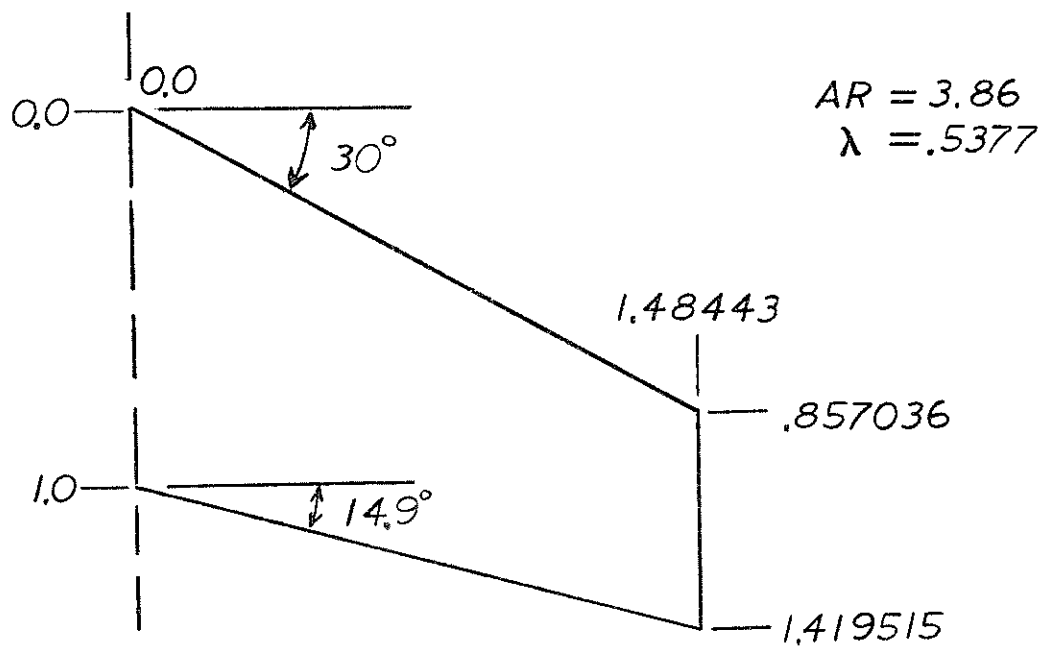
the results obtained from the code will be.

#### j. Advanced Fighter

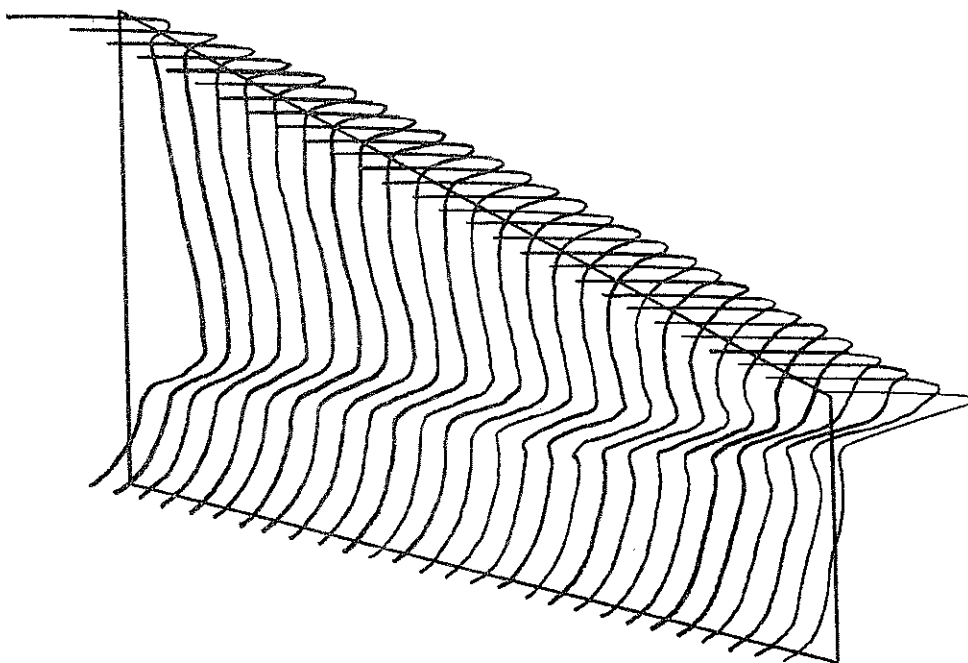
Figure 41a shows a typical advanced fighter concept for which data is available (Reference 61). For this case, we see that a strong shock is predicted at the wing root in the calculation, as shown in Figure 41b. The experimental data shown in Figure 41c indicates that the calculations are incorrect at the root. This problem continues to dominate the flowfield until about midspan. At 62% semispan, the predictions begin to show reasonable agreement with experiment. The striking error now occurs on the lower surface, where the small disturbance theory solution consistently over-predicts the high pressure on the lower surface uniformly over the entire chord. In addition, the comparison suggests that the calculation is being made at a Mach number that is too low. There is no question that the main problem in this prediction occurs at the root station. One source of the error in this case is the decambering of the airfoil section in the glove region, which could only be approximately modeled in the present calculation. However, this simplification does not explain the lower surface pressure discrepancy, which occurs consistently across the span.

#### k. Summary

The preceding results show that the program can reliably predict the transonic flow over a variety of configurations. The extreme sensitivity of transonic flows to a precise specification of freestream conditions has been demonstrated by the RAE "A" calculation. For wings with conventional sections and advanced transonic transports, the program is capable of making good predictions up to the angles-of-attack at which massive shock induced separation is predicted. The advanced fighter predictions require further study. In this case, the flowfield is well removed from a "small-disturbance" state and the wing-root-glove fuselage disturbances are becoming important and should be investigated. Nevertheless, these predictions reflect the enormous advances in the ability to compute three-dimensional wing-body viscous transonic flows during the course of the present effort.



(a) ONERA M6 configuration



(b) Upper surface pressure distribution

FIG. 32 ONERA M6

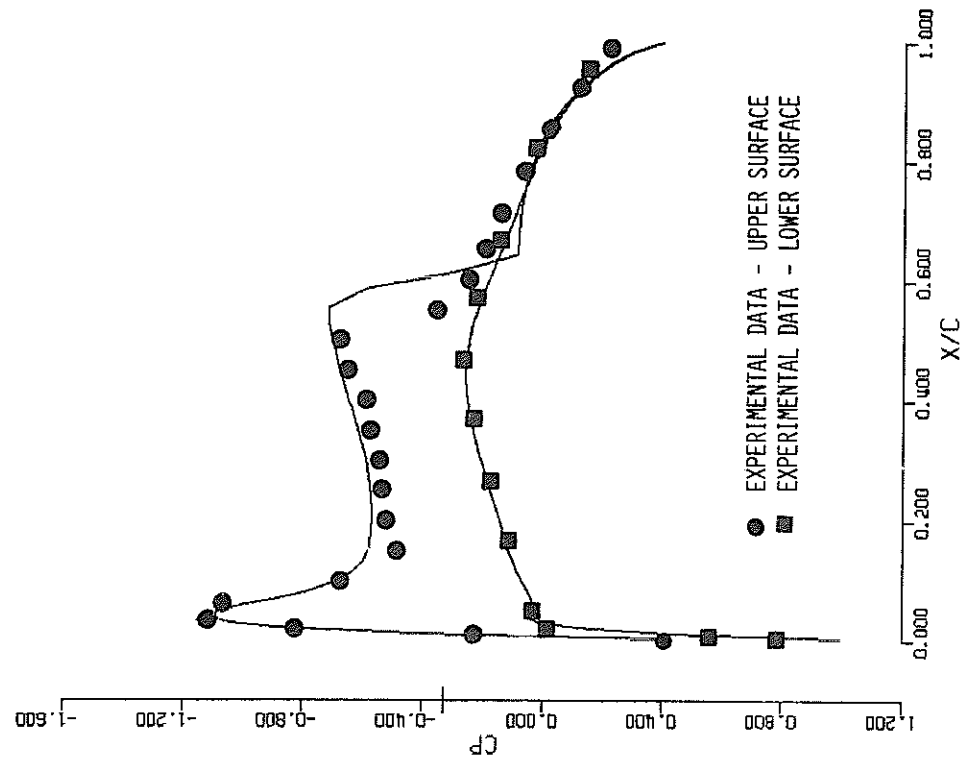


FIGURE 32c. ONERA M6 WING  
 $M = 0.840$   $ALF = 3.000$   $CONV = .327E-04$   
 $LOCAL CL = 0.284$   $LOCAL CM = -0.144$   $LOCAL CD = 0.0138$   
 $SPAN STATION 6$   $Y/S = 0.182$  44 MESH PTS ON CHD

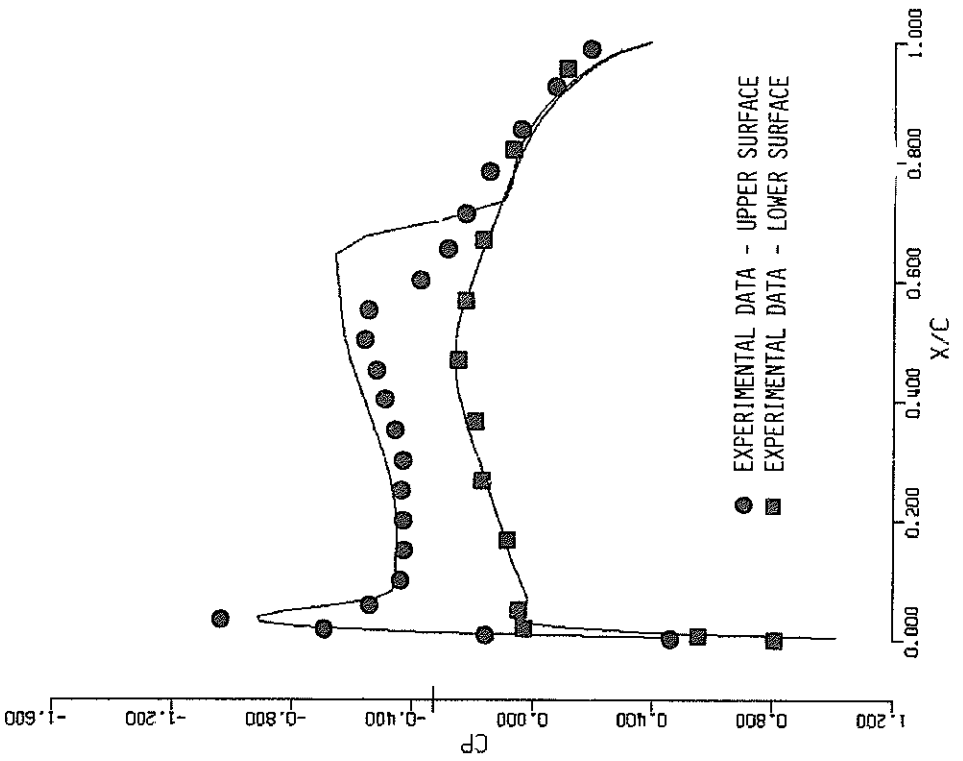


FIGURE 32d. ONERA M6 WING  
 $M = 0.840$   $ALF = 3.000$   $CONV = .327E-04$   
 $LOCAL CL = 0.301$   $LOCAL CM = -0.218$   $LOCAL CD = 0.0034$   
 $SPAN STATION 13$   $Y/S = 0.436$  44 MESH PTS ON CHD

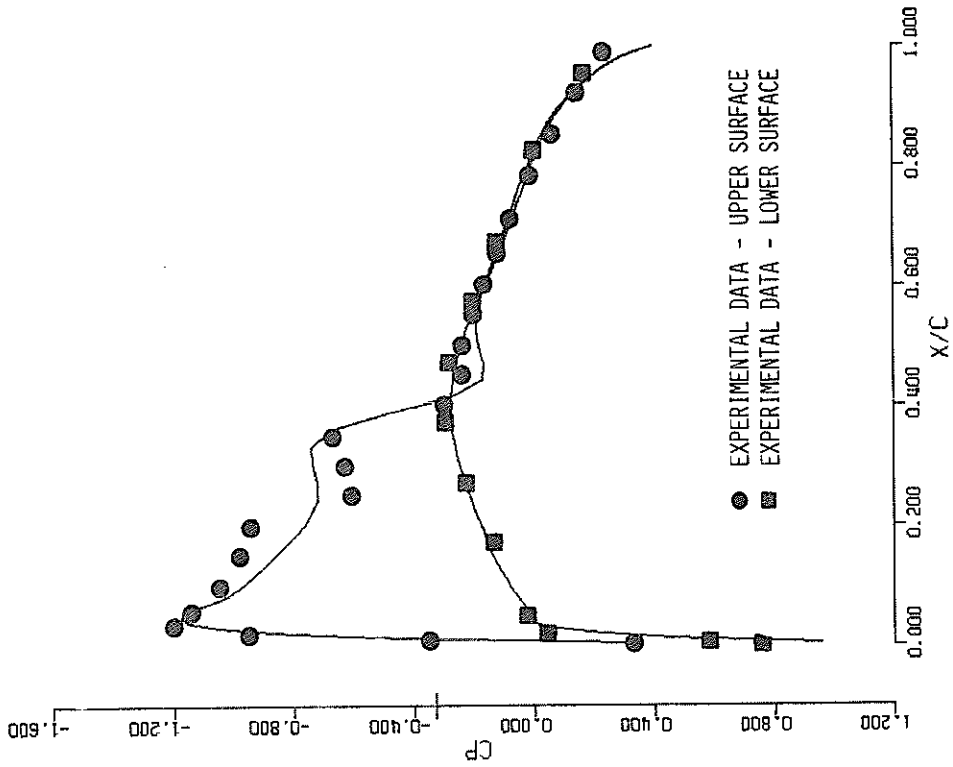


FIGURE 32F. ONERA M6 WING  
 M = 0.840 ALF = 3.000 CONV = .327E-04  
 LOCAL CL = 0.258 LOCAL CM = -0.312 LOCAL CD = -.0089  
 SPAN STATION 23 Y/S = 0.800 44 MESH PTS ON CHD

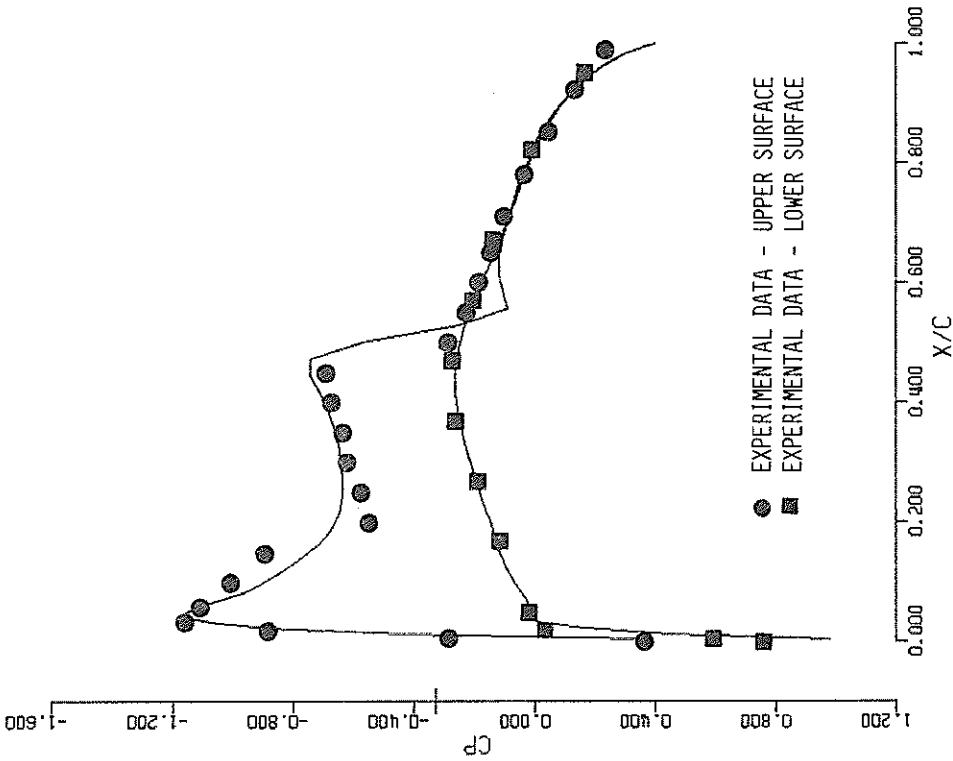


FIGURE 32E. ONERA M6 WING  
 M = 0.840 ALF = 3.000 CONV = .327E-04  
 LOCAL CL = 0.292 LOCAL CM = -0.288 LOCAL CD = -.0032  
 SPAN STATION 19 Y/S = 0.655 44 MESH PTS ON CHD

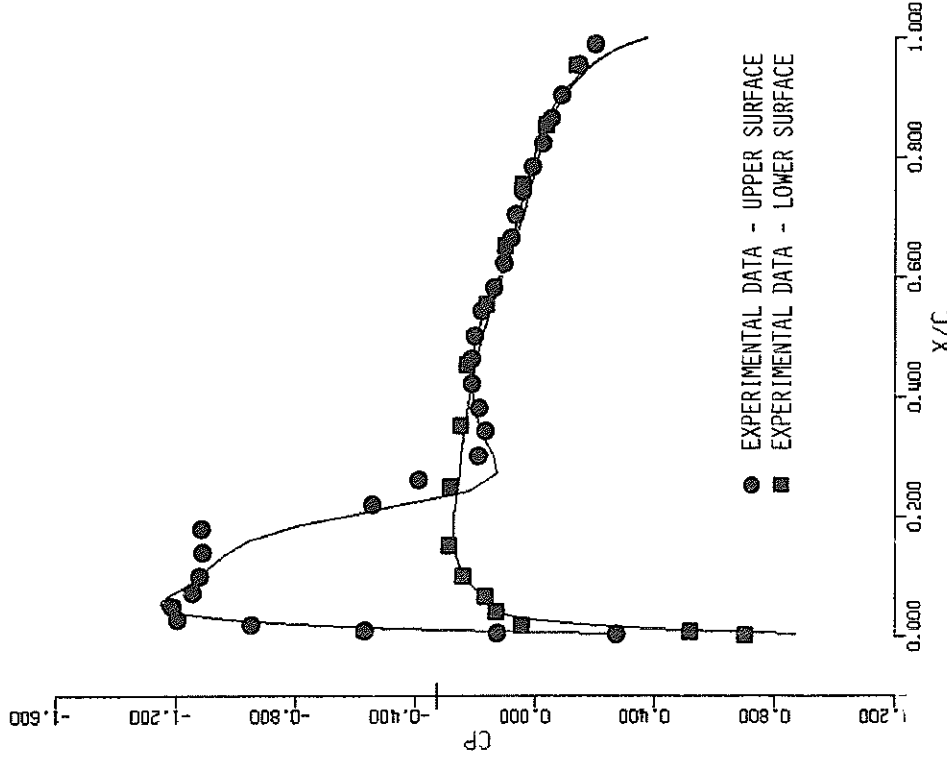


FIGURE 32g. ONERA M6 WING  
 M = 0.840 ALF = 3.000 CONV = .327E-04  
 LOCAL CL = 0.200 LOCAL CM = -0.281 LOCAL CD = -.0152  
 SPAN STATION 26 Y/S = 0.909 44 MESH PTS ON CHD

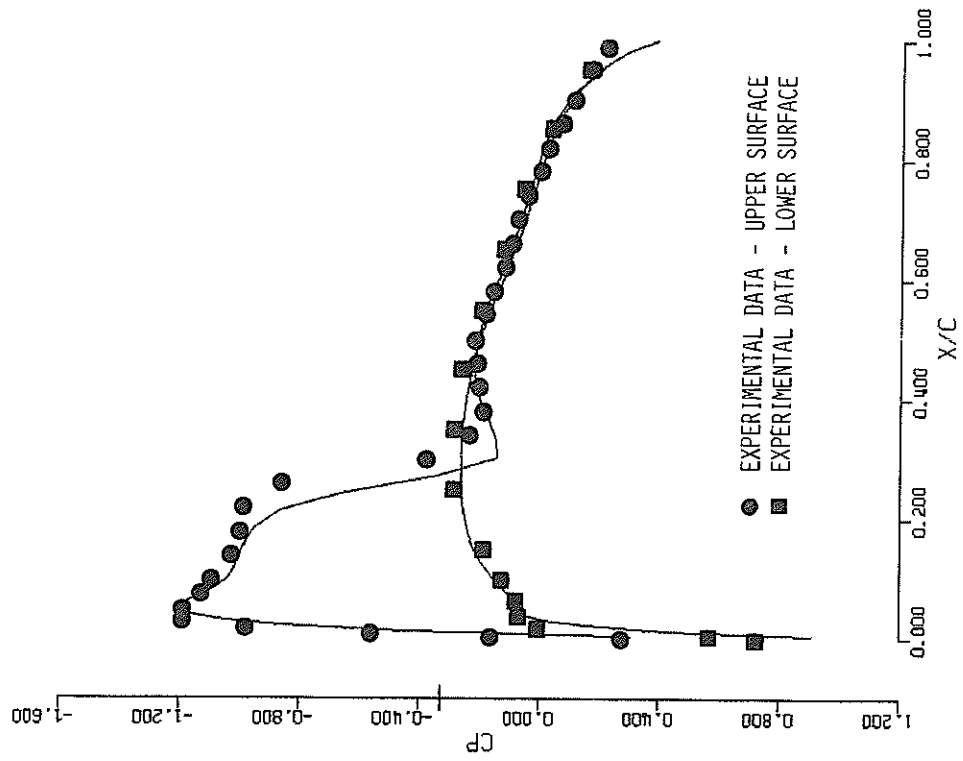
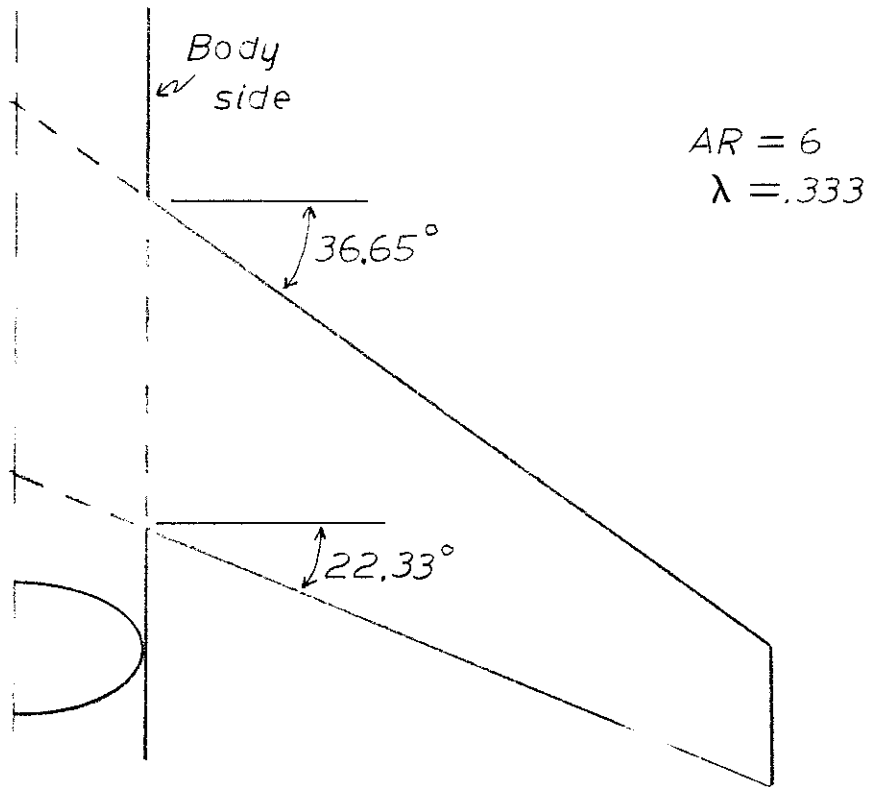
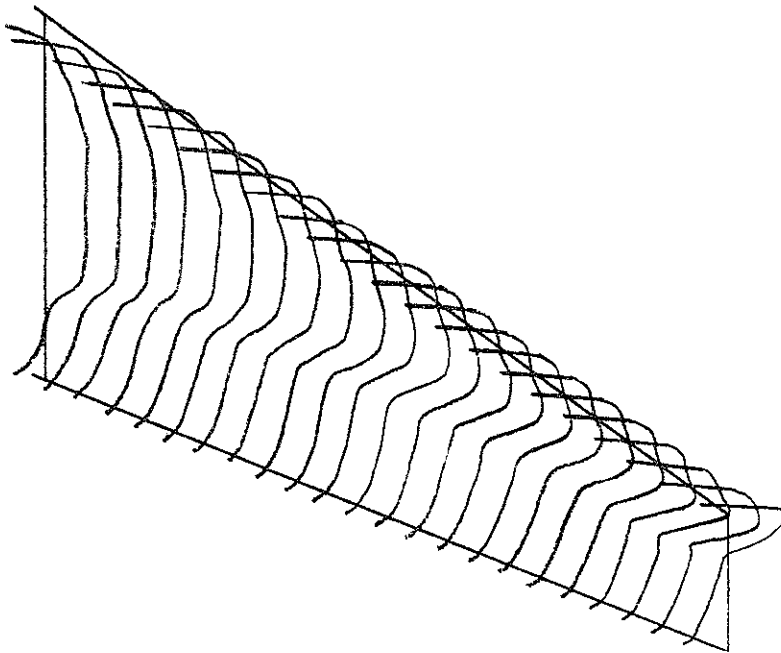


FIGURE 32h. ONERA M6 WING  
 M = 0.840 ALF = 3.000 CONV = .327E-04  
 LOCAL CL = 0.166 LOCAL CM = -0.245 LOCAL CD = -.0189  
 SPAN STATION 27 Y/S = 0.945 44 MESH PTS ON CHD





(a) RAE "A" configuration



(b) Upper surface pressure distribution  
FIG. 33 RAE "A"

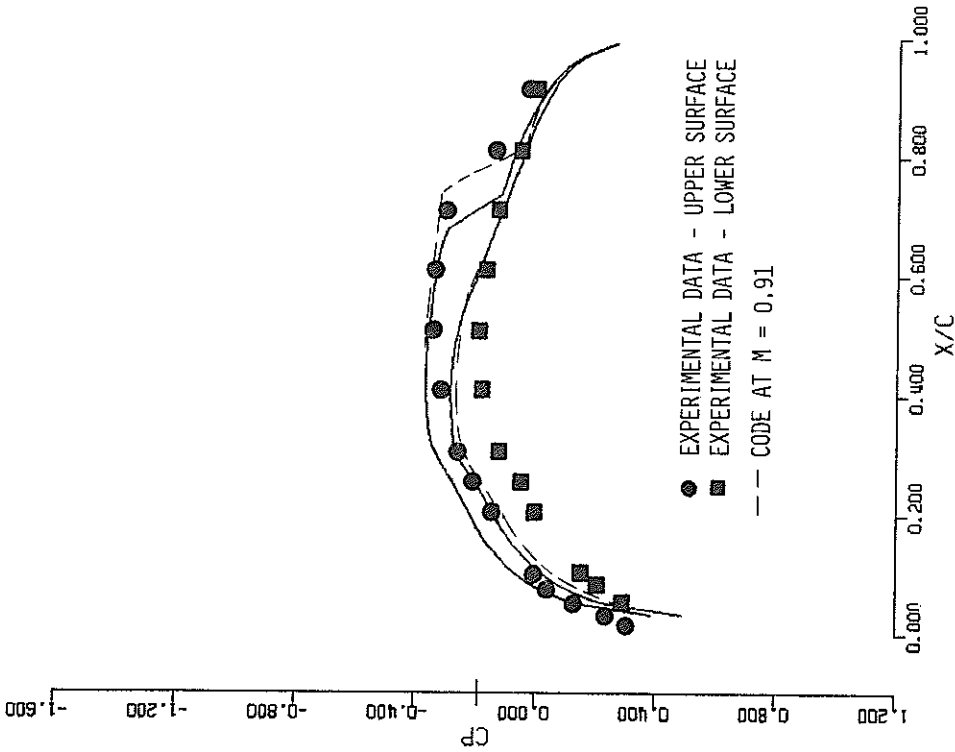


Figure 33c. RAE WING BODY CONFIGURATION  
 M = 0.900 ALF = 1.000 CONV = .991E-05  
 LOCAL CL = 0.075 LOCAL CM = -0.035 LOCAL CD = 0.0147  
 SPAN STATION 6 Y/S = 0.182 46 MESH PTS ON CHD

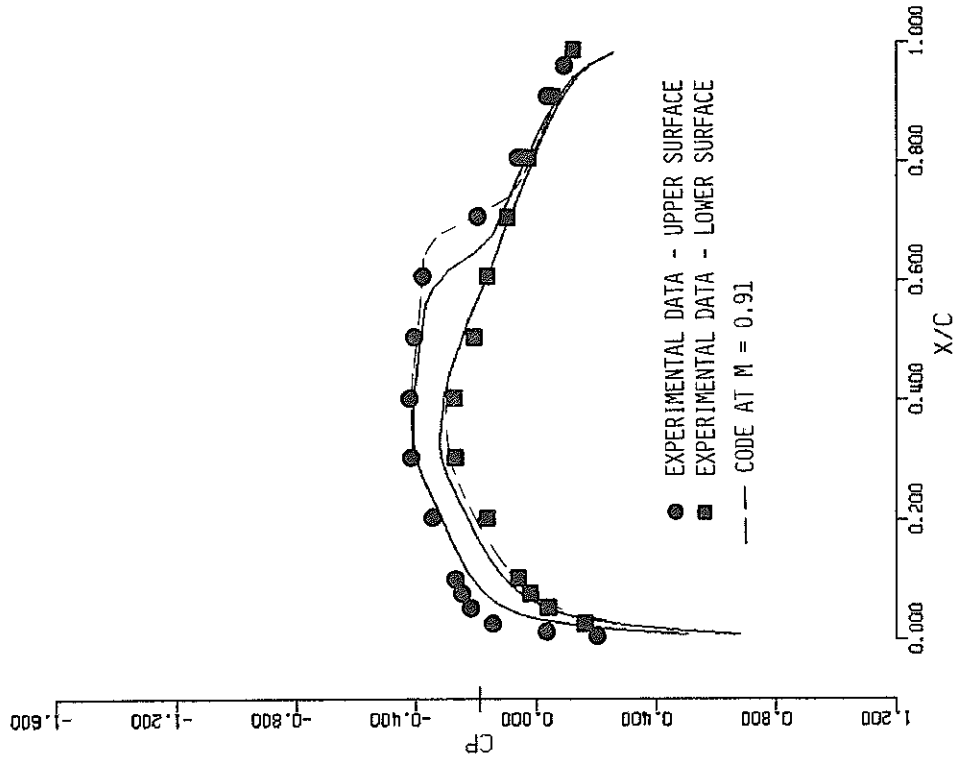


Figure 33d. RAE WING BODY CONFIGURATION  
 M = 0.900 ALF = 1.000 CONV = .991E-05  
 LOCAL CL = 0.080 LOCAL CM = -0.043 LOCAL CD = 0.0100  
 SPAN STATION 8 Y/S = 0.255 43 MESH PTS ON CHD

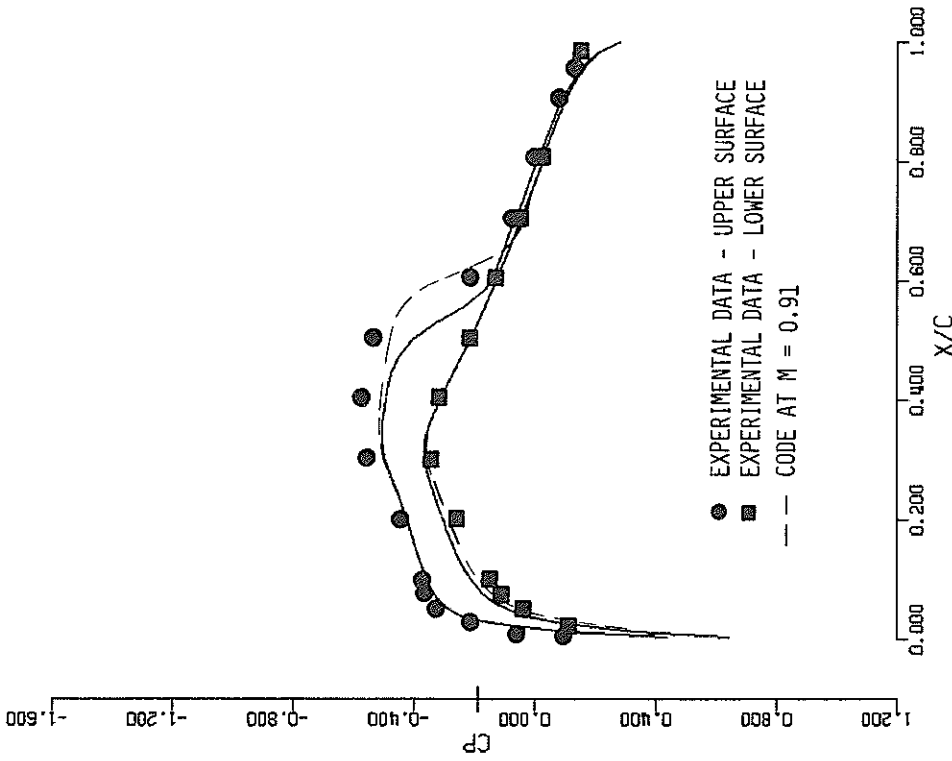


FIGURE 33e, RAE WING BODY CONFIGURATION  
 M = 0.900 ALF = 1.000 CONV = .991E-05  
 LOCAL CL = 0.094 LOCAL CM = -0.074 LOCAL CD = -.0010  
 SPAN STATION 12 Y/S = 0.400 44 MESH PTS ON CHD

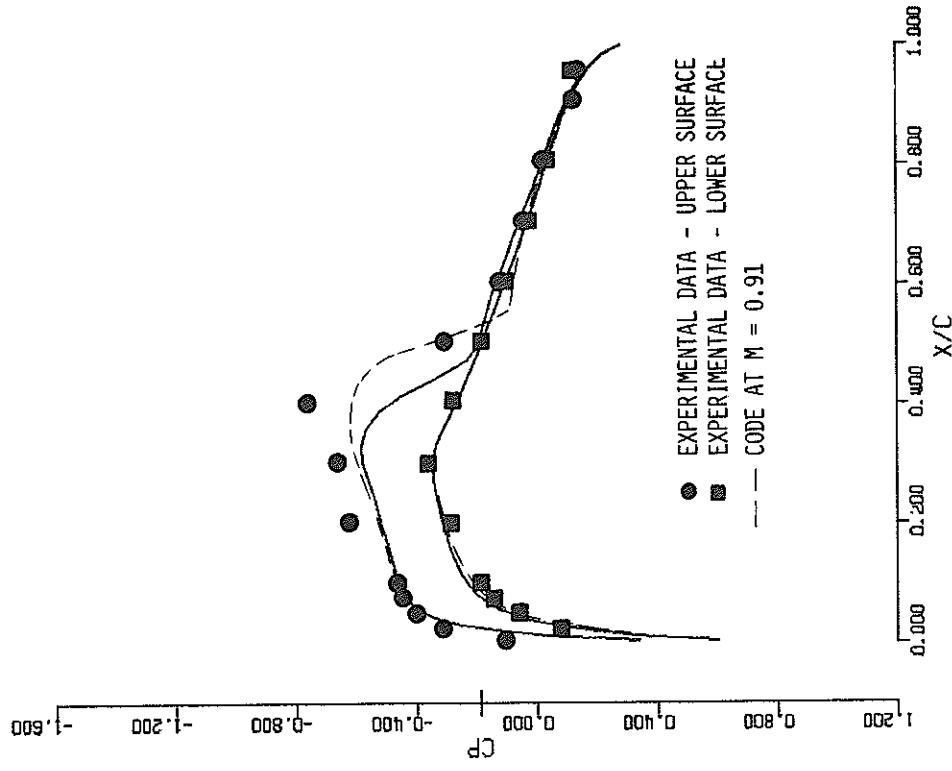


FIGURE 33f, RAE WING BODY CONFIGURATION  
 M = 0.900 ALF = 1.000 CONV = .991E-05  
 LOCAL CL = 0.111 LOCAL CM = -0.155 LOCAL CD = -.0072  
 SPAN STATION 18 Y/S = 0.618 44 MESH PTS ON CHD

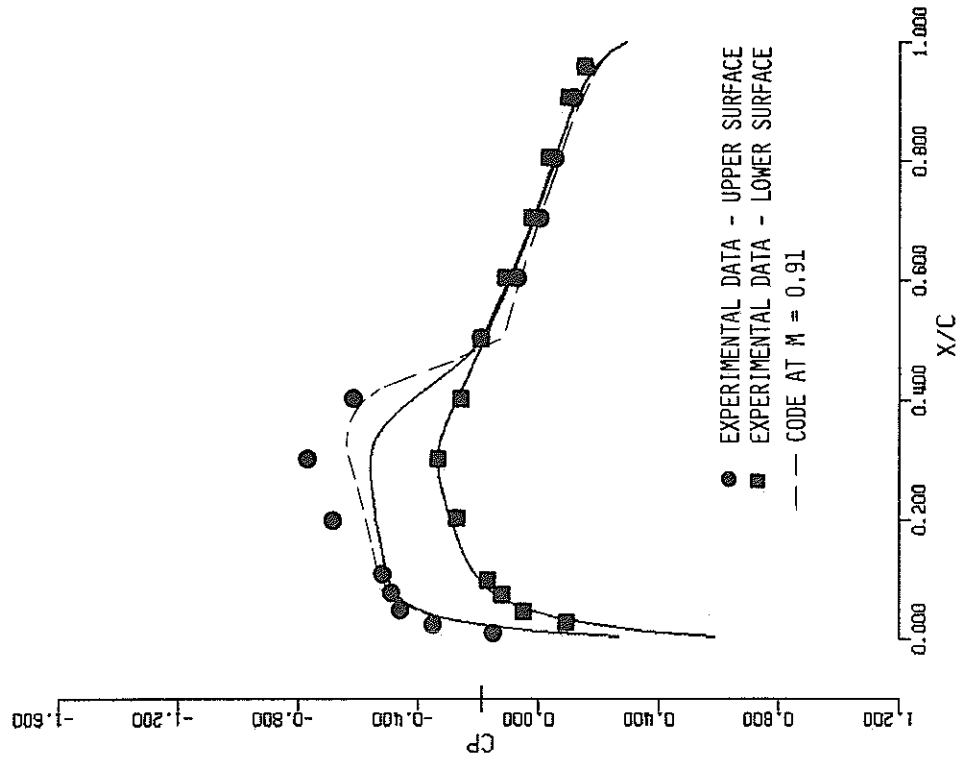


Figure 33h, RAE WING BODY CONFIGURATION  
 M = 0.900 ALF = 1.000 CONV = .991E-05  
 LOCAL CL = 0.112 LOCAL CM = -0.275 LOCAL CD = -.0090  
 SPAN STATION 24 Y/S = 0.836 44 MESH PTS ON CHD

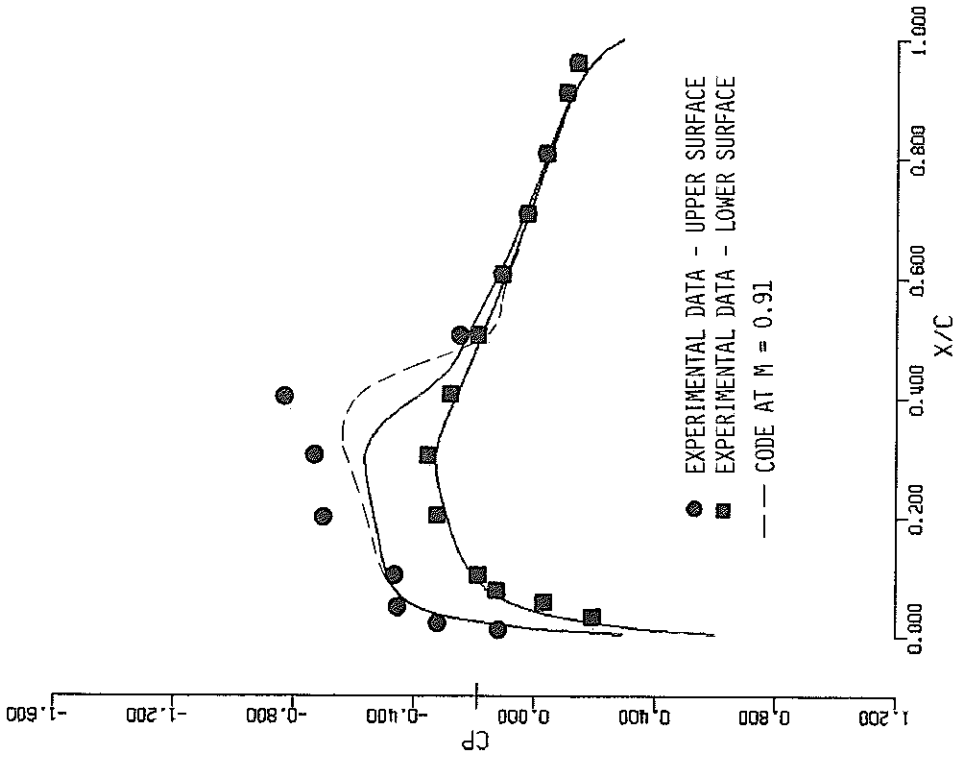
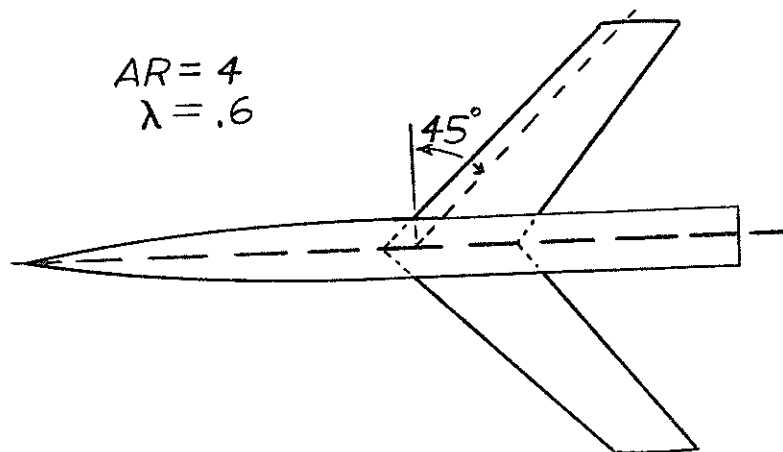
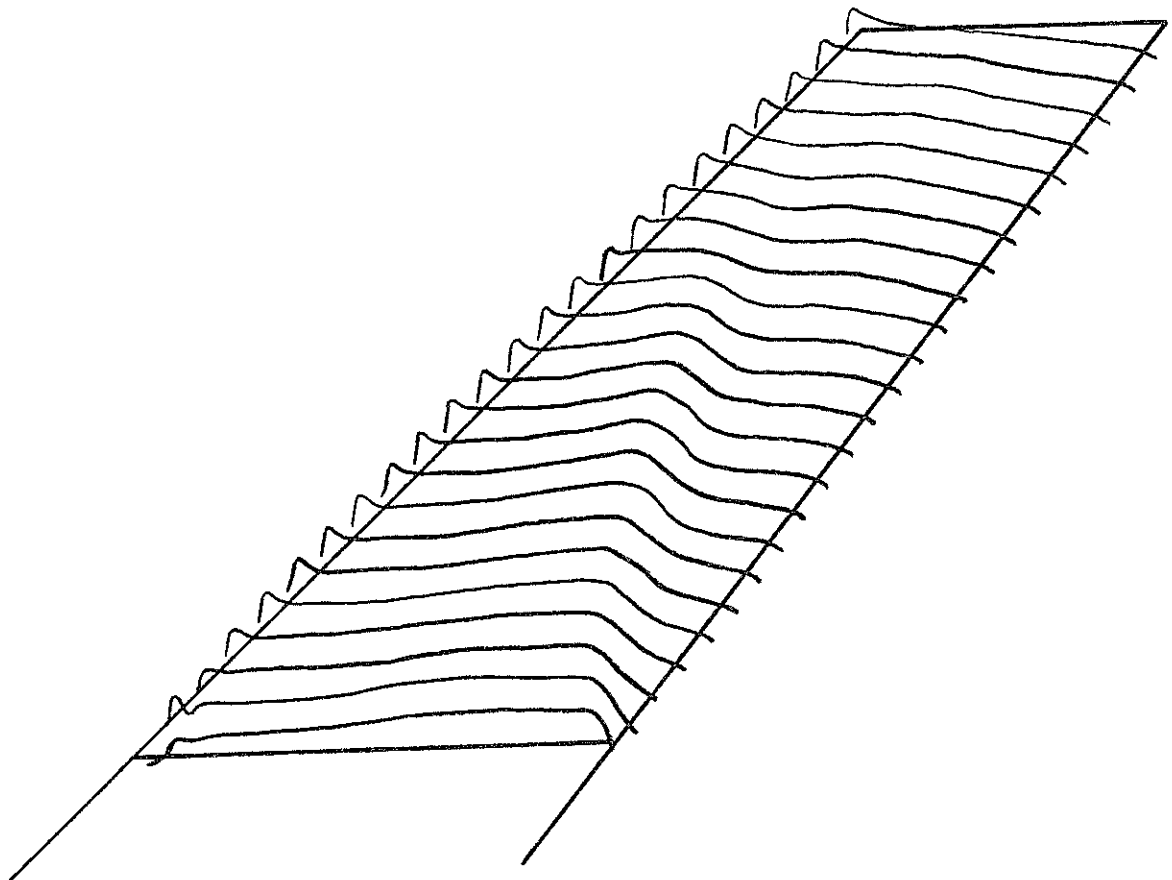


Figure 33g, RAE WING BODY CONFIGURATION  
 M = 0.900 ALF = 1.000 CONV = .991E-05  
 LOCAL CL = 0.116 LOCAL CM = -0.235 LOCAL CD = -.0077  
 SPAN STATION 22 Y/S = 0.764 44 MESH PTS ON CHD



(a) L54H18 configuration



(b) Upper surface pressure distribution

FIG. 34 L54H18

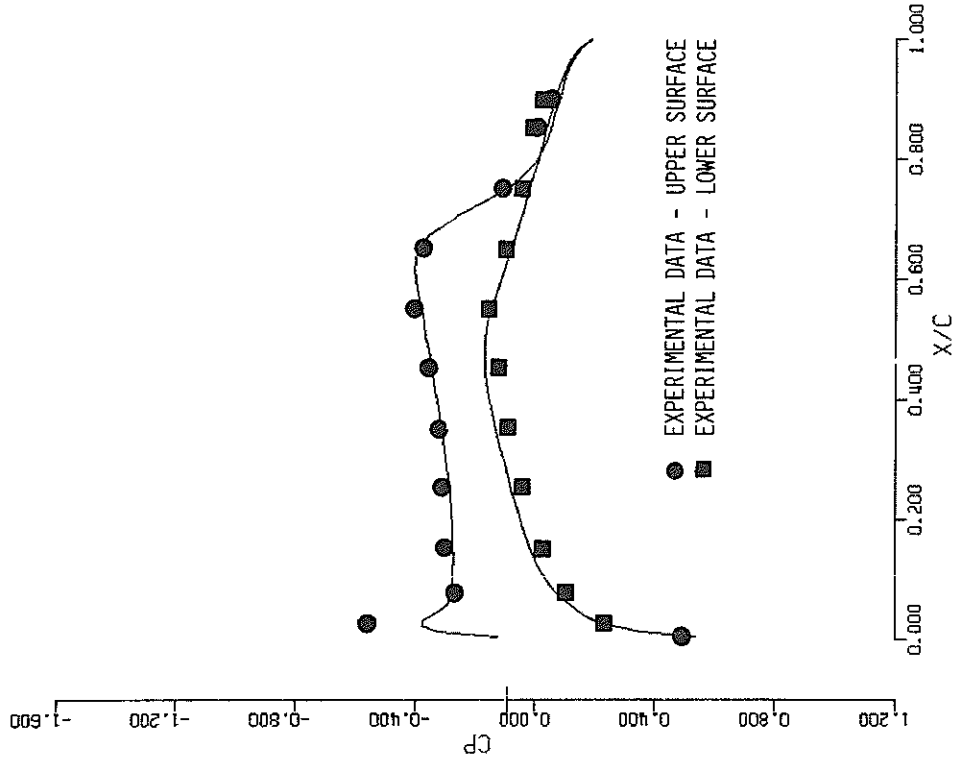


Figure 34b, NACA RM L54H18  
 M = 0.950 ALF = 4.000 CONV = .305E-03  
 LOCAL CL = 0.189 LOCAL CM = -0.793 LOCAL CD = 0.0044  
 SPAN STATION 12 Y/S = 0.400 44 MESH PTS ON CHD

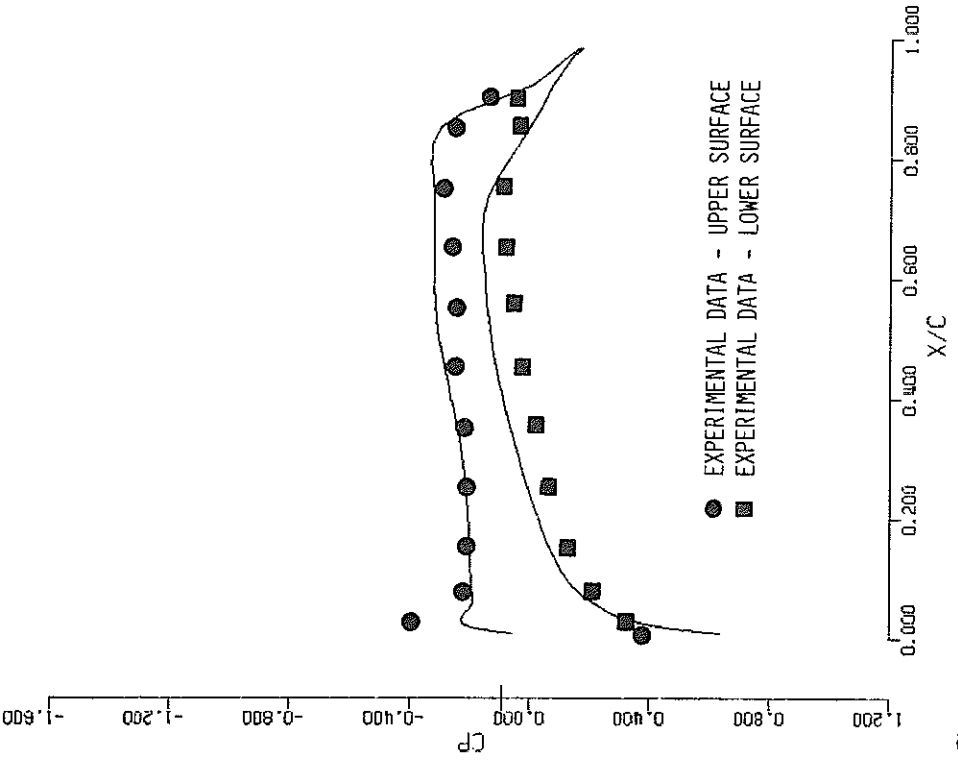


Figure 34c, NACA RM L54H18  
 M = 0.950 ALF = 4.000 CONV = .305E-03  
 LOCAL CL = 0.210 LOCAL CM = -0.767 LOCAL CD = 0.0202  
 SPAN STATION 7 Y/S = 0.218 43 MESH PTS ON CHD

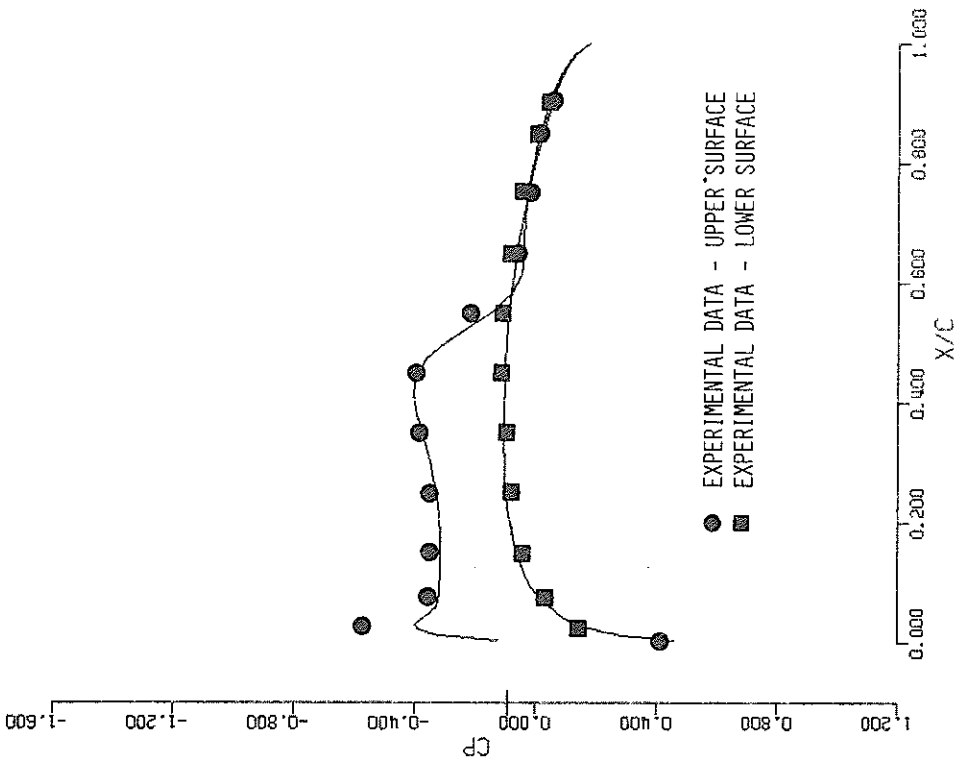


Figure 34e. NACA RM L54H18  
 M = 0.950 ALF = 4.000 CONV = .305E-03  
 LOCAL CL = 0.152 LOCAL CM = -0.744 LOCAL CD = -.0038  
 SPAN STATION 17 Y/S = 0.582 44 MESH PTS ON CHD

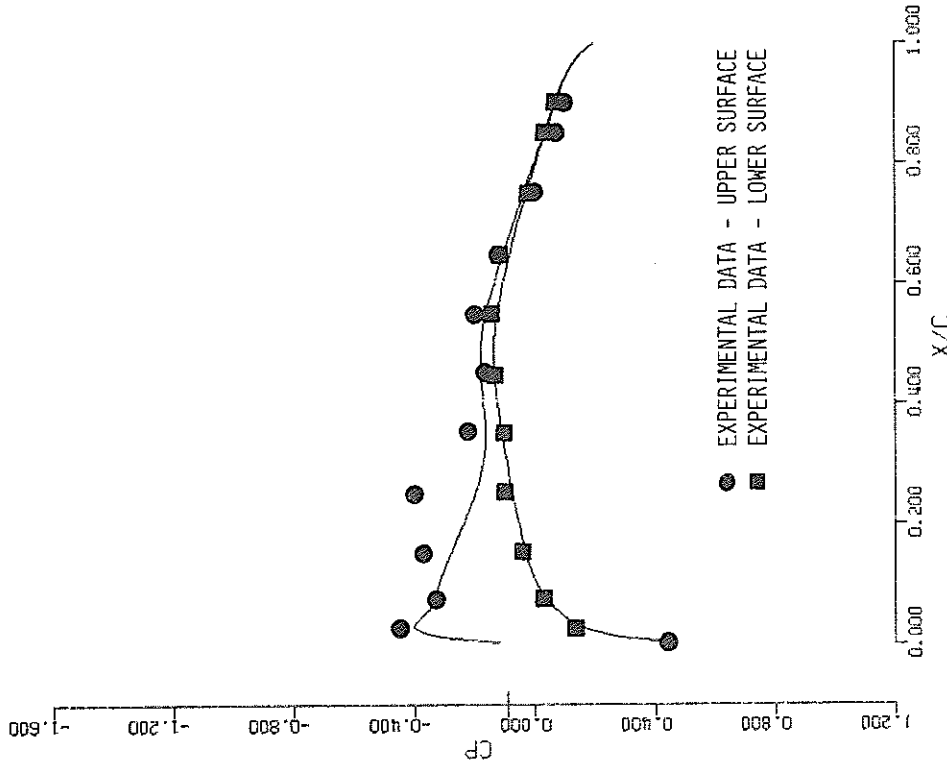


Figure 34f. NACA RM L54H18  
 M = 0.950 ALF = 4.000 CONV = .305E-03  
 LOCAL CL = 0.100 LOCAL CM = -0.593 LOCAL CD = -.0049  
 SPAN STATION 23 Y/S = 0.800 44 MESH PTS ON CHD

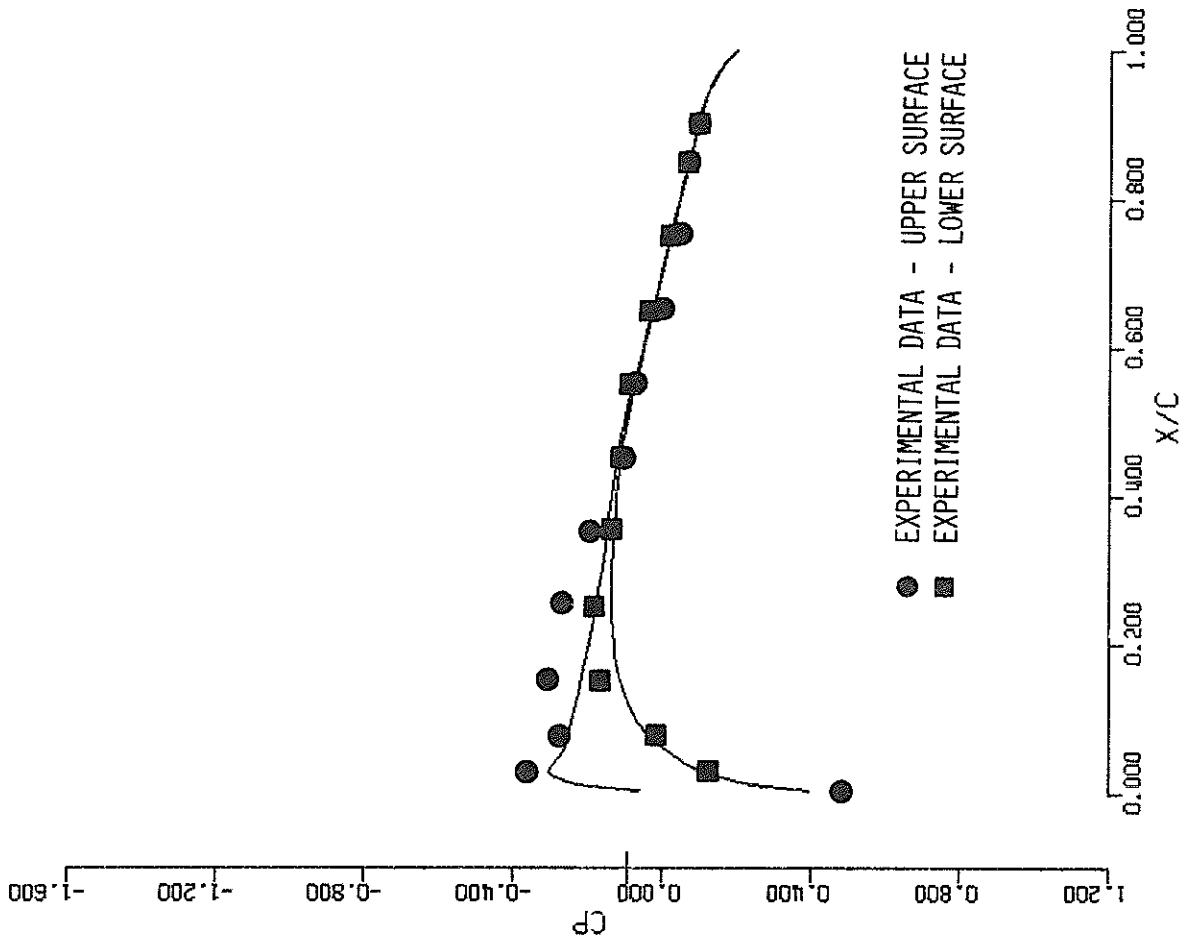
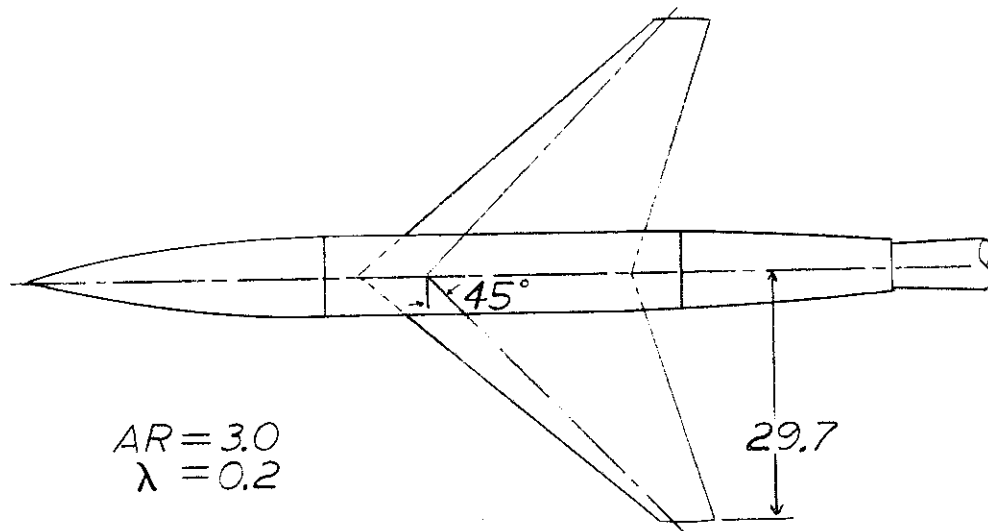
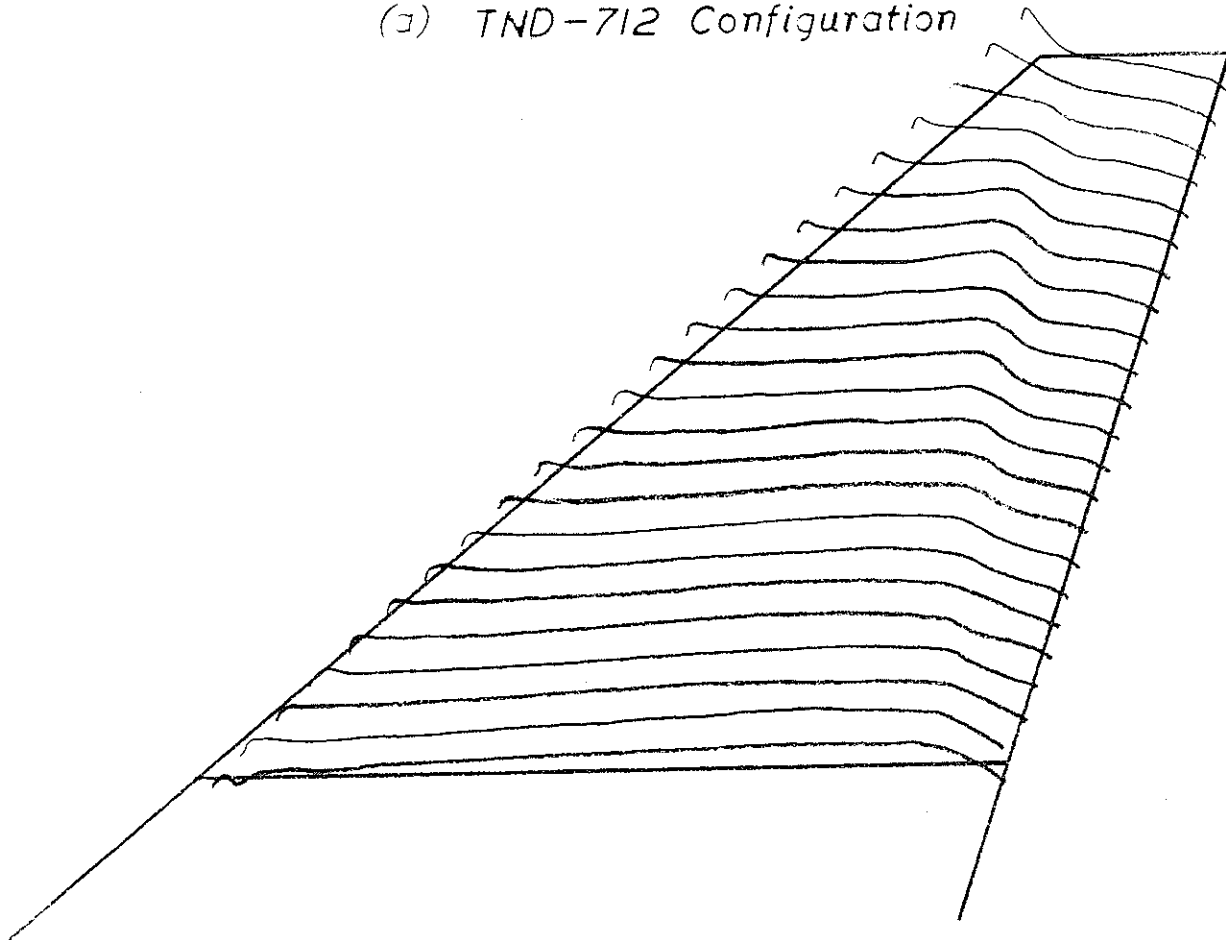


FIGURE 34g. NACA RM L54H18  
 $M = 0.950$   $ALF = 4.000$   $CONV = .305E-03$   
 $LOCAL CL = 0.050$   $LOCAL CM = -0.342$   $LOCAL CD = -.0077$   
 $SPAN STATION 27$   $Y/S = 0.945$  44 MESH PTS ON CHD





(a) TND-712 Configuration



(a) Upper surface pressure distribution  
FIG. 35 TND-712

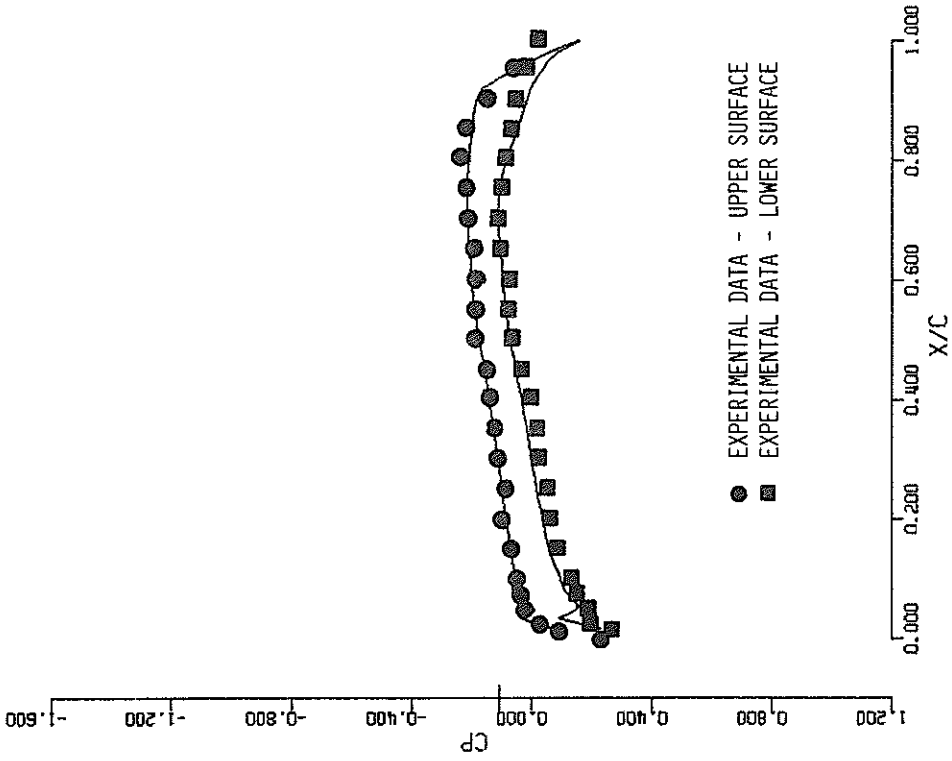


Figure 35c, NACA TN D-712 BRICK BODY  
 $M = 0.940$   $ALF = 2.400$   $CONV = .231E-02$   
 $LOCAL CL = 0.120$   $LOCAL CM = -0.257$   $LOCAL CD = 0.0100$   
 SPAN STATION 6  $Y/S = 0.182$  48 MESH PTS ON CHD

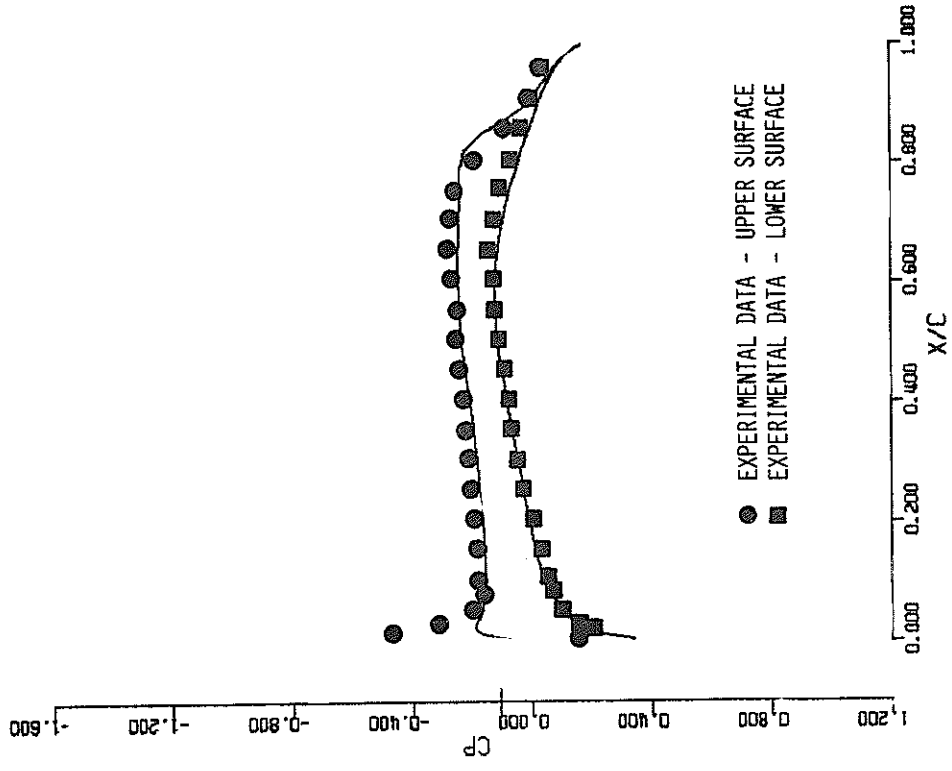


Figure 35d, NACA TN D-712 BRICK BODY  
 $M = 0.940$   $ALF = 2.400$   $CONV = .231E-02$   
 $LOCAL CL = 0.141$   $LOCAL CM = -0.400$   $LOCAL CD = 0.0080$   
 SPAN STATION 12  $Y/S = 0.400$  44 MESH PTS ON CHD

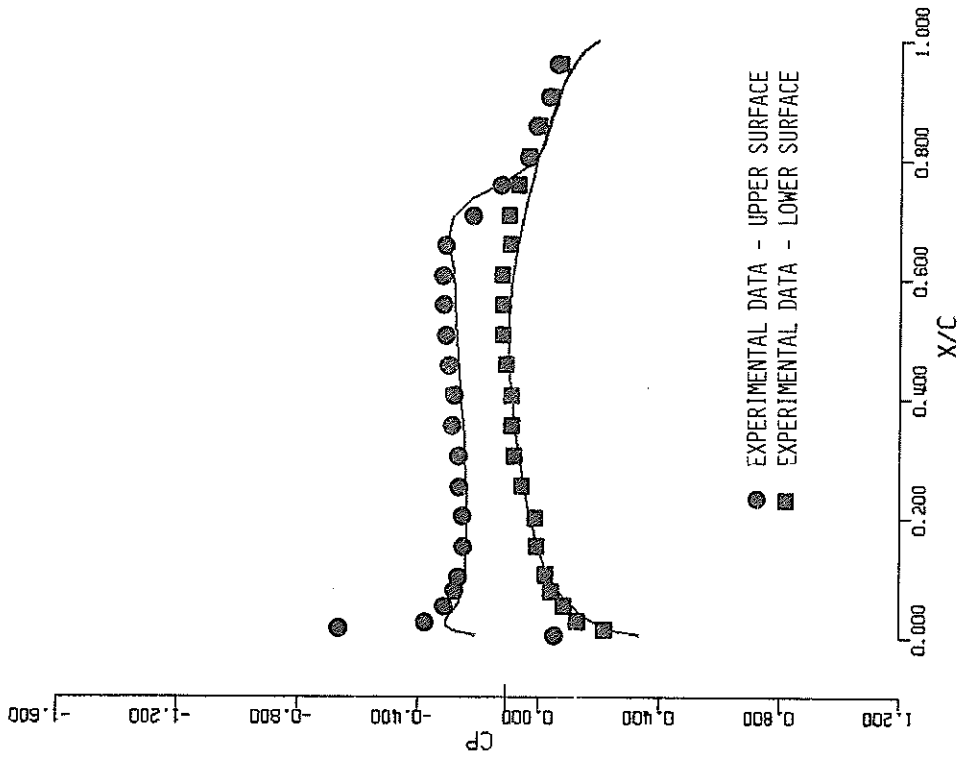


FIGURE 35E. NACA TN D-712 BRICK BODY  
 $M = 0.940$   $ALF = 2.400$   $CONV = .231E-02$   
 $LOCAL CL = 0.168$   $LOCAL CM = -0.685$   $LOCAL CD = 0.0058$   
 $SPAN STATION 18$   $Y/S = 0.618$  44 MESH PTS ON CHD

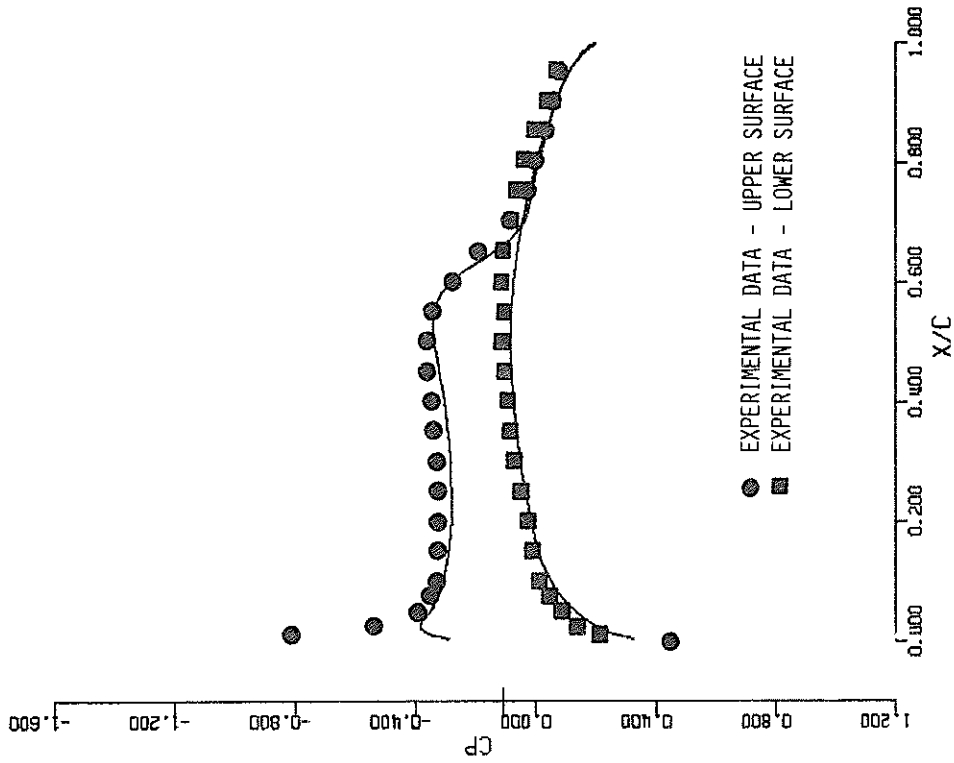


FIGURE 35F. NACA TN D-712 BRICK BODY  
 $M = 0.940$   $ALF = 2.400$   $CONV = .231E-02$   
 $LOCAL CL = 0.182$   $LOCAL CM = -1.004$   $LOCAL CD = 0.0041$   
 $SPAN STATION 22$   $Y/S = 0.764$  44 MESH PTS ON CHD

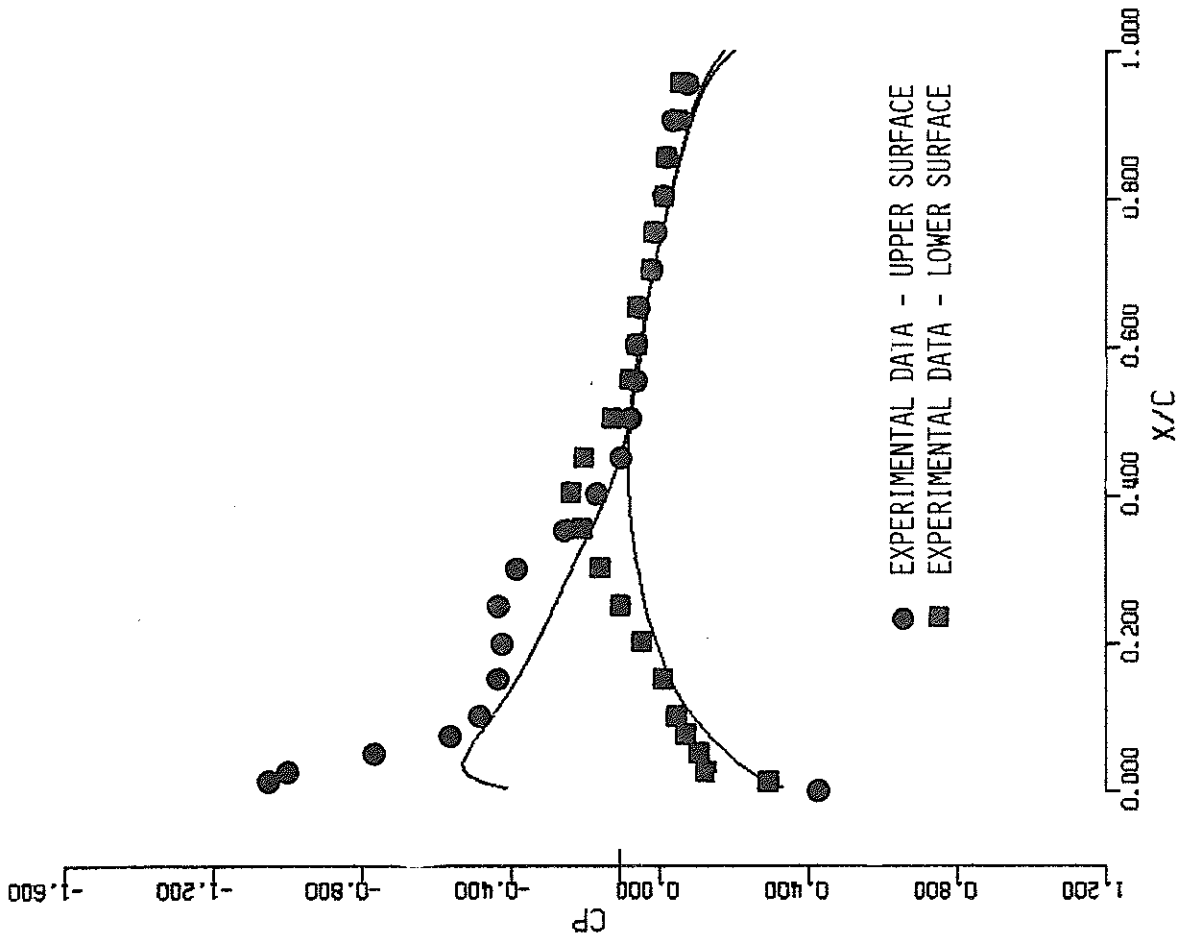
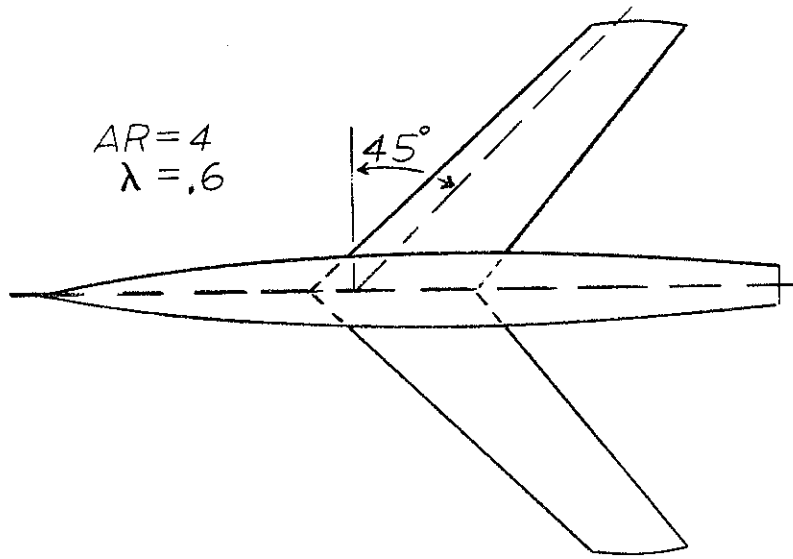
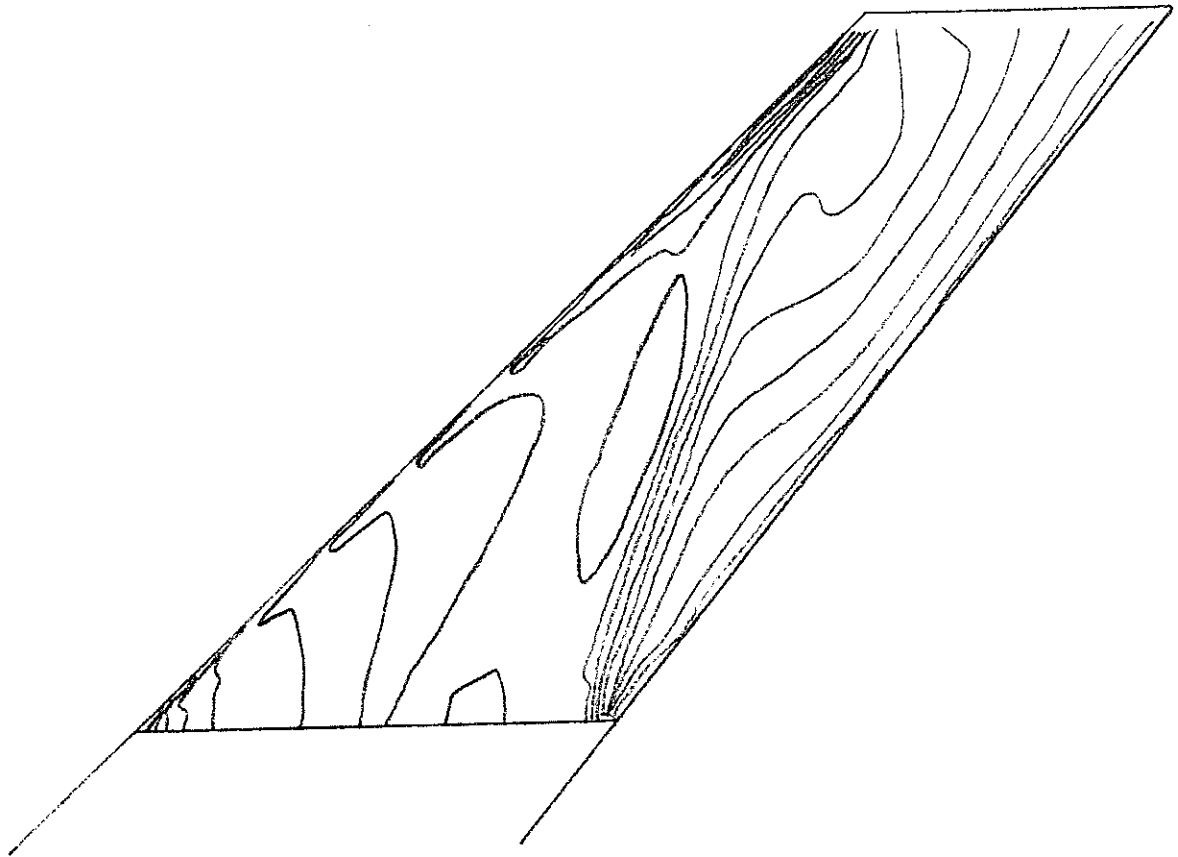


FIGURE 35g, NACA TN D-712 BRICK BODY  
 $M = 0.940$   $AI/F = 2.400$   $C_{MN}V = .231E-02$   
 $LOCAL\ CL = 0.145$   $LOCAL\ CM = -1.354$   $LOCAL\ CD = .0003$   
 $SPAN\ STATION\ 27$   $Y/S = 0.945$  44 MESH PTS ON CHD



(a) L5IF07 configuration



(b) Upper surface isobars  
FIG. 36 L5IF07

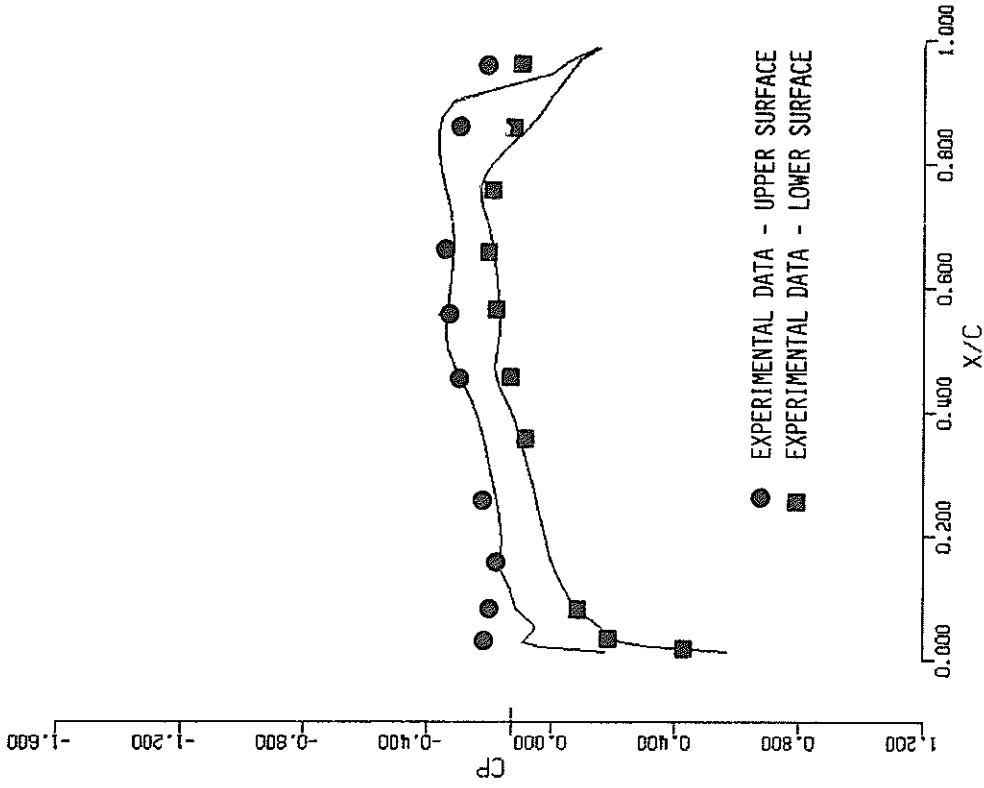


FIGURE 36D, NACA RM L51F07  
 $M = 0.930$   $ALF = 2.000$   $CONV = .533E-03$   
 $LOCAL CL = 0.153$   $LOCAL CM = -0.086$   $LOCAL CD = 0.0163$   
 $SPAN STATION 6$   $Y/S = 0.182$   $45$  MESH PTS ON CHD

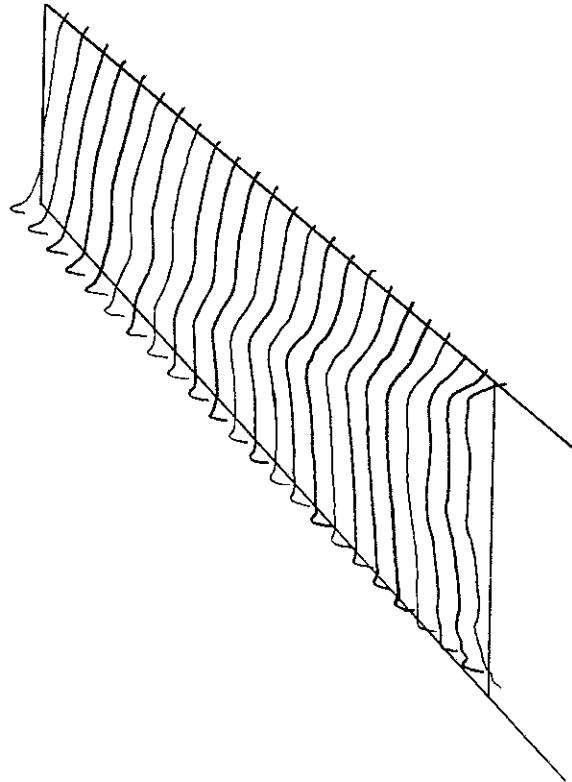


FIG. 36 (c) Upper surface pressure distribution

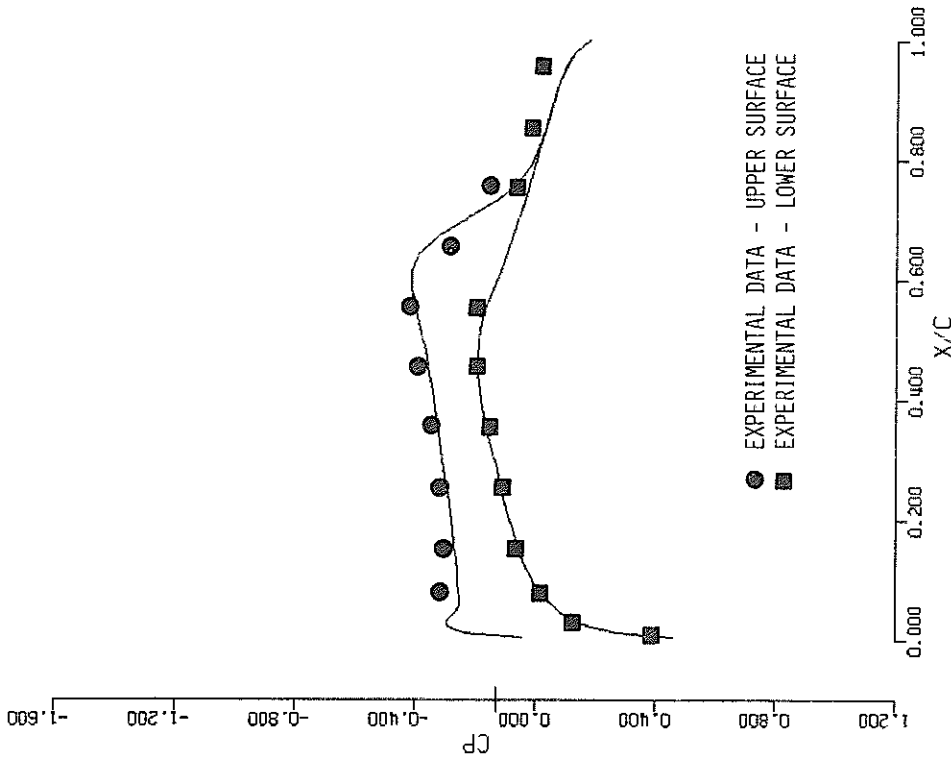


FIGURE 36E, NACA RM L51F07  
 M = 0.930 ALF = 2.000 CONV = .533E-03  
 LOCAL CL = 0.164 LOCAL CM = -0.144 LOCAL CD = 0.0040  
 SPAN STATION 12 Y/S = 0.400 44 MESH PTS ON CHD

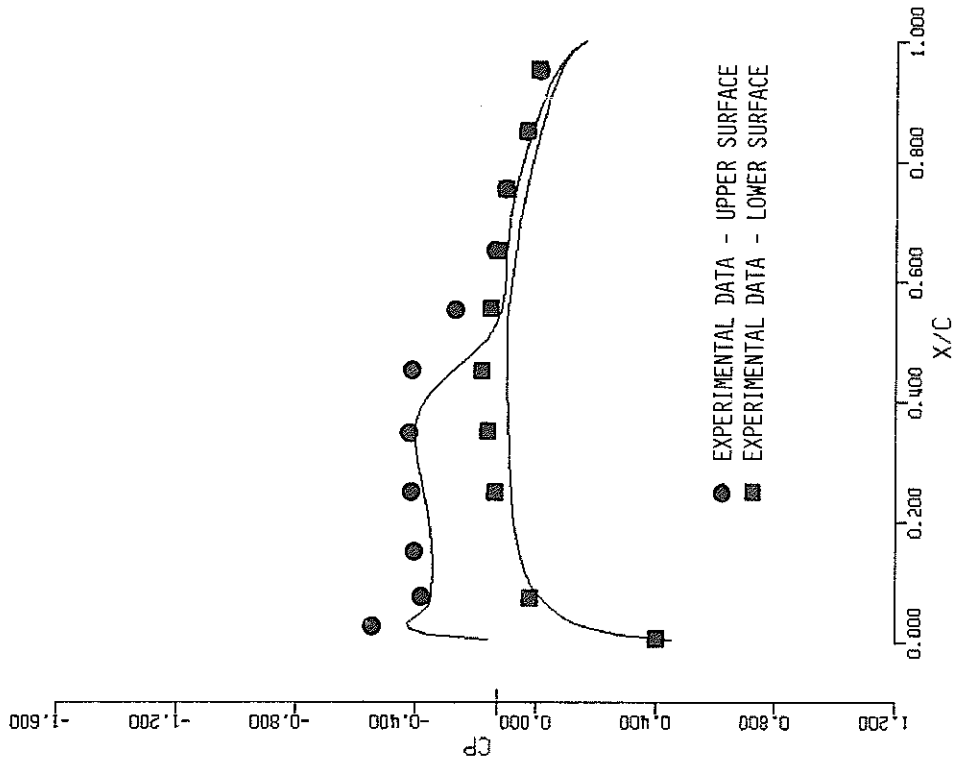


FIGURE 36F, NACA RM L51F07  
 M = 0.930 ALF = 2.000 CONV = .533E-03  
 LOCAL CL = 0.164 LOCAL CM = -0.218 LOCAL CD = -.0007  
 SPAN STATION 18 Y/S = 0.618 44 MESH PTS ON CHD

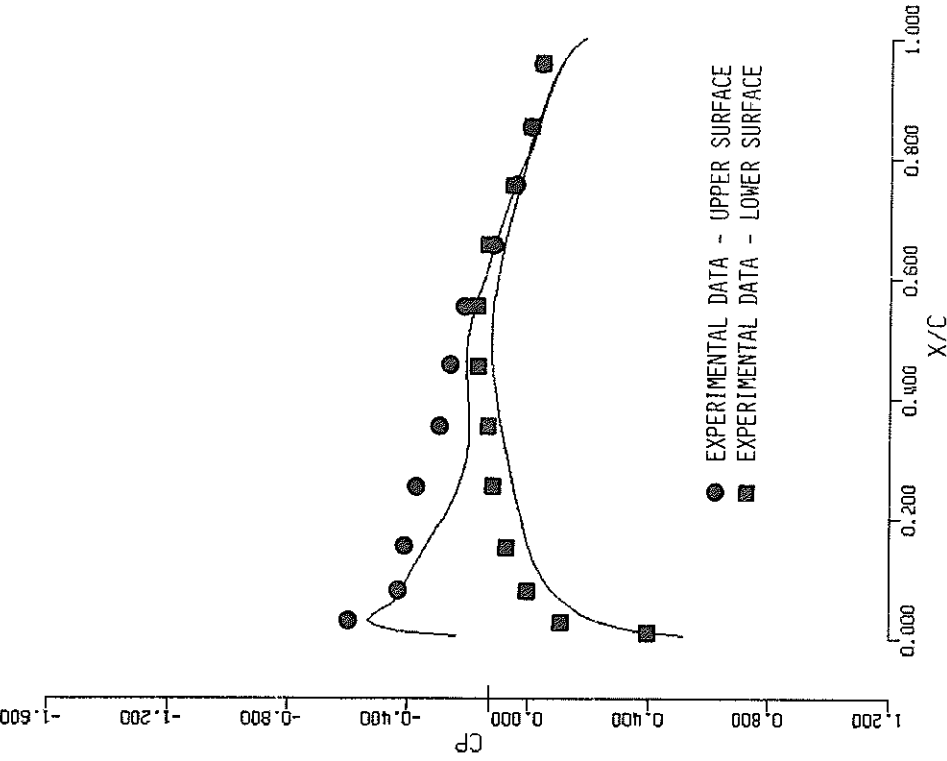


Figure 36g, NACA RM L51F07  
 M = 0.930 ALF = 2.000 CONV = .533E-03  
 LOCAL CL = 0.144 LOCAL CM = -0.265 LOCAL CD = -.0007  
 SPAN STATION 23 Y/S = 0.800 44 MESH PTS ON CHD

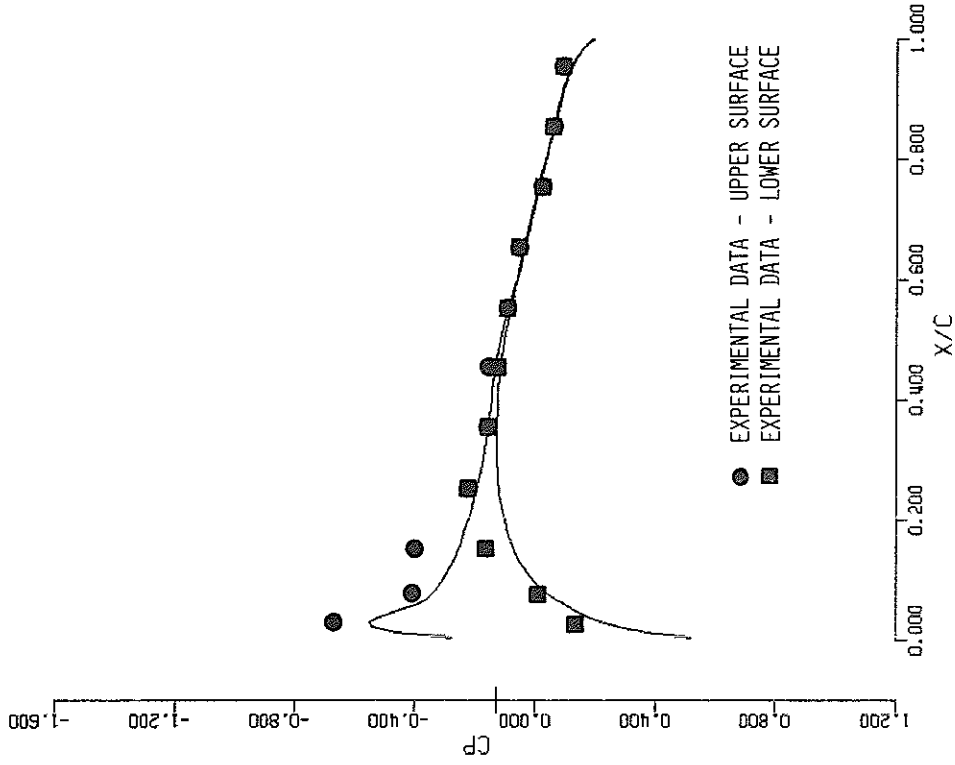
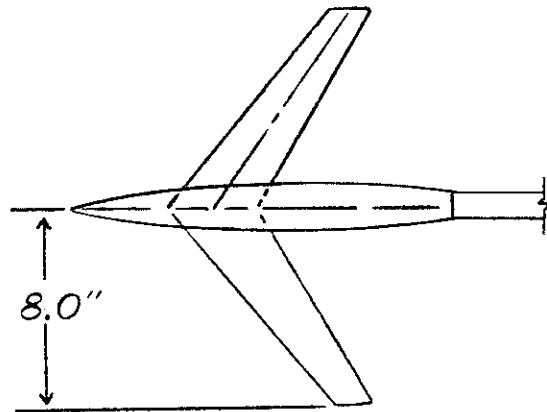


Figure 36h, NACA RM L51F07  
 M = 0.930 ALF = 2.000 CONV = .533E-03  
 LOCAL CL = 0.088 LOCAL CM = -0.202 LOCAL CD = -.0052  
 SPAN STATION 27 Y/S = 0.945 44 MESH PTS ON CHD





(a) Basic model.

Wing geometry

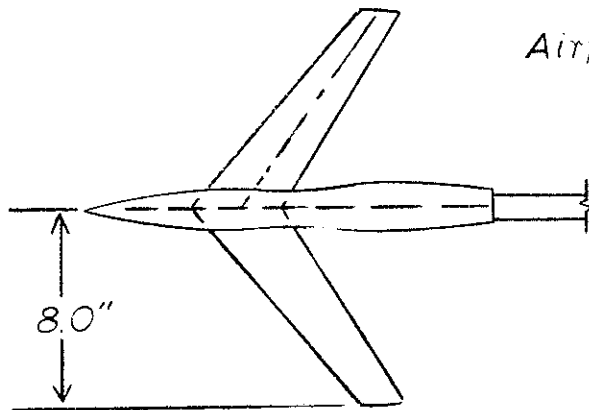
$$\angle_{c/2} = 35^\circ$$

$$AR = 6.0$$

$$\lambda = 0.5$$

$$\bar{c} = 2.74''$$

Airfoil section 64<sub>2</sub>A015



(b) Area rule model.

FIG. 37  
A55B21 Configurations

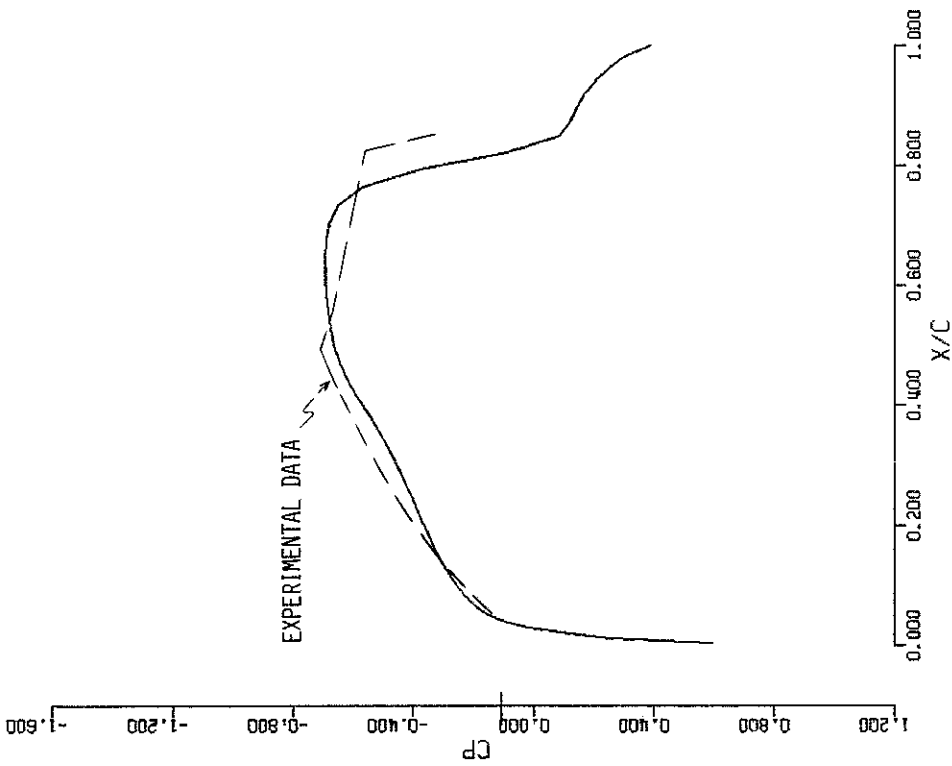


FIGURE 37c. NACA RM A55B21 BASIC BODY MODEL  
 $M = 0.940$  ALF = 0.0 CONV = .261E-03  
 LOCAL CL = 0.000 LOCAL CM = -0.000 LOCAL CD = 0.0241  
 SPAN STATION 14 Y/S = 0.473 44 MESH PTS ON CHD

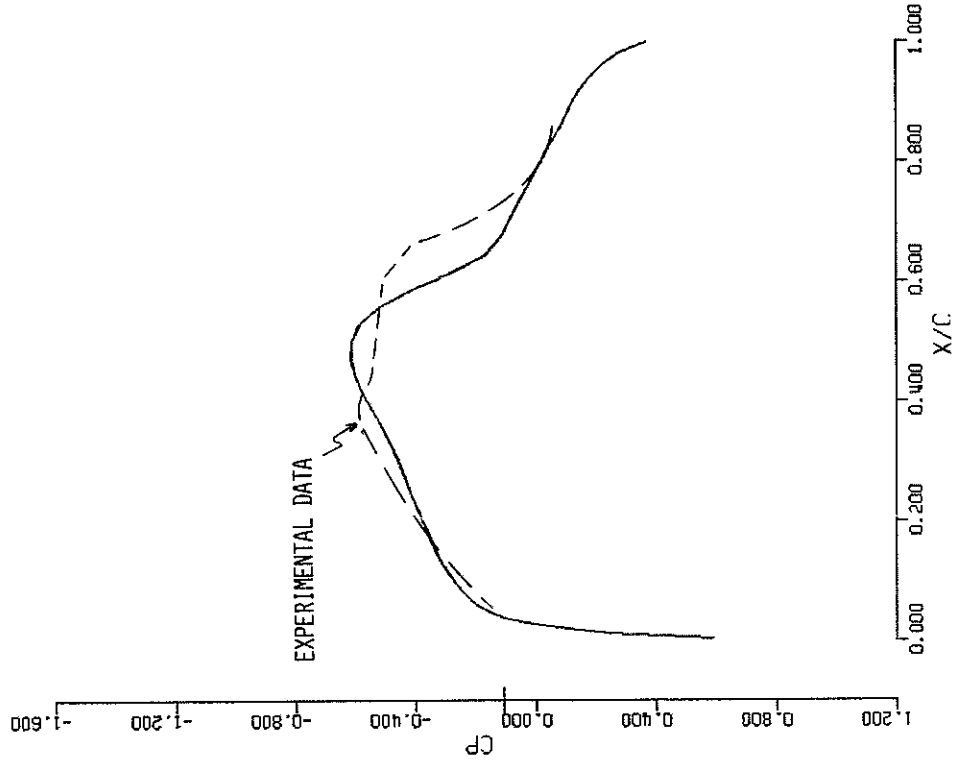


FIGURE 37d. NACA RM A55B21 AREA RULED BODY 3  
 $M = 0.940$  ALF = 0.0 CONV = .247E-04  
 LOCAL CL = -0.000 LOCAL CM = -0.001 LOCAL CD = -.0067  
 SPAN STATION 14 Y/S = 0.473 44 MESH PTS ON CHD

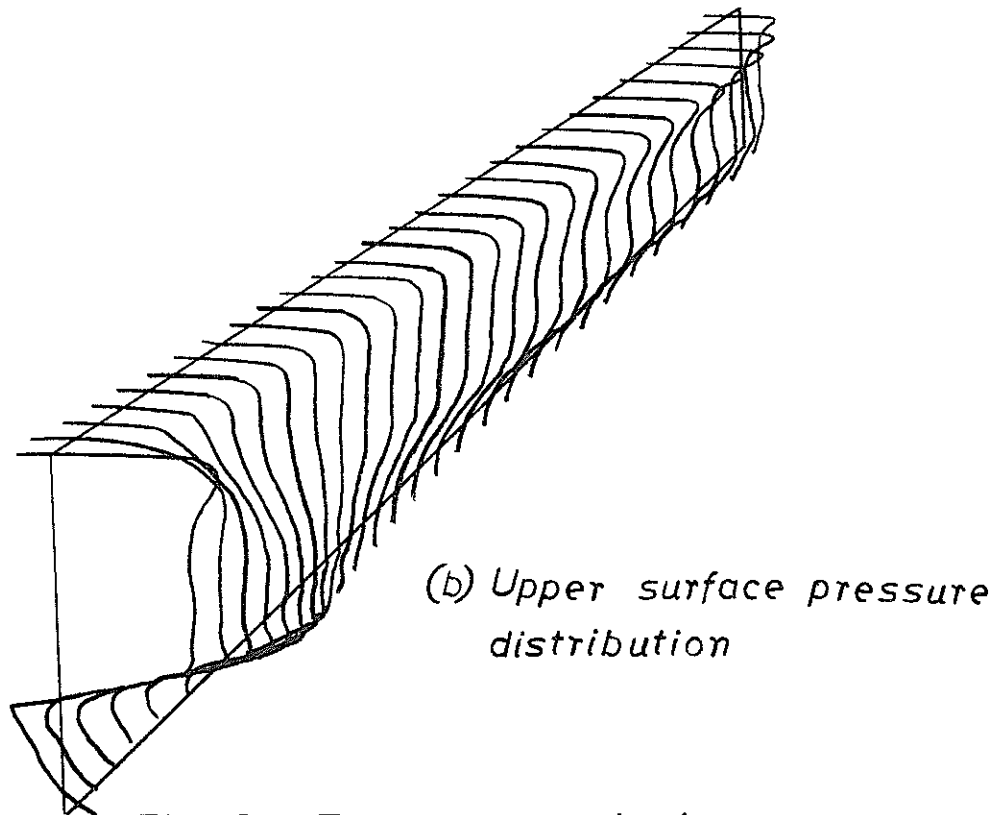
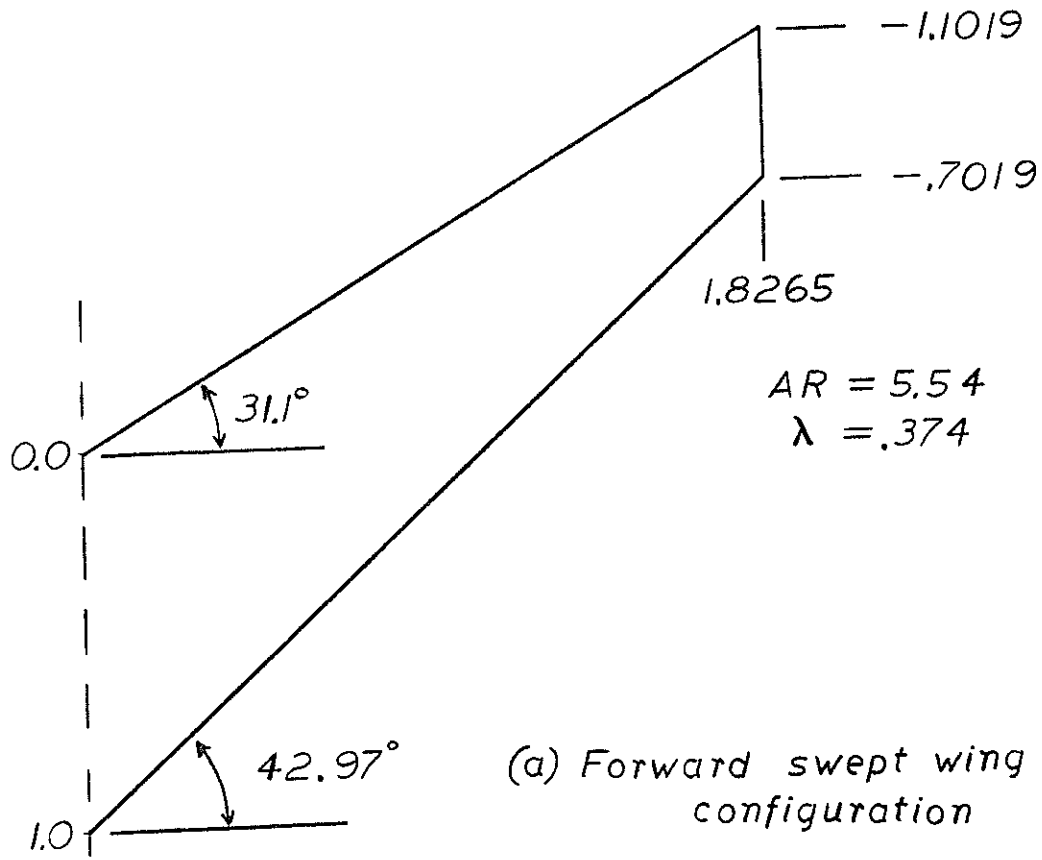
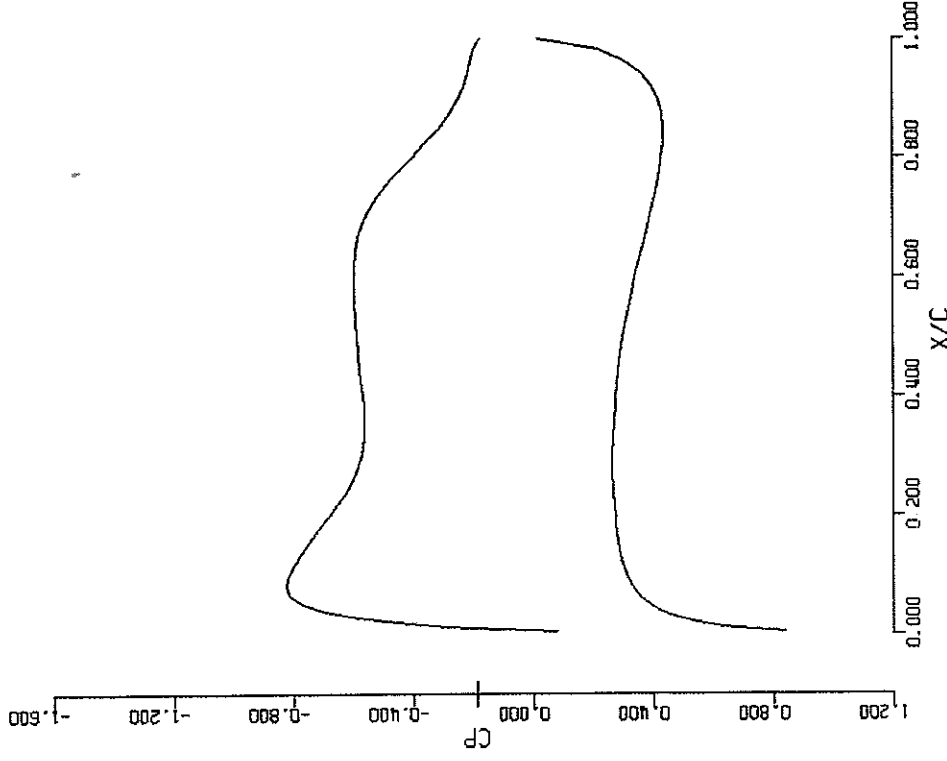
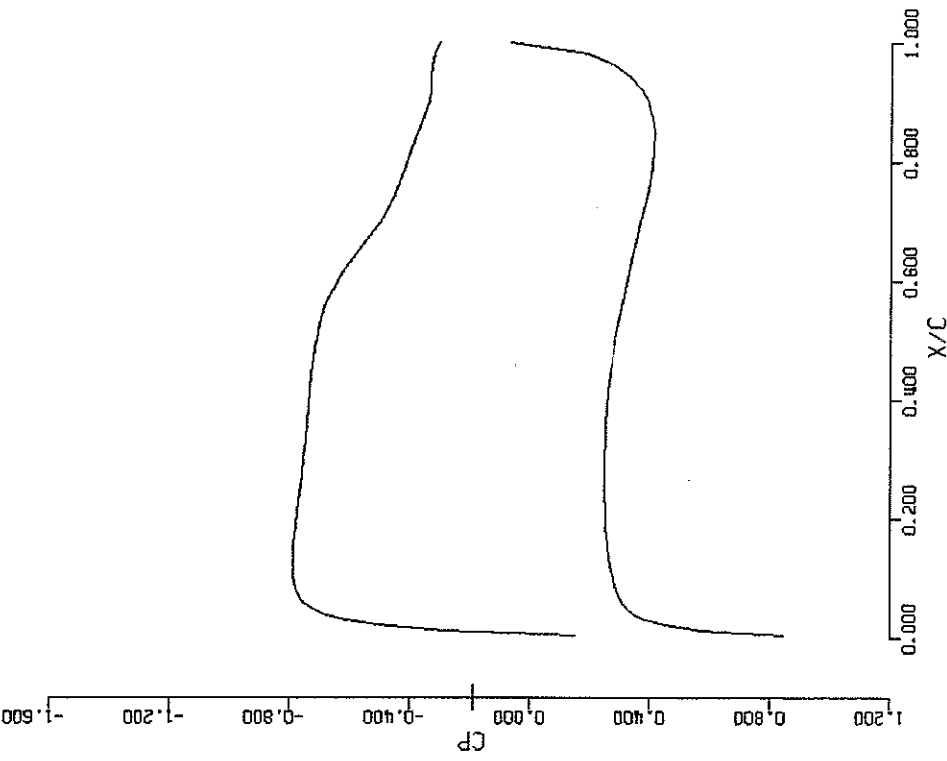
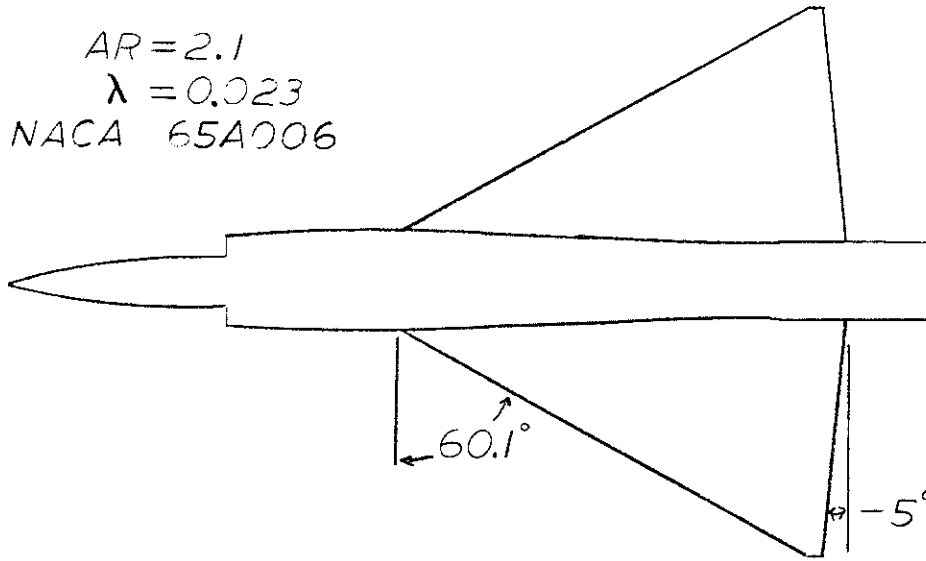


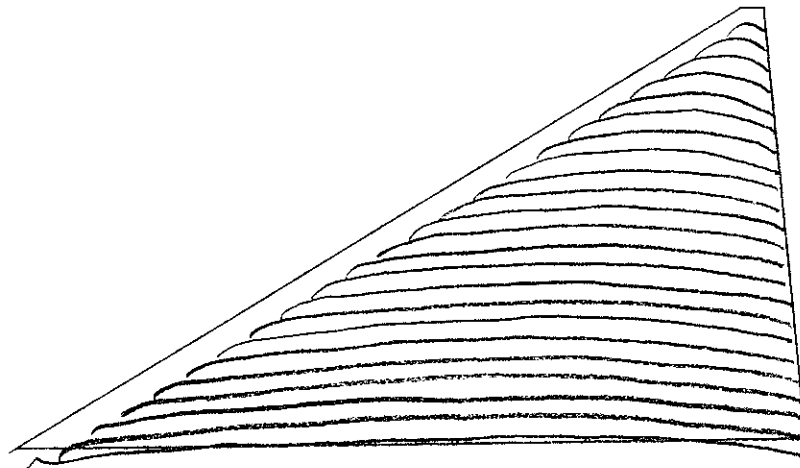
FIG. 38 Forward swept wing



$AR=2.1$   
 $\lambda=0.023$   
NACA 65A006



(a) Low aspect ratio configuration



(b) Upper surface pressure distribution

FIG. 39 Low aspect ratio

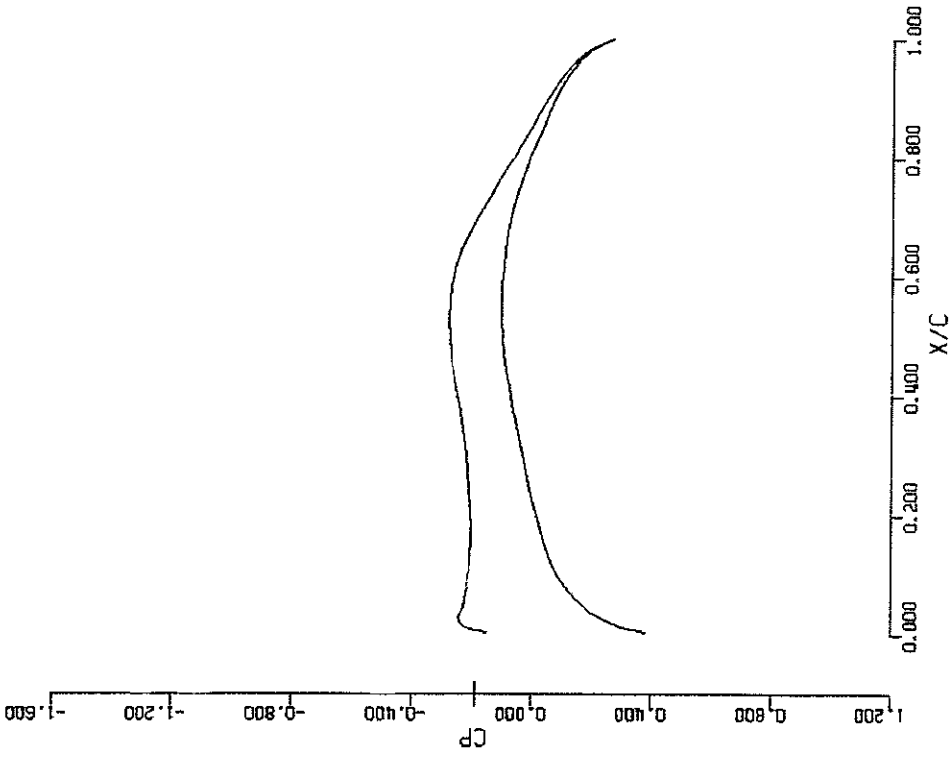


Figure 39c. LOW ASPECT RATIO CASE  
 M = 0.900 ALF = 4.000 CONV = .495E-02  
 LOCAL CL = 0.165 LOCAL CM = -0.092 LOCAL CD = 0.0111  
 SPAN STATION 12 Y/S = 0.400 44 MESH PTS ON CHD

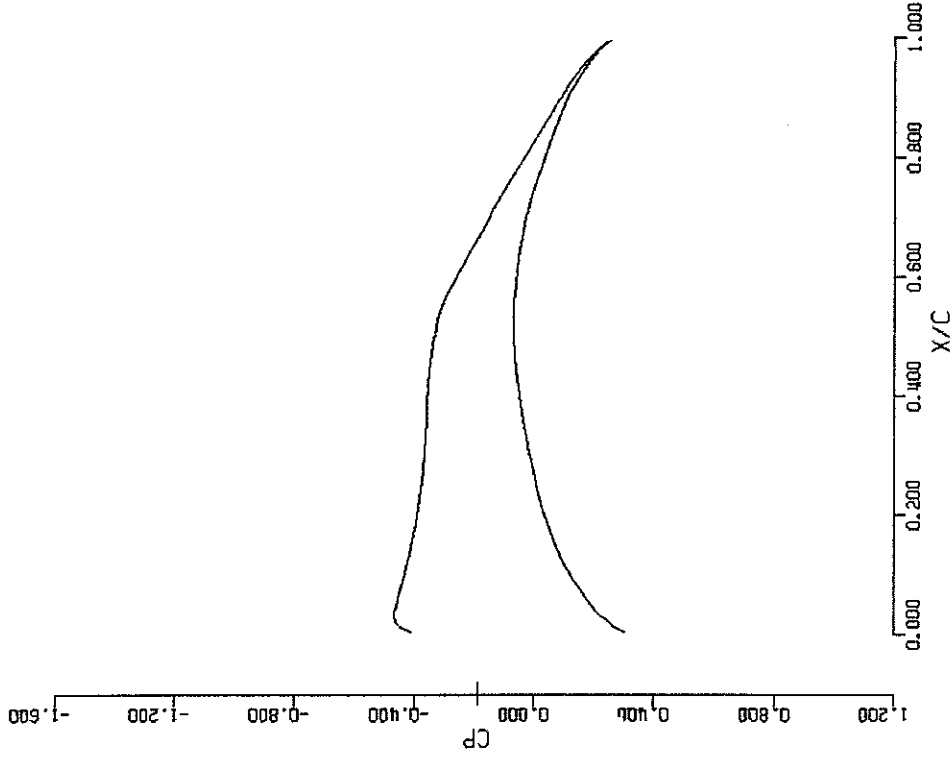
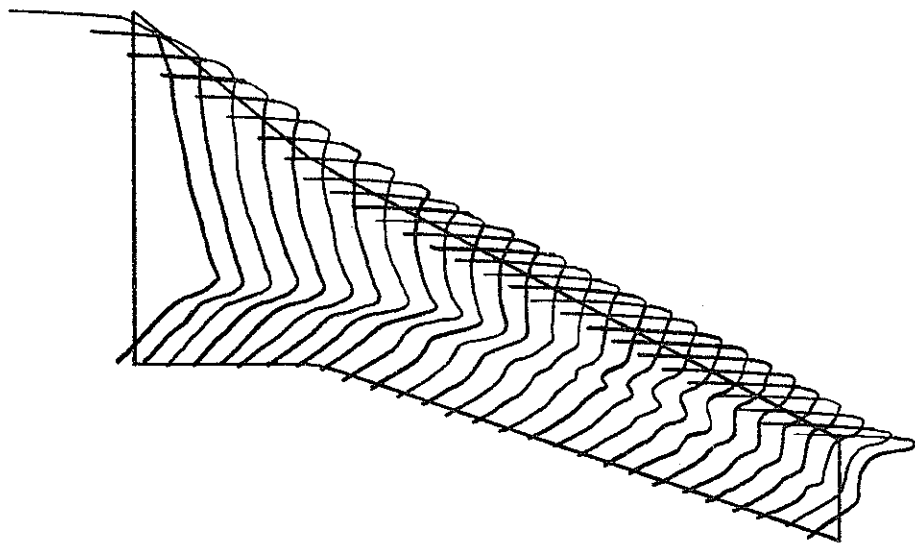
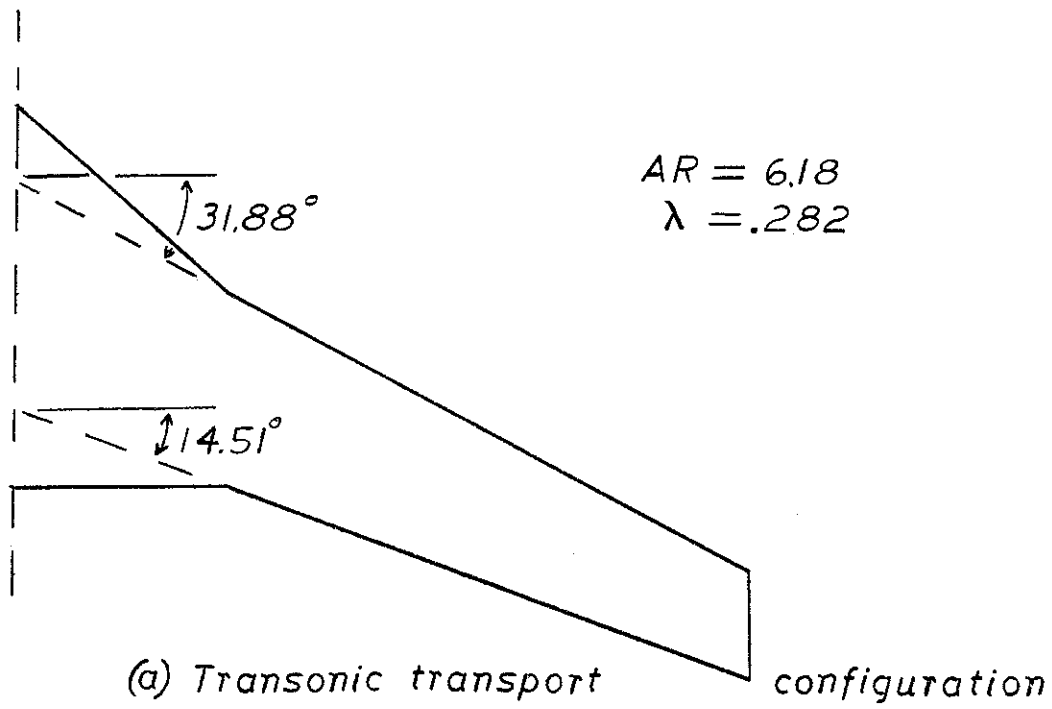


Figure 39d. LOW ASPECT RATIO CASE  
 M = 0.900 ALF = 4.000 CONV = .495E-02  
 LOCAL CL = 0.267 LOCAL CM = -0.703 LOCAL CD = 0.0096  
 SPAN STATION 23 Y/S = 0.800 44 MESH PTS ON CHD



(b) *Upper surface pressure distribution*

FIG. 40 *Transonic Transport*

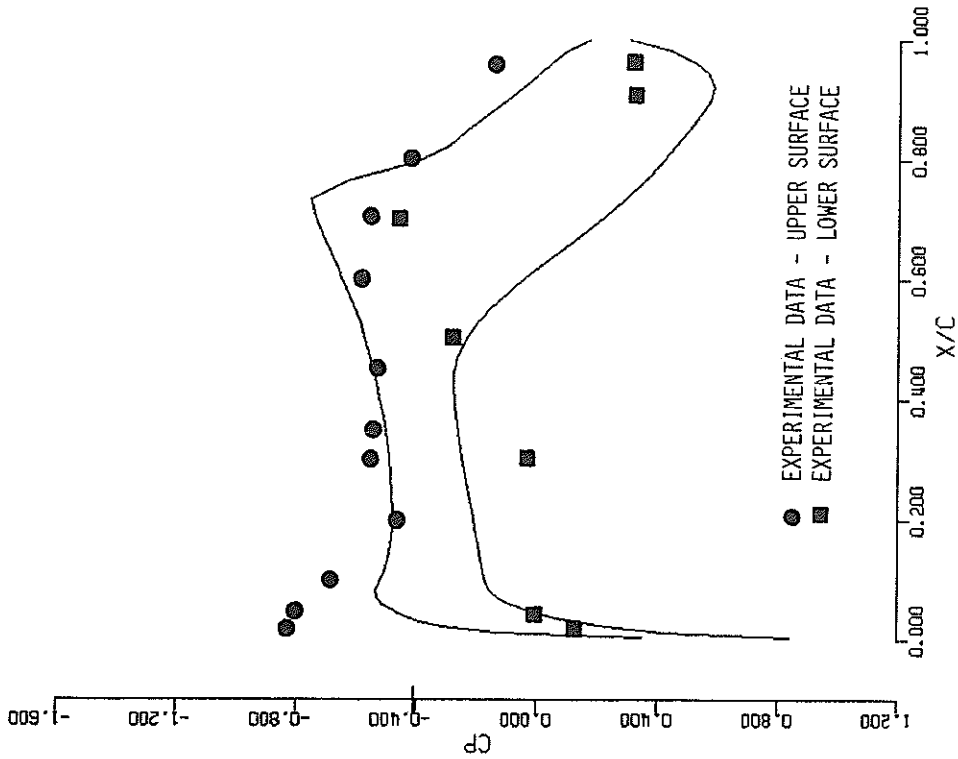


FIGURE 40c. TRANSONIC TRANSPORT  
 M = 0.810 ALF = 2.000 CONV = .330E-04  
 LOCAL CL = 0.492 LOCAL CM = -0.448 LOCAL CD = 0.0240  
 SPAN STATION 5 Y/S = 0.145 44 MESH PTS ON CHD

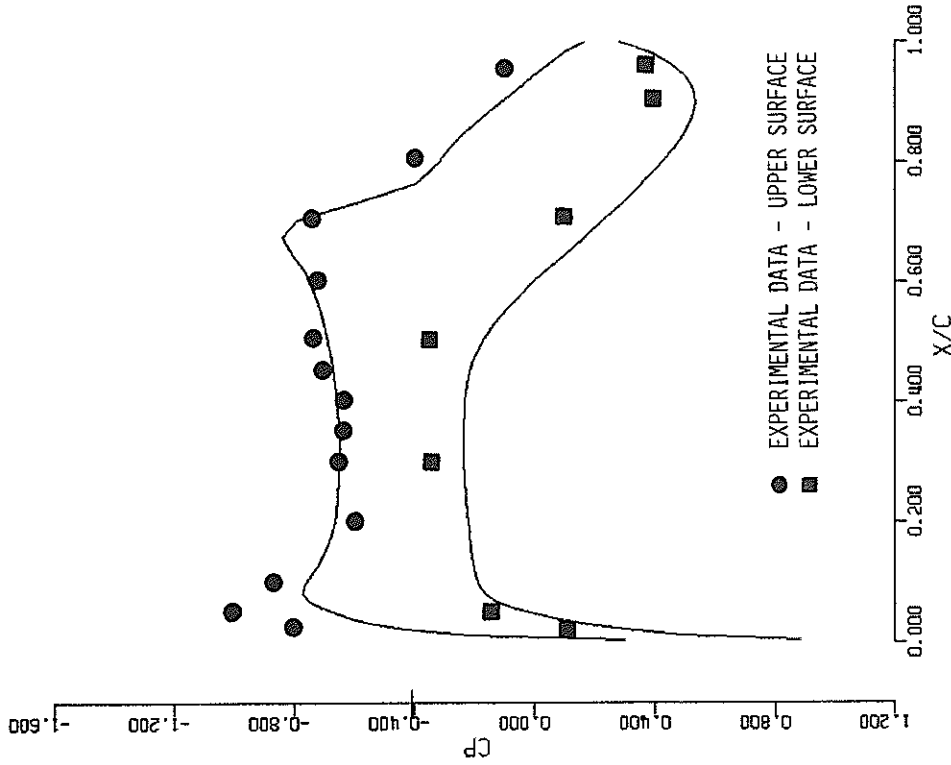


FIGURE 40d. TRANSONIC TRANSPORT  
 M = 0.810 ALF = 2.000 CONV = .330E-04  
 LOCAL CL = 0.594 LOCAL CM = -0.840 LOCAL CD = 0.0111  
 SPAN STATION 9 Y/S = 0.291 44 MESH PTS ON CHD



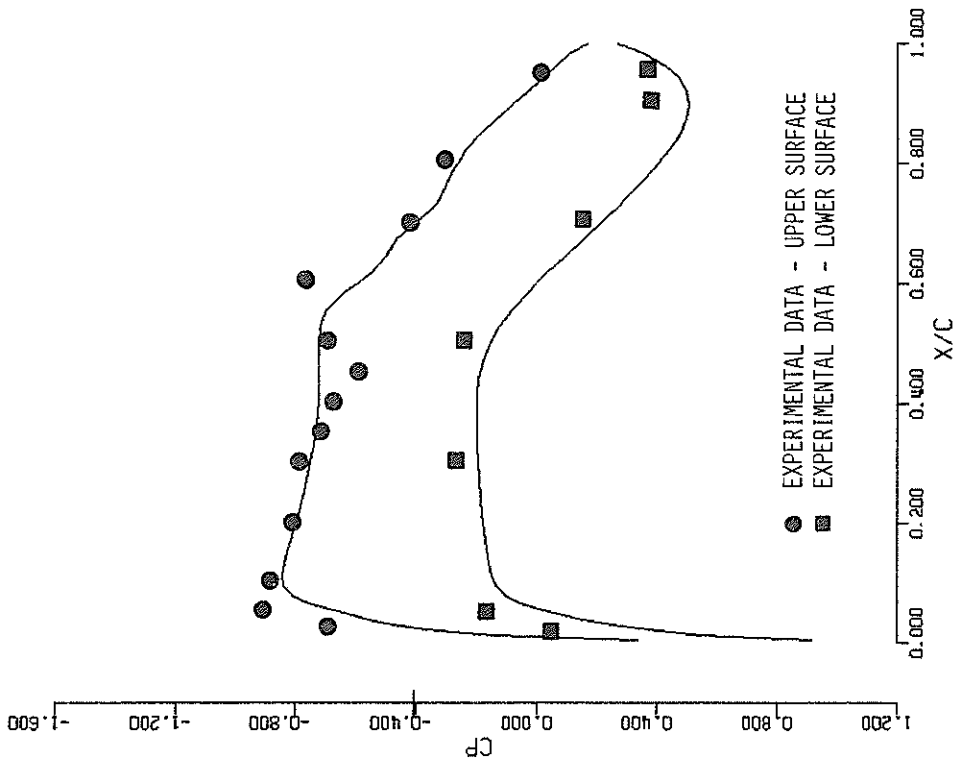


FIGURE 40e. TRANSONIC TRANSPORT  
 $M = 0.810$   $ALF = 2.000$   $CONV = .330E-04$   
 $LOCAL CL = 0.588$   $LOCAL CM = -1.201$   $LOCAL CD = 0.0012$   
 SPAN STATION 15  $Y/S = 0.509$  44 MESH PTS ON CHD

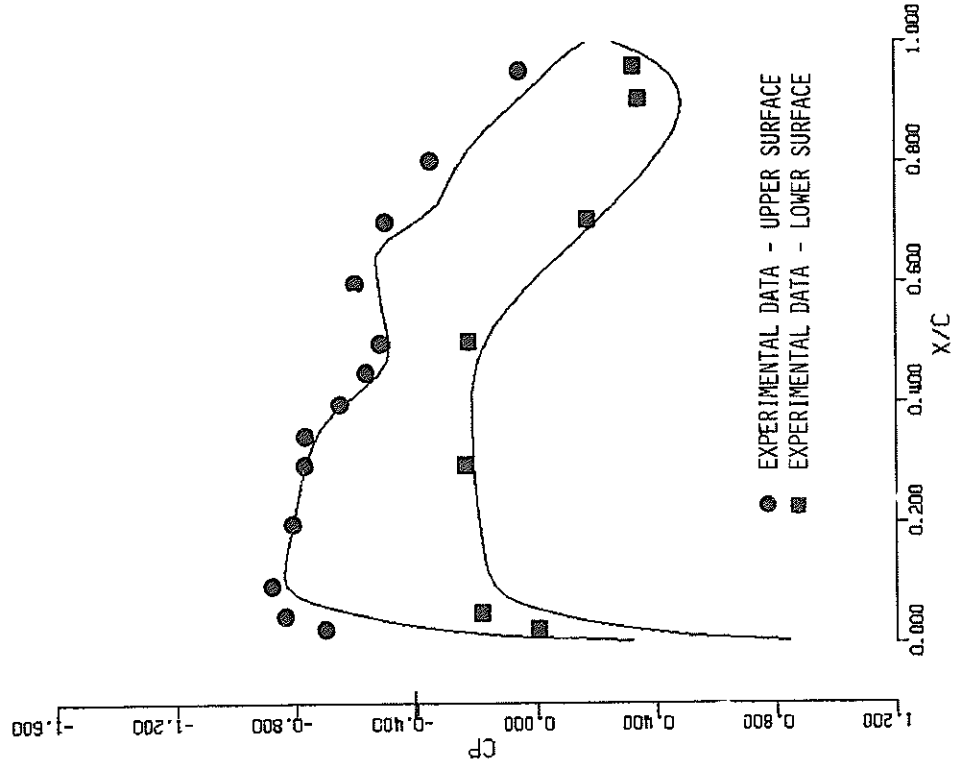
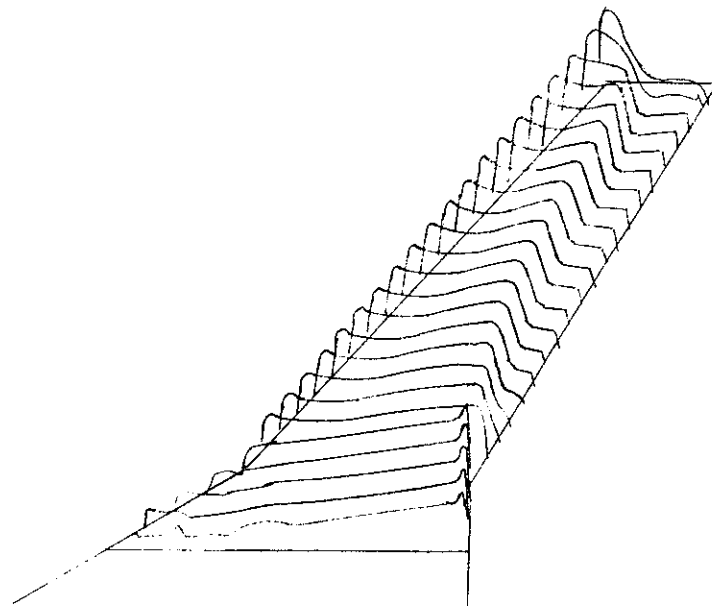
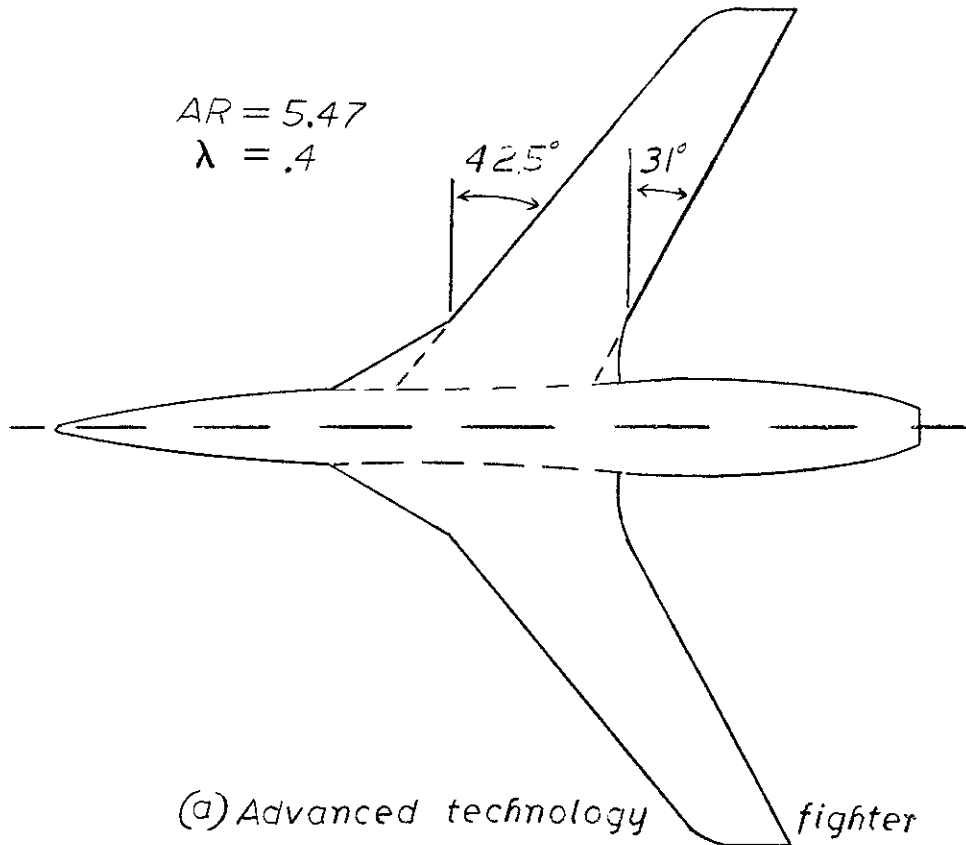


FIGURE 40f. TRANSONIC TRANSPORT  
 $M = 0.810$   $ALF = 2.000$   $CONV = .330E-04$   
 $LOCAL CL = 0.532$   $LOCAL CM = -1.589$   $LOCAL CD = -.0072$   
 SPAN STATION 21  $Y/S = 0.727$  44 MESH PTS ON CHD



(b) Upper surface pressure distribution  
FIG. 41. Advanced fighter

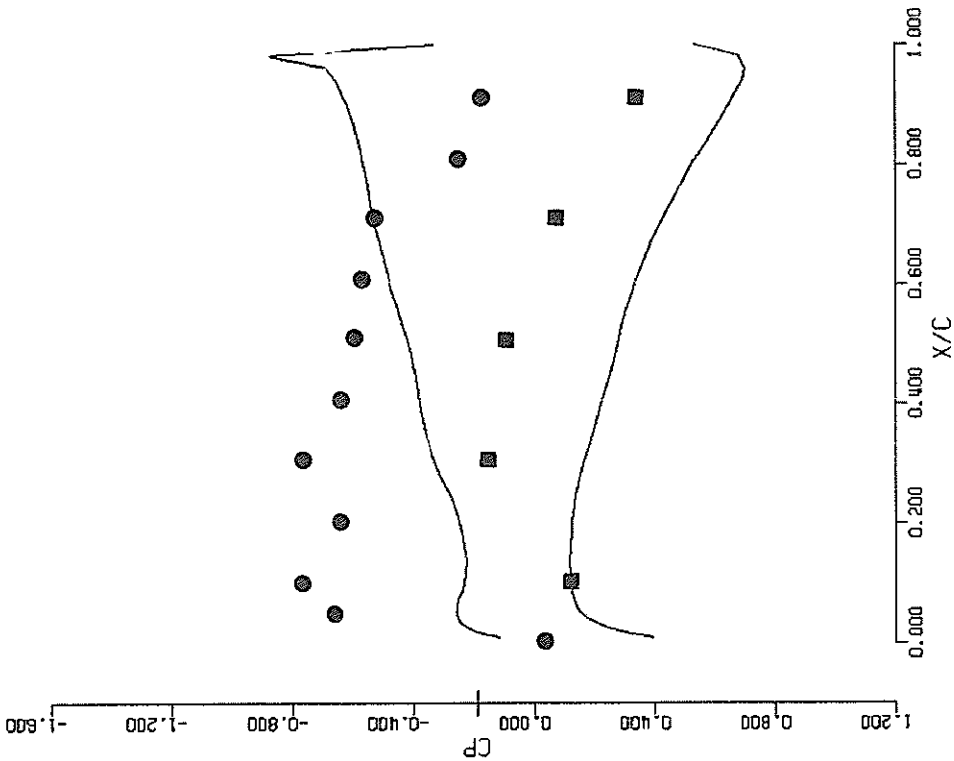


Figure 41c, ADVANCED FIGHTER  
 M = 0.900 ALF = 7.050 CONV = .886E-01  
 LOCAL CL = 0.753 LOCAL CM = 0.954 LOCAL CD = 0.1100  
 SPAN STATION 6 Y/S = 0.182 44 MESH PTS ON CHD

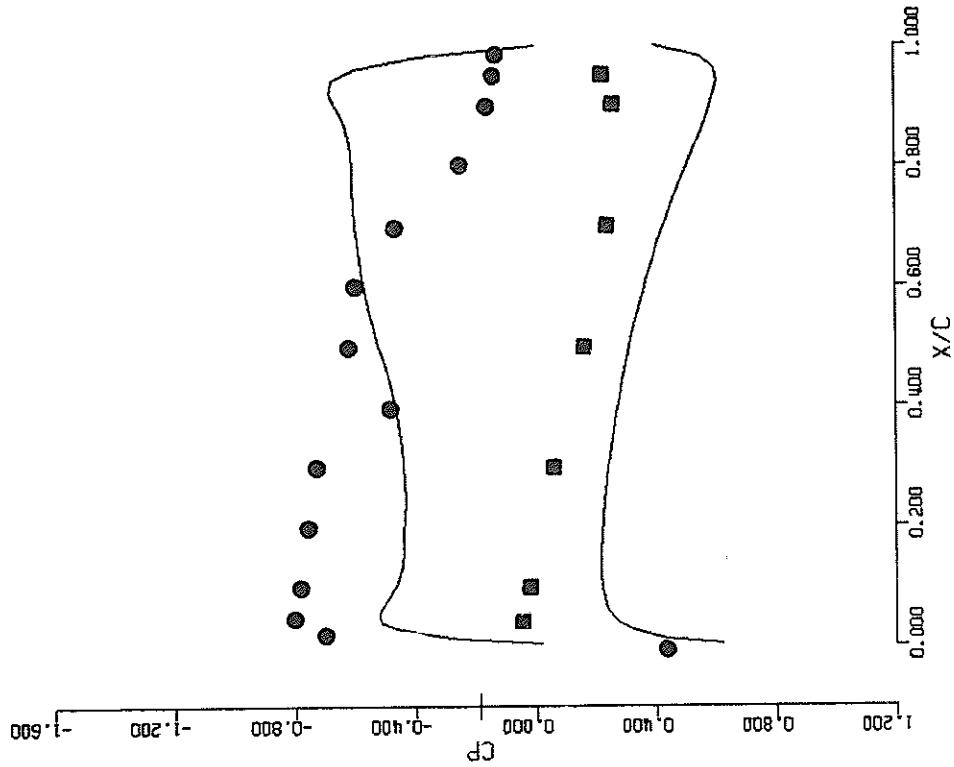


Figure 41d, ADVANCED FIGHTER  
 M = 0.900 ALF = 7.050 CONV = .886E-01  
 LOCAL CL = 0.874 LOCAL CM = 1.325 LOCAL CD = 0.0884  
 SPAN STATION 9 Y/S = 0.291 44 MESH PTS ON CHD

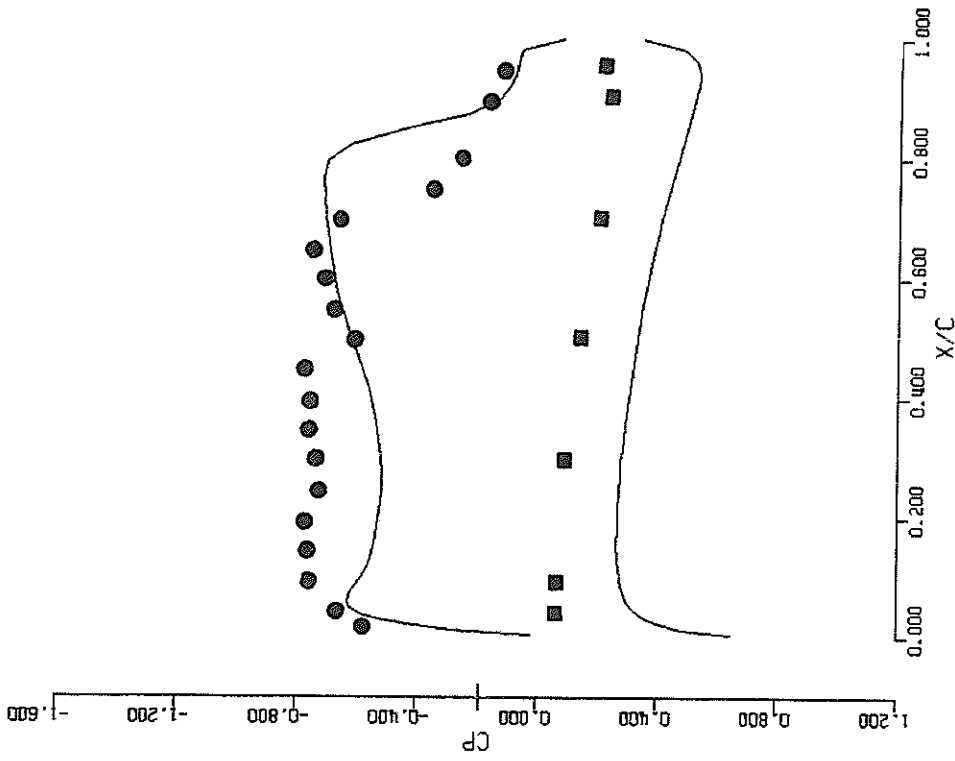


FIGURE 4Ie, ADVANCED FIGHTER  
 M = 0.900 ALF = 7.050 CONV = .886E-01  
 LOCAL CL = 0.890 LOCAL CM = 1.306 LOCAL CD = 0.0585  
 SPAN STATION 13 Y/S = 0.436 44 MESH PTS ON CHD

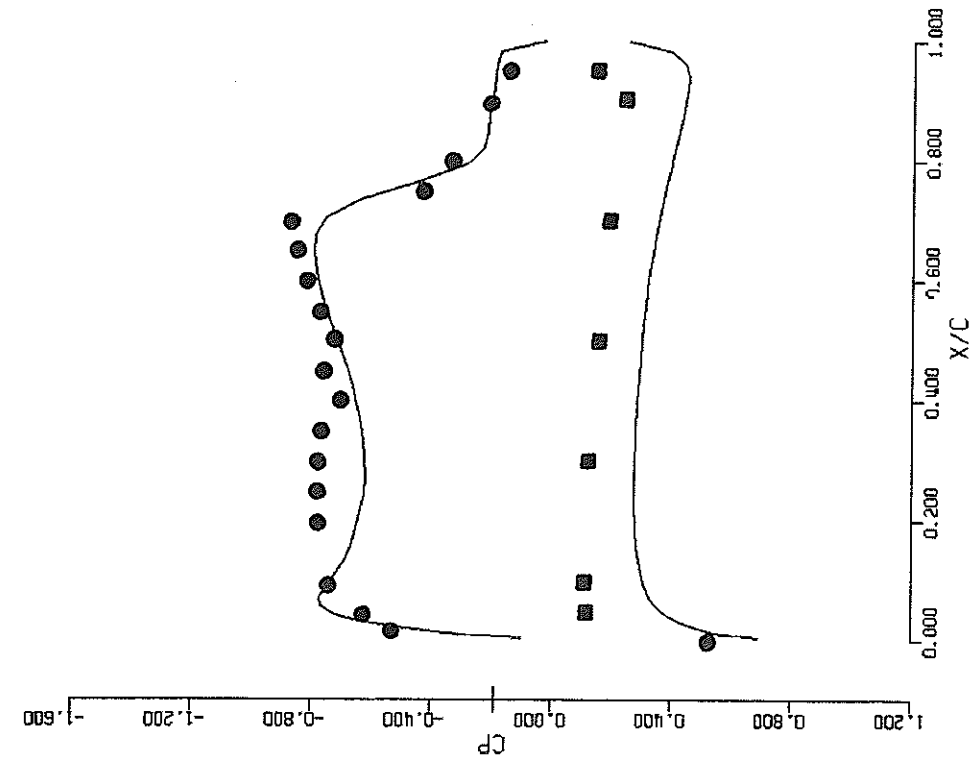


FIGURE 4If, ADVANCED FIGHTER  
 M = 0.900 ALF = 7.050 CONV = .886E-01  
 LOCAL CL = 0.911 LOCAL CM = 1.218 LOCAL CD = 0.0357  
 SPAN STATION 18 Y/S = 0.618 44 MESH PTS ON CHD

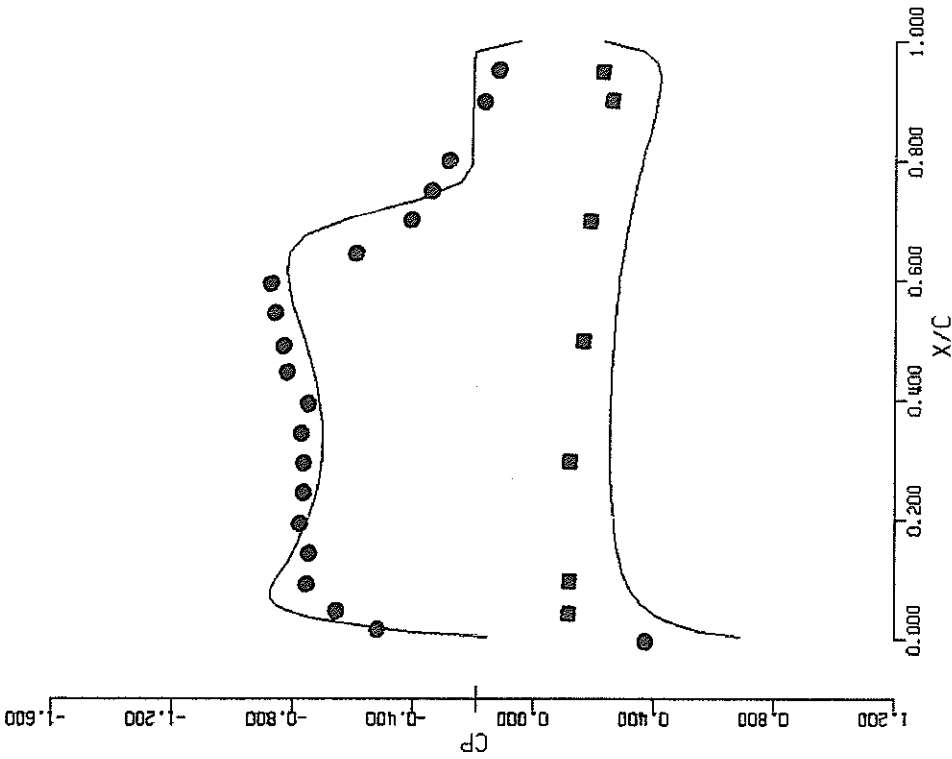


Figure 416. ADVANCED FIGHTER

M = 0.900 ALF = 7.050 CONV = .886E-01  
 LOCAL CL = 0.910 LOCAL CM = 1.075 LOCAL CD = 0.0206  
 SPAN STATION 22 Y/S = 0.764 44 MESH PTS ON CHD

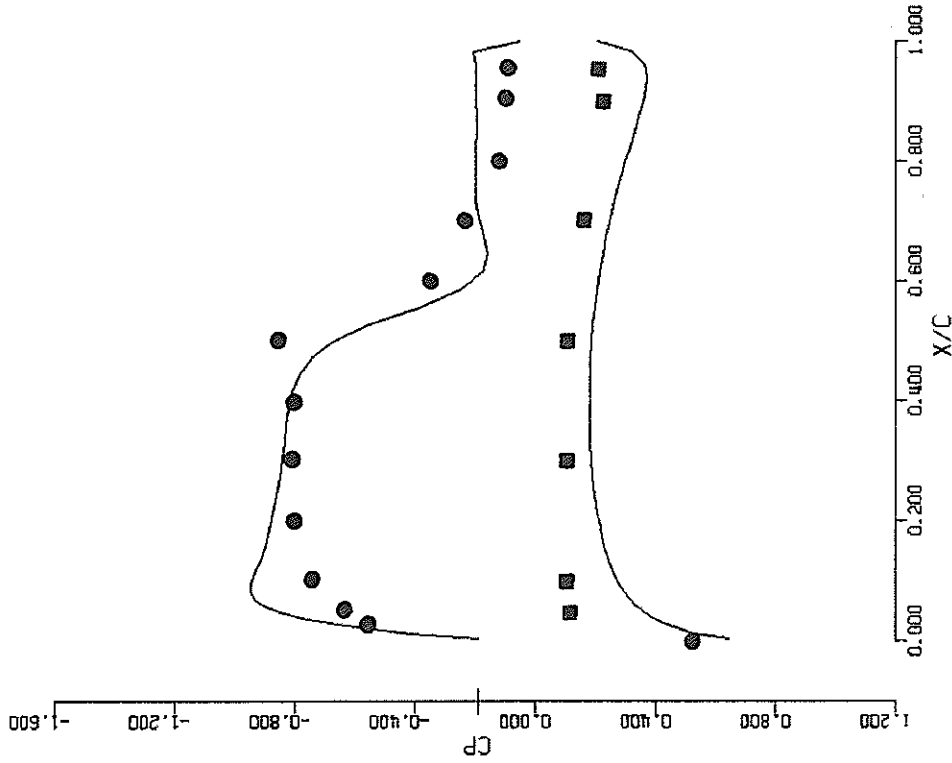


Figure 414. ADVANCED FIGHTER

M = 0.900 ALF = 7.050 CONV = .886E-01  
 LOCAL CL = 0.782 LOCAL CM = 0.766 LOCAL CD = -.0012  
 SPAN STATION 26 Y/S = 0.909 44 MESH PTS ON CHD

#### 4. DETAILED DATA COMPARISONS - TACT AND F-8

##### a. TACT

The Transonic Aircraft Technology (TACT) program provides an extensive set of wind tunnel and flight data on a modern supercritical wing design with which the computer code can be compared. The TACT program is described in Reference 62. The general aircraft layout is shown in Figure 42. For the transonic flight conditions of interest, the wing sweep was  $26^{\circ}$ . A typical TACT airfoil section is shown in Figure 43, which was taken from Reference 63. The glove sections were assumed to be the same as the extrapolated wing sections for the calculations presented here. The characteristic wing twist (which is contained in the ordinate definition) is shown in Figure 44. Figure 45 shows the aeroelastic twist increment for  $M = .91$  (Reference 64). A similar increment was applied to the  $M = .86$  case. The pressure orifice locations at which pressure data from Reference 65 and 66 is available are shown in Figure 46. The calculations were carried out for this case using the MSD Theory equation, with six viscous-inviscid iterations required to obtain a converged solution. The Reynolds number based on mean aerodynamic chord was 25.3 million, which corresponded to the flight test condition. The case was run at a second angle-of-attack to demonstrate the sensitivity of the calculation to angle-of-attack change. For this configuration, NCR differencing was employed due to the FCR prediction of the shock exactly at the trailing edge, which made the initiation of the viscous interaction difficult due to the absence of an adverse pressure gradient at the trailing edge.

The effect of the aeroelastic twist increments on the calculated pressure distributions can be seen in Figure 47. The dashed line in these curves represents the calculated pressure distributions over the wing with only the built-in twist modeled. The solid lines represent the calculated pressure distributions with the inclusion of the aeroelastic twist increments in flight article. Figures 47a through 47b show the effect, at a Mach number of 0.9 and an angle-of-attack of  $5.2^{\circ}$ . Figures 47e through 47h show the effect at a Mach number of 0.85 and an angle-of-attack of  $7^{\circ}$ . The effect is significant and, as would be expected from the aeroelastic twist increments shown in Figure 45, the effect

increases at the outboard span stations.

Figure 48 shows the comparison of predictions and measurements at Mach 0.91. The solid lines represent the calculations at an angle-of-attack of  $5.2^\circ$  and the dashed lines represent an angle-of-attack of  $6.2^\circ$ . The measurements were made at an angle-of-attack of  $6.2^\circ$ . The first span station shown (Figure 48a) is at  $\eta = 0.400$ . As can be seen, the leading edge pressures are generally underpredicted. In the mid-chord region, the lower surface is better represented by  $\alpha = 5.2^\circ$ . An increase in computational Mach number would probably give better correlation over the leading edge. Figure 48b shows the correlation at  $\eta_{\text{exp}} = 0.570$ ,  $\eta_{\text{pre}} = 0.618$ . Again, the upper surface shows better correlation at  $\alpha = 6.2^\circ$ , except at the trailing edge. The lower surface is not well predicted at either angle-of-attack, probably due to the fact that the glove and, in particular, the flowfield around the engine intakes is not modeled. The effect of the flowfield about the engine intakes can be expected to have a large effect on the lower surface pressure distribution. Figure 48c ( $\eta_{\text{pre}} = 0.764$ ,  $\eta_{\text{exp}} = 0.756$ ) again shows better correlation on the upper surface at  $\alpha = 6.2^\circ$ . The lower surface shows better correlation at  $\alpha = 5.2^\circ$ . At  $\eta_{\text{pre}} = 0.909$  ( $\eta_{\text{exp}} = 0.921$ ), the same trends hold (Figure 48d). Over the entire span, the upper surface generally shows better correlation when the computational angle-of-attack agrees with the experimental angle-of-attack, in contrast to previous efforts, which indicated that the lower angle-of-attack should be used.

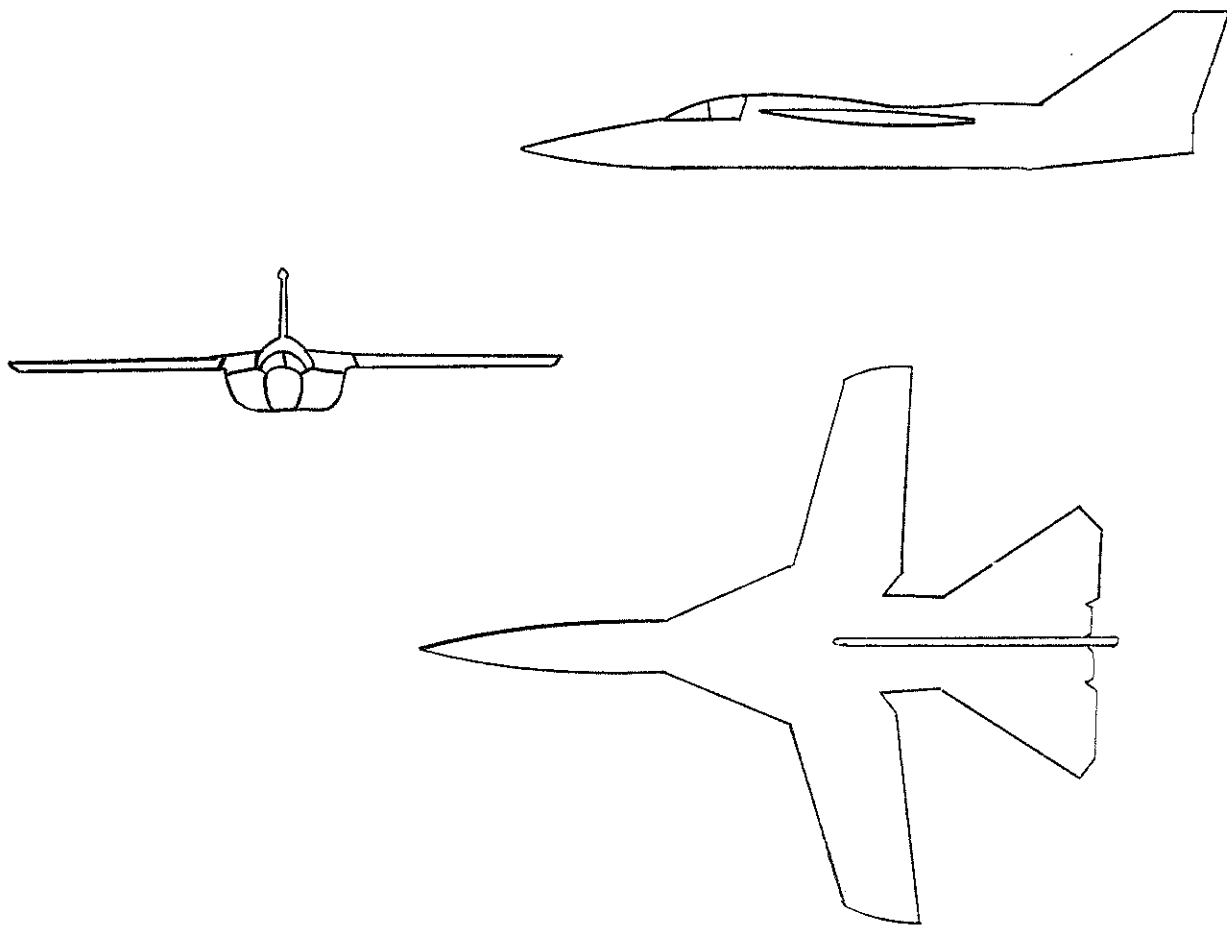
The correlations at Mach 0.86 are significantly better than those at Mach 0.91. The solid line represents calculations at an angle-of-attack of  $7^\circ$  and the dashed lines represent an angle of attack of  $8^\circ$ . The measurements were made at an angle of attack of  $8^\circ$  for the flight tests and  $7.31^\circ$  for the wind tunnel tests. The upper surface at  $\eta_{\text{pre}} = 0.400$  (Figure 49a) shows considerable scatter between the wind tunnel and flight test results. The predictions again show better agreement at the actual angle of attack on the upper surface. The correlation here is much better with flight test data than with wind tunnel data. The lower surface correlation is again rather disappointing, for the same reasons noted above. Figure 49b again shows the same trends, and in fact, these trends are duplicated over the rest of the span. Figure 49c ( $\eta_{\text{pre}} = 0.764$ ,  $\eta_{\text{exp}} = 0.756$ ) shows excellent agreement as to the location and strength of the mid-chord shock at  $\alpha = 8^\circ$ . At  $\alpha = 7^\circ$ , the shock is predicted too far forward. At this span

station, correlation is better with wind tunnel measurements than with flight test data. Figure 49d also shows better correlation with wind tunnel measurements.

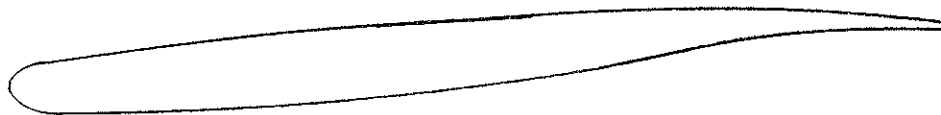
It is apparent that upper surface agreement is better when the computational angle of attack is the same as the experimental angle of attack. The inboard upper surface would show better correlation with experiment if the glove was modeled explicitly. The lower surface agreement may be dominated by the effects of the engine intakes. The correlation would be greatly improved if the flow field around the intakes was modeled by modifying the body slopes to include the effect of this flow field. In the absence of such modeling, the lower surface correlation seems to be improved by decreasing the computational angle of attack.

Figure 50a shows the TACT outer panel locating the separation regions occurring on the panel. On the upper surface, as shown, there is a shock induced separation region near the trailing edge. This region covers most of the mid-span region. On the lower surface, there is a large separation region occurring in the cove. The extent of this region generally decreases on the outboard sections of the span. Figure 50b shows the three main regions requiring special treatment on a super critical section such as is present on TACT. The effect of adding a boundary layer on the solution, can be seen in Figure 50c.





*FIG. 42 Three view drawing of TACT aircraft*



*FIG. 43 TACT wing section*

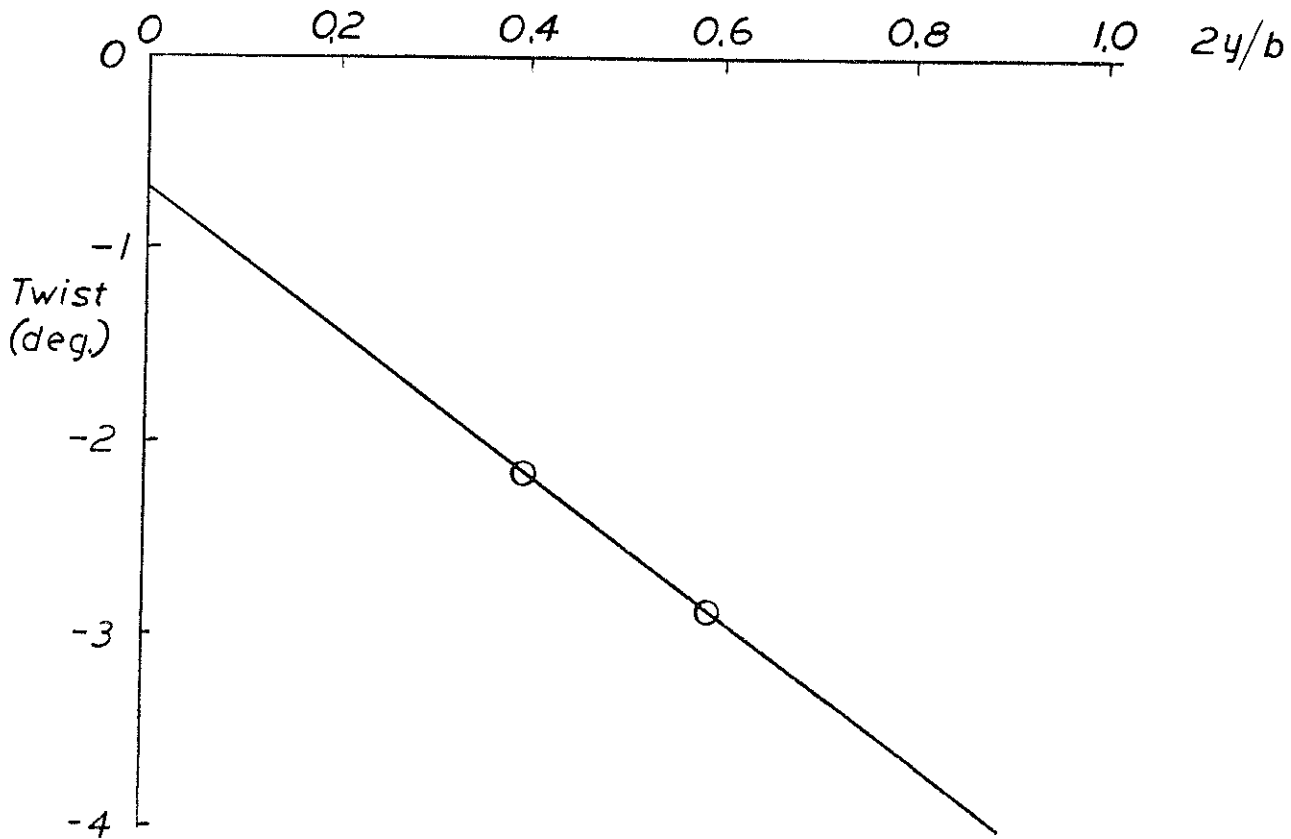


FIG. 44 TACT wing twist

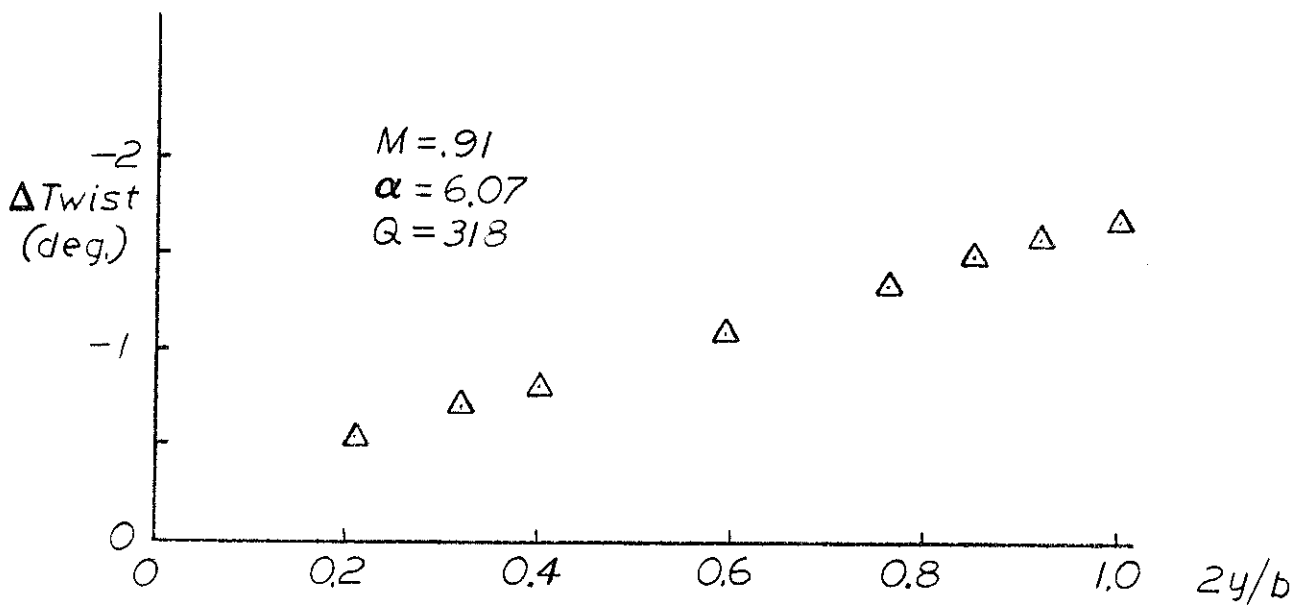


FIG. 45 Wing twist increments

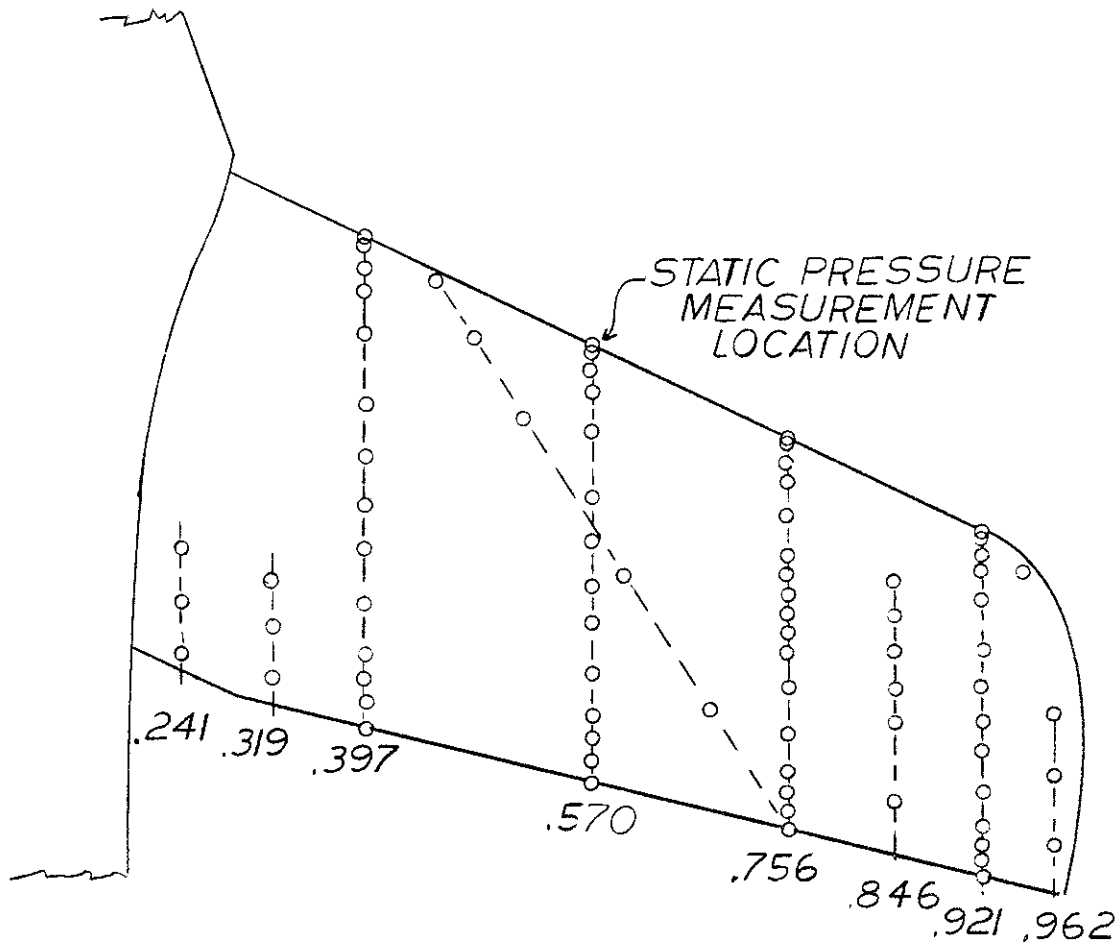


FIG. 46 TACT wing pressure orifices

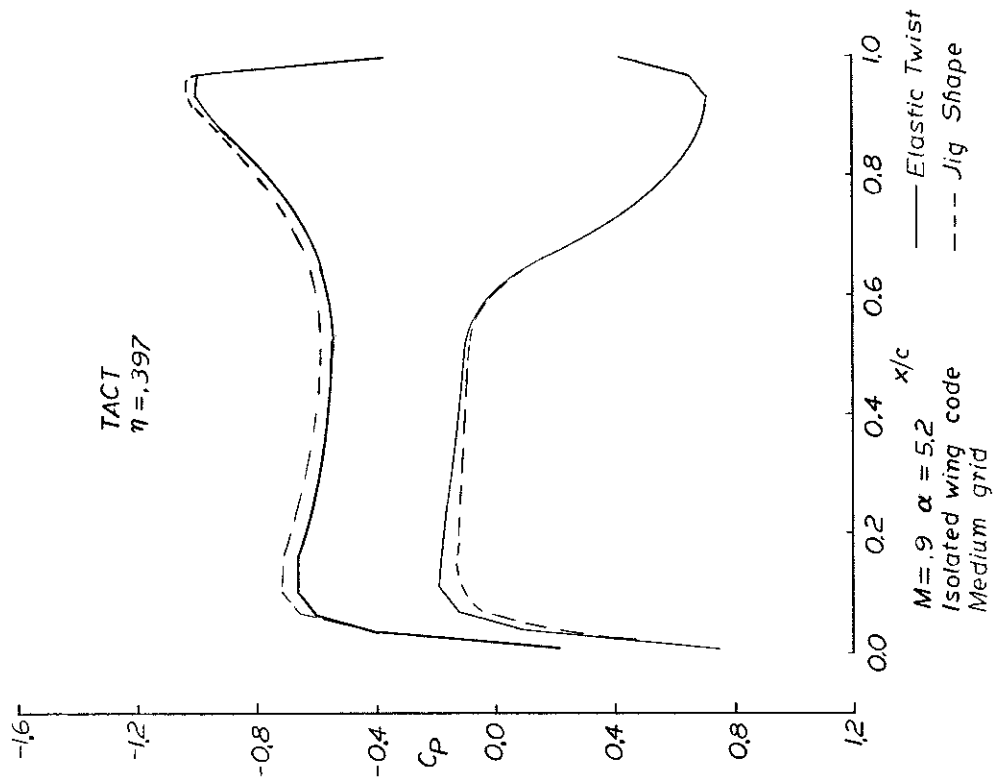


FIG. 47a Aeroelastic effects

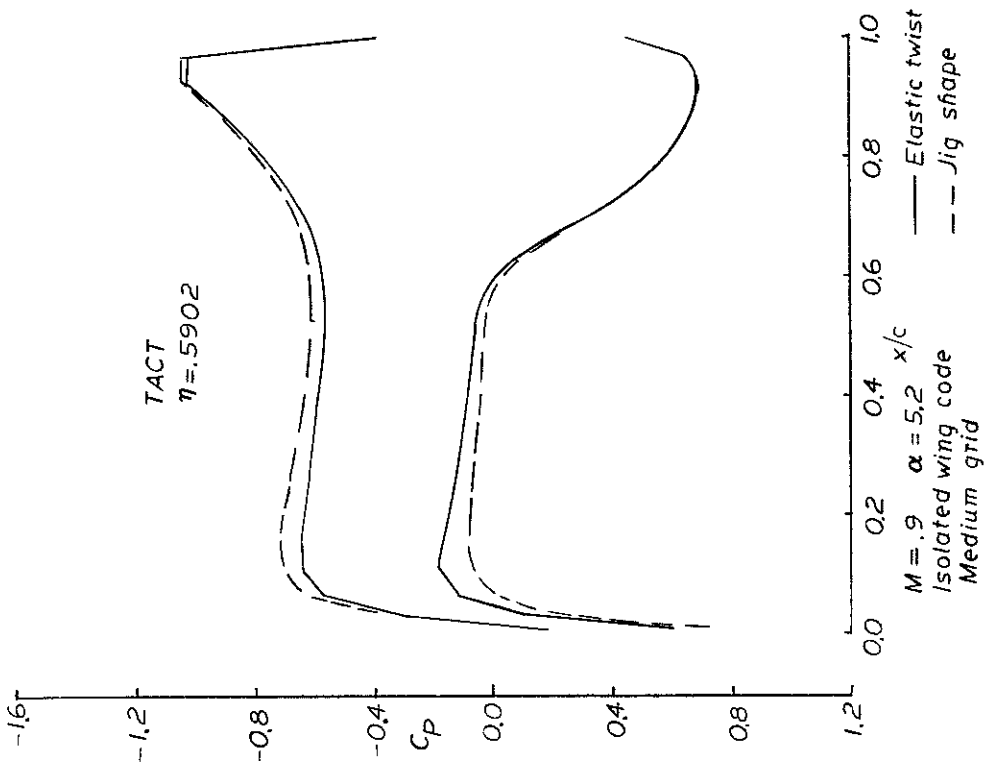


FIG. 47b Aeroelastic effects

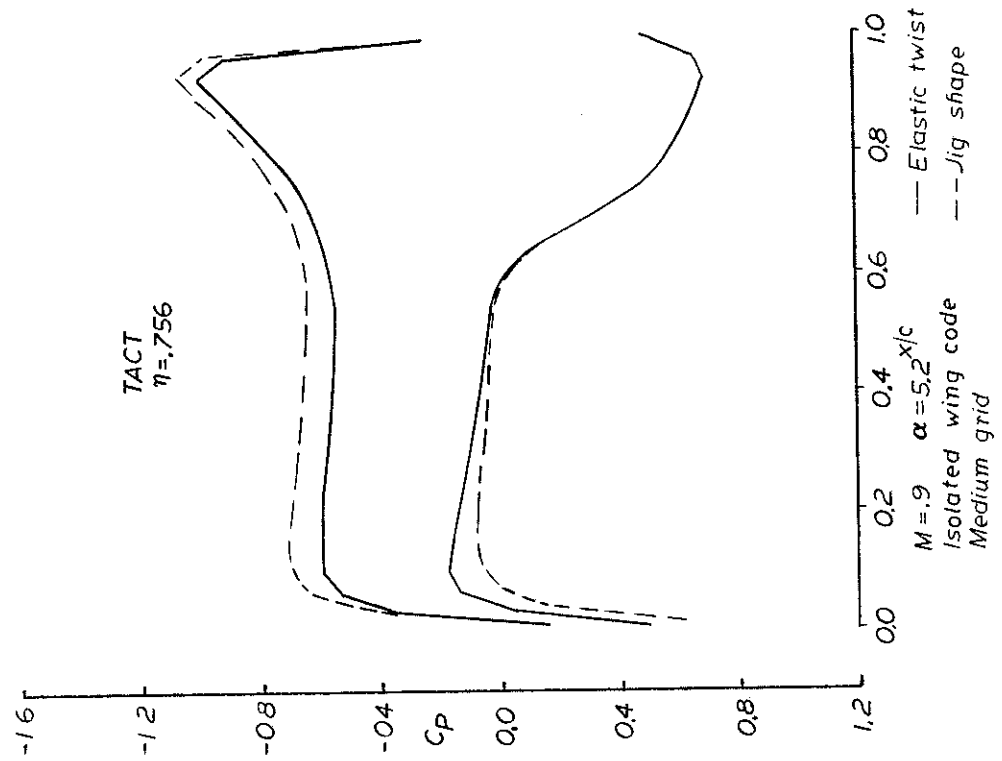


FIG. 47c Aeroelastic twist

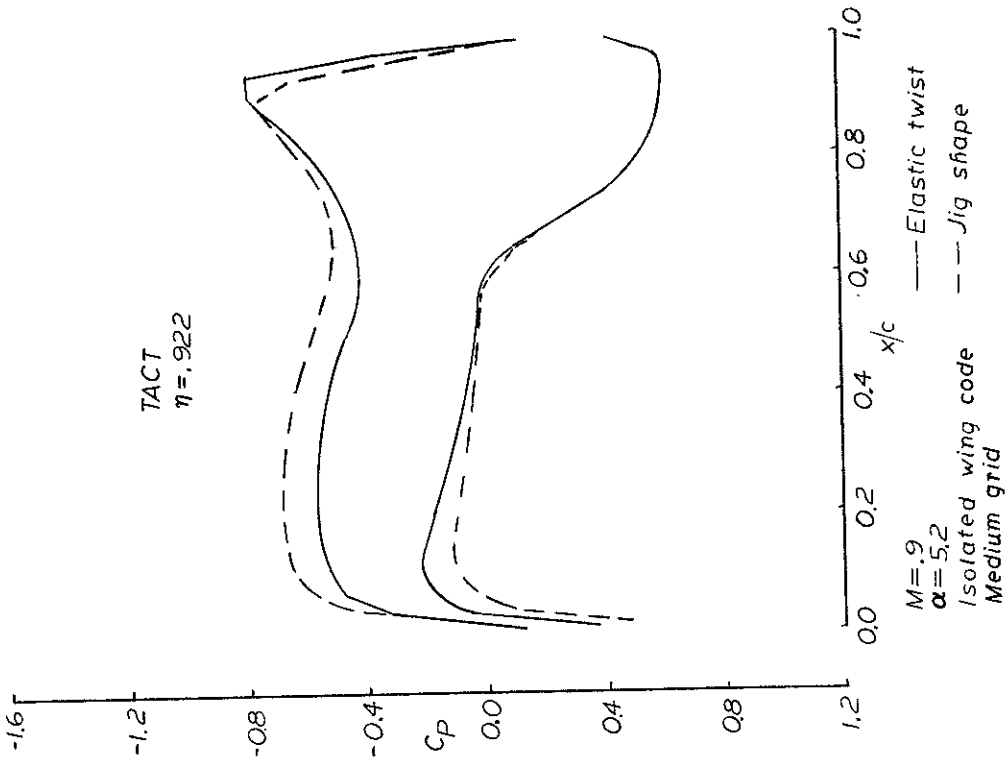


FIG. 47d Aeroelastic effects

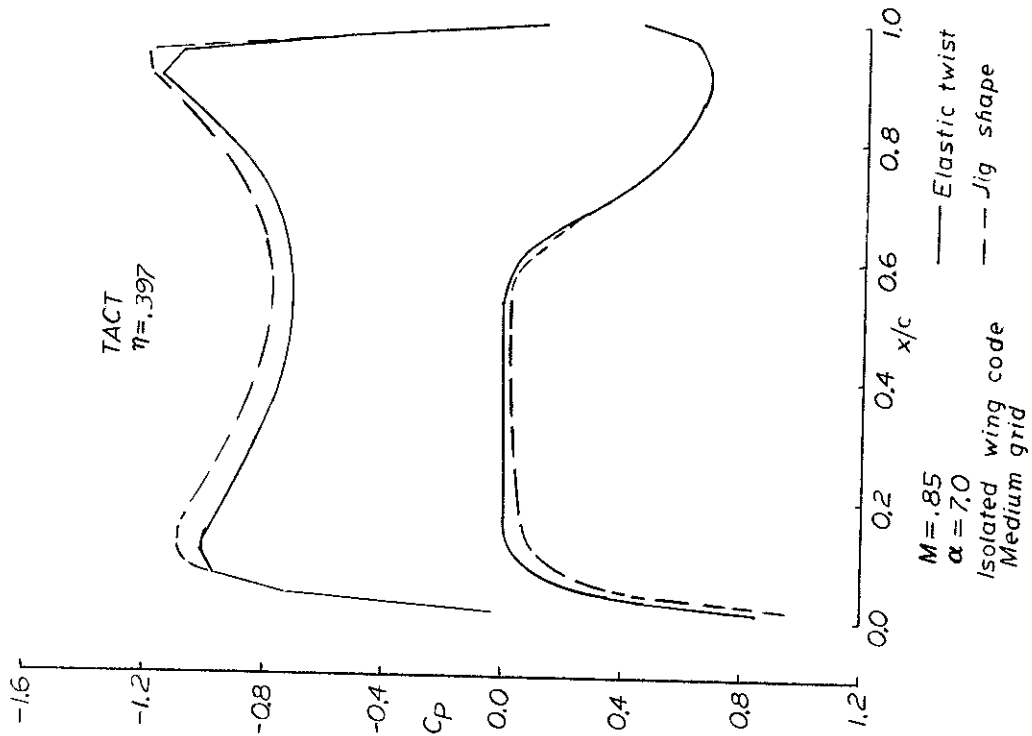


FIG. 47e Aeroelastic effects

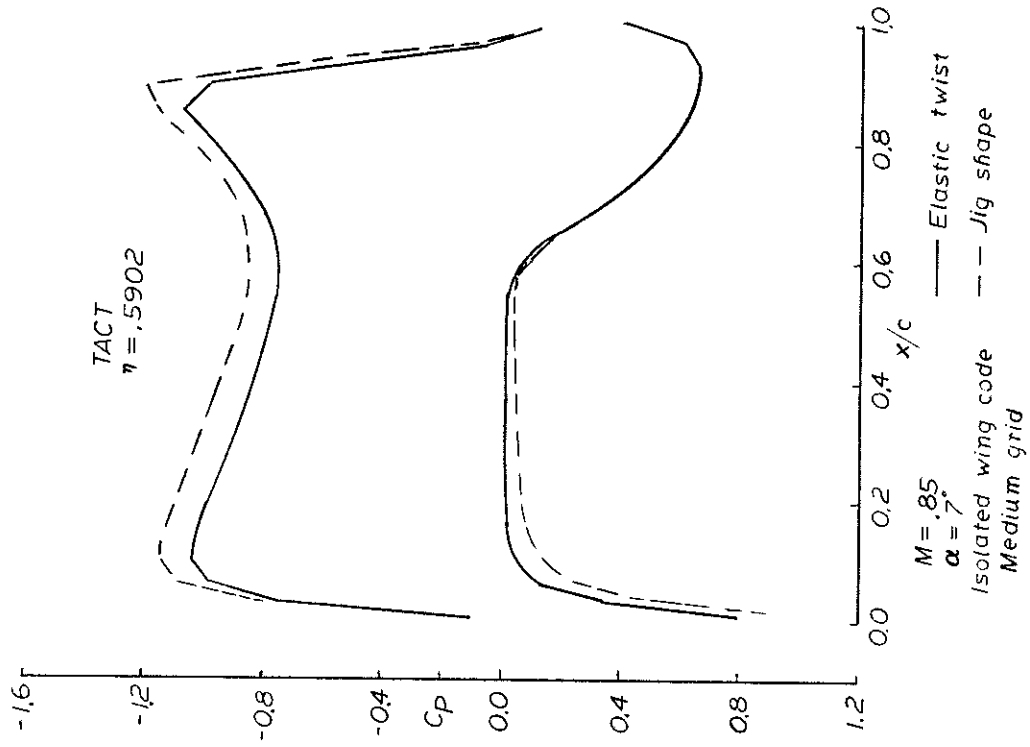


FIG. 47f Aeroelastic effects

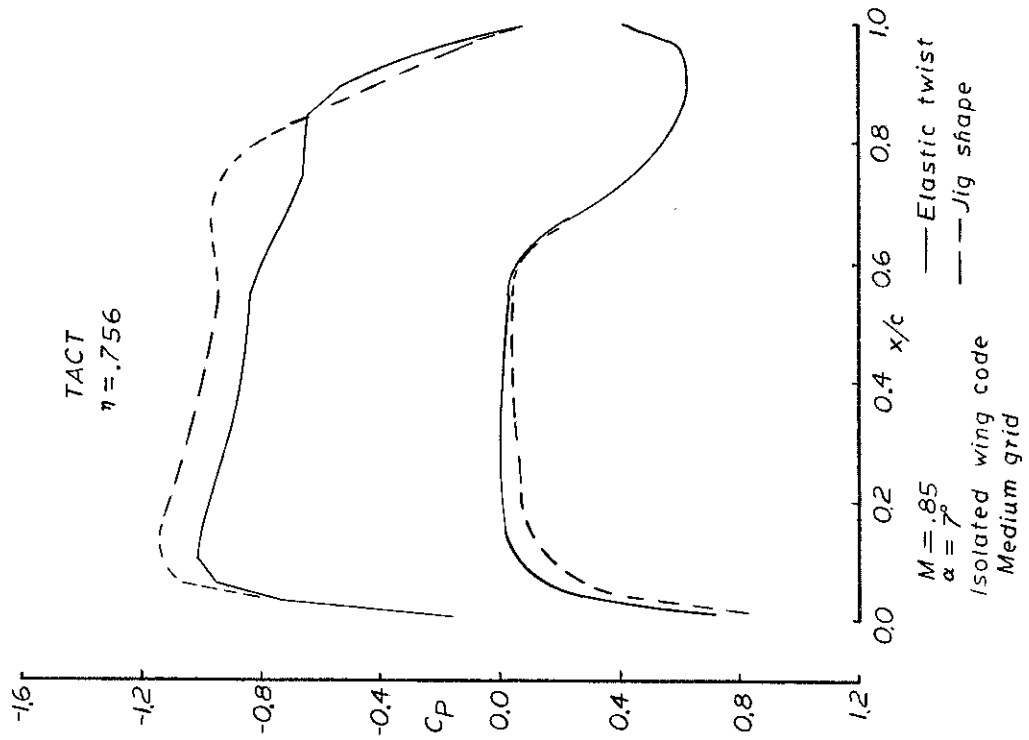


FIG. 47g Aeroelastic effects

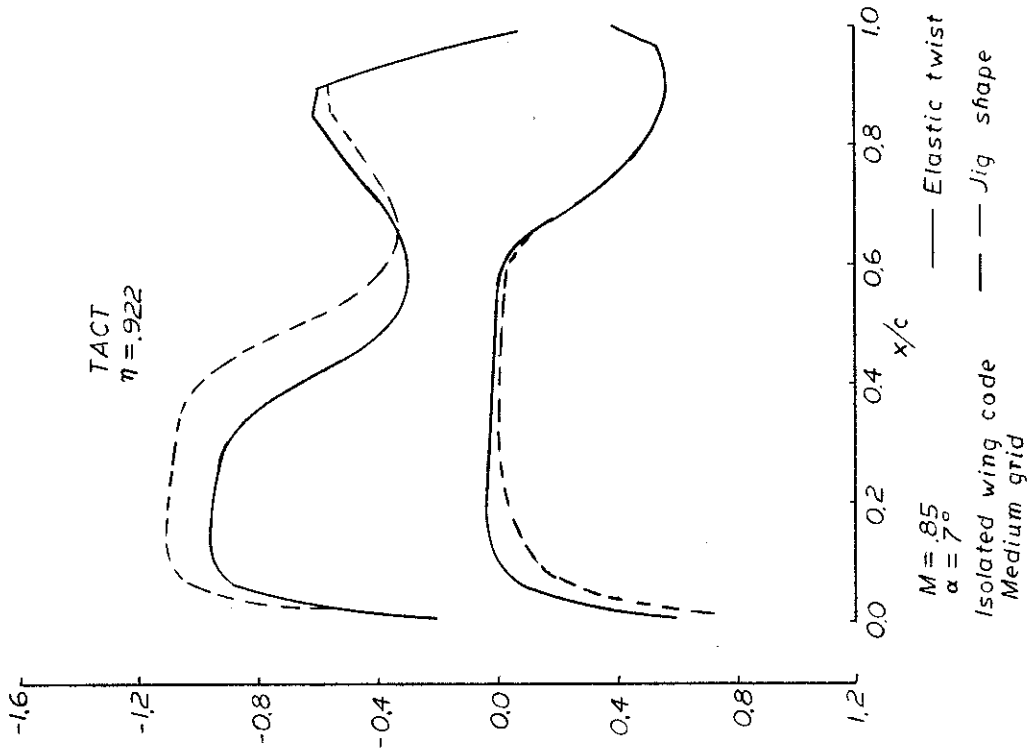
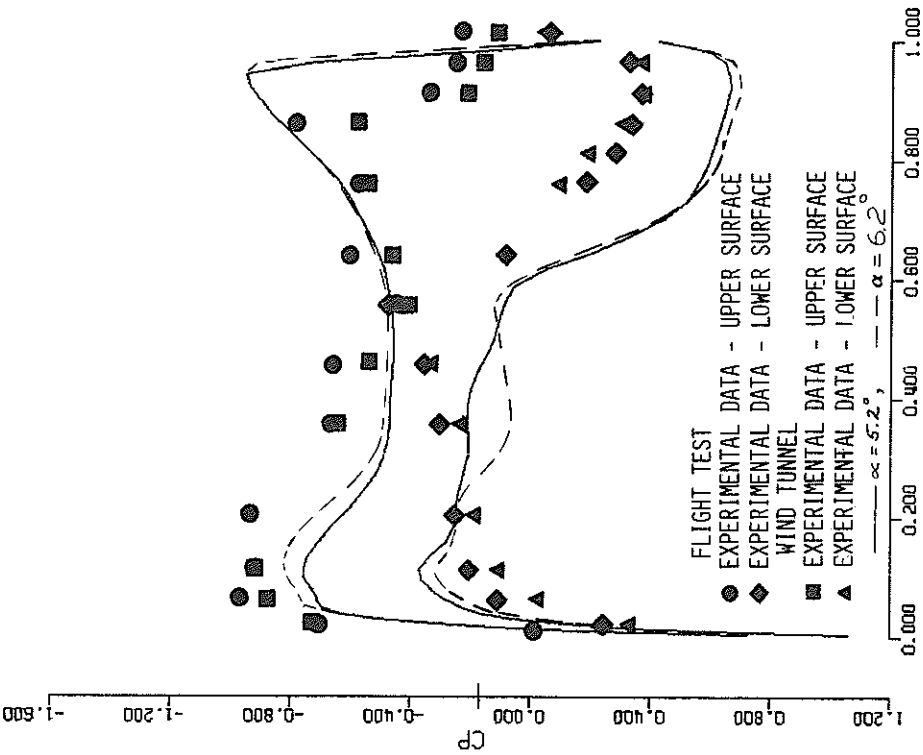
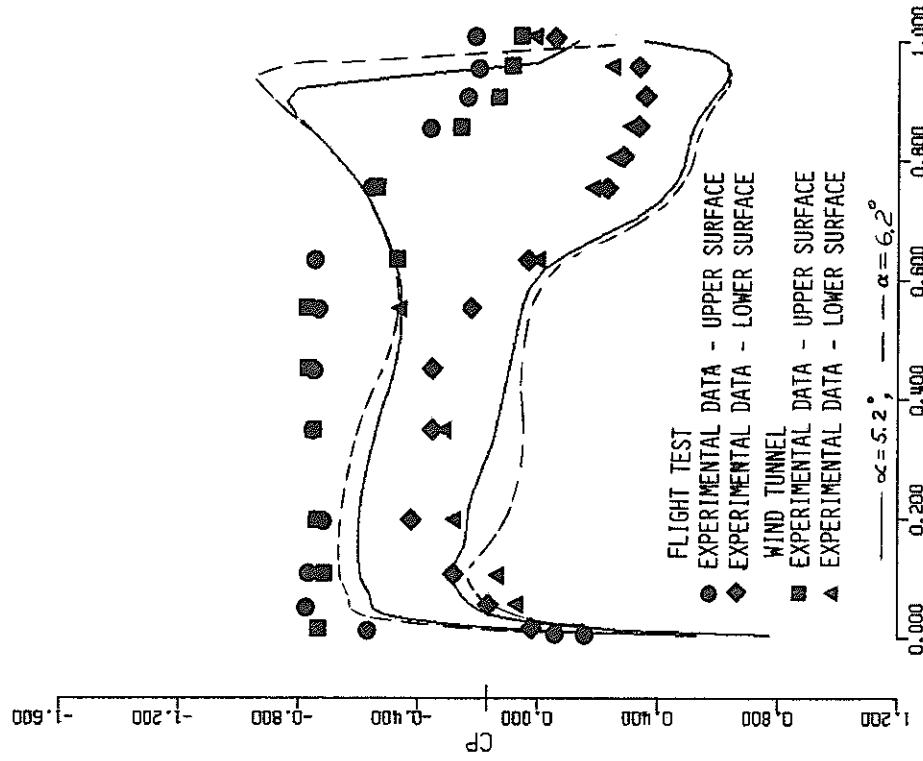


FIG. 47h Aeroelastic effects



**FIG 48a.**  
 TACT WITH AEROELASTIC TWIST  
 M = 0.910 ALF = 5.200 CONV = .0  
 LOCAL CL = 0.669 LOCAL CM = -2.749 LOCAL CD = 0.0436  
 SPAN STATION 12 Y/S = 0.400 44 MESH PTS ON CHD



**FIG 48b.**  
 TACT WITH AEROELASTIC TWIST  
 M = 0.910 ALF = 5.200 CONV = .0  
 LOCAL CL = 0.606 LOCAL CM = -2.934 LOCAL CD = 0.0152  
 SPAN STATION 18 Y/S = 0.618 44 MESH PTS ON CHD



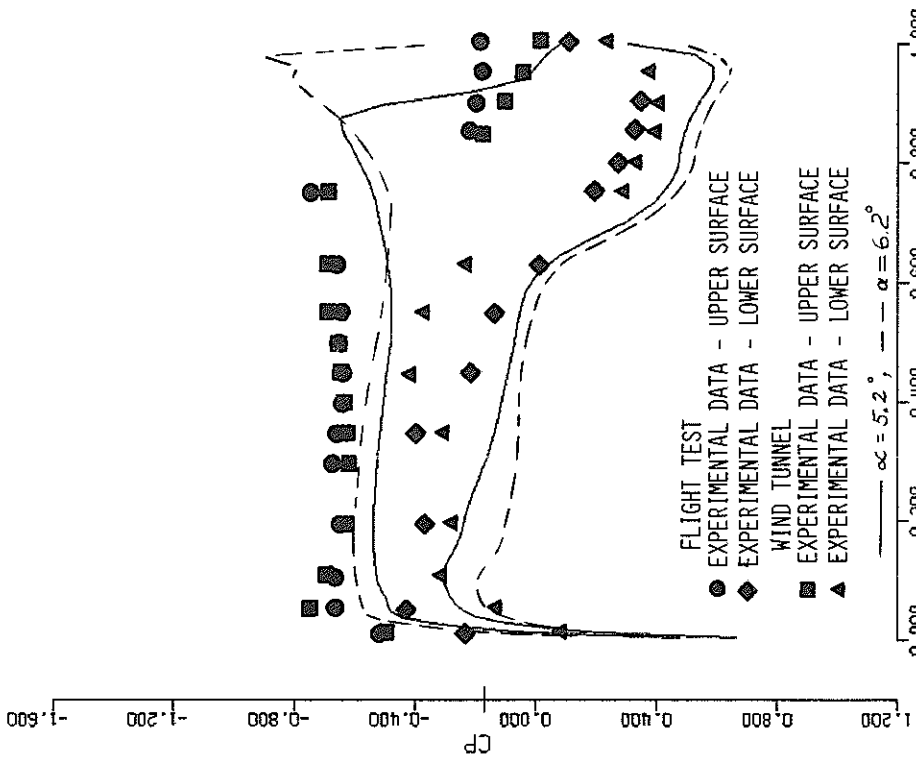


FIG. 48c.  
 TACT WITH AEROELASTIC TWIST  
 M = 0.910 ALF = 5.200 CONV = .0  
 LOCAL CL = 0.536 LOCAL CM = -2.931 LOCAL CD = -.0013  
 SPAN STATION 22 Y/S = 0.764 44 MESH PTS ON CHD

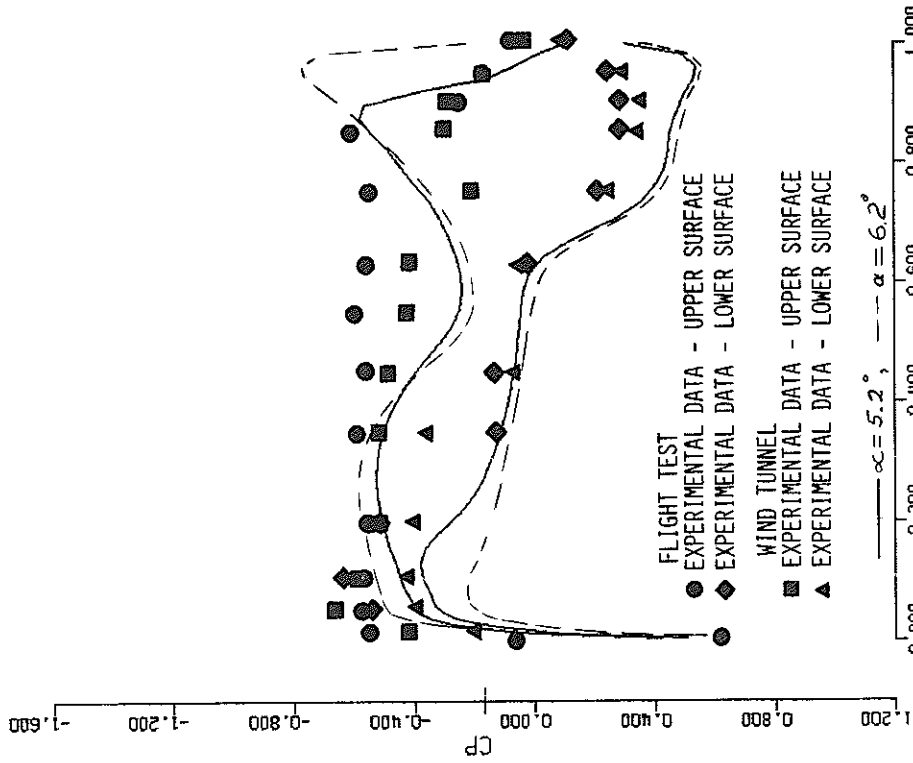
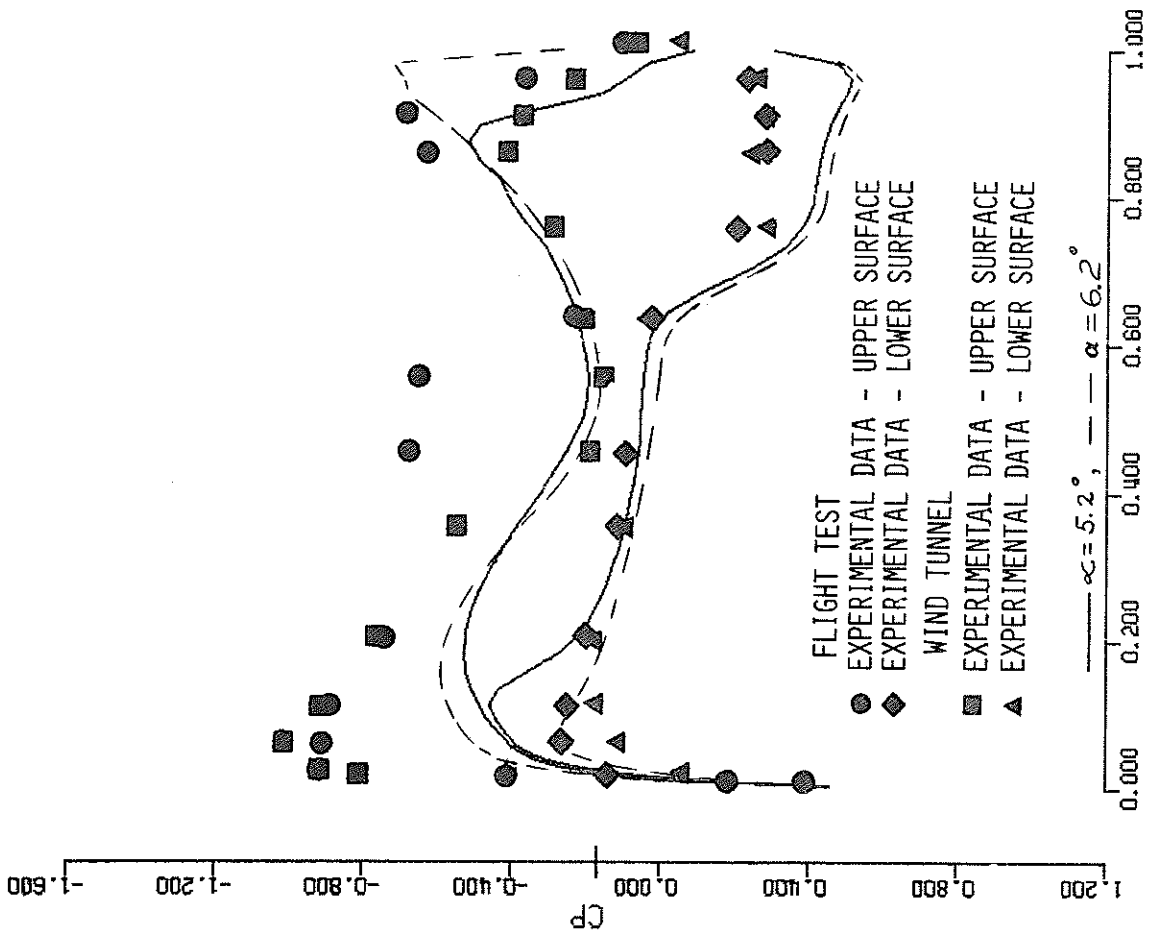


FIG. 48d.  
 TACT WITH AEROELASTIC TWIST  
 M = 0.910 ALF = 5.200 CONV = .0  
 LOCAL CL = 0.423 LOCAL CM = -2.654 LOCAL CD = -.0094  
 SPAN STATION 26 Y/S = 0.909 44 MESH PTS ON CHD



**FIG. 48e.**  
 TACT WITH AEROELASTIC TWIST  
 $M = 0.910$   $ALF = 5.200$   $CONV = .0$   
 $LOCAL CL = 0.370$   $LOCAL CM = -2.410$   $LOCAL CD = .0111$   
 $SPAN STATION 27$   $Y/S = 0.945$  44 MESH PTS ON CHD

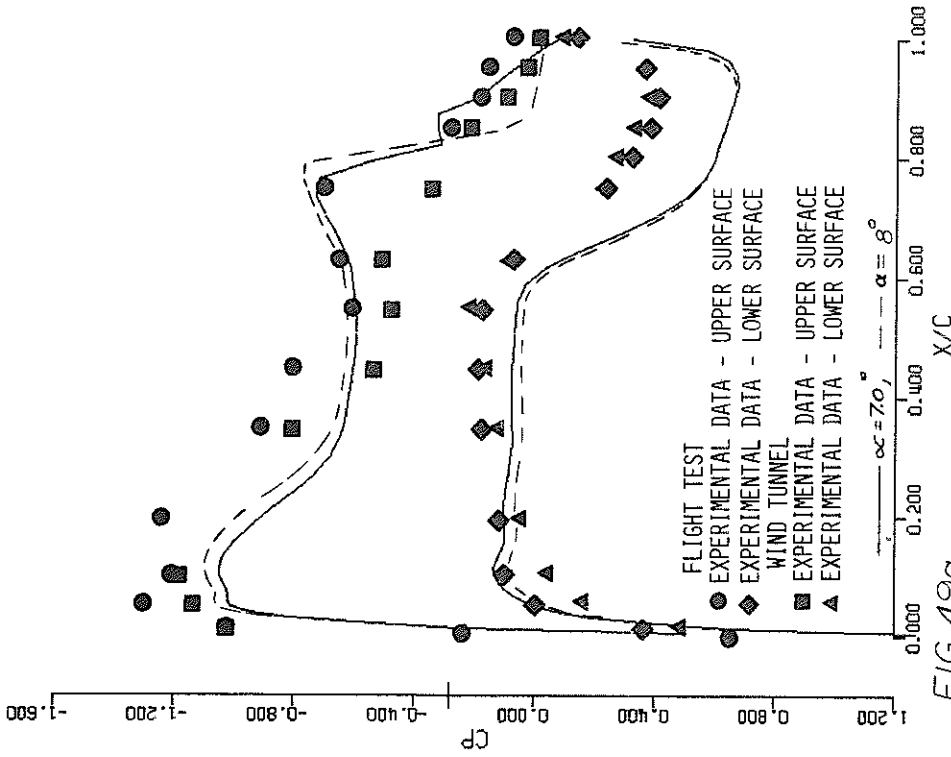


FIG. 49a.  
TACT

M = 0.860 ALF = 7.000 CONV = .299E+29  
 LOCAL CL = 0.785 LOCAL CM = -3.101 LOCAL CD = 0.0429  
 SPAN STATION 12 Y/S = 0.400 44 MESH PTS ON CHO

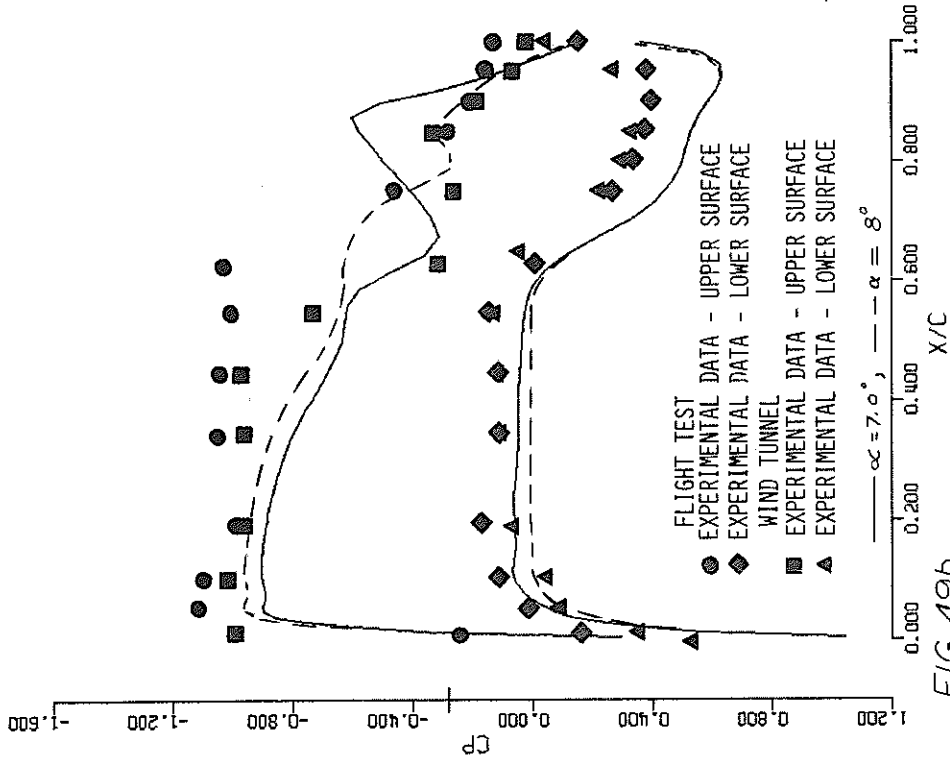


FIG. 49b.  
TACT

M = 0.860 ALF = 7.000 CONV = .299E+29  
 LOCAL CL = 0.768 LOCAL CM = -3.503 LOCAL CD = 0.0294  
 SPAN STATION 17 Y/S = 0.582 44 MESH PTS ON CHO

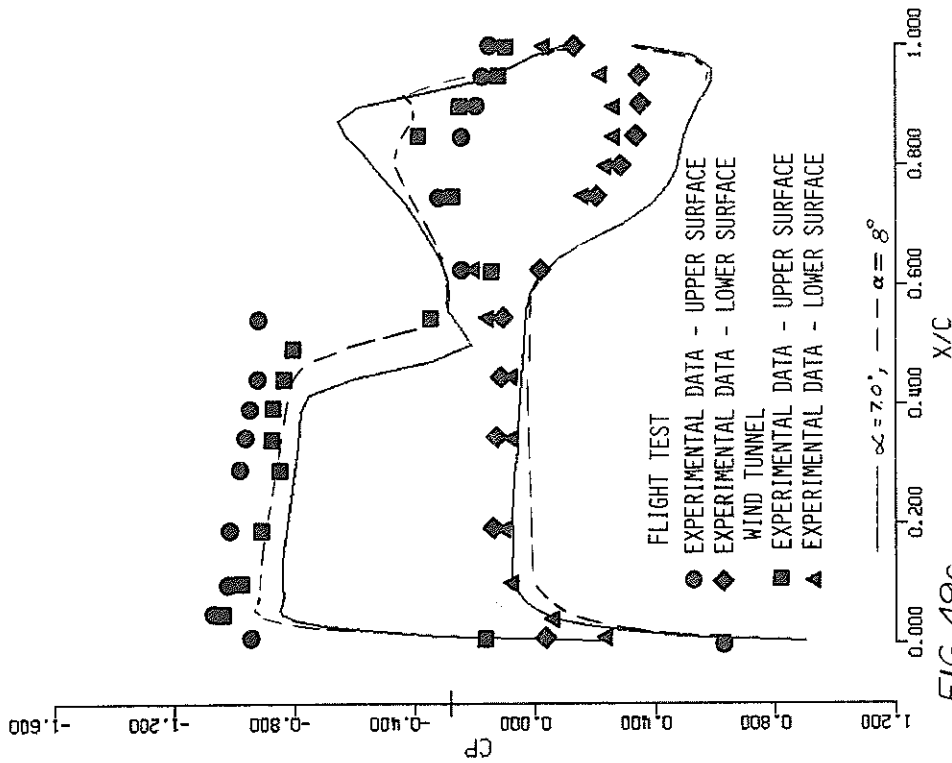


FIG 49c  
TACT

M = 0.860 ALF = 7.000 CONV = .299E+29  
 LOCAL CL = 0.691 LOCAL CM = -3.694 LOCAL CD = 0.0144  
 SPAN STATION 22 Y/S = 0.764 44 MESH PTS ON CHD

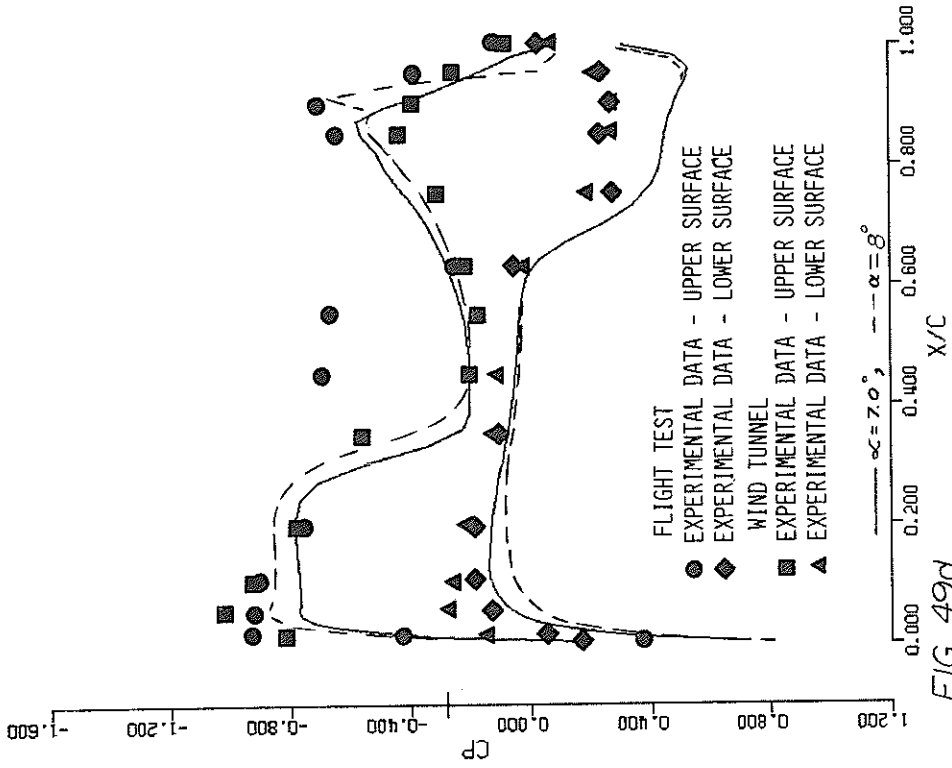
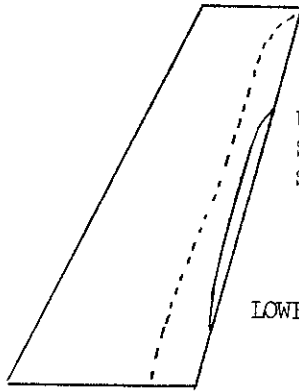


FIG 49d  
TACT

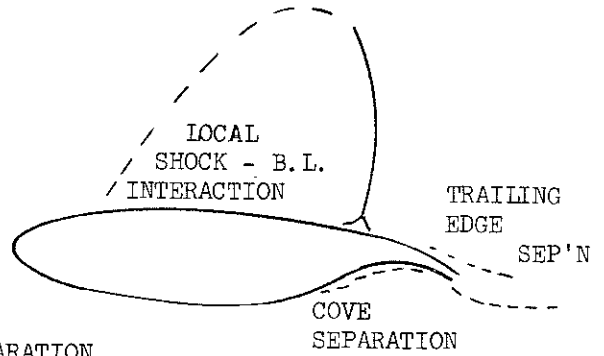
M = 0.860 ALF = 7.000 CONV = .299E+29  
 LOCAL CL = 0.534 LOCAL CM = -3.281 LOCAL CD = 0.0008  
 SPAN STATION 26 Y/S = 0.909 44 MESH PTS ON CHD



UPPER SURFACE  
SHOCK INDUCED  
SEPARATION

LOWER SURFACE COVE SEPARATION

(a) TACT OUTER PANEL

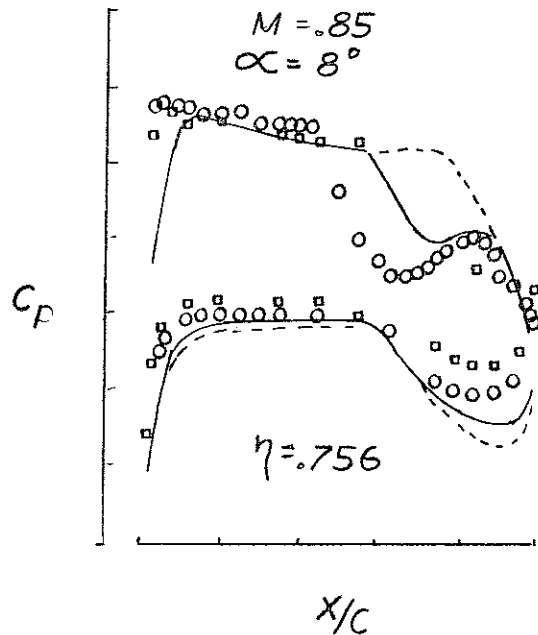
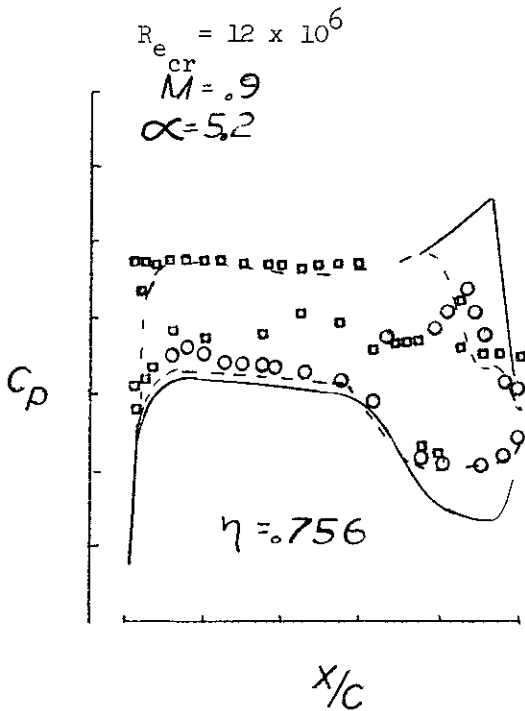


LOCAL  
SHOCK - B. L.  
INTERACTION

TRAILING  
EDGE  
SEP'N

COVE  
SEPARATION

(b)



(c)

FIG. 50 Local Trailing Edge and Cove Separation

b. F-8

The NASA F-8 Supercritical Wing Program provides an excellent opportunity for comparing the computer program with an extensive set of recently declassified wind tunnel and flight data. The details of the experimental program are surveyed in Reference 67. The F-8 supercritical wing was designed for a cruise lift coefficient of .4 at a Mach number of .99. After further testing, area rule fuselage modifications were developed with the intention of producing a weaker shock pattern at speeds approaching Mach 1.0. In addition, vortex generators were added to the lower surface leading edge of each wing. These vortex generators were designed to alleviate an unstable pitching moment problem that occurred at high lift coefficients. Both the model and flight test vehicle were tested with area rule body additions and vortex generators on and off. The configuration for which predictions were made and results were compared had the area rule body additions on and the vortex generators off.

The basic configuration tested is shown in Figure 51. Note that the wing is mounted at the top of the body with a glove extending far forward over the fuselage. The amount of blending between the wing and the body is extensive. This blending was not specifically modeled in the geometry input to the program. Instead, the body geometry computational input was based on the area distribution given in Reference 68, which included the area rule fuselage additions. Figure 52 shows a typical streamwise section of the supercritical airfoil used in the F-8 program. The wing twist present in the model, together with the loaded and unloaded flight test wing twist, is shown in Figure 53. The twist distribution input into the program is that shown for the model with the model airfoil sections employed. The experimental pressure distributions were measured at the locations shown in Figure 54. The experimental data, used for the comparisons to follow, was obtained from References 68-70.

The calculations were carried out with the viscous interaction option for a Reynolds number based on the mean aerodynamic chord of 10 million for the  $M = .99$  case and 9 million for the  $M = .90$  case, which corresponds to the flight condition. Transition was specified at 5 percent chord. Starting from a saved inviscid solution, with 4 inviscid-viscous iterations required in order to converge, such that the wing lift coefficient changed by less

than .002 between iterations. Figure 55a shows the experimental spanloads obtained from flight and wind tunnel test at a Mach number of approximately 0.90. From this, the cases chosen for comparison were the flight test at an angle-of-attack of  $4.03^\circ$  and the wind tunnel at an angle-of-attack of  $3.56^\circ$ . The computational angle-of-attack was  $3.56^\circ$ . The calculated spanload appears as the solid line in the figure. Figure 55b shows the measured spanloads at  $M = 0.99$ . The cases chosen for comparison at  $M = 0.99$  are a wind tunnel angle-of-attack of  $3.43^\circ$  and a model angle-of-attack of  $3.33^\circ$ . The calculated spanload is shown as the solid line in the figure. Calculations are compared for both  $3.33$  and  $4.33$  degrees angle-of-attack.

Figure 56a begins the detailed pressure comparisons as can be seen, the computational span station was at  $\eta_{pre} = .327$ . The experimental span station was at  $\eta_{exp} = 0.306$ . As noted in some of the other cases, this close to the body, where the spanwise gradients are relatively high, the agreement would probably be better if the experimental and computational span stations were closer. The upper surface is not well predicted, possibly due to the relatively simple body model used, without the wing/fuselage blending and body carry-over effects. With a more detailed body input, the results could be expected to improve at the inboard wing sections. Figure 56b ( $\eta_{pre} = 0.473$ ,  $\eta_{exp} = 0.480$ ) shows better agreement near the trailing edge, especially with the wind tunnel data. The forward part of the upper surface is still not well predicted, although the lower surface leading edge pressure distribution is well predicted. It can be seen in Figure 56c, that the agreement improves moving outboard on the span. This span station ( $\eta_{pre} = 0.655$ ,  $\eta_{exp} = 0.653$ ) shows better agreement over the entire upper surface. Even the leading edge peak is relatively well predicted. The next span station ( $\eta_{pre} = 0.800$ ,  $\eta_{exp} = 0.804$ ) again shows better agreement on the upper surface (Figure 56d). The final span station ( $\eta_{pre} = 0.945$ ,  $\eta_{exp} = .933$ ) shows decent overall agreement with experimental data (Figure 56e) although as in the previous span station, the predicted lower surface  $C_p$ 's are somewhat lower than the measured values. It appears that some adjustment of computational angle-of-attack and/or Mach number would yield better results, although the primary factor would be a better body model.

The Mach = 0.99 comparisons begin with Figure 57a ( $\eta_{pre} = 0.291$ ,  $\eta_{exp} = 0.307$ ). The solid line in the figure is the prediction at an angle-of-attack

of  $3.33^\circ$ , the dashed line represents predictions at an angle-of-attack of  $4.33^\circ$ . As can be seen,  $\alpha = 4.33^\circ$  tends to give a more realistic leading edge peak although again, the body effect may be incorrectly incorporated and the overall agreement is somewhat disappointing. Over the rest of the section,  $\alpha = 3.33^\circ$  yields somewhat better results. Figure 57b shows the results at  $\eta_{\text{pre}} = 0.473$ ,  $\eta_{\text{exp}} = 0.480$ . An angle-of-attack of  $4.33^\circ$  again yields better results at the leading edge. The scatter in the experimental data over the rest of the section makes comparison with prediction somewhat difficult. However, it appears that the lower surface leading edge flight test data is better predicted at  $\alpha = 3.33^\circ$ , while the wind tunnel data is better predicted at  $\alpha = 4.33^\circ$ . In Figure 57c ( $\eta_{\text{pre}} = 0.655$ ,  $\eta_{\text{exp}} = 0.653$ ), it can be seen that the entire upper surface is better predicted at  $\alpha = 4.33^\circ$ . The lower surface is not well predicted at either angle-of-attack. Again, there is significant scatter in the experimental data. The next span station ( $\eta_{\text{pre}} = 0.800$ ,  $\eta_{\text{exp}} = 0.804$ ) again shows better upper surface agreement at  $\alpha = 4.33^\circ$ , and again, the lower surface data is reproduced at neither angle-of-attack (Figure 57d). It appears that an increase in the computational Mach number would lead to improved correlation. The final span station ( $\eta_{\text{pre}} = 0.945$ ,  $\eta_{\text{exp}} = 0.933$ ) shows better agreement with flight test at  $\alpha = 3.33^\circ$  and better agreement with wind tunnel data at  $\alpha = 4.33^\circ$  on the upper surface (Figure 57e). Again, the lower surface is not well predicted at either angle-of-attack and an increase in computational Mach number would improve the correlation.

The overall correlation between the computational predictions and the flight and wind tunnel experimental results is perhaps disappointing. However, the highly blended fighter type configurations present the most challenging cases for the present program. The complex contributions of both body and viscous effects, together with the potentially large effect of aeroelastic corrections provide several sources to investigate for the disagreement between computation and experiment. Supercritical flows are relatively sensitive to the various effects so that configurations such as the F-8 provide a good baseline for further investigation of the computational methods.



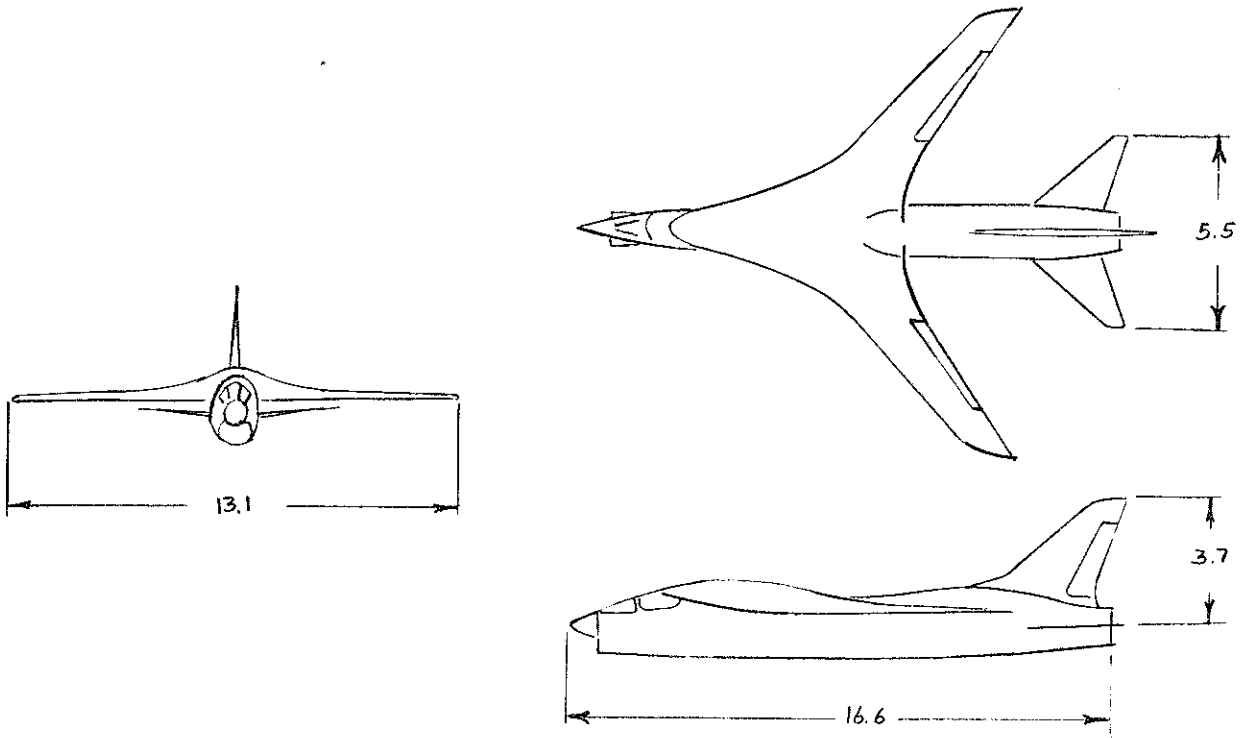


Figure 51. Three View Drawing of F-8 Supercritical Wing Aircraft



Figure 52. F-8 Supercritical Wing Section Near Mid-semispan

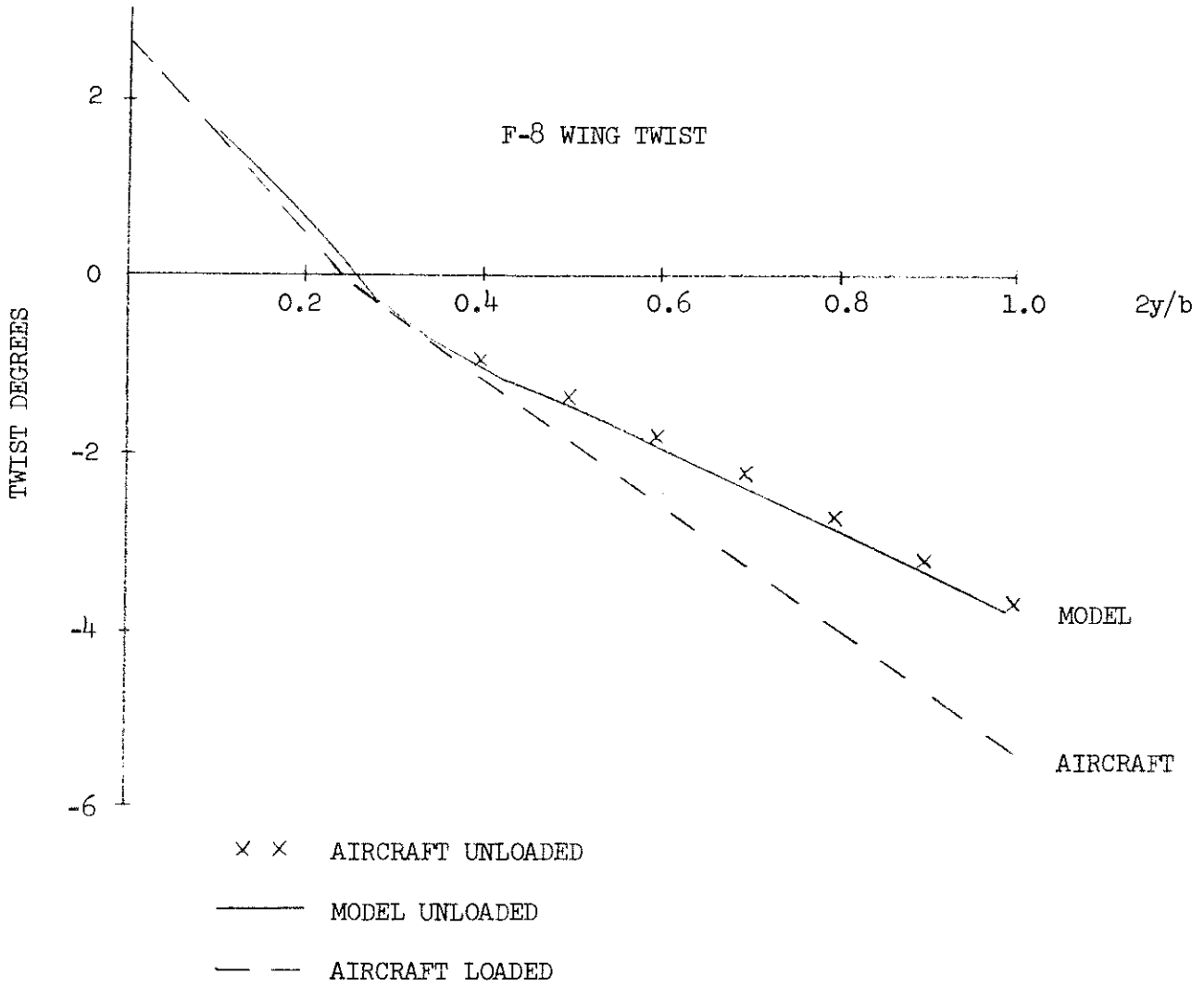
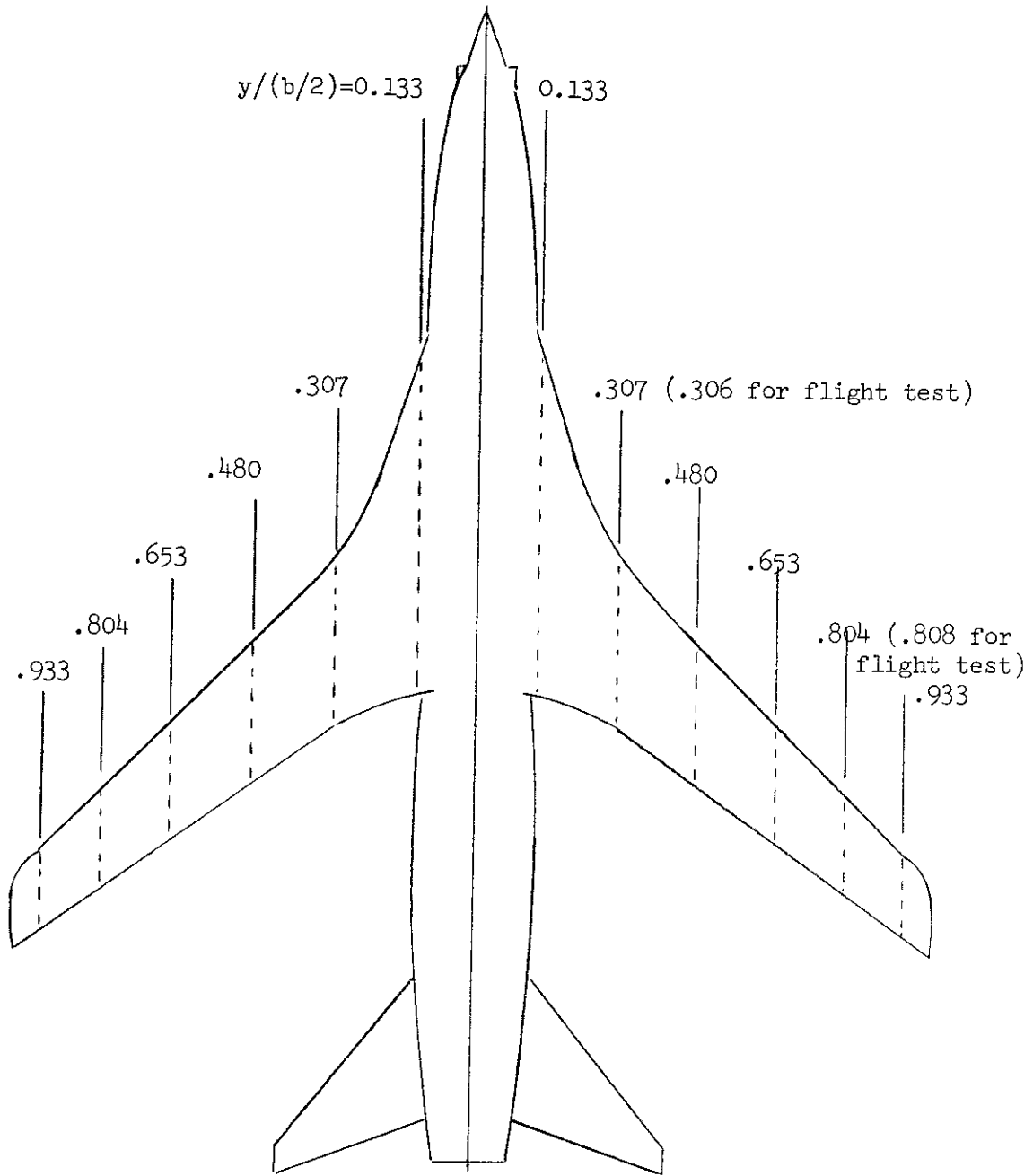


Figure 53. Wing Twist

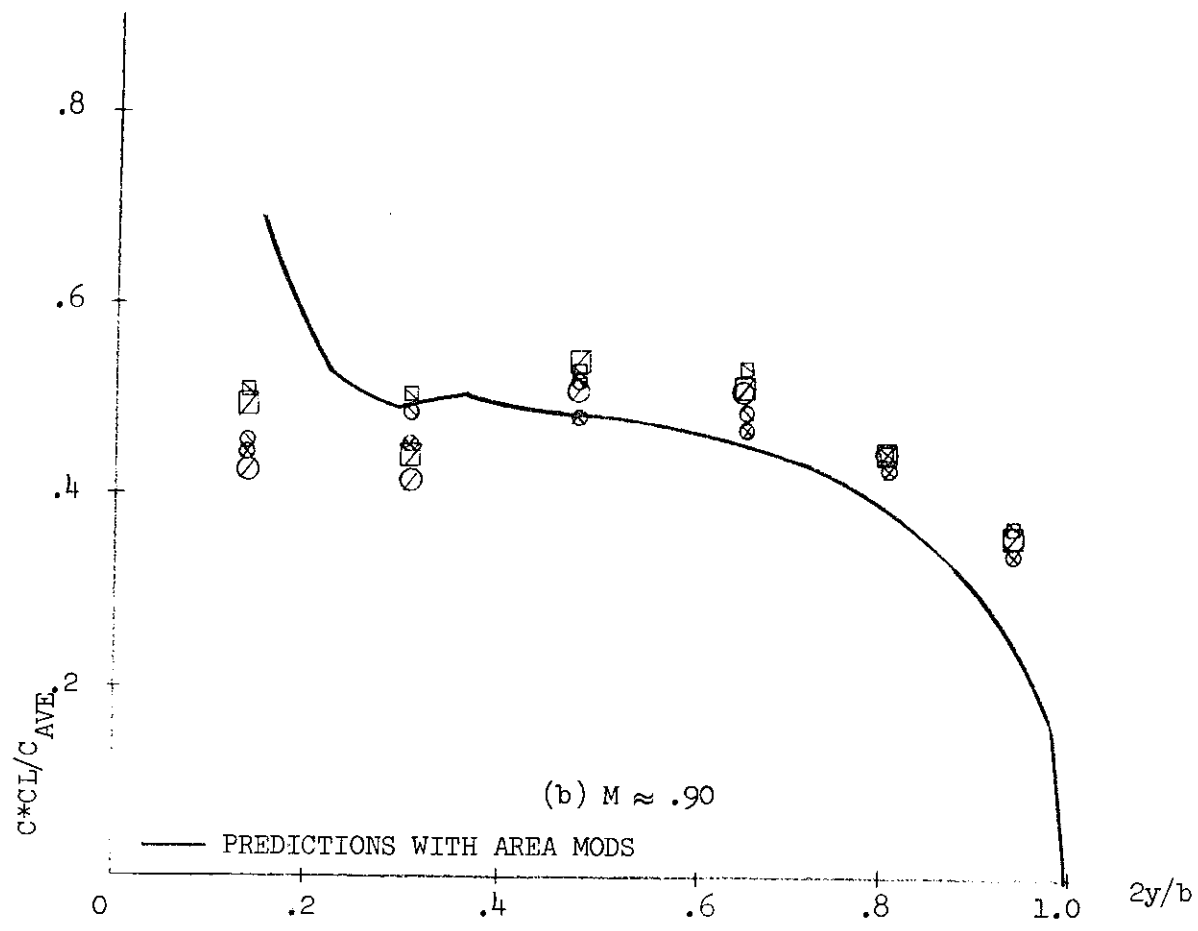


LOWER SURFACE ORIFICES

UPPER SURFACE ORIFICES

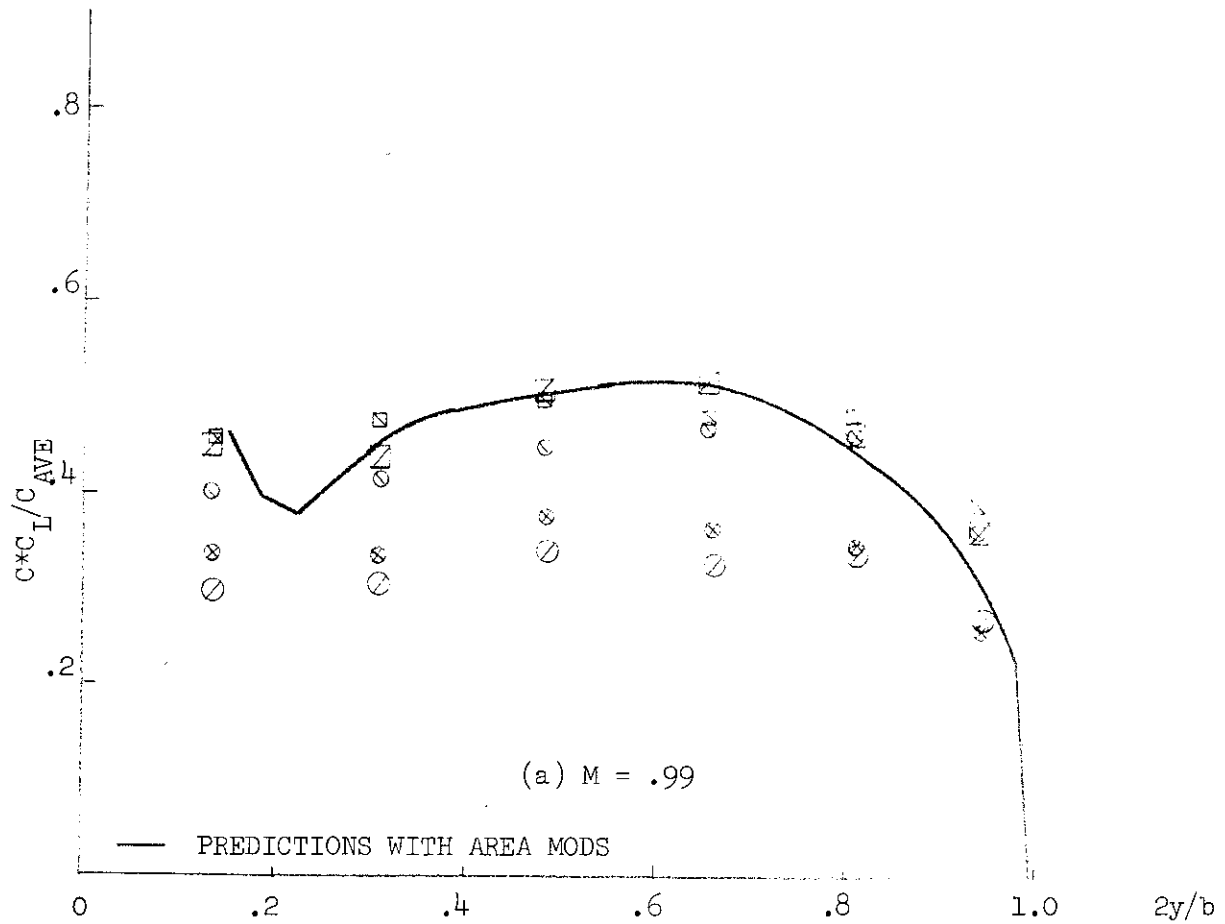
NOTE: FOR FLIGHT TEST, BOTH UPPER AND LOWER SURFACE ORIFICES ARE ON RIGHT WING

Figure 54. Location of Wing Pressure Orifices



AREA MOD ON	}	◻ FLIGHT $\alpha = 4.03$ $M = .891$ ◻ TUNNEL $\alpha = 3.97$ $M = .90$
AREA MOD OFF	}	○ FLIGHT $\alpha = 4.55$ $M = .898$ ⊙ TUNNEL $\alpha = 3.93$ $M = .90$ ⊗ TUNNEL $\alpha = 3.56$ $M = .90$

Figure 55a. Tunnel and Flight Test Spanload for NASA F-8 Supercritical Wing



AREA MOD ON	}	<table border="0"> <tr> <td style="padding-right: 10px;">◻</td> <td>FLIGHT</td> <td><math>\alpha = 3.72</math></td> <td><math>M = .987</math></td> </tr> <tr> <td style="padding-right: 10px;">◻</td> <td>TUNNEL</td> <td><math>\alpha = 3.43</math></td> <td><math>M = .99</math></td> </tr> </table>	◻	FLIGHT	$\alpha = 3.72$	$M = .987$	◻	TUNNEL	$\alpha = 3.43$	$M = .99$				
◻	FLIGHT	$\alpha = 3.72$	$M = .987$											
◻	TUNNEL	$\alpha = 3.43$	$M = .99$											
AREA MOD OFF	}	<table border="0"> <tr> <td style="padding-right: 10px;">⊙</td> <td>FLIGHT</td> <td><math>\alpha = 3.33</math></td> <td><math>M = .990</math></td> </tr> <tr> <td style="padding-right: 10px;">⊙</td> <td>TUNNEL</td> <td><math>\alpha = 3.06</math></td> <td><math>M = .99</math></td> </tr> <tr> <td style="padding-right: 10px;">⊗</td> <td>TUNNEL</td> <td><math>\alpha = 2.50^\circ</math></td> <td><math>M = .99</math></td> </tr> </table>	⊙	FLIGHT	$\alpha = 3.33$	$M = .990$	⊙	TUNNEL	$\alpha = 3.06$	$M = .99$	⊗	TUNNEL	$\alpha = 2.50^\circ$	$M = .99$
⊙	FLIGHT	$\alpha = 3.33$	$M = .990$											
⊙	TUNNEL	$\alpha = 3.06$	$M = .99$											
⊗	TUNNEL	$\alpha = 2.50^\circ$	$M = .99$											

Figure 55b. Tunnel and Flight Test Spanload for NASA F-8 Supercritical Wing (continued)

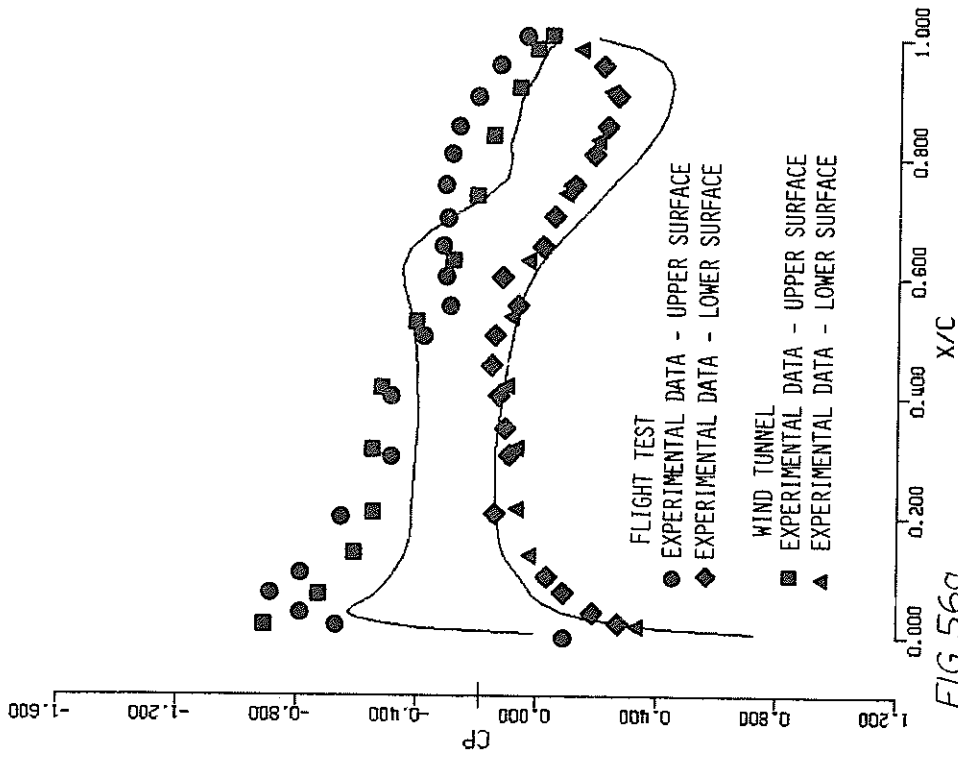


FIG. 56a.  
 F-8 CASE

M = 0.900 ALF = 3.560 CONV = .929E-04  
 LOCAL CL = 0.388 LOCAL CM = -1.048 LOCAL CD = 0.0111  
 SPAN STATION 10 Y/S = 0.327 44 MESH PTS ON CHD

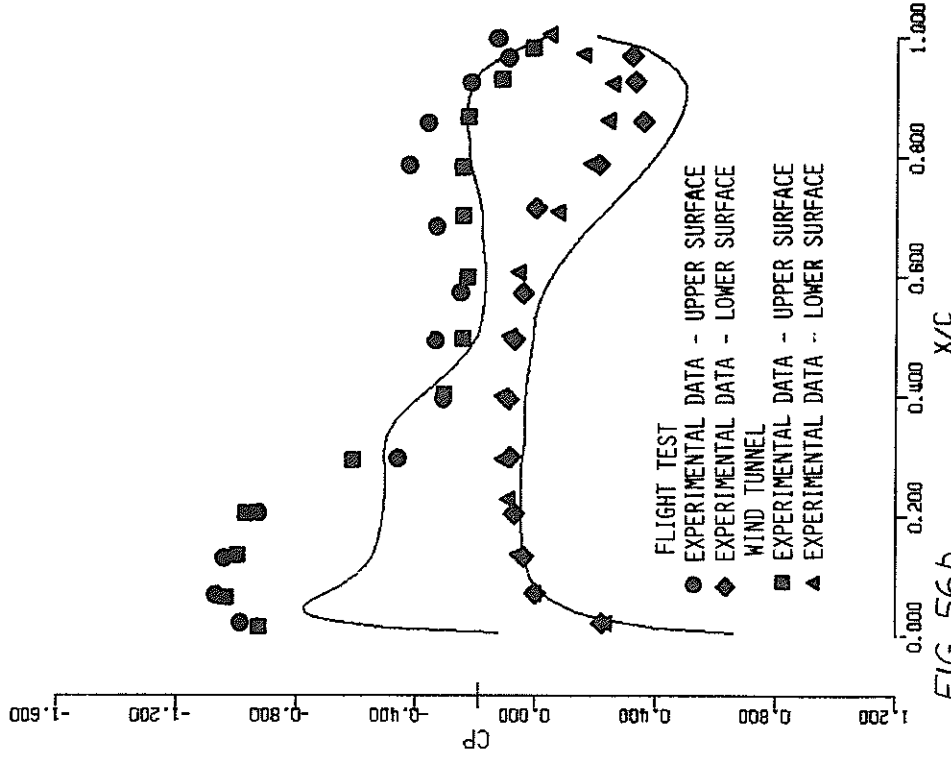


FIG. 56b.  
 F-8 CASE

M = 0.900 ALF = 3.560 CONV = .929E-04  
 LOCAL CL = 0.466 LOCAL CM = -1.774 LOCAL CD = 0.0047  
 SPAN STATION 14 Y/S = 0.473 44 MESH PTS ON CHD

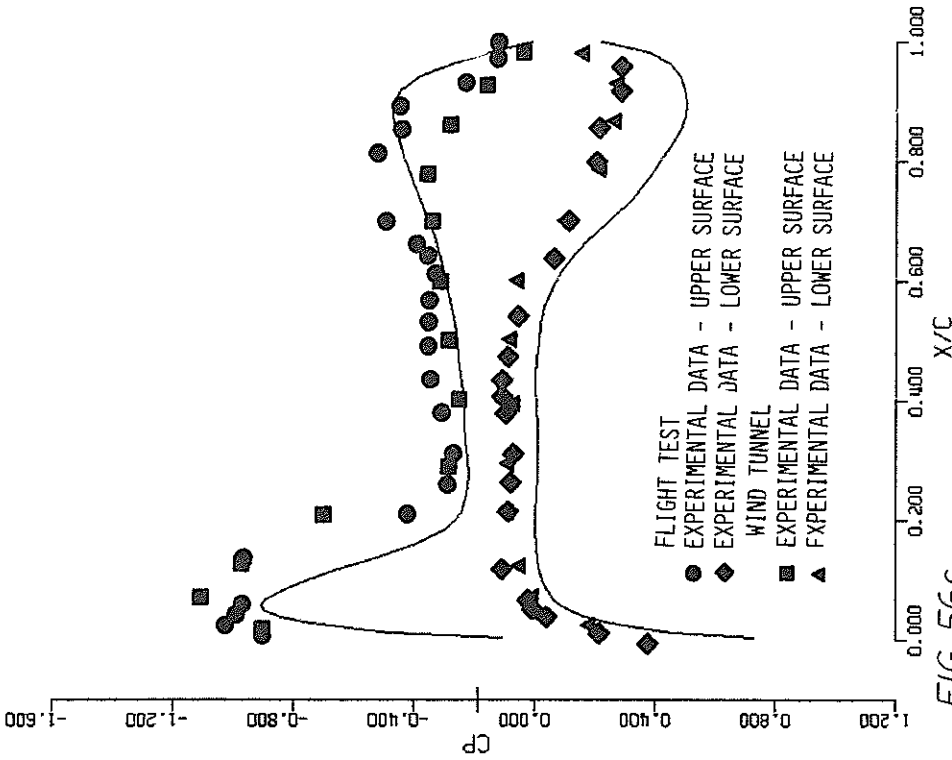


FIG 56c  
 F-8 CASE

M = 0.900 ALF = 3.560 CONV = .929E-04  
 LOCAL CL = 0.529 LOCAL CM = -2.768 LOCAL CD = 0.0038  
 SPAN STATION 19 Y/S = 0.655 44 MESH PTS ON CHD

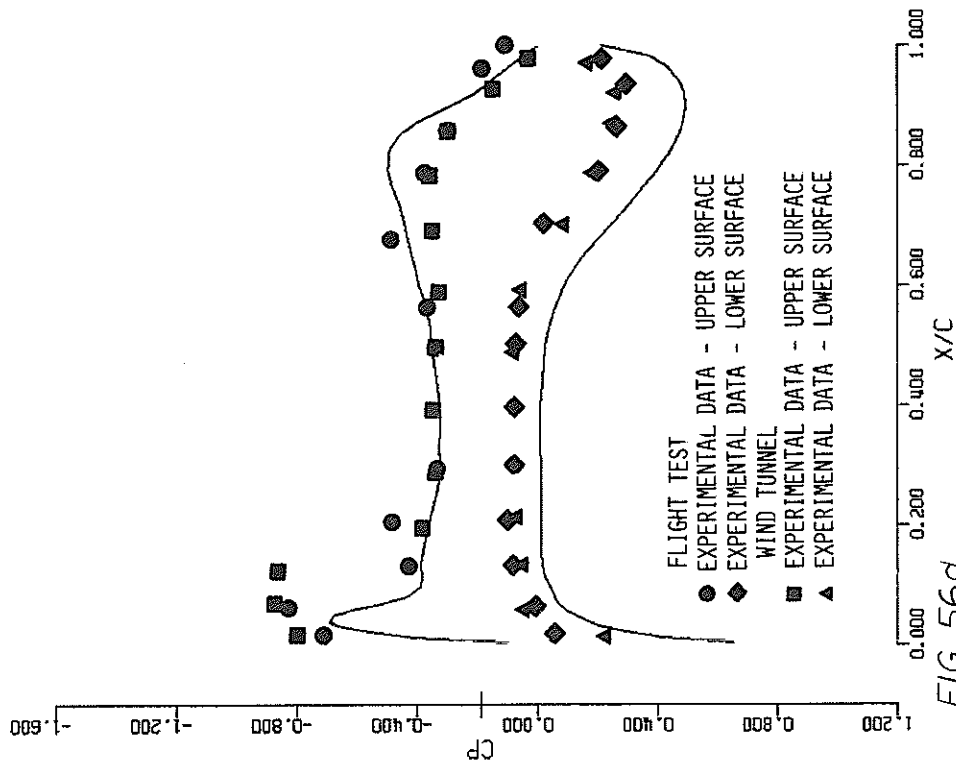


FIG 56d  
 F-8 CASE

M = 0.900 ALF = 3.560 CONV = .929E-04  
 LOCAL CL = 0.537 LOCAL CM = -3.637 LOCAL CD = -.0052  
 SPAN STATION 23 Y/S = 0.800 44 MESH PTS ON CHD

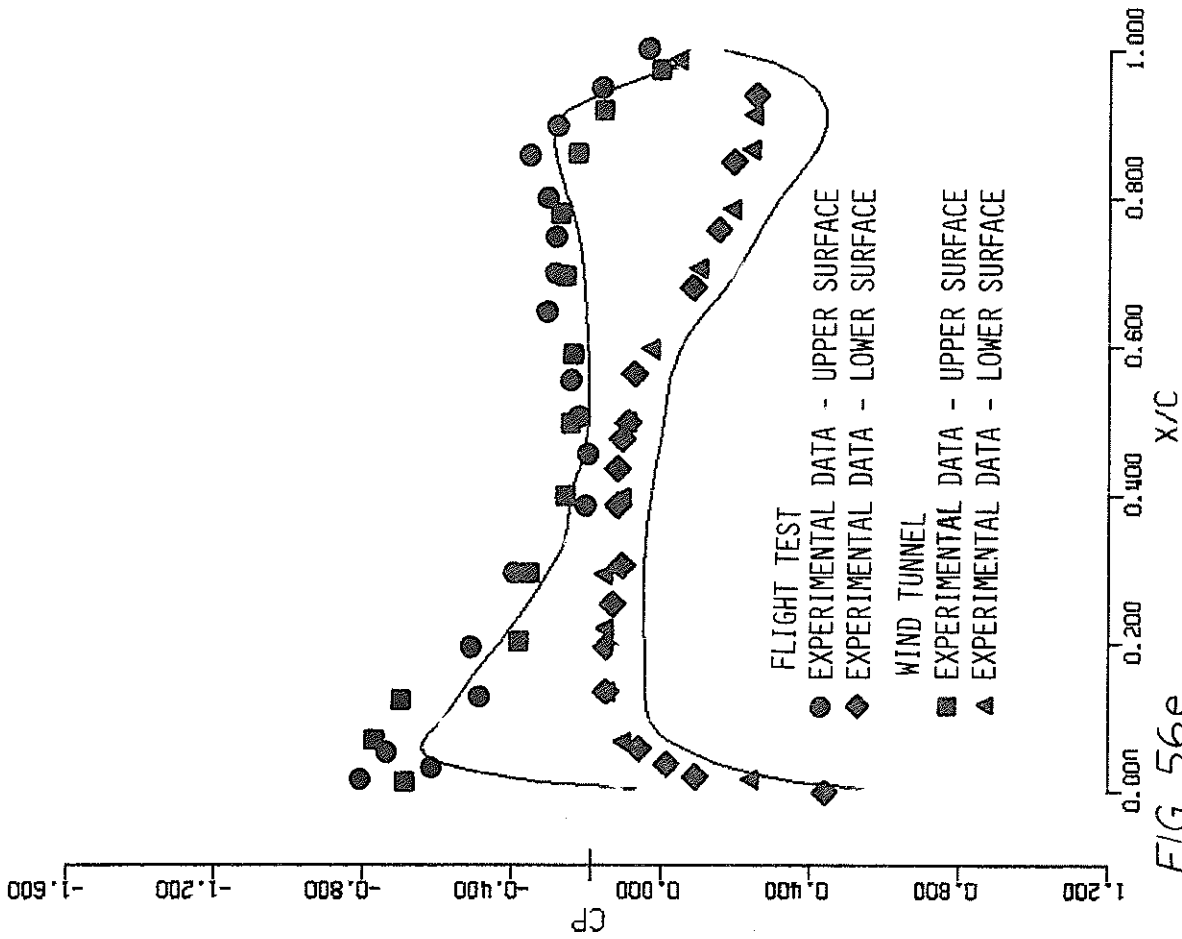


FIG. 56e.  
F-8 CASE

M = 0.900 ALF = 3.560 CONV = .929E-04  
 LOCAL CL = 0.404 LOCAL CM = -3.631 LOCAL CD = -.0155  
 SPAN STATION 27 Y/S = 0.945 44 MESH PTS ON CHD



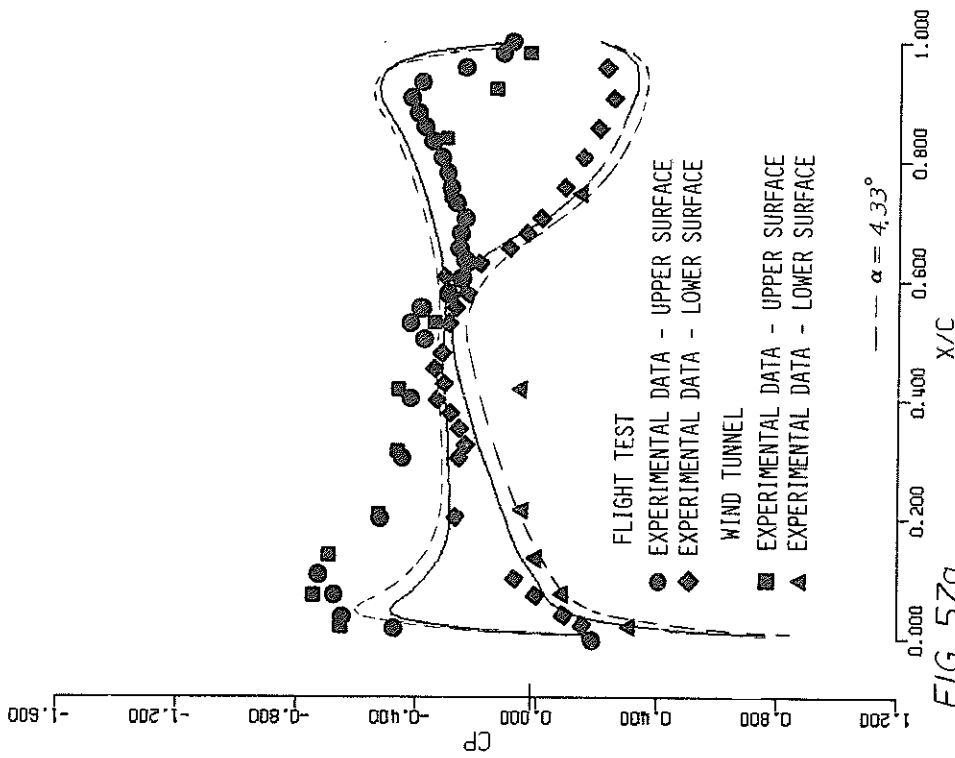


FIG. 57a.  
F-8 CASE

M = 0.990 ALF = 3.330 CONV = .0  
 LOCAL CL = 0.327 LOCAL CM = -0.854 LOCAL CD = 0.0359  
 SPAN STATION 9 Y/S = 0.291 44 MESH PTS ON CHD

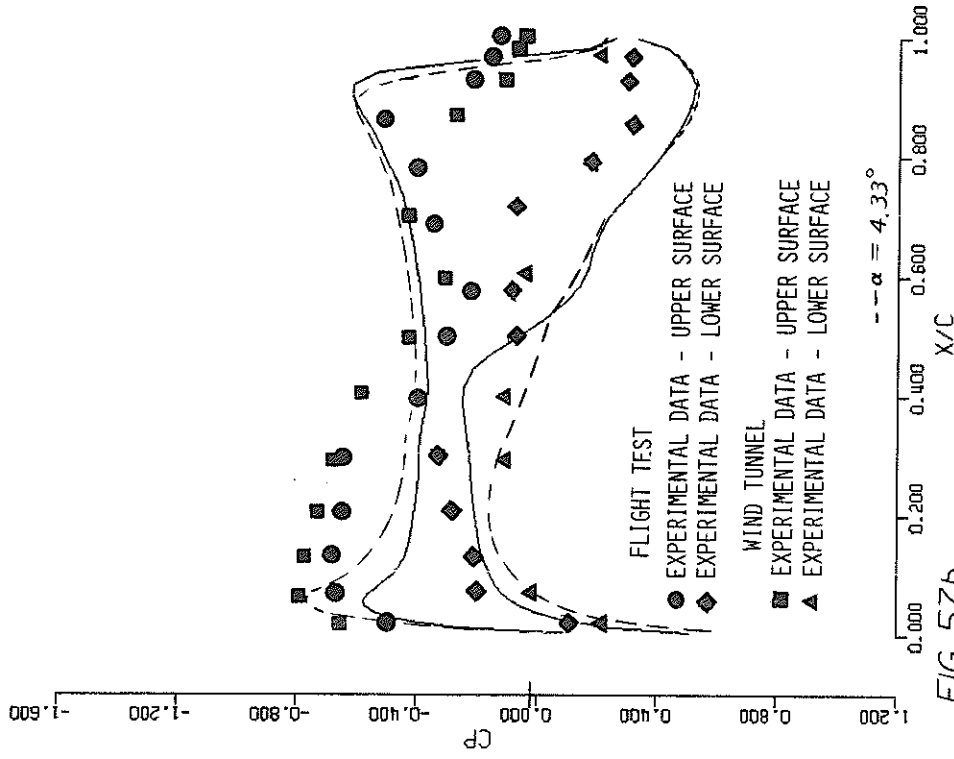


FIG. 57b.  
F-8 CASE

M = 0.990 ALF = 3.330 CONV = .0  
 LOCAL CL = 0.485 LOCAL CM = -1.915 LOCAL CD = 0.0125  
 SPAN STATION 14 Y/S = 0.473 44 MESH PTS ON CHD

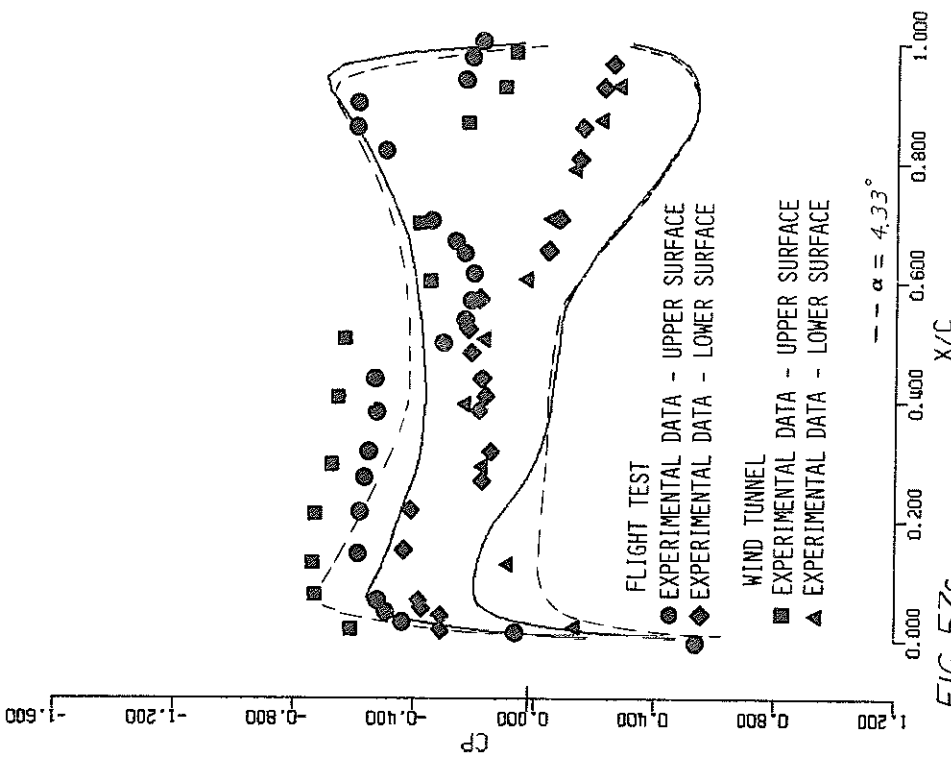


FIG. 57c  
 F-8 CASE

M = 0.990 ALF = 3.330 CONV = .0  
 LOCAL CL = 0.600 LOCAL CM = -3.190 LOCAL CD = 0.0081  
 SPAN STATION 19 Y/S = 0.655 44 MESH PTS ON CHD

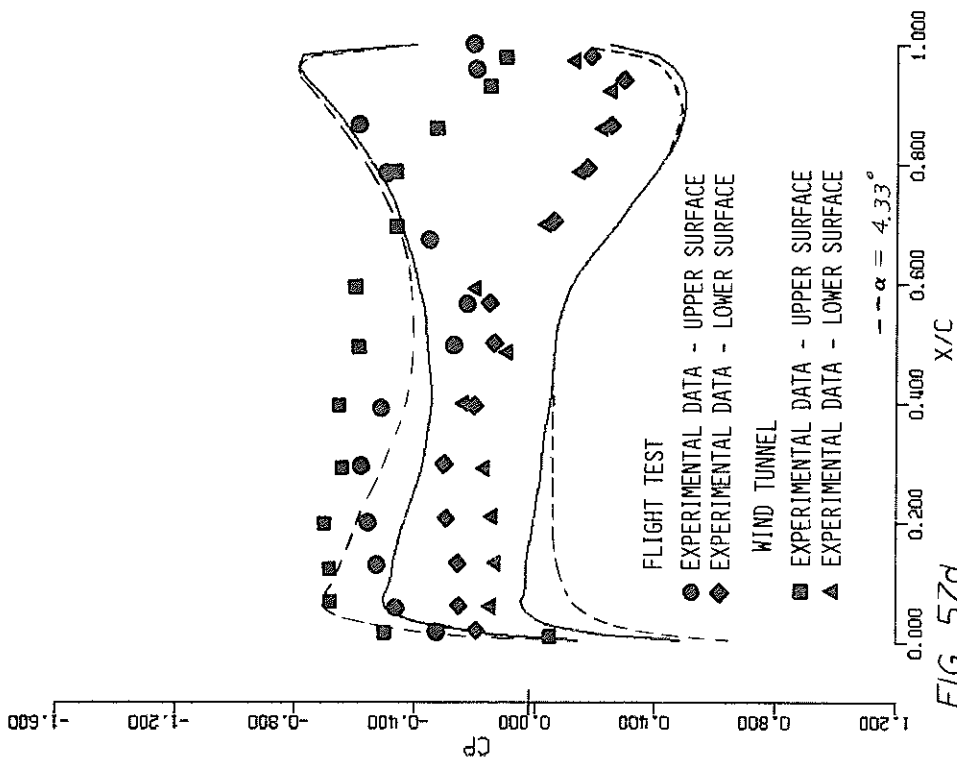
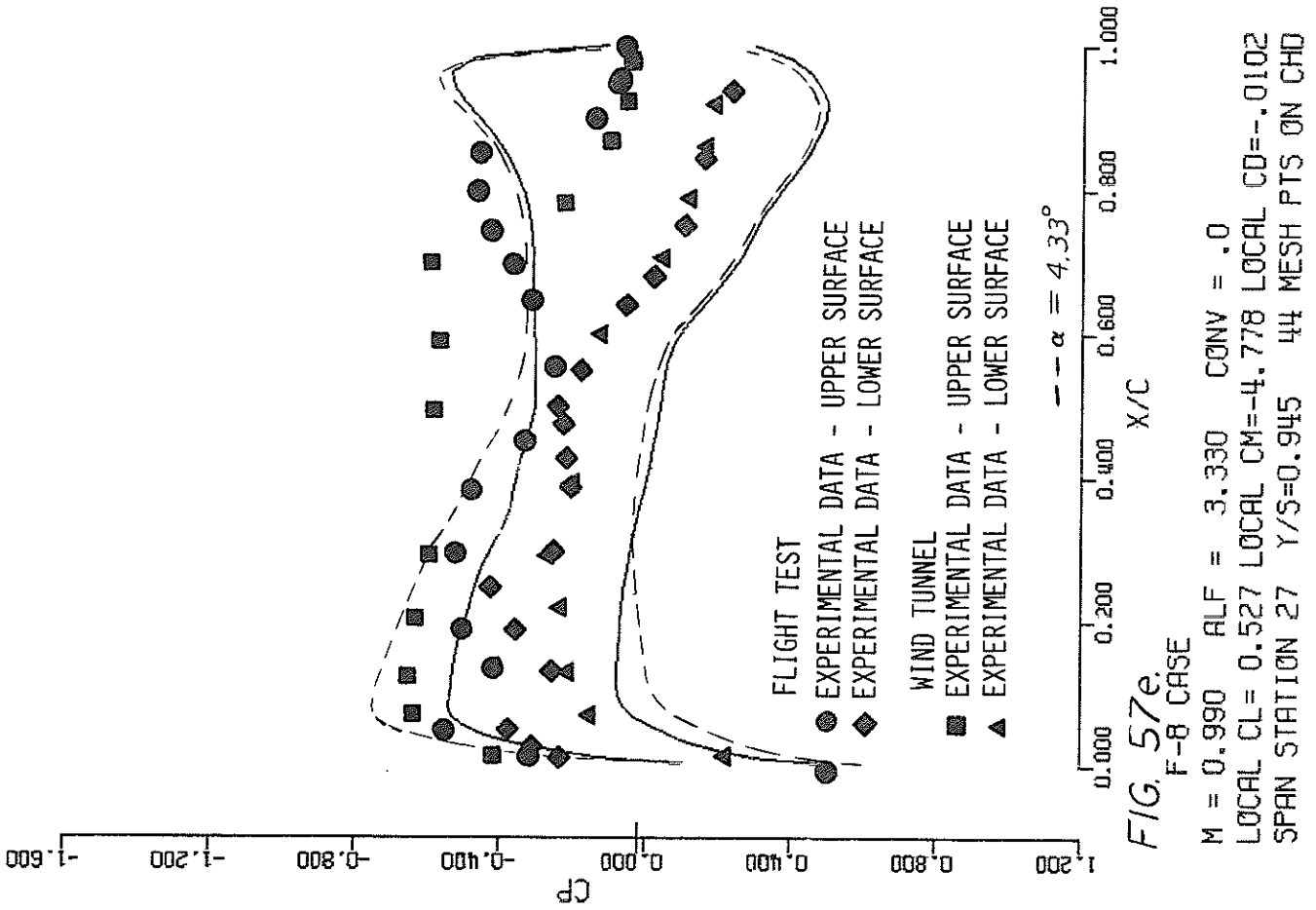


FIG. 57d  
 F-8 CASE

M = 0.990 ALF = 3.330 CONV = .0  
 LOCAL CL = 0.623 LOCAL CM = -4.265 LOCAL CD = 0.0061  
 SPAN STATION 23 Y/S = 0.800 44 MESH PTS ON CHD



## 5. COMMON INPUT/OUTPUT FEASIBILITY

### a. Introduction

Typical aerodynamic analysis and design assignments require the aerodynamicist to draw on a variety of previously obtained aerodynamic data and computational aids, as well as experience and judgement. As computer capabilities have expanded, correspondingly elaborate aerodynamic flowfield prediction computer codes have been developed. These codes can now provide reliable predictions for some fairly realistic configurations and flight conditions. These advances have led to a greatly increased reliance on computer codes to provide aerodynamic predictions. The increased dependence on the computer leads to some fundamental changes in the approach to large engineering jobs in general, as well as to the specific aerodynamic jobs. In this feasibility study, we make a brief survey of the modern engineering environment and identify the procedures required to maximize the use of the available computing resources. Clearly, the proper interfacing of the various computer codes via the input/output data streams is one of the crucial steps in efficient use of computer systems.

### b. Common I/O - A Systems Viewpoint

Large government procurement programs involving the development of technologically advanced systems require precise planning and management in order to proceed on schedule and within budgetary constraints. The systems approach to the management of the engineering tasks is usually termed an "integrated design procedure." Grumman's integrated design procedure is RAVES - Rapid Aerospace Vehicles Evaluation System (Reference 71). RAVES evolved from a previous system used at Grumman to manage the F-14 structural design.

In concept, RAVES includes all major aerospace vehicle analyses which are formulated via computer programs. The main function of RAVES is to develop a systems framework or architecture into which computer programs from all technical disciplines can be integrated, resulting in a data management system that can dynamically pass data from one program to another. RAVES can function for the full scope of the engineering design effort, from preliminary design through detail design. The system

uses a time-share computer with remote job entry links to the batch computer. The time-share computer is used for user/computer hardware communications, to assemble data, and to run the smaller computer programs; the batch machine is used for the execution of the larger computer programs. Users run programs from remote terminals equipped with scope and digitizer facilities.

By making block diagrams of the flow of information required for a design effort, the input and output requirements of individual computer analysis can be integrated into the entire system. This approach then leads to a set of consistent I/O specifications for all computer codes in the RAVES system. The resulting system ensures a smooth flow of data from one program to the next, with a minimum of routine data manipulation at the interface between analysis programs. Figures 58 and 59 contain samples of the block diagrams which can be used to manage the data flow.

Aerodynamic routines contained in the block diagrams are labeled as AXX, where XX refers to a specific aerodynamic program. One aerodynamic program is actually used solely for the conversion of the preliminary 3-view drawing to an analytic description of the surface definition. This program is shown in Figure 58 and is designated A9-QUICK. Figure 59 indicates the location of the panel method wing/body codes in the design environment. The present code will supplement these codes at the same location in the diagram. The need for common input/output is evident from this diagram, since all these codes occur in the same location in the functional diagram and a typical design effort will require predictions from each of these codes.

#### c. Common I/O - The Aerodynamicist

Aerodynamic analysis requires the ability to operate a large number of different programs. Thus, in addition to a knowledge of aerodynamics, the job requires familiarity with the input peculiarities of each program as well as the particular notations used in the output of the solution of each program. Differences between these programs often lead to painful time delays and confusion. It is, of course, the immense range of powerful aerodynamic simulations available to the aerodynamicist via the computer that brings about these problems. Without careful planning, we in fact, have an embarrassment of riches. Unless this situation is brought under control now, the future promises to bring

even more confusion. More and more codes are becoming available, each with its unique data structure and output format. The final result could be that the improving computational capabilities will not be fully reflected in actual engineering practice due to common I/O limitations.

d. Common I/O - NASF

NASF, the Numerical Aerodynamic Simulation Facility, is a NASA proposed centralized facility that would be made available to the aerospace community in much the same manner that NASA Wind Tunnels are made available (Reference 72). The facility would house a new special purpose computer designed specifically for the prediction of aerodynamic flowfields and a hierarchy of computer codes that would be dedicated to this particular machine, each code providing the flowfield simulation at a different level of sophistication. Any internal or external common I/O efforts must be closely coordinated with this effort, since the coordination of the data set for NASF with in-house aerodynamic tools will be by far the most important requirement for effective use of this facility.

e. QUICK - A Baseline Code For Generating Body Definition

The tool for generating the basic body definition for aerodynamic simulation is presently available. Designated A9, QUICK is already part of the Grumman RAVES system. Reference 73 describes this code. Briefly, QUICK provides a simple method of rapidly defining an accurate computer model of complex vehicle geometry. The primary motivation which guided the development of QUICK-GEOMETRY was the elimination of the redundant task of remodeling geometry input to run different programs. With this system, only a single effort is made to extract a mathematical model from the design drawing. This math model can then be manipulated by computer subroutines to generate the required geometry input data decks. The math model is quite general and meets all the fundamental requirements of a geometry model:

(1) It is independent of the reference source of configuration geometry, hence the model can be developed with equal facility from a conceptual description, a lines drawing, or a configuration as stored in the Grumman Master Dimensions System.

(2) It is adaptable to both manual input using ruler and template to specify local geometry, and to machine assisted digitized input, which can measure selected points or trace out a series of points along

an arc.

(3) The model is sufficiently flexible to adapt to various types of analysis. It will develop comparable models for different analyses and comparable models for different configurations. It will easily adapt models to various restrictions imposed by analysis limitations.

(4) Subsequent model refinement, when necessary to support a more detailed analysis, or to keep pace with actual configuration changes can be rapidly made to the initial quick response model.

(5) Uses a "building block" approach which defines each configuration component in its own natural coordinate system to simplify its geometric definition. This also makes it possible to modify existing models by scaling, translating or rotating components and to select components from a catalog of standard ones.

(6) The model is very concise and can, therefore, be stored efficiently in a computer data bank (such as RAVES).

The QUICK-GEOMETRY system is being applied in a number of ways. As part of RAVES, it is used as a common source of vehicle geometry which is drawn upon to generate a variety of geometry input data decks. In particular, data decks conforming to the Harris input format (Reference 74), which has become a standard at NASA Langley, can be generated. In another RAVES application, QUICK-GEOMETRY has been adapted to a vehicle lofting system. The most sophisticated application to date, has been to integrate the QUICK-GEOMETRY system with a numerical flow code which calculates the steady/supersonic/hypersonic inviscid flow around real configurations (Reference 75). In this application, vehicle geometry (surface coordinates, slopes and normals) are generated as required by the flow analysis code.

Figure 60 shows some examples of the typical model produced by QUICK. Because the code described in this report contains a very basic body simulation, the QUICK code has not been incorporated. This allows the present code to retain its stand alone configuration. The body modeling used in the present code has, however, been strongly influenced by QUICK. It appears that the proper use of QUICK would be to continue to operate QUICK as a stand alone format, with capability of simultaneously generating data sets for the various aerodynamic programs.

Although QUICK-GEOMETRY modeling might not be required for all appli-

cations, this body oriented system (which is generally available through NASA) would allow for a universal input set that would meet the requirements of all the various aerodynamic programs. Grumman is presently considering constructing a processor to automatically generate body panel models for sub- and supersonic linearized codes. We can conclude that common body input is feasible and the basic elements already exist for common subsonic, transonic and supersonic code input. The main consideration in the construction of common input is the particular system of codes and the particular time-sharing system.

f. Wing Definition

The planform/section modeling problem is less complicated than the body case. The representation of the planform by  $(y, x)$  pairs is relatively simple and very good accuracy can be achieved. Because QUICK is oriented toward body cross-sections (which are natural for bodies), it is not appropriate for most wing section definitions, although low aspect ratio wings are adequately treated by QUICK. The wing thickness should be defined by inputting streamwise sections. The method of input employed in the present code should form a baseline for I/O standardization. In fact, by using the thickness scaling option, it should be possible to use the same airfoil ordinate deck for both this code and the various 2-D airfoil analysis codes in most cases.

g. Feasibility of Including Graphical Results

Common output should include a uniform set of plots and a uniform nomenclature. This allows for verification of the geometry and should also be sufficient for report and presentation figures. The graphics package included with the present program provides wing/body geometry verification level consistent with the actual geometric treatment.

h. Common Output

We also endorse a uniform output of results for various codes. At present there is usually a significant confusion factor concerning just exactly what each different code outputs. Subtle changes in the various definitions of output quantities between various codes is a continued source of frustration. In the present program, the output will be presented in as clear and definitive manner as possible. In fact, the output appears to be one of the best formats of any of the contemporary codes.



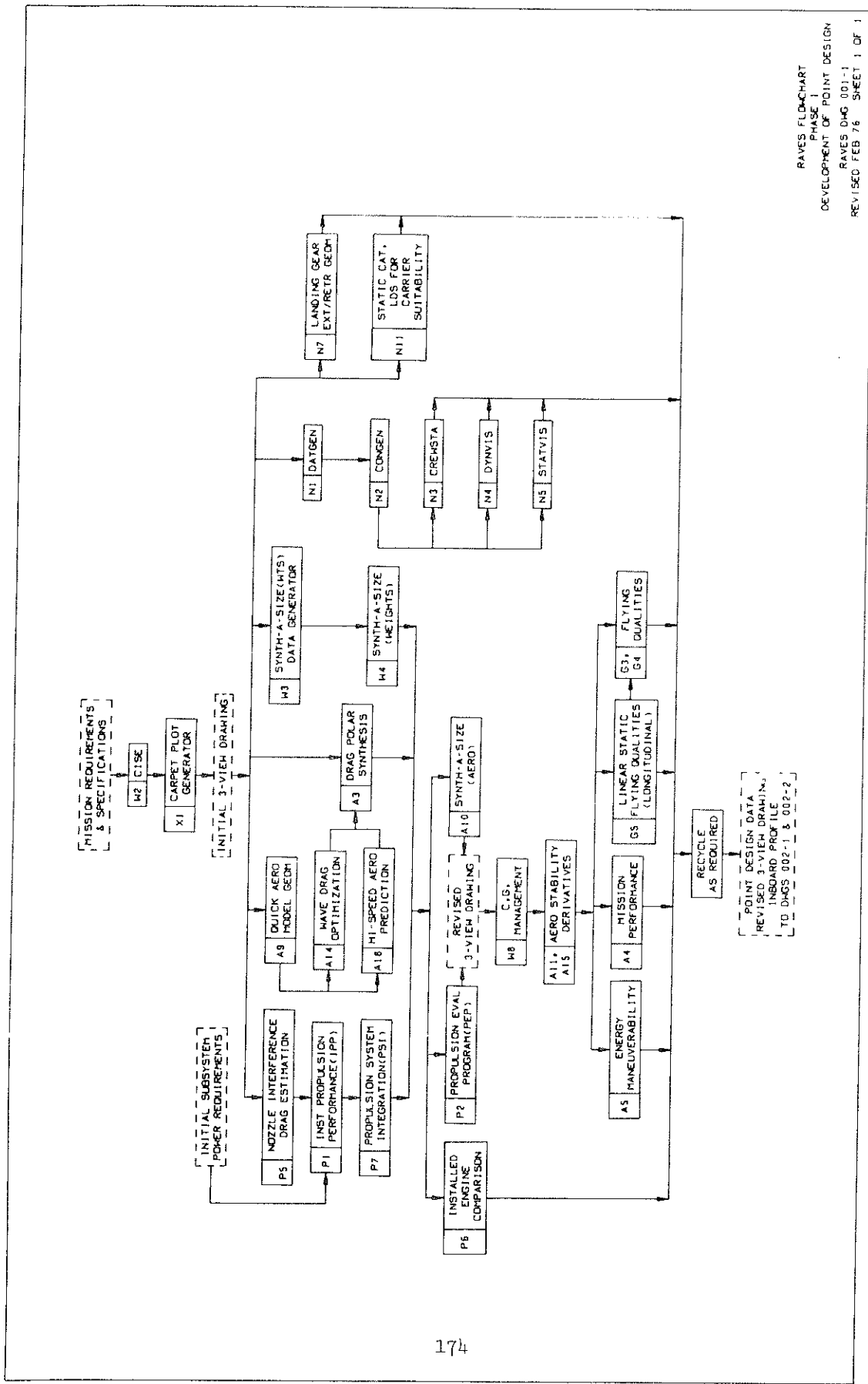
i. Recommendations for Common I/O

(1) The field of computational aerodynamics has reached a sufficiently high maturity level that commonality between code input/output must be a consideration in code development.

(2) Practical operation of the NASF concept will require a standardization of I/O.

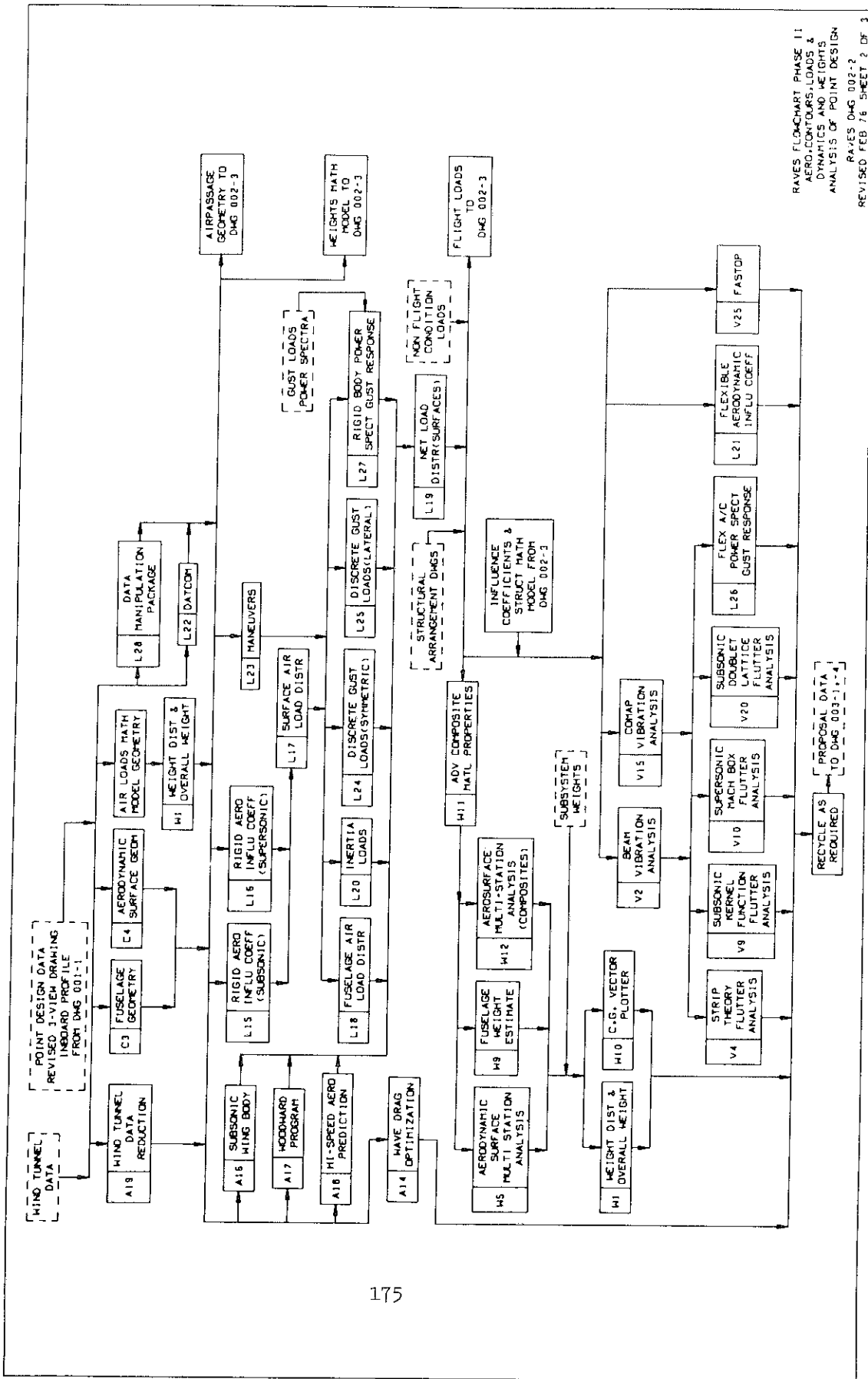
(3) Grumman's QUICK Geometry Modeling should form the basis for body and low aspect ratio wing modeling.

(4) The present code I/O has been developed with an awareness of common I/O considerations, so that it could easily be modified to conform to any standardization of I/O for aerodynamic simulation -- it is feasible to couple this code to QUICK.



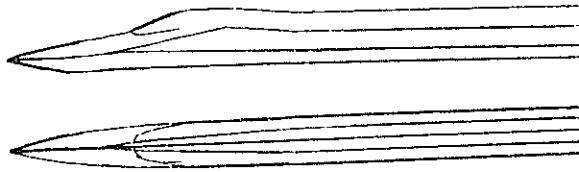
RAVES FLD-CHART  
 PHASE 1  
 DEVELOPMENT OF POINT DESIGN  
 RAVES DMG 001-1  
 REVISED FEB 76 SHEET 1 OF 1

FIGURE 58 Typical Point Design Data Flow



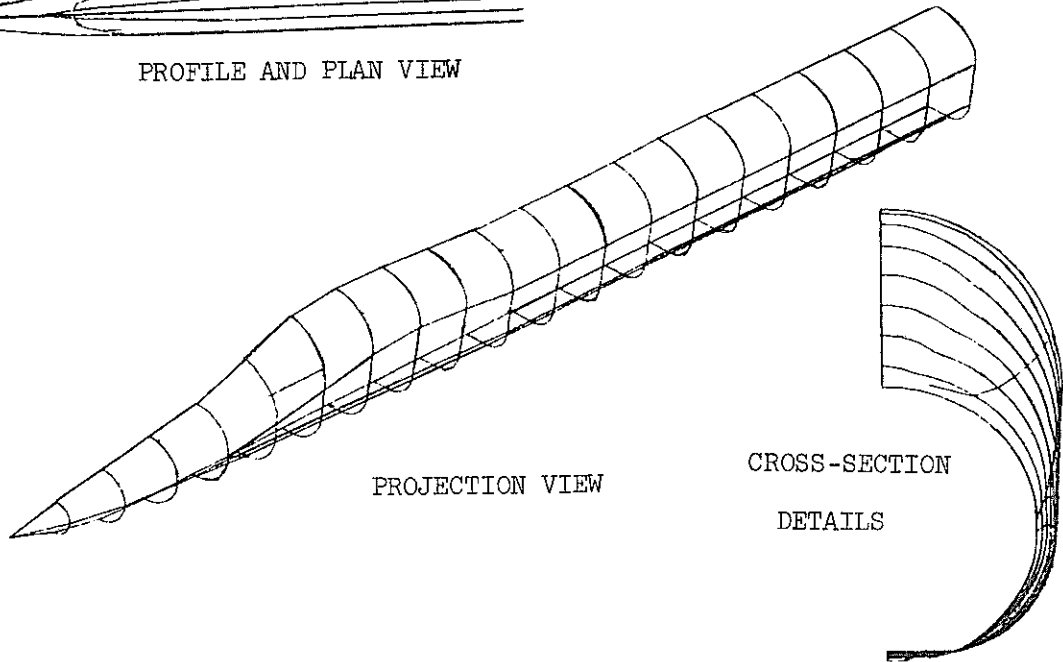
RAVES FLOWCHART PHASE 11  
 AERO, CONTOURS, LOADS &  
 DYNAMICS AND WEIGHTS  
 ANALYSIS OF POINT DESIGN  
 RAVES DMG 002-2  
 REVISED FEB 76 SHEET 2 OF 3

FIGURE 59 Typical Design Data Flow Requirements



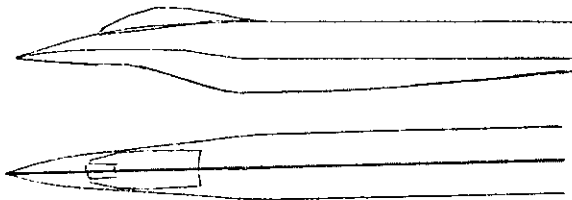
PROFILE AND PLAN VIEW

TACT FUSELAGE



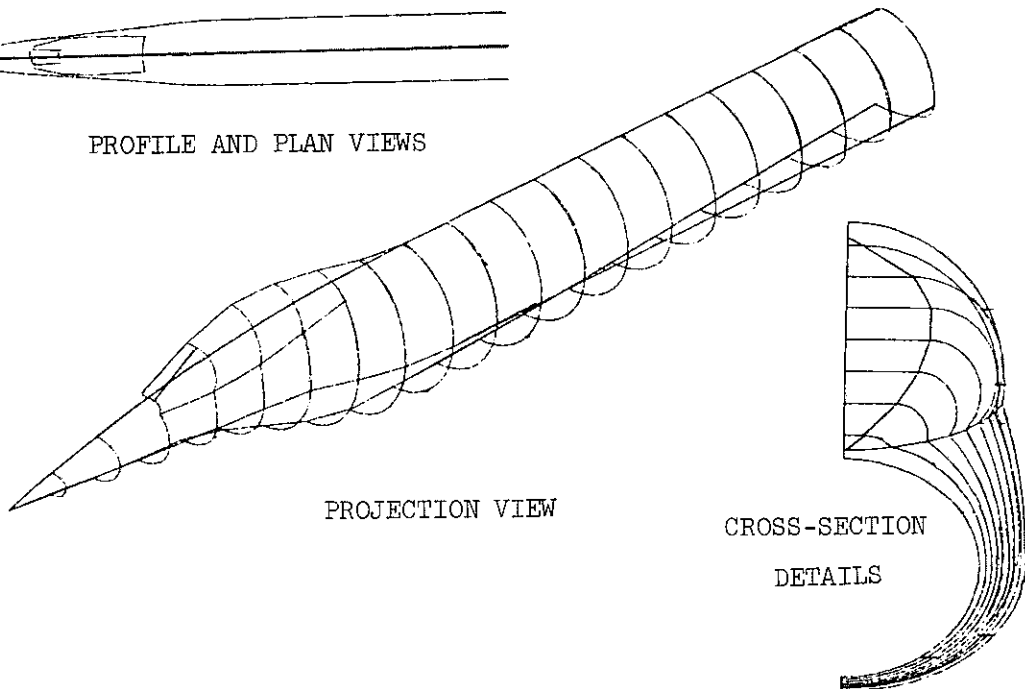
PROJECTION VIEW

CROSS-SECTION  
DETAILS



PROFILE AND PLAN VIEWS

HIMAT FUSELAGE



PROJECTION VIEW

CROSS-SECTION  
DETAILS

FIGURE 60 QUICK-GEOMETRY

## 6. DESIGN FEASIBILITY

### a. Introduction

Although the use of the computer to simulate the flowfield about a vehicle with a specific geometric configuration is an extremely useful and important capability, it is an indirect response to the aerodynamic design question. The aerodynamic design question is, of course, typically posed at several levels, starting with some vague and general question about the "best" shape of the airplane for a particular mission, and proceeds to more specific and detailed questions concerning the actual wing lines, subject to a large variety of constraints. Often, a wing is designed using computer programs, "submitted" and wind tunnel tested. In the analysis mode, the aerodynamic computer programs are being used to simulate a wind tunnel. Of course, the computer simulation can be used much sooner in the design cycle than a wind tunnel test and this strategy should produce an improved final design at a reduced cost, in a shorter time period. This is, of course, the proper initial introduction of the computer simulations into the wing design process. Indeed, this technique has been adopted for subsonic and supersonic wing design for some time. Transonic wing design efforts have only recently started using fully transonic three-dimensional wing-body computer simulations in the design cycle.

Once the computer is introduced into the design cycle, it becomes evident that it can be used in a fundamentally different mode than to simply supplement wind tunnel testing. The use of flowfield simulation in this manner is naturally referred to as the "design mode," as opposed to the "analysis mode" of operation. A "design mode" has been available for linearized subsonic and supersonic flowfields since shortly after the analysis codes became available. The most extensive use of a "design mode" appears to have been the elaborate system of supersonic wing design codes that evolved from the work of Carlson and Middleton (Reference 76). After a brief review of the design problem and some of the presently employed tools, we attempt in this study to identify a reasonable approach to the use of the present three-dimensional transonic methodology in a design mode, which is then illustrated with some examples.

b. Review of the Design Process

A variety of possibilities emerge when the problem formulation for a "design mode" of operation is explored. The reason for this range of possibilities can be attributed to the manner in which the design problem is posed, as noted above. Ideally, the aircraft designer would specify the aircraft mission (or missions) and a computer program would provide the detailed lines of the optimum aircraft. Of course, we do not expect that such a smart computer program will exist for some time. However, most aircraft companies and governmental agencies routinely employ programs that predict the gross features of an optimum aircraft for a particular mission with some assumption regarding the rate of development of various technologies. These programs also include a large data base developed from previous aircraft designs. Typical aerodynamic outputs from the programs are i) Aspect Ratio, AR; ii) Taper Ratio,  $\lambda$ ; iii) Sweepback,  $\Lambda$ ; and iv) Thickness Ratio,  $t/c$ . Usually a target drag level for the configuration is also specified. Typical examples of this type of program are the Grumman CISE program (Reference 77) and the Ames ACSYNT program (Reference 78).

Hence, the computer is used to determine the overall features of the required airplane. The typical aerodynamic design problem thus becomes less vague and more manageable, with the statement being reduced to something along the following line:

Given:	o AR, $\lambda$ , $\Lambda$ , $t/c$ o $M_\infty$ , $R_e$ o $C_{L_{CRUISE}}$ or o $C_{D_{MAX}} \text{ ALLOWABLE}$	(basic geometric requirement) (flight regime)	
	}	Design Goal	
Find:*	o $C_{D_{MIN}}$ for $C_{L_{CRUISE}}$ or o $C_{L_{MAX}}$ for $C_{D_{MAX}} \text{ ALLOWABLE}$		} Design Goal

\* Note that although this is the typical problem statement, each is actually a requirement to obtain  $(L/D)_{max}$ . In one case, L is specified, in the other, D (or thrust) is specified and thus, from the mathematical point of view, each of these statements are essentially equivalent.

- o Detailed Geometry → Detailed Aerodynamic Aircraft Design, Definition,

subject to geometric constraints on twist, camber, root bending moment, etc., and aerodynamic requirements on performance at other flight conditions. At this point, we could begin to consider the use of a computer code directly to help determine the optimum aerodynamic shape and performance that can be obtained for the specified problem. More typically, the designer employs his experience and judgement to specify a desired pressure distribution. This type of program is usually described as an "inverse method," while a program that attempts to address the problem more immediately is usually termed an "optimization method." Each of these approaches has its own strengths and weaknesses.

A contrast between optimization and inverse methods can be summarized as follows:

Optimization

- o Requires many analysis submissions for a single design case.
- o Solution depends critically on the user assumed form of the answer.
- o Can handle a variety of geometric and off design constraints.
- o If performed through large optimization code, solution is not obtained from "aerodynamic thinking."

Inverse

- o Generally as fast as a single analysis.
- o The geometry may not always exist for a given pressure distribution.
- o Difficult to treat off design and geometric constraints.
- o Solution is a direct result of best current "aerodynamic thinking."

Another drawback of the optimization approach is that the path taken to the final result is often rather obscure and the relative importance of the various aspects of the final design produced in this manner are not readily apparent.

The optimization techniques presently employed in the design methods are of the "search" type, and do not employ any of the elements of calculus of

variations in order to obtain the maxima. Although an entire book (Reference 79) has been devoted to aerodynamic optimization using calculus of variations, these concepts have not yet proven to be valuable for the class of optimization problems under study here. It would not, however, be wise to automatically dismiss these methods from consideration in general, although we will not discuss these methods further in the present study.

### c. Review of 2-D Transonic Design Methods

A variety of numerical approaches have been used to design transonic airfoils. The book by Thwaites (Reference 80) discusses the classical approaches to the incompressible inverse methods and points out that some judgement must be used by the designer in specifying the desired pressure distribution; a solution does not necessarily exist. Inverse methods for transonic speed airfoil design have to contend with this same problem. However, in practice the aerodynamicist has been able to use inverse methods without any undo hardship. Typical inverse methods are due to Tranen (Reference 81), Volpe (Reference 82) and Carlson (Reference 83). The programs have proven to be very useful and Figures 61 and 62 show examples of the application of Volpe's program to high performance and cruise section design, respectively. The cruise section is an example of a mixed design, where the top of the original design airfoil was retained and the bottom of a section designed to have the same upper surface pressure distribution as the original and a lower surface pressure distribution with reduced pitching moment was employed. This example shows how the inverse methods are in practice quite versatile.

The "numerical optimization" approach to airfoil design appears to be a very recent concept, unlike the inverse methods, which were available in the forties for subsonic flows (like many of the currently used aerodynamics methods, inverse methods for detailed aircraft work were not routine engineering tools until the widespread availability of computers). An initial study of numerical optimization was presented in 1974 by Hicks, Murman and Vanderplaat (Reference 84). The underlying idea in this approach is to couple a modern optimization code with an aerodynamic analysis code. The airfoil design problem is then cast as an optimization problem and the entire apparatus associated with optimization methods can be brought to bear on the problem. Hicks and co-workers are continuing to work along these lines and the evolution of the concept has been very interesting. The most attractive aspect of



the optimization method is its ability to handle design constraints. These constraints include both off design performance requirements and design point geometry restrictions. Ballhaus (Reference 14) has recently reviewed the procedure and the report by Vanderplaats and Hicks (Reference 85) provides the most detailed description of the techniques used to formulate the design problem as an optimization problem.

Another approach to transonic airfoil design must be mentioned in any review. Hodograph methods have been used to design some very good airfoil sections. The method has proven to be very productive in hands of the proficient operators at the Courant Institute (Reference 86). However, because the method seems to have no application in three-dimensions, it will not be discussed further in the present study.

The optimization method of aerodynamic design is one of the more promising methodologies under development; there are some drawbacks at present which need to be examined. These drawbacks are mainly related to computer run times. In optimization methods jargon, optimization methods minimize some "objective function," which is a function of a set of "design variables" subject to a set of constraints. The "objective function" could be drag, for example, while the "design variables" are typically the variables used to specify the shape of the airfoil. The constraints could be airfoil thickness, off-design drag values, or virtually any other requirement that might arise in practice.

The selection of the appropriate objective function and design variables are crucial to the success of the optimization methods. Although drag is the most direct measure of aerodynamic performance, the transonic methods do not presently predict drag within the extreme accuracies required for aerodynamic design. Indeed, the computation of 2-D transonic drag is only now becoming a possibility, with accurate engineering codes for general application still not available. Although incremental drag changes are quite useful, an optimization procedure that compares absolute values of wave drag, induced drag and profile drag demands an accurate prediction of absolute drag values of each of these components. The pilot calculations performed by Hicks and co-workers have concentrated on minimizing the wave drag of transonic airfoils. Although wave drag can be computed over an inviscid foil, the shock which generates wave drag also increases the form drag due to the thickening of the boundary layer at the shock wave. Experience suggests that for typical modern transonic

airfoils, the wave drag is small compared to the form drag and reliable computational methods which could be used to accurately investigate the trade-off in various drag components are only now being developed. This is an example of the present difficulty in specifying a valid objective function.

As an example of the application of the optimization method to transonic airfoil design, we examine a pressure distribution from a recent publication by Hicks and Vanderplaats (Reference 85) presented here as Figure 63. In this case, the wave drag is reduced from that of the baseline foil by altering the pressure distribution from one which accelerated continuously into the shock wave to a constant rooftop type pressure distribution which maintains the section lift while decreasing the shock Mach number. This is entirely consistent with current practice in airfoil design. It might be more instructive to begin with a section designed by the hodograph method or an inverse method and investigate improvements to these foils using optimization techniques. This would appear to be the appropriate method by which the relative effectiveness of optimization methods could be illustrated. A particularly interesting example would be a case in which the off design characteristics of a foil designed by the hodograph method are improved using optimization techniques.

The "design variable" specification is perhaps the biggest challenge in the application of optimization methods. In principle, the number of airfoil ordinates used to specify the shape could each be used as design variables, however, if 60 upper surface and 40 lower surface points (a typical number of ordinates) are used, then there are 100 design variables. In practice, no more than about 10 independent design variables can be treated reliably. Thus, the airfoil shape must be constructed from shape functions that describe more than a single ordinate; i.e., coefficients of polynomials used to approximate airfoil shapes. Experience led to the realization that polynomials were not appropriate "shape functions", and schemes that use linear combinations of present supercritical shapes and local geometric perturbations to these shapes appear to be the most practical method to obtain useful results with a small number of design variables. It is important to realize that the optimization method will only identify the best of a particular set of possible airfoil shapes arising from the shape functions. If the actual optimum airfoil is not among this set of shapes, the method cannot find this shape. Hence, the optimization methods require the user to apply as much (and pos-

sibly more) insight into the problem than in the use of inverse methods.

In summary, optimization methods would seem to deserve more attention than they are presently receiving outside of NASA Ames. Attention should be concentrated on developing optimization algorithms that incorporate aerodynamic concepts more directly, while also providing information on the relative importance of the various design variables. Advanced airfoil section designs will remain critically dependent on the aerodynamic insights that are not directly a part of the optimization theory; i.e., it appears that good airfoils are not described by simple analytical functions. Finally, the direct relationship between viscous effects and airfoil design has been difficult to include in a reasonable optimization approach.

#### d. Review of 3-D Transonic Design Methods

No general three-dimensional transonic wing design programs are presently available in this country. Normally, transonic wings are designed by procedures that employ 2-D transonic tools, panel-method wing-body programs in the design mode, and 3-D transonic wing-body programs in the analysis mode. The detailed design procedures are usually proprietary, however, insight into typical industry procedures can be gained by studying Reference 88 and 89. One pilot 3-D transonic inverse method calculation has been reported by Steger and Klineberg (Reference 90). Moreover, Schmidt and Hedman (Reference 91) have reported results obtained using an inverse method available at Dornier (Germany) and the FFA (Sweden). In addition, Hall and Firmin (Reference 7) and Haines (Reference 92) have reported the unpublished work by Langley and Forsey at ARA, Bedford, England. Pilot calculations applying optimization methods to 3-D wing design have been reported in Reference 93.

The comments concerning inverse and optimization methods in 2-D in the previous section carry over to the 3-D design case. Because there has been very little work reported, the review of 3-D transonic design methods is necessarily short. The work on inverse methods by Schmidt and Hedman (Reference 89) indicates that a stable iterative procedure can be found and a converged design obtained. One disturbing aspect of the 3-D inverse method is the possibility that the solution may be non-unique near the wing root, a result which was recently reported by Sloof (Reference 94). The extension of

the optimization methods to 3-D is straightforward. In fact, shape functions for spanwise variations would presumably be less critical and easier to construct than the airfoil shape functions.

In the next section, we illustrate the possible use of the three-dimensional transonic methodology in a design environment by application to two model problems.

e. Application of the 3-D Transonic Program to Wing Design Problems

The feasibility of using the present computer program in transonic wing design as more than a straightforward analysis tool was investigated through two model problems. The first model problem\* was conducted without using the transonic code, but making use of the NASA optimization program CONMIN. The main purpose of the exercise was to gain familiarity with the use of optimization codes in aerodynamic applications. The second model problem was undertaken in order to assess the effort required to introduce an automatic geometry alteration loop driven by the results of a previous iteration into the code. The stability of this type of iterative procedure was also of interest. An inverse method was not investigated because the work of Schmidt and Hedman (Reference 89) demonstrated clearly that such a scheme could be implemented.

The first model problem provided an opportunity to obtain a great deal of experience using CONMIN. The problem was specified simply as follows: Using lifting line theory for the aerodynamic representation of the finite wing, have CONMIN determine the twist distribution required to minimize the induced drag. In this case the exact solution can be found to be

$$\alpha_g(\eta) = \frac{C_L}{\pi AR} \left\{ 1 + \frac{AR(1+\lambda)}{\pi} \cdot \frac{(1-\eta^2)^{\frac{1}{2}}}{[1-(1-\lambda)\eta]} \right\} \quad (66)$$

for straight tapered wings. For an untapered wing, equation (66) for  $\alpha_g$  shows that the basic incidence variation along the span is elliptic. Observing the functional form of the exact solution, we note that this particular ratio of the root of a second order polynomial to a first order polynomial would have been an unlikely selection for the assumed variation of spanwise twist. To repeat, unless Equation (66) was contained as a subset of the functional forms selected for the optimization study the true optimum twist distribution would not have been found. This fact serves to demonstrate the importance of using the insight gained from analytical theories in order to maximize the benefits of numerical solutions.

---

\* The effort described here concerning the first model problem was conducted with internal Grumman funding, but is included in this report for completeness and perspective.

Indeed, initial efforts to obtain the minimum solution using a cubic polynomial for the span variation of twist were not particularly satisfying. The results never approached the true minimum, and apparently there were several combinations of coefficient values that were equally close to true minimum, such that several substantially different answers for the twist variation could be obtained, depending on the initial guess supplied to the program. These calculations typically took on the order of ten iterations, each of which required a number of function evaluations in order to obtain the local gradient of the objective function. In aerodynamic terms this means that there were ten main executions of the aerodynamic program, and a number of "small" executions which were required to be run long enough to provide the local gradient of the solution with respect to each design variable. It is clear that this can quickly lead to an immense amount of computational effort.

Finally, the optimization scheme was run with the design variables consisting of a coefficient to equation (66) and the coefficient of an additional term added to equation (66). Figure 64 shows the path through design space for this two parameter optimization run. Note that the minimum occurs when  $\beta_2 = 0$ , and  $\beta_1 \approx 1$  ( $\beta_1 \neq 1$  exactly because a lift curve slope slightly different than  $2\pi$  was employed). The run terminated after eight iterations, with the numerical solution predicting that the optimum had been achieved. The result demonstrated that the program could in fact select the true optimum if it was embedded in the design variable space. This effort demonstrated both the difficulties and possibilities associated with the use of optimization methods.

The second model problem was considerably different in concept. For this problem the question posed was simply: For a given planform and spanload, determine the twist required to produce the spanload. Initially lifting line theory was employed to verify that the basic iteration scheme adopted would converge for a simple aerodynamic model before attempting to incorporate the iteration into the main program. The twist was determined by adjusting the section incidence at the finite set of span stations at which the computation provided results, without making any assumption concerning the functional relationship between the incidence at adjacent span stations. The basic iteration tested was

$$\alpha_{Dj} = \alpha_j^K + \left( \frac{C_{1Dj} - C_{1j}^K}{C_{1\alpha_j}^{K-1}} \right) \quad (67)$$

where  $j$  denotes the particular span station,  $D$  denotes the design condition and  $k$  indicates the iteration number,  $C_{1\alpha}$  is approximated by

$$C_{1\alpha}^k = \frac{C_1^k - C_1^{k-1}}{\alpha^k - \alpha^{k-1}} \quad (68)$$

For the lifting line simulation this iteration procedure converged to the exact solution given by Equation (66) in about four or five iterations. This result was obtained without difficulty even though the  $C_{1\alpha}$  approximation given in Equation (68) is very poor for numerical computation due to the progressively smaller differences between the values as the iteration converges.

Equation (67) is equivalent to a more general form:

$$\{\alpha_D\} = \{\alpha^k\} + [\tilde{A}^{k-1}]^{-1} \{C_{1D} - C_1^k\}$$

Where  $[\tilde{A}]$  is an approximation to the actual influence coefficient matrix which relates  $C_1$  and  $\alpha$ :

$$\{C_1\} = [A] \{\alpha\}. \quad (69)$$

In the present method  $[\tilde{A}]$  has been given by the extremely simplified relationship in Equation (68) for the diagonal terms, with the off-diagonal terms assumed to be zero. This result shows that  $[A]$  can be crudely approximated if an iteration to determine the final result is allowed. Naturally, as the approximation to  $[A]$  improves, the number of iterations required is reduced.

Modifications to the basic inviscid program to include this type of iteration scheme were incorporated without difficulty. It was found that a relatively fine grid was required in order to obtain the straight wing result computed previously using the lifting line aerodynamic mode. Refinements to the iteration included the use of underrelaxation of the twist increment and the use of the initial  $C_{1\alpha}$  value for all iterations. These refinements led to a smoothly converging solution that took about fifty percent longer than the basic solution. The method was then applied to a  $45^\circ$  swept untapered wing. The refined procedure led to a solution with the results obtained shown in Figure 65, which also contains the straight wing results. In this case, attempts to compute the result while  $C_{1\alpha}$  changed from iteration to iteration led to a diverging result at the point where no shift in angle was required (about 45% semispan), and shows

that in an actual production program an improved approximation be  $[A]$  should be included. However, this improved  $[\tilde{A}]$  could undoubtedly be constructed without difficulty so that a design option of the type described above could be included in the basic program without difficulty.

In this section we have demonstrated the variety of possibilities that arise when incorporation of design options is suggested. One of the options would provide immediate benefits to the designer, while the optimization approach, although quite promising, would take much more study in order to produce a reliable design tool.

f. A Practical Approach to an Intermediate Design Code

The results of the efforts reported thus far provide a basis for considering how best to approach the question of actually implementing a design option in the present code. The preceding discussion and examples have shown that a variety of design methods could be adopted. The goal of the approach described in this section is to provide a rational foundation for a code which would provide the designer with a reliable tool quickly, while also demonstrating basic techniques that could be adopted in more sophisticated transonic methodologies as they are developed. Any resulting code must be easy to use. One of the keys to a successful result is to incorporate a number of features one at a time in order to reduce the risk. Each one of these items could be tested separately in order to assess its practicality before including it in the actual design option program. The approach described here meets these requirements by proposing a "blended" methodology which combines inverse and optimization methods in a manner that eliminates the weaknesses of each of the methods when used separately.

The transonic wing design procedure we envision proceeds as follows:

(1) A "target" pressure distribution should be specified in the manner of present wing design work. This requires some experience on the part of the aerodynamicist, but this step is the one in which he can contribute his insights and knowledge. Readers not familiar with the typical isobar design procedures employed in industry should consult the papers by Haines (References 95 and 96). It will be some time before the computer optimization procedures can competently eliminate this step.



(2) The related baseline 2-D airfoil section (or sections) should be designed with 2-D inverse methods in the manner presently used. The numerical resolution available in 2-D programs exceeds any 3-D program, so that baseline sections should always be designed using the 2-D methods. The 3-D design efforts will then consider perturbations to these baseline shapes.

(3) The basic wing twist required to obtain the desired spanload using the 2-D sections found in step 2 should be determined by an iterative procedure that would be an extension of the model problem procedure described above. At this point, the designer should have a good first wing design, which could be considered the baseline wing for further improvements.

(4) In regions on the wing where the target pressure distribution has not been achieved, the aerodynamicist should specify the desired pressure distribution and an inverse method should be employed in order to determine the required geometry modification necessary to achieve the target pressure distribution.

(5) The key step in the procedure is to examine the geometry modifications found in step 4. The results found in that step probably violated some basic constraints associated with the design, such as section thickness or closure. However, the inverse method should have provided the desired shape function which can then be used in an optimization procedure, which can then be used to minimize the difference between the target pressure distribution and the best possible pressure distribution which can be obtained while also meeting constraints such as geometric limitations and off-design performance.

The 5 step procedure outlined above requires the modification of the small disturbance theory program to include a 'local' inverse method wherein geometry and pressures can both be specified over different portions of the planform. The other requirement is an optimization class of algorithm which can minimize the difference between two pressure distributions, subject to a variety of constraints. Both of these capabilities can be incorporated without difficulty.

The novel idea contained in this approach is the use of the inverse method to suggest the shape functions which can be used as design variables in the optimization procedure. This procedure removes the main deficiency in the optimization methods by introducing a "natural" shape function which

should allow the optimization procedure to converge quickly to the final result. This fast convergence is further aided by the fact that the initial starting point for the optimization program should be "close" to the final result. Because the inverse method is not required to produce a design meeting the geometrical constraints, its major drawback is removed. By blending the two methodologies in the proposed manner, an outstanding transonic wing design tool could be developed.

#### g. Conclusions On Design Feasibility

It is feasible to construct an outstanding transonic wing design tool based on the present transonic analysis methodology. This code would be a blend of inverse and optimization methods that would remove the restrictions inherent in either approach when considered separately. The resulting program would make only slight additional demands on computing system resources.

Having outlined in the last section the approach that would provide this tool, we recommend that the development of a blended inverse/optimization method be undertaken. This effort would be based on methods which have already been demonstrated separately, insuring the success of the new effort. Particular attention should be placed on the fundamental aspects of the methodology in order to provide a solid foundation for continued development along the lines outlined. One of the more significant features of the blended approach is that the optimization method is basically independent of the aerodynamic methods and will be particularly insensitive to the refinement of the aerodynamic methodology.

INPUT/OUTPUT PRESSURE DISTRIBUTIONS

RESULTING EQUIVALENT INVISCID SECTIONS

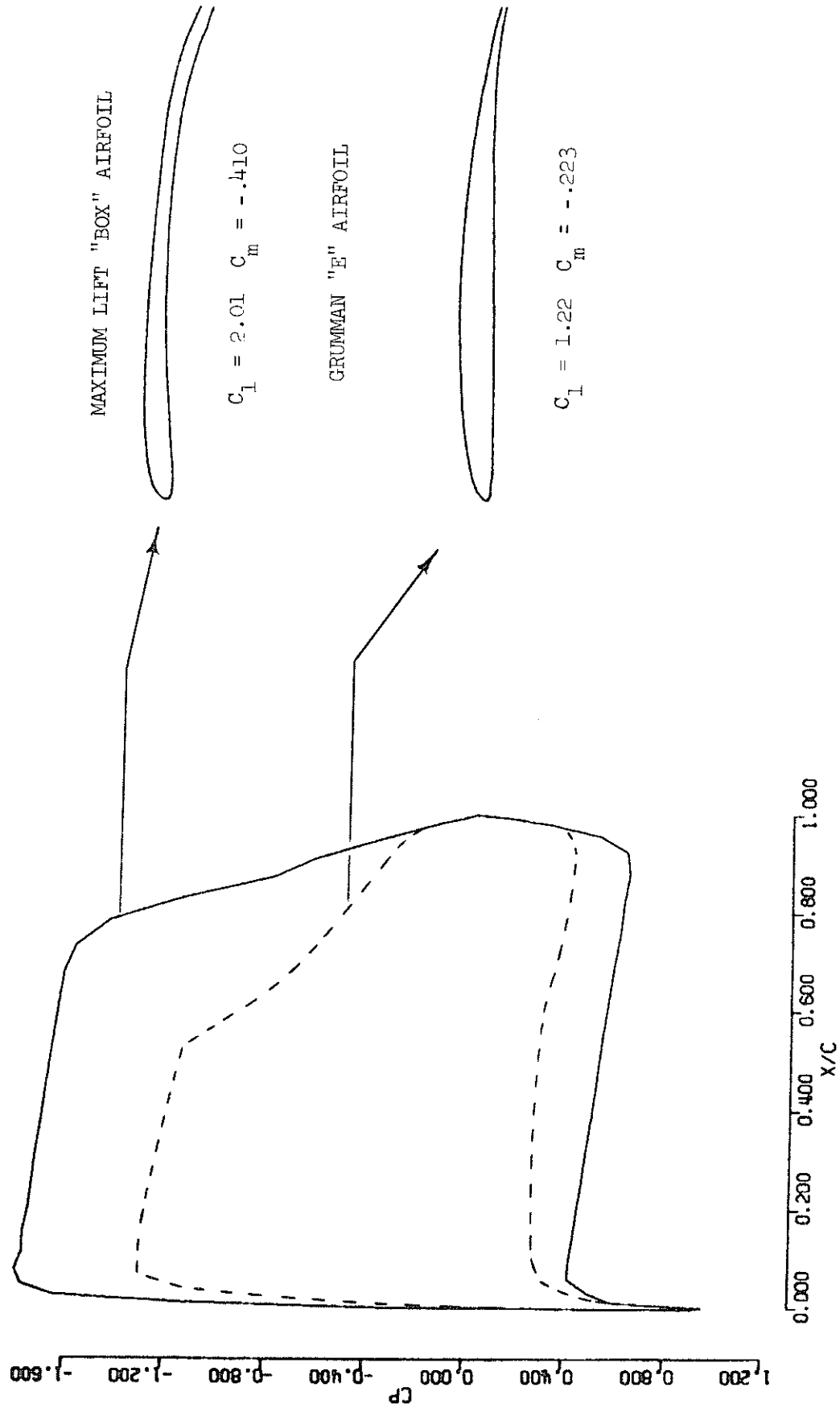
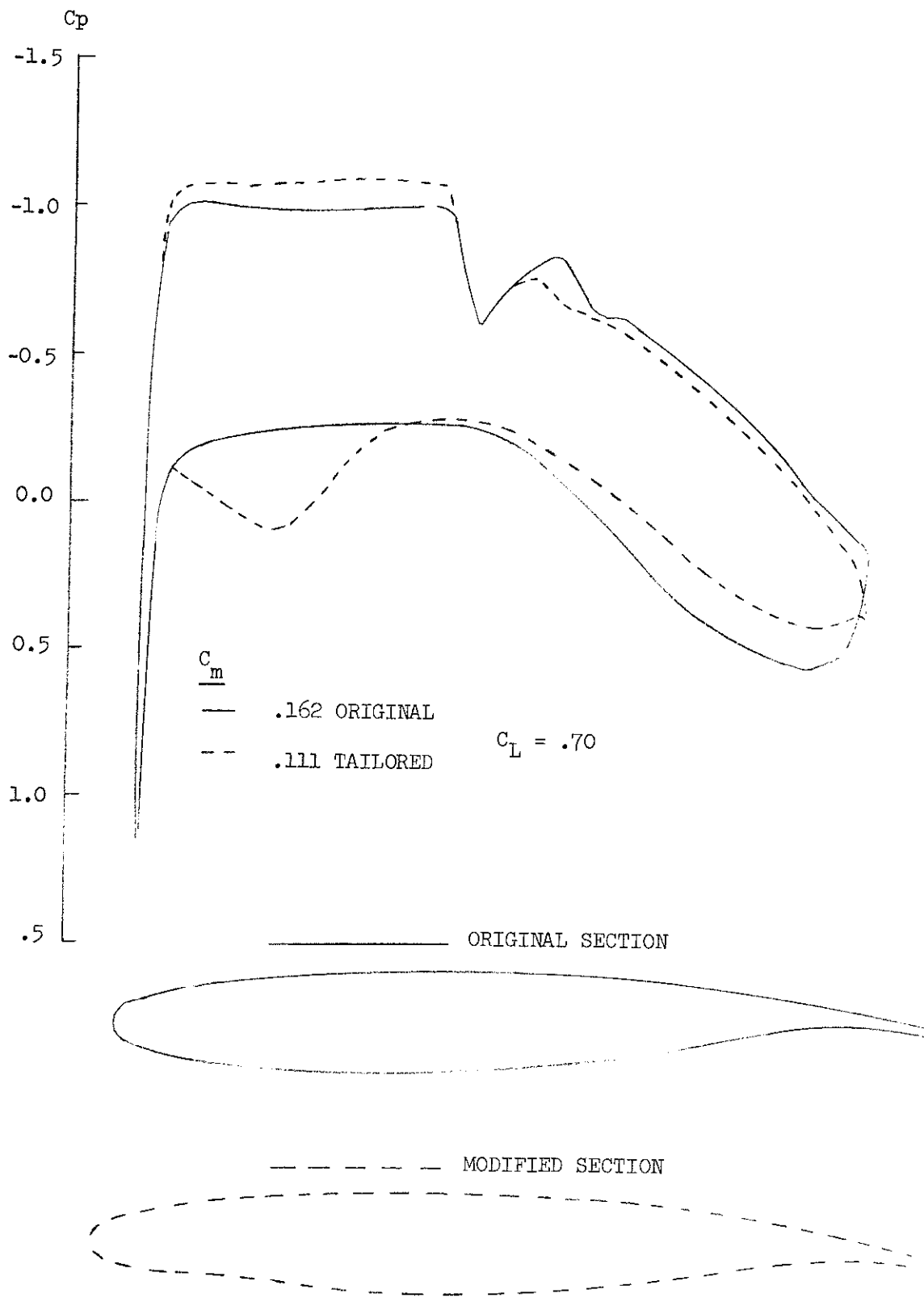


Figure 61. Advanced Airfoil Synthesis M = .683



$M_\infty = .735$

Figure 62. Low  $C_{m0}$  Tailored Airfoil

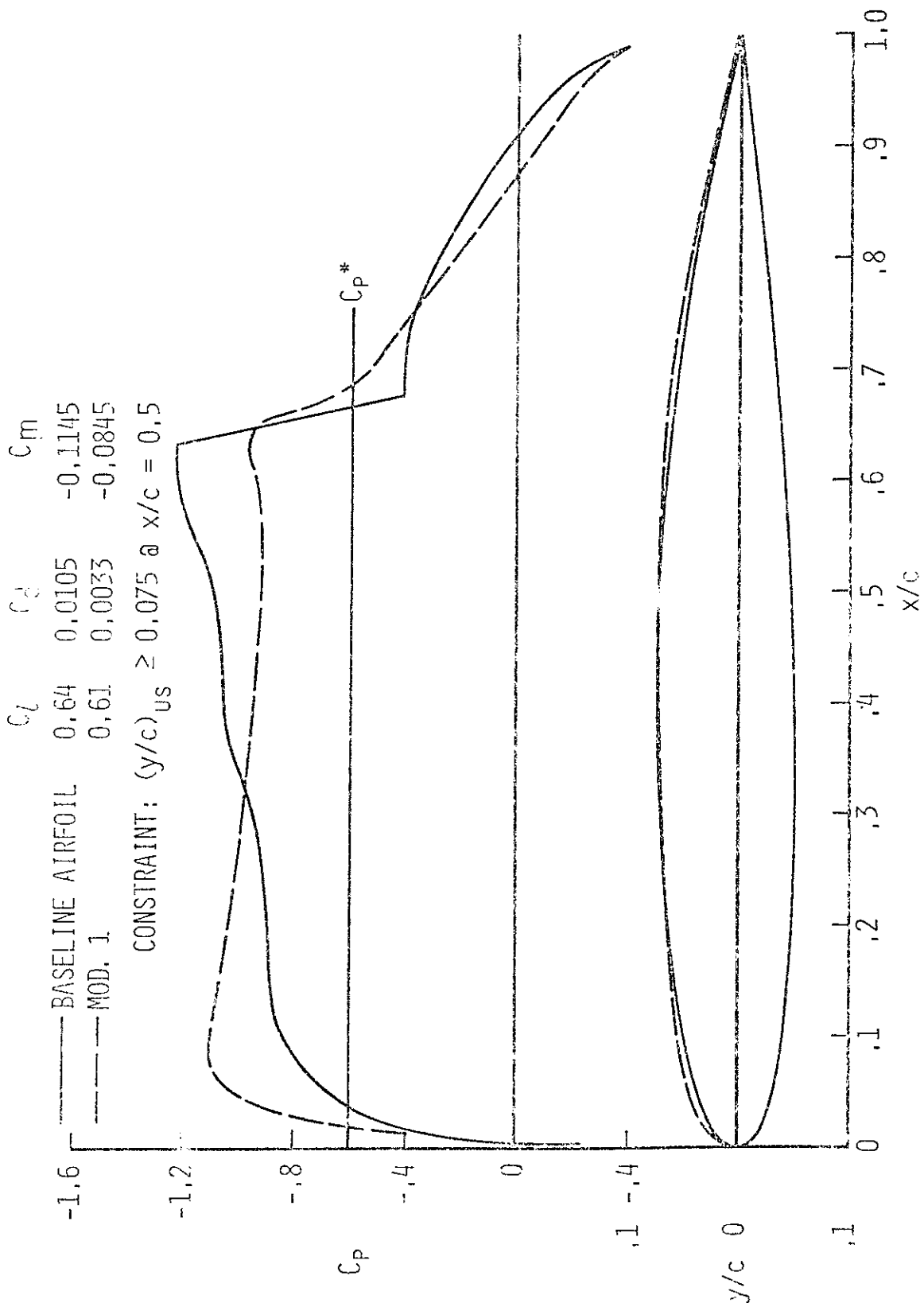


Figure 63. Inviscid Drag Minimization;  $M = .75$   $\alpha = 1^\circ$  Via Optimization Techniques  
(From Hicks, Reference 87)

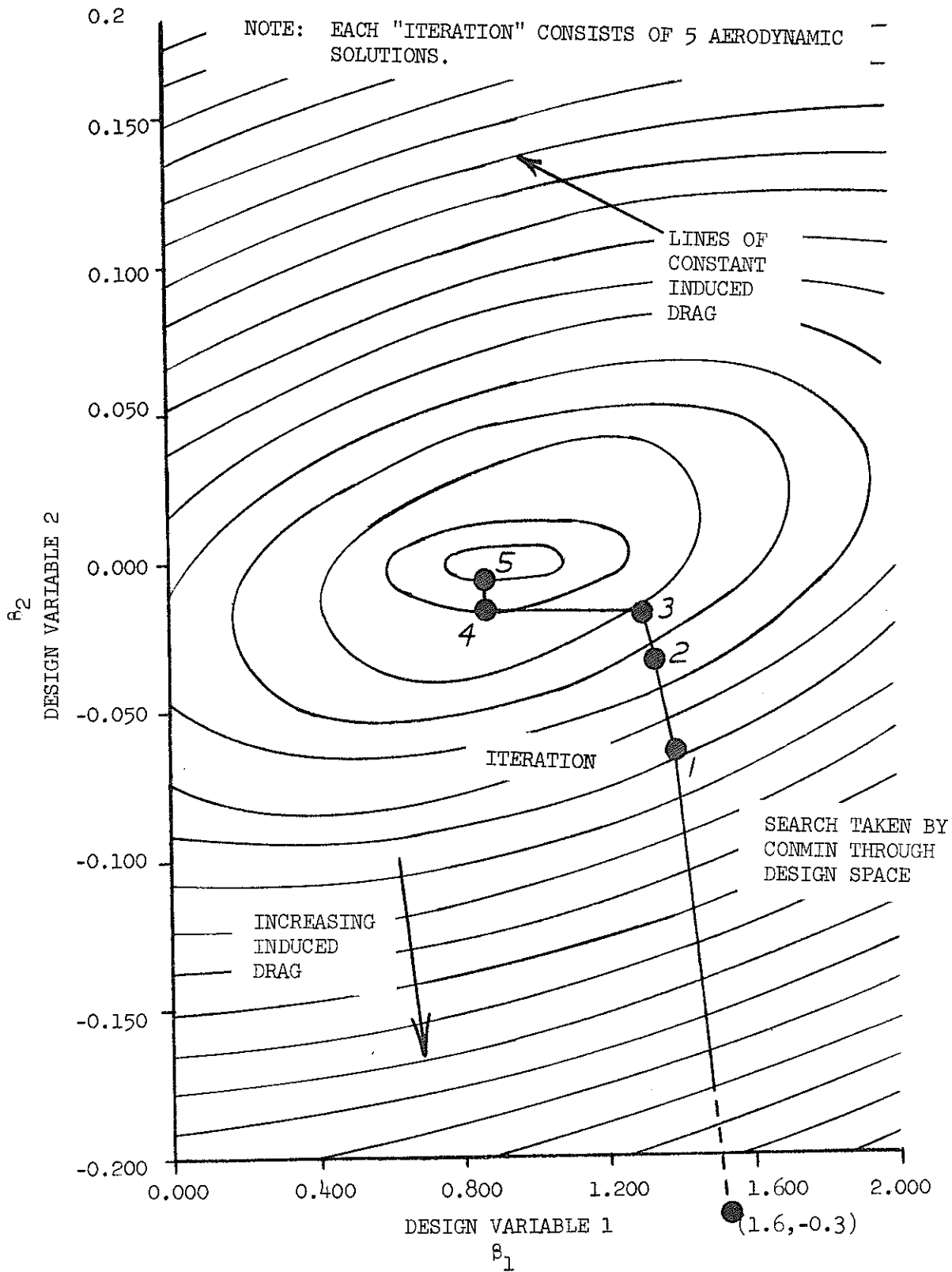


Figure 64a. Example of Finite Wing Aerodynamic Model Coupled With Large Optimization Program - Search For Minimum Induced Drag Using Two Parameter Twist Function

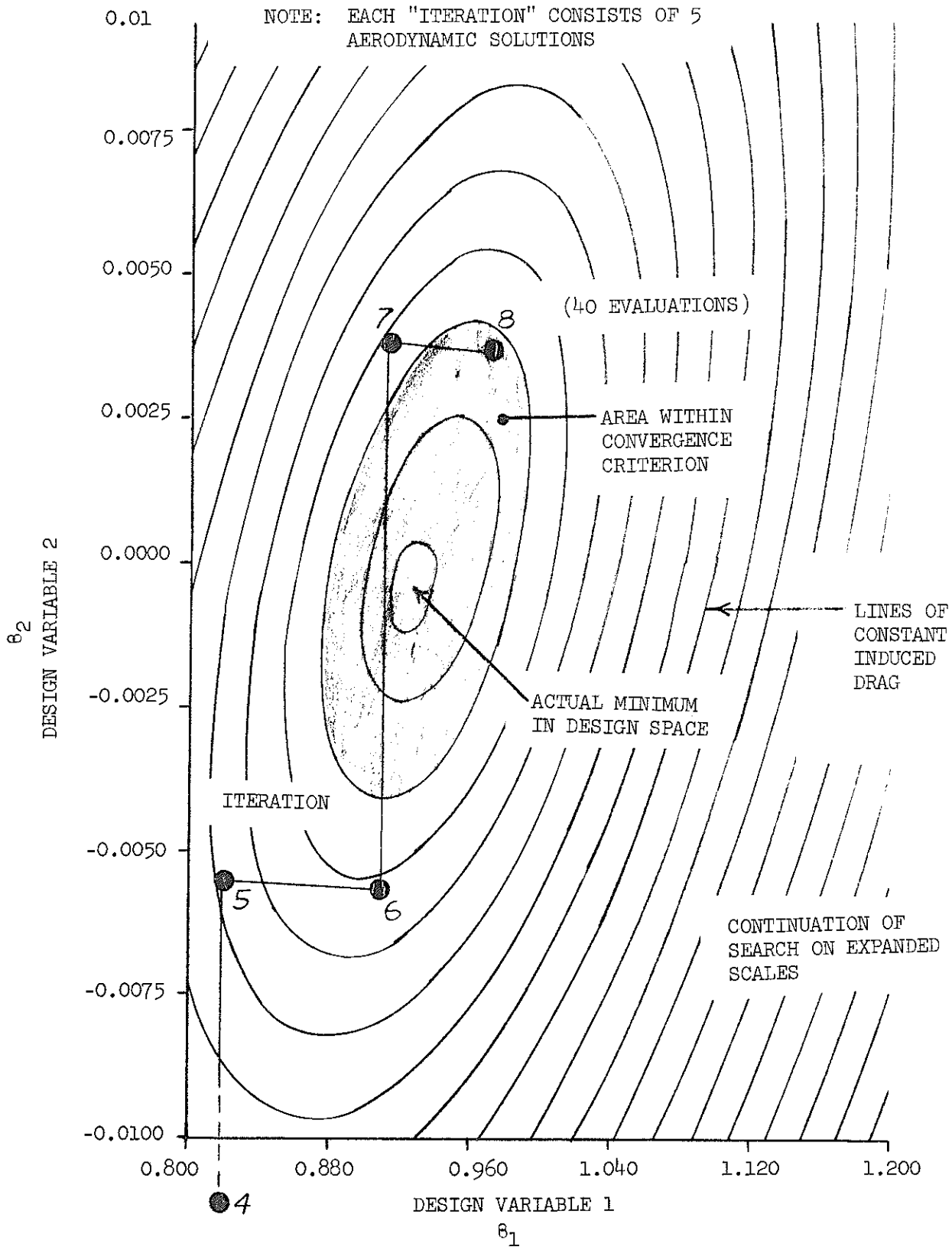


Figure 64b. Example of Finite Wing Aerodynamic Model Coupled With Large Optimization Program - Search For Minimum Induced Drag with 2 Parameter Twist Function

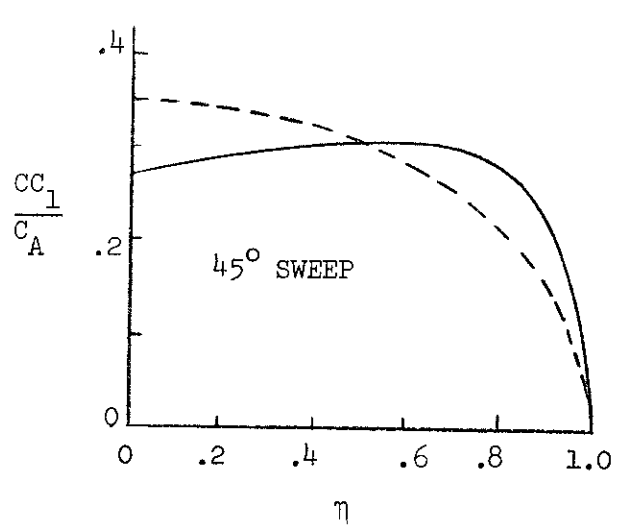
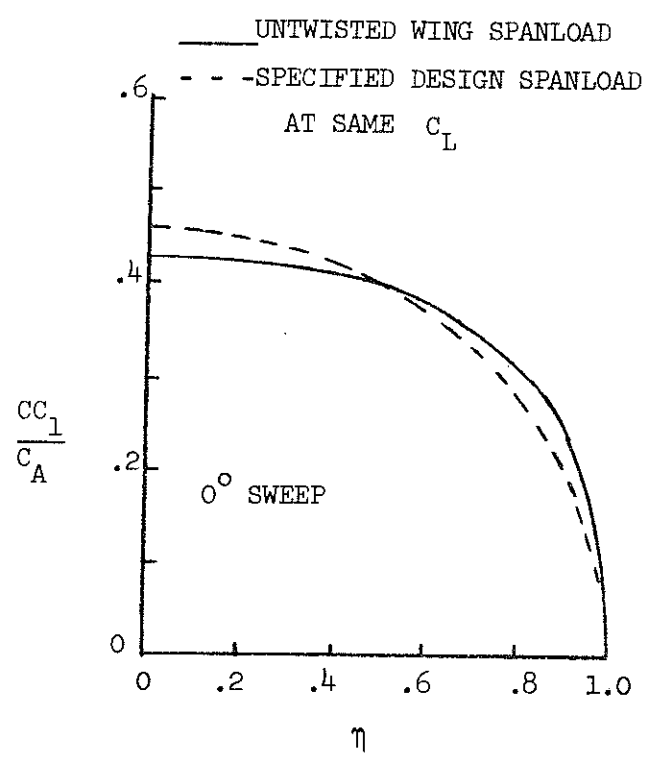
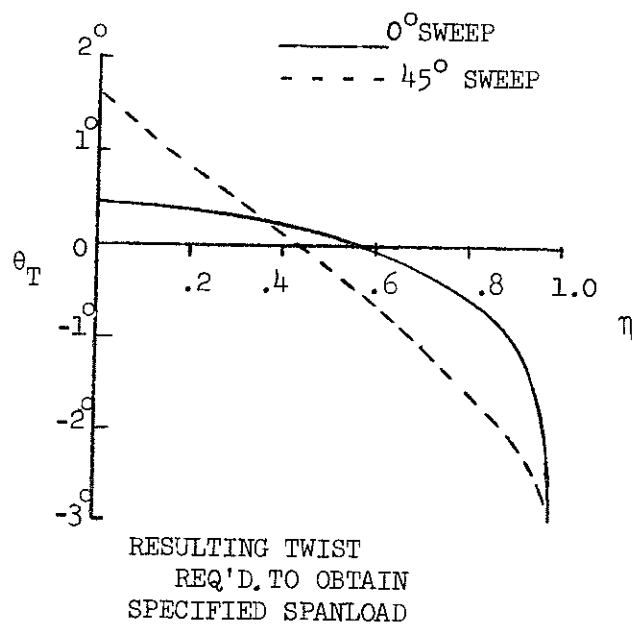
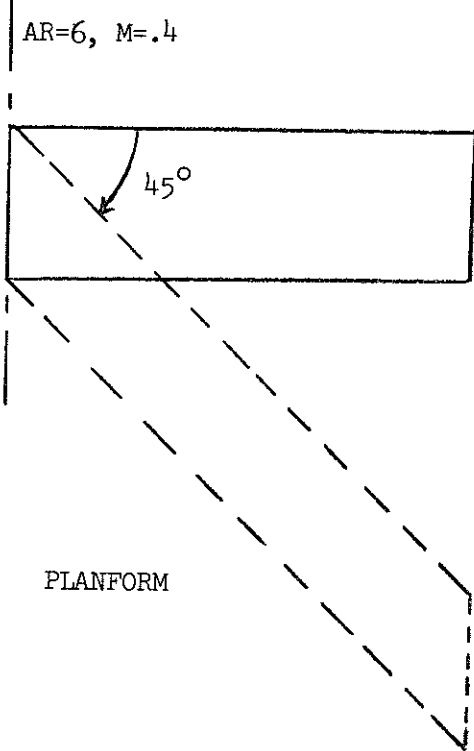


Figure 65. Wing Design Example



### SECTION III

#### CONCLUSIONS

Major advances are being made in the computation of transonic flows over wing-body combinations. In the present work an inviscid three-dimensional small disturbance theory program has been coupled with a boundary layer program and the resulting code re-designed to be extremely easy to use.

In the new program the user has the ability to examine a number of effects:

- o Viscous effects via a fully coupled strip boundary layer of infinite swept wing type.
- o Local strong shock interaction at shock waves
- o Shallow separations at the trailing edge and in the cove region of supercritical airfoils
- o Reynolds number and boundary layer transition location
- o Infinite yawed wing results including 2-D cases
- o Fully conservative (FCR) and non-conservative (NCR) inviscid solution procedures
- o Modified small disturbance theory (MSD) or classical small disturbance theory governing equations (CSD)
- o Riegels' Rule effects
- o Body effects on wing pressures, including simple area ruling effects via body lines input, or detailed fuselage effects via body slope input
- o Fully three-dimensional boundary layer predictions via automatic data set-up for the new boundary layer program written during the present effort.

In order to provide a user-oriented program the following special provisions were included:

- o A complete visualization of the program input and results are available via the automated graphics package.

- o An internal check is made of input data sets for consistency, and the program stops when the solution is either converged or encountering difficulties in order to conserve computing time.

The resulting computer code was applied to numerous configurations, wherein the identical code was used for each case without any special "tuning".

The conclusions resulting from these studies can be summarized as follows:

- o For relatively simple conceptual type aircraft configurations, the program provides excellent results for a wide range of Mach numbers, sweep angles and taper ratios.
- o The agreement with the advanced technology transonic transport results provide confidence in the program for transport type aircraft
- o Advanced technology fighter configurations present special problems which still require some resolution, such as the detailed treatment of wing-glove-body blending. Nevertheless, encouraging results have been obtained in several instances although in many cases a number of complicating factors prevent a final determination of the source of the disagreement.

Perhaps the single most important result of this effort has been the development of a code which allows the routine use of the new 3-D transonic methods outside of a few government and industrial research labs. The present code and its documentation provides a baseline upon which an aerodynamicist has extreme flexibility to investigate both aerodynamic configurations and program modifications. The resulting program should have major impact on the design of advanced aircraft.

## SECTION IV

### RECOMMENDATIONS FOR FUTURE WORK

Due to the extremely broad range of aerodynamic effects investigated in the present work, the recommendation for future work tends to be all encompassing. The various requirements can be divided between basic research, general requirements for aerodynamic code development and specific extensions and investigations related to the present program.

Basic research programs which would have a direct application to the computation of transonic flowfields over wing-body configurations are:

- o A baseline experimental three-dimensional boundary layer study for a typical supercritical wing body combination. This study is required in order to validate the fully three-dimensional boundary layer prediction methods and to assess the range of applicability of the more approximate methods such as the infinite swept wing strip boundary layer approach.
- o Basic theoretical work in the area of separated flows is required, with the specific goal of producing rational engineering methods that could be incorporated into codes designed along the lines of the present program. This work should include the calculation of the three-dimensional viscous wake downstream of finite wings.
- o Basic numerical research into the acceleration of the inviscid solution process is required in order to reduce the computational cost of the calculation.

General requirements for future computational aerodynamic code development should include:

- o A uniform input format for body and wing geometry should be adopted.
- o Standard output format and nomenclature should be adopted.

Specific extensions of the present code that would prove invaluable in the future use of the method include:

- o A general re-examination of the body-glove-wing juncture, and the mapping bending near the body is needed in order to improve the quality of the local solution.
- o Geometric extensions to the configurations that can be handled should be considered. Many advanced technology configurations will require the explicit treatment of canards and winglets. In addition, nacelle inlet effects are usually required in order to perform detailed transonic wing designs. These features will have to be incorporated if the program is to fully supplant the present day panel methods as a design tool at transonic speeds.
- o Steady state aeroelastic effects must be included when computing the transonic flow over modern aircraft. The wing deflection could be incorporated at the same time the boundary layer corrections are made with a minimum of additional computational effort. This would greatly enhance the general utility of the code.
- o The restriction to Mach numbers less than one is not a basic limitation of any of the methods, and the code could be extended to the upper transonic regime ( $M = 1.25$ ) without difficulty. This extension would complete the bridging of the linear subsonic and supersonic regimes so that there would be no "gaps" in the range of Mach numbers over which routine aerodynamic predictions can be made.
- o Substantial reductions in the real and computational time required for wing design work could be achieved by the incorporation of some design options into the program. The options should include local inverse solution capability, and a simple application of the geometry alteration iteration procedures analogous to those in optimization techniques.

Although the program outlined above is somewhat ambitious it does in fact reflect the broad scope of the effort undertaken in the present program.

#### REFERENCES

1. Ballhaus, W. F., Bailey, F. R. and Frick, J., "Improved Computational Treatment of Transonic Flow About Swept Wings," Advances in Engineering Sciences, NASA CP-2001, 1976.
2. Murman, E. M. and Cole, J. D., "Calculation of Plane Steady Transonic Flow," AIAA Journal, Vol. 9, No. 1, January 1971, pp. 114-121.
3. Jameson, A., "Transonic Flow Calculations for Airfoils and Bodies of Revolution," Grumman Aerodynamics Report 390-71-1, December 1971.
4. Bavitz, P., "An Analysis Method for Two-Dimensional Transonic Viscous Flow," NASA TN-D-7718, January 1975.
5. Melnik, R. E., Chow, R. and Mead, H. R., "Theory of Viscous Transonic Flow Over Airfoils at High Reynolds Number," AIAA Paper No. 77-680, June 1977.
6. Jameson, A., "Iterative Solution of Transonic Flows Over Airfoils and Wings," Comm. Pure Appl. Math., Vol. 27, 1974, pp. 283-309.
7. Hall, M. G. and Firmin, M. C. P., "Recent Development in Methods for Calculating Transonic Flows Over Wings," ICAS Paper No. 74-18, August 1974.
8. Schmidt, W. and Vanino, R., "The Analysis of Arbitrary Wing-Body Combinations in Transonic Flow Using a Relaxation Method," Symposium Transsonicum II, Springer-Verlag, Berlin, 1976, pp. 523-532.
9. Lomax, H., Bailey, F. R. and Ballhaus, W. F., "On the Numerical Simulation of Three-Dimensional Transonic Flow with Application to the C-141," NASA TN-D-6933, 1973.
10. Boppe, C. W., "Calculation of Transonic Wing Flows by Grid Embedding," AIAA Paper No. 77-207, January 1977.
11. Nash, J. F. and Scruggs, R. M., "An Implicit Method for the Calculation of Three-Dimensional Boundary Layers on Finite, Thick Wings," Sybucon Report SYB-76-102, August 1976 (also issued as Vol. III of the present report).

12. Hedman, S. G., "Pressure Distributions for a Swept Wing-Body Configuration Obtained from Coupling Transonic Potential Flow Calculations and Boundary Layer Calculations," Prediction of Aerodynamic Loading, AGARD-CP-204, February 1977.
13. Kordulla, W., "Investigations Related to the Inviscid-Viscous Interaction in Transonic Flows About Finite 3-D Wings," AIAA Paper No. 77-209, January 1977.
14. Ballhaus, W. F., "Some Recent Progress in Transonic Flow Computations." VKI Lecture Series in Computational Fluid Dynamics, Von Karman Institute for Fluid Dynamics, Rhode-St.-Genese, Belgium, March 1976.
15. Krupp, J. A., "The Numerical Calculation of Plane Steady Transonic Flows Past Thin Lifting Airfoils," Boeing Scientific Research Laboratories, D180-12958-1, June 1971
16. Klunker, E. B., "Contribution to Methods for Calculating the Flow About Thin Lifting Wings at Transonic Speeds - Analytical Expression for the Far Field," NASA TN-D-6530, 1971.
17. Jameson, A., "Transonic Flow Calculations," VKI Lecture Series in Computational Fluid Dynamics, Von Karman Institute for Fluid Dynamics, Rhode-St. Genese, Belgium, March 1976.
18. Jameson, A., "Numerical Solution of Nonlinear Partial Differential Equations of Mixed Type," in Numerical Solution of Partial Differential Equations III, Academic Press, New York, 1976, p. 275-320.
19. Van Dyke, M. D., "Second-Order Subsonic Airfoil Theory Including Edge Effects," NACA R-1274, 1956.
20. Keyfitz, B. L., Melnik, R. E. and Grossman, B., "The Leading Edge Singularity in Transonic Small-Disturbance Theory," Grumman Research Department Report RE-525, October 1976.
21. Jameson, A. and Caughey, D. A., "A Finite Volume Method for Transonic Potential Flow Calculation," AIAA Paper No. 77-635, June 1977.
22. Bradshaw, D., Mizner, G. A. and Unsworth, K., "Calculation of Compressible Turbulent Boundary Layers on Straight-Tapered Swept Wings," AIAA J., March 1976, p. 399-400.
23. Moore, F. K., "Three Dimensional Boundary Layer Theory," Advances in Applied Mechanics, Vol, IV, Academic Press, New York, 1956, p. 187-191.

24. Nash, J. F. and Scruggs, R. M., "Three-Dimensional Compressible Boundary Layer Computations for a Finite-Swept Wing," NASA CR-112158, 1972.
25. Nash, J. F. and Tseng, R. R., "The Three-Dimensional Turbulent Boundary Layer on an Infinite Yawed Wing," The Aeronautical Quarterly, November 1971, p. 346-362.
26. Bradshaw, P., and Ferriss, D. H., "Calculation of Boundary Layer Development Using the Turbulent Energy Equation. Compressible Flow on Adiabatic Walls," J. Fluid Mech, Vol. 46, 1971 p. 83.
27. Kuethe, A. M., McKee, P. B. and Curry, W. H., "Measurements in the Boundary Layer of a Yawed Wing," NACA TN-1946, September 1949.
28. Altman, J. M. and Hayter, N. F., "A Comparison of the Turbulent Boundary Layer Growth on an Unswept and Swept Wing," NACA TN 2500, September 1951.
29. Adams, J. C., Jr., "Numerical Calculation of the Subsonic and Transonic Turbulent Boundary Layer on an Infinite Yawed Airfoil," AEDC-TR-73-112, July 1973.
30. Bradshaw, P., "Calculation of Three-Dimensional Turbulent Boundary Layers," JFM, Vol. 46, Pt. 3, p. 417-445, 1971
31. Prandtl, L., "The Mechanics of Viscous Fluids," Aerodynamic Theory, W. F. Durand, Ed. Springer, Berlin, Vol. 3, p. 90, 1935.
32. Bauer, F. and Korn, D., "Computer Simulation of Transonic Flow Past Airfoils with Boundary Layer Correction," AIAA 2nd Computational Fluid Dynamics Conference Proceedings, June 1975.
33. Preston, J. H., "The Effect of the Boundary Layer and Wake on the Flow Past A Symmetrical Airfoil at Zero Incidence," ARC R&M No. 2107, July 1945.
34. Lighthill, M. J., "On Displacement Thickness," JFM, Vol. 4, 1958, p. 383-392.
35. Pinkerton, R. M., "Calculated and Measured Pressure Distributions Over the Mid-Span Section of the NACA 4412 Airfoil," NACA Report No. 563, 1936.
36. Rogers, E. W. L., and Hall, I. M., "An Introduction to the Flow about Plane Swept-back Wings at Transonic Speeds," Journal of the Royal Aeronautical Society, Vol. 64, No. 596, August 1960.

37. Maskew, B. and Dvorak, F. A., "Investigations of Separation Models for the Prediction of  $C_{LMAX}$ ," AHS Preprint 77.33-01, May 1977.
38. Milgram, J. H., "Calculation of Attached or Partially Separated Flow Around Airfoil Sections," Journal of Ship Research, Vol. 21, No. 2, June 1977, p. 69-81.
39. Green, J. T., "A Discussion of Viscous-Inviscid Interactions at Transonic Speeds," RAE TR 720 50, May 1972.
40. Pearcey, H. H., Osbourne, J. and Haines, B., "The Interaction Between Local Effects at the Shock and Rear Separation," AGARD CP No. 35, 1968.
41. Cebeci, T., Kaups, K., and Ramsey, J. P., "A General Method for Calculating Three-Dimensional Compressible Laminar and Turbulent Boundary Layers on Arbitrary Wings," NASA Report CR 2777, 1977.
42. Piers, W. J., Schipholt, G. J. and van den Berg, B., "Calculation of the Flow Around a Swept Wing, Taking into Account the Effect of the Three-Dimensional Boundary Layer," NLR, TR 75076 U, May 1975.
43. Rose, W. C., and Seginer, A. "Calculation of Transonic Flow Over Supercritical Airfoil Sections", AIAA Paper No. 77-681, June 1977.
44. Yoshihara, H. and Zonars, D., "An Analysis of Pressure Distributions on Planar Supercritical Profiles With and Without Jet Flaps at High Reynolds Numbers," GDCA-ERR-1684, December 1971.
45. Inger, G. R. and Mason, W. H., "Analytical Theory of Transonic Normal Shock-Turbulent Boundary Layer Interaction," AIAA J., Vol. 14, No. 9, September 1976, p. 1266-1272.
46. Murman, E. M. and Cole, J. D., "Inviscid Drag at Transonic Speeds," AIAA Journal, Vol. 9, No. 1, January 1971
47. Cole, J. D., "Perturbation Methods in Applied Mechanics," Ginn-Blaisdell, 1968.
48. Ballhaus, W. F. and Bailey, F. R., "Numerical Calculation of Transonic Flow About Swept Wings," AIAA Paper 72-677, June 1972.
49. Ashly, H. and Landahl, M., "Aerodynamics of Wings and Bodies," Addison-Wesley, 1965.



50. Van Der Vooren, J., Sloof, J. W., Huizing, G. H. and Van Essen, A., "Remarks On the Suitability of Various Transonic Small Perturbation Equations to Describe Three-Dimensional Transonic Flow; Examples of Computations Using A Fully-Conservative Rotated Difference Scheme," Symposium Transonicum II.
51. Nash, J. F., "The Calculation of Three-Dimensional Turbulent Boundary Layers in Incompressible Flow," JFM, 37, Pt. 4, p. 625.
52. Monnerie, B., "Etude experimentale d'une aile en fleche dans le domaine transsonique. Paper presented at Euronech 40, Stockholm, 1973.
53. Treadgold, D., Jones, A. F., "An Outline of the Research Program on Swept Wings in the RAE Eight Foot By Six Foot Transonic Wind Tunnel," RAE Technical Memorandum Aero 1282 (1971).
54. Williams, C. V., "An Investigation of the Effects of a Geometric Twist on the Aerodynamic Loading Characteristics of a  $45^\circ$  Sweptback Wing-Body Configuration at Transonic Speeds," NACA RM L54H18, 1954.
55. Runckel, J. F. and Lee, E. E., Jr., "Investigation of Transonic Speeds of the Loading Over a  $45^\circ$  Sweptback Wing Having an Aspect Ratio of 3, Taper Ratio of .2, and NACA 65A004 Airfoil Sections," NASA TN D-712, 1961.
56. Loving, D. L. and Estabrooks, B. B., "Transonic Wing Investigation in the Langley Eight Foot High Speed Tunnel at High Subsonic Mach Numbers and at Mach Number of 1.2," NACA RM L51F07, 1951.
57. McDevitt, J. B., "An Experimental Investigation of Two Methods for Reducing Transonic Drag of Swept Wing and Body Combinations," NACA RMA55B21, April 1955.
58. Spacht, G., Grumman Aerospace Corporation, personal communication, June 1977.
59. Keener, E. R., "Pressure Measurements Obtained in Flight at Transonic Speeds for a Conically Cambered Delta Wing." NASA TM X-48, October 1959.
60. Unpublished Data, Grumman Aerospace Corporation, 1977.
61. Unpublished Data, Grumman Aerospace Corporation, 1975.
62. Cosenza, C. J. and Kummeth, L. J., "Transonic Aircraft Technology (TACT) Program," AIAA 74-620, July 1974.

63. Dickey, D., "Transonic Aircraft Technology TACT Aircraft-Geometric Characteristics," MAIR-595-19, August 1973.
64. Personal communication, TACT Office AFFDL/FXS, WPAFB, Ohio, May 1977 (Aeroelastic Twist).
65. Personal communication, TACT Office AFFDL/FXS, WPAFB, Ohio, May 1976 (Flight Pressures).
66. Personal communication, TACT Office AFFDL/FXS, WPAFB, Ohio, May 1977 (Wind Tunnel Pressures).
67. Supercritical Wing Technology -- A Progress Report on Flight Evaluations. NASA SP-301, 1972.
68. Harris, C. D. and Bartlett, D. W., "Tabulated Pressure Measurements on a NASA Supercritical-Wing Research Airplane Model with and Without Fuselage Area-Rule Additions at Mach 0.25 to 1.00," NASA TM X-2634, 1972.
69. Harris, C. D., "Wind-Tunnel Measurements of Aerodynamic Load Distribution on a NASA Supercritical-Wing Research Airplane Configuration," NASA TM X-2469, 1972.
70. Montoya, L. C. and Banner, R. D., "F-8 Supercritical Wing Flight Pressure, Boundary Layer and Wake Measurements and Comparisons with Wind Tunnel Data," NASA TM X-3544, March 1977.

---

71. Wennagel, G., Loshigian, H. and Rosenbaum, J., "RAVES - Rapid Aerospace Vehicle Evaluation System," ASME Winter Annual Meeting, Houston, Texas, 1975.
72. Yasaki, E. K., "Super-Super Computer," DATAMATION, March 1977.
73. Vachris, A. F. and Yaeger, L. S., "QUICK-GEOMETRY -- A Rapid Response Method for Mathematically Modeling Configuration Geometry," NASA SP-390, October 1975.
74. Craidon, C., "Description of a Digital Computer Program for Airplane Configuration Plots," NASA TM X-2074, 1970.
75. Marconi, F. and Yaeger, L., "Development of A Computer Code for Calculating the Steady Super/Hypersonic Inviscid Flow Around Real Configurations," Volume II, Code Description, NASA CR-2676, May 1976.
76. Carlson, H. W. and Middleton, W. H., "A Numerical Method for The Design of Camber Surfaces of Supersonic Wings with Arbitrary Planforms," NASA TN-D-2341, 1964.

77. CISE Methodology, Grumman Aerospace Engineering Report WT 997R-128, August 1976 (Proprietary).
78. Vanderplaats, G. N., "Automated Optimization Techniques for Aircraft Synthesis," AIAA Paper No. 76-909, September 1976.
79. Miele, A. (Ed.), Theory of Optimum Aerodynamic Shapes, Academic Press, New York, 1965.
80. Thwaites, B. (Ed.), Incompressible Aerodynamics, Oxford University Press, Oxford, 1960.
81. Tranen, T. L., "A Rapid Computer Aided Transonic Airfoil Design Method," AIAA Paper No. 74-501, June 1974.
82. Volpe, G., "Recent Advances in Airfoil Analysis and Design," Grumman Aerodynamics Memorandum 75-27, February 1975.
83. Carlson, L. A., "Transonic Airfoil Analysis and Design Using Cartesian Coordinates," AIAA 2nd Computational Fluid Dynamics Conference, June 1975.
84. Hicks, R. M., Murman, E. M. and Vanderplaats, G. N., "An Assessment of Airfoil Design by Numerical Optimization," NASA TM X-3092, July 1974.
85. Vanderplaats, G. N. and Hicks, R. M., "Numerical Airfoil Optimization Using a Reduced Number of Design Coordinates," NASA TM X-73151, July 1976.
86. Bauer, F., Garabedian, P. and Korn, D., Supercritical Wing Sections, Springer Verlag, Berlin, 1972.
87. Hicks, R. M. and Vanderplaats, G. N., "Application of Numerical Optimization to the Design of Supercritical Airfoils without Drag-Creep," SAE Paper 770440, April 1977.
88. Gingrich, P. B., Child, R. B. and Panageas, G. N., "Aerodynamic Configuration Development of the Highly Maneuverable Aircraft Technology Remotely Piloted Research Vehicle," NASA CR-143841, June 1977.
89. Tulinius, J. R. and Margason, R. J., "Aircraft Aerodynamic Designed Evaluation Methods," AIAA Paper No. 76-15, January 1976.
90. Steger, J. L. and Klineberg, J. M., "A Finite Difference Method For Transonic Airfoil Design," AIAA Journal, Vol. 11, No. 5, May 1973.

91. Schmidt, W. and Hedman, S., "Recent Explorations in Relaxation Methods for Three-Dimensional Transonic Potential Flow," ICAS Paper 76-22, October 1976.
92. Haines, A. B., "Aerodynamics," Aeronautical Journal, July 1976, pp. 277-293.
93. Hicks, R. and Henne, P. A., "Wing Design by Numerical Optimization," AIAA Paper No. 77-1247, August 1977.
94. Sloof, J. W., "Wind Tunnel Tests and Aerodynamic Computations; Thoughts on Their Use in Aerodynamic Design."
95. Haines, A. B., "Computers and Wind Tunnels Complementary Aids to Aircraft Design," Aeronautical Journal, July 1977.
96. Haines, A. B., "Wing Section Design for Swept-Back Wings at Transonic Speeds," Journal of the Royal Aeronautical Society, Vol. 61, April 1957, pp. 238-244.